Exploring Light Sterile Neutrinos and Long-Range Forces in Long-Baseline Experiments

By

Sabya Sachi Chatterjee

PHYS07201204002

Institute of Physics, Bhubaneswar

A thesis submitted to the

Board of Studies in Physical Sciences

In partial fulfillment of requirements

For the Degree of

DOCTOR OF PHILOSOPHY

of

HOMI BHABHA NATIONAL INSTITUTE

January, 2018

Homi Bhabha National Institute

Recommendations of the Viva Voce Board

As members of the Viva Voce Board, we certify that we have read the dissertation prepared by Sabya Sachi Chatterjee entitled "Exploring Light Sterile Neutrinos and Long-Range Forces in Long-Baseline Experiments" and recommend that it may be accepted as fulfilling the dissertation requirement for the Degree of Doctor of Philosophy.

____ Date:
Chairman -

____ Date:
Guide/Convener -

____ Date:
External examiner -

____ Date:
Member 1 -

____ Date:
Member 2 -

Final approval and acceptance of this dissertation is contingent upon the candidate's submission of the final copies of the dissertation to HBNI.

I hereby certify that I have read this dissertation prepared under my direction and recommend that it may be accepted as fulfilling the dissertation requirement.

Date:

Place:

Co-guide (if applicable) **Guide**

STATEMENT BY AUTHOR

This dissertation has been submitted in partial fulfillment of requirements for an advanced degree at Homi Bhabha National Institute (HBNI) and is deposited in the Library to be made available to borrowers under rules of the HBNI.

Brief quotations from this dissertation are allowable without special permission, provided that accurate acknowledgement of source is made. Requests for permission for extended quotation from or reproduction of this manuscript in whole or in part may be granted by the Competent Authority of HBNI when in his or her judgement the proposed use of the material is in the interests of scholarship. In all other instances, however, permission must be obtained from the author.

Sabya Sachi Chatterjee

DECLARATION

I, hereby declare that the investigation presented in the thesis has been carried out by me. The work is original and has not been submitted earlier as a whole or in part for a degree / diploma at this or any other Institution / University.

Sabya Sachi Chatterjee

List of Publications arising from the thesis

Journal

1. "Exploring Flavor-Dependent Long-Range Forces in Long-Baseline Neutrino Oscillation Experiments" by **Sabya Sachi Chatterjee**, Arnab Dasgupta, and Sanjib Kumar Agarwalla. **JHEP 1512 (2015) 167**.
2. "Discovery Potential of T2K and NOνA in the Presence of a Light Sterile Neutrino" by Sanjib Kumar Agarwalla, **Sabya Sachi Chatterjee**, Arnab Dasgupta, and Antonio Palazzo. **JHEP 1602 (2016) 111**.
3. "Physics Reach of DUNE with a Light Sterile Neutrino" by Sanjib Kumar Agarwalla, **Sabya Sachi Chatterjee**, and Antonio Palazzo. **JHEP 1609 (2016) 016**.
4. "Octant of θ_{23} in danger with a light sterile neutrino" by Sanjib Kumar Agarwalla, **Sabya Sachi Chatterjee**, and Antonio Palazzo. **Phys.Rev.Lett. 118 (2017) no.3, 031804**.

Conferences

1. "Long-Range Forces in Long-Baseline Neutrino Oscillation Experiments", at "XXI DAE-BRNS High Energy Physics Symposium 2014", 09.12.2014, IIT Guwahati, India.
2. "Exploring Flavour dependent Long-Range Forces in Long-Baseline Neutrino Oscillation Experiments", at "IPM school and conference on Particle Physics (IPP15: Neutrino Physics, dark matter and B-physics", 27.09.2015, Tehran, Iran.
3. "Exploring Flavour dependent Long-Range Forces in Long-Baseline Neutrino Oscillation Experiments", at "AAPCOS 2015", 16.10.2015, SINP, Kolkata, India.

4. “Impact of Sterile Neutrino in Long Baseline Experiments”, at “Nu HoRIzons VI”, 18.03.2016, HRI, India.
5. “Octant of theta23 in danger with a light Sterile Neutrino”, at “XXII DAE-BRNS High Energy Physics Symposium 2016”, 12.12.2016, University of Delhi, India.

Sabya Sachi Chatterjee

Dedicated to
my family

ACKNOWLEDGEMENTS

It is rightly said that there are no shortcuts to success, hard work is the only way. This thesis is a culmination of my lot of hard work and efforts carried out in the last couple of years. At the same time, it also includes contributions of several people who stood by me at each and every step of this wonderful journey.

I take this opportunity to express my sincere and profound gratitude to my supervisor Dr. Sanjib Kumar Agarwalla for his excellent guidance, indefatigable help, and constant support to me both academically and non-academically since the day I joined him as a Ph.D student. His stimulating stance has always motivated me to carry forward whenever I got stuck. It has always been a great pleasure for me learning from him and working with him during my whole Ph.D days. In many ways I shall always remain indebted to him.

I am greatly thankful to my collaborator Dr. Antonio Palazzo whose contribution in my research career is simply immense. Apart from constant support and encouragement, his guidance has also changed my way of thinking towards a research problem. I also feel fortunate to have received constant support, help, and valuable suggestions from all my collaborators Prof. J.W.F. Valle, Prof. S.T. Petcov, Dr. Arnab Dasgupta, Dr. Mehedi Masud, and Pedro Pasquini during my doctoral tenure. I also thank my own group collaborator Amina for many useful discussions. All these have helped me a lot in improving my theoretical understanding and technical ability.

At this point I would also like to thank my thesis committee members Prof. Ajit M. Srivastava, Prof. Pankaj Agrawal, and Prof. Bedangadas Mohanty for their support, useful comments, and invaluable suggestions throughout this period. I also extend my sincere thanks to all the faculty members of IOP who taught me during my pre-doctoral course from which I have learnt a lot. I am also highly grateful to all my respected teachers in school, college, and university for their support, encouragements, and blessings throughout my career. My honest and humble thanks also goes to the high energy physics group of IOP for useful discussions, suggestions, and inspiring comments regarding my research works. I also greatly appreciate and acknowledge the support of all other staffs of IOP in any situation.

It is now time to say few words about my favourite IOP, a “home away from home” for the last five years or so. It would not have been possible without the love and affections I have got from all my colleagues I met on the way of this beautiful journey. Although I believe that few words are not sufficient to express my gratefulness towards all those, nonetheless I would like to make an honest effort to accomplish this inevitable task. I start by thanking all my junior and senior research friends for their love, care, and concern in all situations which not only made me feeling happy always but also made my campus life more memorable. My special thanks goes to my batchmates Priyo, Puspendu, Shreyansh, Bidisha, and Sudipta who have always been with me since the day I started my journey in IOP.

There are few persons whom I have met in IOP also deserve special words of thanks. Bidisha, Shreekant, Atanu da, Sudipto (Paul chowdhury) da, Younus da, Surasree di, Arnab da, Srikumar da, Partha da, Kirtiman da, Manimala di, and Debottam da are amongst them. I had spent large amount of time with them and enjoyed every bit of it. I am highly thankful to all of them for their constant support, encouragement, and valuable suggestions in my good and bad times. At this point I must mention that Kirtiman da, Manimala di, and Debottam da truely deserve a big thanks for making my campus life more enjoyable and memorable during the last one year or so. From the academic perspective their guide, support, and encouragements have always been immense helpful to me. Now non-academically I guess it is impossible to describe my attachment with them in few words. Nonetheless, I must say that almost each and every moment I have enjoyed with them starting from long "adda", enjoying different kind of cuisines in different restaurants, tasting awesome foods prepared by Manimala di and Kirtiman da in their respective apartments, going to cinema together, and many others. I would like to express my sincere thanks and gratefulness to all of them.

I think no word is sufficient to express my gratefulness to my loving parents. It is because of their love, affection, encouragement, blessings, and unconditional support, I have successfully overcome all the ups and downs not only in this significant journey but also in the journey of my whole life so far. Thank you maa and baba for always being with me, for always giving me confidence and for always believing in me. I would also like to thank my loving brother Choton and my loving elder sister Priyanka for their love and constant support throughout this journey. I would also like to thank all my family members for their love, support, and encouragement. Finally I would like to express my biggest thanks, profound love, and greatest respect to a very special one, my best friend and my loving wife Puja. It would not have been possible without her great company, love, all kind of support, and encouragement at each and every moment of the last one decade of my life. I always feel blessed to have her in my life.

Contents

Synopsis

Neutrino physics is one of the most important fields of research in the intensity frontier of high energy particle physics. Following the discovery of neutrino oscillations, understanding the neutrino properties, specially its mass and mixing through the oscillation experiments, have been one of our main priorities for the last few decades. To accomplish that goal, lots of experimental efforts have been put together in the atmospheric, accelerator, solar and reactor sectors. All these greatest efforts have established the 3-flavor (ν_e, ν_μ, and ν_τ) regime of neutrinos very firmly which involves two distinct mass-squared splittings (atmospheric splitting, $|\Delta m^2_{31}| = |m^2_3 - m^2_1|$ or $|\Delta m^2_{32}| = |m^2_3 - m^2_2|$, and solar splitting, $\Delta m^2_{21} = m^2_2 - m^2_1$), three mixing angles ($\theta_{12}$, θ_{13}, θ_{23}), and one CP-phase δ_{CP}, where, m_1, m_2, and m_3 are the masses of three mass eigenstates ν_1, ν_2, and ν_3 respectively. However, despite the greatest experimental efforts, there are two fundamental oscillation parameters, namely θ_{23} and δ_{CP} remain poorly determined. In addition, although the sign of Δm^2_{21} is known to be positive, but the sign of Δm^2_{31} remains unknown and this is known as mass hierarchy (MH) problem. It can be either positive ($m_1 < m_2 < m_3$), known as normal hierarchy (NH) or it can be negative ($m_3 < m_1 < m_2$), denoted as inverted hierarchy (IH). On the other hand, any value of δ_{CP} other than 0 or π will lead to the discovery of leptonic CP-violation (CPV). Now concerning the value of θ_{23}, current global neutrino data and the recent result from the NOνA experiment [1] hints towards non-maximal θ_{23} with two nearly degenerate solutions: one $< \pi/4$, termed as lower octant (LO), and the other $> \pi/4$, denoted as higher octant (HO). The identification of the θ_{23} octant is a crucial goal in neutrino physics due to its deep implications for the theory of neutrino masses and mixing. From a phenomenological perspective, the information on the θ_{23} octant is also a vital input. In fact, it is well known that the identification of the two unknown properties MH and CPV is strictly intertwined with the determination of θ_{23} because of parameter degeneracy. A rich experimental program is already underway and, at the forefront of intensity frontier, the ongoing and upcoming future generation LBL experiments are expected to play a bigger role to identify all these unknown properties, and to refine the estimates of the known mass-mixing parameters.

All of the above discussions lie within the standard 3×3 unitary mixing scheme, where it is assumed that the only relevant interactions of neutrinos with the matter occur through the standard model weak interactions. However, there may be large number of possibilities for which the standard framework needs to be modified and in addition, some new interactions may also arrise. We call these possibilities as new physics. For example, Non Standard Interaction (NSI), CPT violation, presence of long-range force, existence of sterile neutrino, unitarity violation of leptonic mixing matrix, and many others. All of them may pose a great challenge to disentangle their effects from the so-called standard 3ν neutrino oscillation picture. In this thesis, we discuss two of those new physics scenarios namely, presence of an eV-scale sterile neutrino and presence of long-range force along with their impact in long-baseline neutrino oscillation experiments.

Impact of an eV-scale sterile neutrino in LBL experiments: Let us now start our discussion with sterile neutrino. The standard 3-flavor framework is a very very successfull framework in explaining almost all the neutrino data available so far. However there have been few anomalies observed at the short-baseline (SBL) experiments, which cannot be accommodated in the 3-flavor scheme. All of them indicate towards the existence of at least one new heavy mass eigenstate ν_4 which gives rise a much larger mass-squared difference $O(\mathrm{eV}^2)$. This hypothetical fourth mass eigenstate known as sterile. It is assumed to be weakly mixed with the active neutrino flavors $(\nu_e, \nu_\mu, \nu_\tau)$, and it is separated from the standard mass eigenstates (ν_1, ν_2, ν_3) by a large $O(\mathrm{eV}^2)$ splitting, giving rise to the hierarchical pattern $|\Delta m^2_{21}| \ll |\Delta m^2_{31}| \ll |\Delta m^2_{41}|$. The 3+1 scheme involves six mixing angles and three (Dirac) CP-violating phases. In this scheme, the mixing can be parameterized as, $U = \tilde{R}_{34} R_{24} \tilde{R}_{14} R_{23} \tilde{R}_{13} R_{12}\,,$
where, R_{ij} $(\tilde{R}_{ij})$ is a real (complex) rotation in the (i, j) plane. The details of the parametrization of U can be seen in [2]. Hence, in case of discovery of a sterile neutrino, we would face the formidable challenge of identifying six more properties namely, 3 mixing angles

(θ_{14}, θ_{24}, and θ_{34}), 2 CP-phases (δ_{14} and δ_{34}), and the sign of Δm^2_{41}, in addition to those involved in the standard 3-flavor framework.

It is now interesting to ask if there exists any extra mass eigenstate(s) in Nature then does it affect the standard expectations of the so-called 3-flavor phenomena like MH determination, CPV discovery, and Octant discovery which are expected to be well addressed by the long-baseline (LBL) experiments in near future. Therefore, in view of the potential discovery of a light eV-scale sterile neutrino at the SBL experiments, a reassessment of the performance of the planned LBL projects appears to be mandatory. To accomplish that goal, a few attempts have been persued in the literature and as a consequence, few interesting outcomes have come out from that studies. However, the knowledge is not fully complete and it requires an extensive study to investigate the known and unknown features in LBL setups assuming full exposure of each experiment. In this direction, we present a detailed and prospective study of the physics potential of the two currently running LBL setups T2K and NOνA, and one future generation highly sophisticated experiment DUNE in presence of an eV-scale sterile neutrino, taking into account the future full exposure of each experiment. All our findings have been published in the following journal articles [3, 4, 5]. The important observations arising out of these studies can be stated as follows:

In our work [3], we have explored the physics potential of T2K and NOνA in presence of an eV-scale light sterile neutrino assuming an expected full exposure regime of each experiment. We start with a detailed discussion of the analytical and numerical behavior of the 4-flavor $\nu_\mu \to \nu_e$ and $\bar{\nu}_\mu \to \bar{\nu}_e$ transition probabilities. Along with the off-axis event spectra for both the experiments, we have also represented the bi-probability and bi-events plots for the first time in more general 3+1 scheme, commonly used in the 3-flavor framework. Without going into the details of chi-squared measurement, these representations give us a bird-eye view of the physics potential of these experiments. After having a rough overview, we have performed an elaborative study to assess the sensitivity of both these experiments (taken alone or in combined mode) in the context of mass hierachy and CP-violation dicovery. We found that in 3+1 scheme, both the CP-violation induced by the standard CP-phase $\delta_{13} \equiv \delta_{CP}$, and the neutrino mass hierarchy discovery potential of these two experiments gets substantially deteriorated with respect to the standard 3ν scheme. The degree of loss of sensitivity depends on the value of the unknown CP-phase δ_{14}. We have also assessed the discovery potential of total CP-violation (i.e., induced simultaneously by the two CP-phases δ_{13} and δ_{14}) taking into account the combined data of both these experiments. The most important message from this assessment is that if we do not know the exact source of the CP-violation (induced by δ_{13} or δ_{14}) then we may have chance to observe CP-violation at more than 3σ confidence level which is ofcourse a strong indication of the new physics. Now likewise the CPV discovery analysis, it is also important to analyse how good these experiments are in reconstructing the true values of such CP-phases irrespective of the fact that these phases may or may not contribute to the CPV discovery. In this regard, we have found that the typical (1σ level) uncertainty on the reconstructed phases is approximately 40^0 for δ_{13} and 50^0 for δ_{14}.

After exploring the physics potential of T2K and NOνA, in [4], we have investigated the impact of an eV-scale sterile neutrino at the more sensitive future-generation LBL facility DUNE. We have mainly addressed two fundamental issues namely MH and CP sensitivity in detail. We have started our discussion by introducing the theoretical framework and presented a detailed discussion of the behavior of the 4-flavor $\nu_\mu \to \nu_e$ transition probabilities both in vacuum and in matter. From these discussions we realize that apart from θ_{14} and its associated CP-phase δ_{14}, the impact of the active-sterile mixing angle θ_{34} and its associated CP-phase δ_{34} can be significant for the DUNE baseline which we have clearly shown in the bi-probability and bi-events plots. After having all those discussions in detail, we have presented the results of the sensitivity study of the mass hierarchy in the 3+1 scheme. We found that the discovery potential of the neutrino mass hierarchy (MH), remains well above the 5σ level if all the three active-sterile mixing angles are relatively small ($\theta_{14} = \theta_{24} = \theta_{34} = 9^0$). In contrast, if the third mixing angle θ_{34} is taken at its upper limit ($\theta_{34} = 30^0$), the MH sensitivity can drop to 4σ level. From the analysis it is clear that the spectral information of the wide-band beam in DUNE plays a fruitful role in preserving a good MH sensitivity even in the 3+1 scheme. We have also assessed the sensitivity to the CPV induced both by the standard CP-phase $\delta_{13} \equiv \delta_{CP}$ and by the new CP-phases (δ_{14} and δ_{34} in our parameterization). We have found that the performance of DUNE in claiming the discovery of CPV induced by δ_{13} is appreciably degraded with respect to the 3-flavor case. In particular, the maximal sensitivity (reached around $\delta_{13} = \pm 90^0$) decreases from the 5σ to the 4σ level if all the three new mixing angles are small ($\theta_{14} = \theta_{24} = \theta_{34} = 9^0$) and can drop almost to the 3σ level for $\theta_{34} = 30^0$. The sensitivity to the CP-violation induced by the new CP-phase δ_{14} can reach the 3σ level for an appreciable fraction of its true values but never reaches the 4σ level. The sensitivity to the third CP-phase δ_{34}, which arises exclusively through matter effects, is appreciable only if θ_{34} is large. Now as a most general case we have also evaluated the capability of DUNE in reconstructing the true CP phases specially in $[\delta_{13} - \delta_{14}]$ plane. We found that the typical 1σ level uncertainty on the reconstructed CP-phases is approximately 20^0 (30^0) for δ_{13} (δ_{14}) in the case $\theta_{34} = 0$, whereas the reconstruction of δ_{14} but not that of δ_{13} appreciably degrades if θ_{34} is large.

Now concerning to octant issue, in [5], we have addressed for the first time the impact of a light eV-scale sterile neutrino in identifying the octant of the mixing angle θ_{23} in the context of DUNE. Here our main goal is to discriminate one octant from another assuming that we generate data with some true choice say LO (or, HO) and then we distinguish it from the test choice HO (or, LO) respectively. We commence our discussions with a detail theoretical framework in the context of θ_{23} octant which is then followed up by the bi-events plot cultivation. From the bi-events plot, the message is very clear and it says that in 3-flavor scheme, the two ellipses (running parameter is δ_{13}) corresponding to LO and HO respectively are well separated from each other in $[\nu_e, \bar{\nu}_e]$ appearance events plane, whereas the blobs (the ellipses becomes blobs in 3+1 scheme due to two running parameters δ_{13} and δ_{14}) corresponding to LO and HO respectively overlap with each other in 3+1 scheme in the same plane. This gives us a rough idea that the sensitivity of discriminating one octant from another gets lost in 3+1 scheme with respect to 3-flavor scheme due to octant and CP phase degeneracy. To justify this result, we have shown our results in further details in chi-squared level. All the results confirm that the sensitivity to the octant of θ_{23} can be completely lost in the presence of active-sterile oscillations and this can be attributed to the following reasons. In 3+1 scheme, the $\nu_\mu \to \nu_e$ transition probability acquires a new interference term which was first identified in [2]. This new interference term can perfectly mimic a swap of the θ_{23} octant, even when we use the spectral information from both the neutrino and antineutrino channels. This is a very very important result we have obtained in this thesis. We have checked that this result is also valid for any accelerator based LBL experiments like T2K, T2HK, NOνA, and others. It remains to be seen if other kinds of experiments, in particular those using atmospheric neutrinos, can lift or at least alleviate this octant and CP phase degeneracy. Our educated guess is that this would prove to be very difficult since obtaining a satisfying θ_{23} octant sensitivity with atmospheric neutrinos is a very hard task already in the 3-flavor framework, and in the enlarged 3+1 scheme, the situation should naturally worsen.

As a whole it is worth to mention that we have addressed various issues in detail in presence of one eV-scale sterile neutrino and we hope that all our works would certainly give much deeper insight in exploring the light sterile neutrino in LBL experiments.

Long-range force and its impact in LBL experiments: Let us now discuss another new physics issue namely the impact of long-range force (LRF) in long-baseline experiments and in that regard we have considered two LBL experiments DUNE and LBNO as case study. As long as this new physics is concerned, it arises as a cosequence of the addition of an extra $U(1)'$ gauge boson along with the standard $SU(2)\otimes U(1)$ gauge group. If the mass of this new gauge boson is light enough then the range of the force induced by it may have terrestrial range and the force is known as long-range force. The concept of LRF in particle physics was first introduced by Yang-Lee [6] and Okun [7]. It has been noticed that there are three leptonic combinations of $U(1)'$ symmetries possible, namely $L_e - L_\mu$, $L_e - L_\tau$, and $L_\mu - L_\tau$, which can be gauged in an anomaly free way with minimal matter content and they lead to new non-universal flavor-diagonal neutral current (FDNC) interactions.

For an example, the LRF between the electrons inside the Sun and the neutrinos in Earth can generate a flavor-dependent long-range potential $V_{e\mu/e\tau}$ which can give rise to non-trivial three neutrino mixing affects in terrestrial experiments, and could influence the neutrino propagation through matter. This potential for $L_e - L_\mu$ symmetry can be written as,

$$\begin{aligned} V_{ee} &= +\frac{g_{z'}^2}{4\pi}\frac{N_e^\odot}{R_{ES}} \equiv \alpha_{e\mu}\frac{N_e^\odot}{R_{ES}} \equiv V_{e\mu}, \\ V_{\mu\mu} &= -\frac{g_{z'}^2}{4\pi}\frac{N_e^\odot}{R_{ES}} \equiv -\alpha_{e\mu}\frac{N_e^\odot}{R_{ES}} \equiv -V_{e\mu}, \\ V_{\tau\tau} &= 0. \end{aligned}$$

$\alpha_{e\mu}$ is the effective gauge coupling parameter of $L_e - L_\mu$ symmetry, $N_e^\odot \approx 10^{57}$ is the total number of electrons inside the Sun, and $R_{ES} \approx 1.5 \times 10^{13}$ cm is the distance between Earth and Sun. So the potential due to Sun can be written as,

$$V_{e\mu} = \frac{\alpha_{e\mu} N_e^\odot}{R_{ES}} \approx \frac{\alpha_{e\mu} \times 10^{57}}{7.6 \times 10^{26}\, GeV^{-1}} \approx 1.3 \times 10^{-11} eV \left(\frac{\alpha_{e\mu}}{10^{-50}}\right)$$

The sign of this potential is opposite for antineutrinos, and affects the neutrino and antineutrino oscillation probabilities in different fashion. The key point here is that for long-baseline neutrinos, $\Delta m^2/2E \sim 2.5 \times 10^{-13}$ eV (assuming $\Delta m^2 \sim 2.5 \times 10^{-3}$ eV^2 and $E \sim 5$ GeV) which is comparable to $V_{e\mu}$ even for $\alpha_{e\mu} \sim 10^{-52}$, and can influence the long-baseline experiments significantly. For the Fermilab-Homestake (1300 km) and CERN-Pyhäsalmi (2290 km) baselines, the Earth matter potentials are also around 10^{-13} eV (see Table 1), suggesting that V_{CC} can also interfere with $V_{e\mu}$ and $\Delta m^2_{31}/2E$, having substantial impact on the oscillation probability. In [8], we have explored few interesting possibilities which can be studied in these LBL experiments in presence of LRF. All our findings are briefly described below.

Set up	1^{st} Osc. max. (GeV)	$\frac{\Delta m^2_{31}}{2E}$ (eV)	V_{CC} (eV)	$V_{e\mu}$ (eV)	
				$\alpha_{e\mu} = 10^{-52}$	$\alpha_{e\mu} = 10^{-53}$
DUNE	2.56	4.8×10^{-13}	1.1×10^{-13}	1.3×10^{-13}	1.3×10^{-14}
LBNO	4.54	2.7×10^{-13}	1.3×10^{-13}	1.3×10^{-13}	1.3×10^{-14}

Table 1: Comparison between different potential strengths faced by the neutrinos.

To start with, first we derived the very simple and compact analytical expressions of $\nu_\mu \to \nu_e$ appearance and $\nu_\mu \to \nu_\mu$ survival oscillation probabilities in presence of both LRF and Earth matter effect. There we have also shown the running behavior of all the standard oscillation parameters as a function of neutrino energy, which is quite helpful to have better understanding about the numerical behavior of all the results. Following that we have extended our discussion by making detail spectral analysis of both the experiments DUNE and LBNO with and without the presence of LRF which shows a clear distortion of spectrum between the two cases. This is more evident when we draw the bi-events plot taking the effective gauge coupling strength $\alpha_{e\mu} = 10^{-52}$ as a benchmark value. The behavior of the bi-events ellipses are different for both the cases with and without the presence of LRF. In the very next we have asked an obvious question, namely how good these experiments are in constraining this new physics. In that regard we have put bound on the coupling strength $\alpha_{e\mu}$ arising due to $L_e - L_\mu$ symmetry. We found that for $\delta_{CP}\,(true) = -90^\circ$ and for NH true, the expected bound from the DUNE (35 kt) setup at 90% C.L. is $\alpha_{e\mu} < 1.9 \times 10^{-53}$. The same from the LBNO (70 kt) experiment is $\alpha_{e\mu} < 7.8 \times 10^{-54}$, suggesting that the constraint from LBNO is 2.4 times better than DUNE. We have noticed that these limits are robust with respect to the true choice of δ_{CP} and mass hierarchy. This future limit from the DUNE (LBNO) experiment is almost 30 (70) times better than the existing bound from the SK experiment [9].

We have also studied in detail the CP-violation discovery reach of DUNE (35 kt) and LBNO (70 kt) in the presence of LRF. We have seen that the chance of CP-violation (CPV) discovery gets substantially deteriorated as compared to the standard expectation depending on the true value of $\alpha_{e\mu}$. At 3σ with $\alpha_{e\mu}$(true) = 10^{-52} and true NH, the CPV coverage in δ_{CP}(true) is 41% (30%) for DUNE (LBNO) while in SM case, the coverage is 48% for DUNE and 55% for LBNO. In case of true IH, the impact is even more striking. For example, if $\alpha_{e\mu}$(true) = 10^{-52}, the 3σ C.L. CPV coverage in δ_{CP}(true) is 37% (12%) for DUNE (LBNO), while in the 'SM' framework, DUNE (LBNO) can do so for 53% (60%) values of true δ_{CP}. As the true value of $\alpha_{e\mu}$ approaches toward 10^{-52}, the CPV coverages in δ_{CP}(true) fall sharply for both the set-ups, and ultimately around $\alpha_{e\mu}$(true) = 2×10^{-52}, the coverages almost become zero.

Finally, we have investigated the possibility of mass hierarchy determination in presence of LRF. In the standard case, due to the large Earth matter effects, DUNE and LBNO both can resolve the issue of mass hierarchy at very high confidence level. However, if LRF exists in Nature, then for DUNE, the MH sensitivity remains above the standard expectations provided the true value of $\alpha_{e\mu} < 5 \times 10^{-52}$, and for LBNO, the MH discovery reach does not go below the 'SM' value as long as $\alpha_{e\mu}$ (true) is smaller than 10^{-52}.

It is worth to note that although we have presented all the results considering the $L_e - L_\mu$ symmetry, similar analysis can be followed for the $L_e - L_\tau$ or other kind of anomaly free leptonic symmetries. We have seen that even if the mass of the new gauge boson is very light due to the long-range nature of this new force, and the value of the gauge coupling parameter is very low, it can have significant effect on the standard neutrino oscillation physics. As a consequence, we can either constrain or discover this new physics using the neutrino oscillation data. Another noteworthy point to make is that this is one of such new physics examples where the behavior for neutrinos and antineutrinos is different and for that we do not need to invoke the scenarios like CP or CPT violation. This special characteristic emphasizes the importance of analyzing this double behavior separately. We hope that our rigorous efforts would certainly help to explore this new physics in detail in near future.

Bibliography

[1] **NOvA** Collaboration, P. Adamson *et al.*, "Measurement of the neutrino mixing angle θ_{23} in NOvA," *Phys. Rev. Lett.* **118** no. 15, (2017) 151802, `arXiv:1701.05891 [hep-ex]`.

[2] N. Klop and A. Palazzo, "Imprints of CP violation induced by sterile neutrinos in T2K data," *Phys. Rev.* **D91** no. 7, (2015) 073017, `arXiv:1412.7524 [hep-ph]`.

[3] S. K. Agarwalla, S. S. Chatterjee, A. Dasgupta, and A. Palazzo, "Discovery Potential of T2K and NOvA in the Presence of a Light Sterile Neutrino," *JHEP* **02** (2016) 111, `arXiv:1601.05995 [hep-ph]`.

[4] S. K. Agarwalla, S. S. Chatterjee, and A. Palazzo, "Physics Reach of DUNE with a Light Sterile Neutrino," *JHEP* **09** (2016) 016, `arXiv:1603.03759 [hep-ph]`.

[5] S. K. Agarwalla, S. S. Chatterjee, and A. Palazzo, "Octant of θ_{23} in danger with a light sterile neutrino," *Phys. Rev. Lett.* **118** no. 3, (2017) 031804, `arXiv:1605.04299 [hep-ph]`.

[6] T. Lee and C.-N. Yang, "Conservation of Heavy Particles and Generalized Gauge Transformations," *Phys.Rev.* **98** (1955) 1501.

[7] L. B. Okun, "On muonic charge and muonic photons," *Yad. Fiz.* **10** (1969) 358–362.

[8] S. S. Chatterjee, A. Dasgupta, and S. K. Agarwalla, "Exploring Flavor-Dependent Long-Range Forces in Long-Baseline Neutrino Oscillation Experiments," *JHEP* **12** (2015) 167, `arXiv:1509.03517 [hep-ph]`.

[9] A. S. Joshipura and S. Mohanty, "Constraints on flavor dependent long range forces from atmospheric neutrino observations at super-Kamiokande," *Phys.Lett.* **B584** (2004) 103–108, `arXiv:hep-ph/0310210 [hep-ph]`.

List of Figures

List of Tables

Chapter 1

Introduction

Studying the properties and interactions of neutrinos have been a very very interesting and exciting area in particle physics, astroparticle physics and cosmology ever since Pauli proposed its existence in 1930. Last few decades or so have been a revolution for neutrino physics from the perspective of experimental hunting. Inspite of their very very weakly interacting nature, we have so far gathered a good amount of knowledge about them from all three sectors: cosmology [1, 2, 3], particle [4, 5, 6] and astroparticle [7, 8, 9, 10] physics. Neutrino cosmology offers a profound inter connection between the two exciting branches of physics namely neutrino physics and cosmology and the tremendous success of the standard Big Bang model of cosmology has established the fact that neutrinos play an important role in the anisotropies of the cosmic microwave background radiation, in the primordial nucleosynthesis, in the formation of the large scale structures and so on. Data from different cosmological observations have given a good idea about the scale of absolute value of neutrino masses. The most recent data from the measurement of temparature and low multipole polarization anisotropies of the Cosmic Microwave Background (CMB) combined with the baryon acoustic oscillation and galaxy clustering data from Baryon Oscillation Spectroscopy Survey (BOSS) gives an upper bound on the sum of three active neutrino masses $\sum m_\nu < 0.183$ eV at 95% confidence level [11]. However the further inclusion of high multipole polarization data makes the limit more stronger to

0.176 eV. It is believed that the decays of heavy Majorana neutrinos might have also crucial role in making the universe matter dominant over antimatter via leptogenesis mechanism. Many theorists strongly believe that KeV-scale heavy neutrinos may be one of the major candidates of the dark matter problem [12] even though there is no cosmological evidence till now. Nonetheless, a substantial amount of data from different running and future experiments in the sector of neutrino cosmology is expected to help us in knowing the above unknown issues and provide us more compelling information about the neutrino masses, mixing and CP-violation.

Apart from the cosmological observations, understanding the neutrino properties, specially its mass and mixing through neutrino oscillation phenomenology have been one of our utmost priorities for the last few years, and to accomplish that, lots of experimental efforts have been put together in the atmospheric, accelerator, solar, and reactor sectors. More than fifteen years ago, pioneering observations of neutrinos originating from natural sources (the sun core and the earth atmosphere) led to the first evidence of neutrino oscillations establishing the massive nature of these fundamental particles. Such a discovery, recently awarded with the Nobel Prize [13], has been the first of a long series of milestones in our understanding of neutrinos, whose properties have been gradually clarified by the subsequent findings of several other experiments performed with man-made neutrino sources (reactors and accelerators).

The two apparently disjoint effective 2-flavor descriptions initially introduced to explain separately the solar and the atmospheric neutrino anomalies have been gradually recognized as two pieces of a single and more complex mosaic, which is currently accepted as the standard picture of neutrino oscillations. Such a 3-flavor framework involves two distinct mass-squared splittings (atmospheric splitting, $|\Delta m^2_{31}| = |m^2_3 - m^2_1|$ or $|\Delta m^2_{32}| = |m^2_3 - m^2_2|$, and solar splitting, $\Delta m^2_{21} = m^2_2 - m^2_1$), three mixing angles ($\theta_{12}$, θ_{13}, θ_{23}), and one CP-phase δ_{CP}, where, m_1, m_2, and m_3 are the masses of the three neutrino mass eigenstates ν_1, ν_2, and ν_3 respectively.

The latest fundamental step in the establishment of the 3-flavor scheme has been accomplished very recently (during 2012), with the determination of the long-sought third mixing angle θ_{13} by means of dedicated reactor experiments [14, 15, 16]. This discovery has not only opened the way to the measurement of the last unknown 3-flavor parameters: the CP-phase $\delta_{\rm CP}$ and the neutrino mass hierarchy (MH), i.e. the sign of Δm^2_{31} but also brought us into the precision era. The sign of Δm^2_{31} can be either positive, known as normal hierarchy (NH) or negative, denoted as inverted hierarchy (IH). On the other hand, any value of $\delta_{\rm CP}$ other than 0 or π leads to the leptonic CP-violation (CPV). A rich experimental program is underway to identify these two unknown properties, and to refine the estimates of the known mass-mixing parameters [17, 18, 19, 20, 21].

Apart from the above mentioned two fundamental unknown parameters, there is another oscillation parameter widely known as atmospheric mixing angle θ_{23} which is also poorly determined at present. Current global neutrino data [22, 23, 24, 25] and the recent result from NOνA experiment [26] hints towards non-maximal θ_{23} with two nearly degenerate solutions: one $< \pi/4$, termed as lower octant (LO), and the other $> \pi/4$, denoted as higher octant (HO) (see chapter 4 and chapter 8 for details). The identification of the θ_{23} octant is a crucial goal in neutrino physics due to its deep implications for the theory of neutrino masses and mixing (see [27, 28, 29, 30, 31] for reviews). Notable models where the θ_{23} octant plays a key role are $\mu \leftrightarrow \tau$ symmetry[1] [34, 35, 36, 37, 38, 39, 40, 41], A_4 flavor symmetry [42, 43, 44, 45, 46], quark-lepton complementarity [47, 48, 49, 50], and neutrino mixing anarchy [51, 52]. From a phenomenological perspective, the information on the θ_{23} octant is also a vital input. In fact, it is well known that the identification of the two unknown properties (MH and CPV) is strictly intertwined with the determination of θ_{23} because of parameter degeneracy issues [53, 54, 55, 56, 57, 58, 59, 60, 61].

At the forefront of the intensity frontier, ambitious next-generation long-baseline

---

[1] As shown in [32, 33], in the 3+1 scheme, the condition $\theta_{23} \simeq 45^\circ$ implies an approximate realization of $\mu \leftrightarrow \tau$ symmetry, similarly to what happens in the standard 3-flavor scheme. Therefore, establishing that θ_{23} is maximal (non-maximal) would imply that $\mu \leftrightarrow \tau$ symmetry is unbroken (broken), irrespective of the existence of a light sterile neutrino.

(LBL) neutrino oscillation experiments are under consideration [17, 18, 19, 20, 21], whose mission will be that of deciphering the fundamental properties of these elusive particles, and exploring the interactions to which they participate. The main objectives of the LBL experiments are to determine the leptonic CP-violation (CPV), to identify the neutrino mass hierarchy (MH), and to pin point the correct octant of θ_{23}.

In general, LBL experiments are sensitive to the mass hierarchy[2] because of their long-baseline nature which is well complemented by the high matter effect. The more the baseline is, the more is the advantage to unravel the correct MH. Similarly, the LBL experiments are also regarded as the high-precision neutrino interferometers, such that they are the best place to study CPV, whose manifestation is intimately related to interference phenomena. This is clearly the case of the standard 3-flavor CPV, which is observable through the interference of the oscillations driven by the two distinct (atmospheric and solar) frequencies. Several non-standard neutrino properties are also the sources of additional CPV, and the LBL machines would naturally have a pivotal role in these searches.

As already mentioned above, not only the determination of MH and CPV, but also one of the most promising options to identify the θ_{23} octant is also offered by the long-baseline (LBL) accelerator experiments. In these setups, a synergy between the $\nu_\mu \to \nu_e$ appearance and $\nu_\mu \to \nu_\mu$ disappearance channels exists [53, 56], which confers an enhanced sensitivity to the θ_{23} octant. The $\nu_\mu \to \nu_\mu$ survival probability, at the leading order, depends on $\sin^2 2\theta_{23}$. Then, it is sensitive to deviations from maximality but is insensitive to the octant. On the other hand, the leading contribution to the $\nu_\mu \to \nu_e$ probability is proportional to $\sin^2 \theta_{23}$, and is thus sensitive to the octant. The combination of these two channels provides a synergistic information on θ_{23}. A residual degeneracy persists between the θ_{23} octant and the CP-phase $\delta_{\rm CP}$, but it can be lifted with a balanced exposure of neutrino and antineutrino runs [58].

Even though the attempt to unravel the properties of neutrino is a great success so

---

[2] It is worth mentioning that medium baseline reactor experiment JUNO [62] having 53 km baseline can determine MH using the shape of the spectral information.

far, there may be still many surprises waiting for us in the days to come in which neutrino oscillation experiments can play much much bigger and broader role. If specifically mentioned, then all of the above discussions lie within the standard 3×3 unitary mixing scheme, where it is assumed that the only relevant interactions of neutrinos with the matter occur through the standard model weak interactions. However, there may be large number of possibilities for which the standard framework needs to be modified and in addition, some new interactions may also arise. We call these possibilities as new physics. For example, non-standard interaction of neutrino (NSI) [63, 64, 65, 66, 67, 68], CPT violation [69, 70, 71, 72, 73, 74, 75], presence of long-range force [76, 77, 78, 79, 80, 81], existence of sterile neutrino [82, 83, 84], unitarity violation of leptonic mixing matrix [85, 86, 87, 88, 89, 90, 91] and many others which not only provocate us to think beyond the standard model (SM) but also these new physics may pose a great challenge to disentangle their effects from the standard neutrino physics. So, if they are the reality in Nature, all these issues need to be analysed carefully with perfect framework and with sufficient amount of data in future. In this thesis we discuss two of those new physics scenarios, namely presence of an eV-scale sterile neutrino and presence of long-range force along with their impact in long-baseline neutrino oscillation experiments.

Let us now first discuss some details about an eV-scale sterile neutrino. We know that the neutrino oscillation data available till date can be well explained by the standard 3-flavor framework [22, 23, 24]. However in spite of its tremendous success and of its beautiful structure, the standard 3-flavor framework may not constitute the ultimate description of neutrinos. A few anomalies have been observed at the short-baseline (SBL) experiments, which cannot be accommodated in the 3-flavor scheme (see [82, 83, 84] for a review of the topic). The two standard mass-squared splittings $\Delta m^2_{21} \equiv m^2_2 - m^2_1$ and $|\Delta m^2_{31}| \equiv |m^2_3 - m^2_1|$ are too small to produce observable effects in such setups and (at least) one new much larger mass-squared difference $O(\mathrm{eV}^2)$ must be introduced. The hypothetical fourth mass eigenstate must be essentially sterile. A great number of experimental facilities have already been planned and some of them have already started working to test such an intriguing hypothesis (see the review in [92]), which, if confirmed would represent a revolution in our understanding of neutrinos, as important as the discovery of neutrino oscillations.

At a phenomenological level, the existence of sterile neutrinos would make necessary to extend the standard 3-flavor framework. The enlarged scheme must be realized in such a way to preserve the very good description of all the other (non short-baseline) data. In the minimal extension, involving only one sterile species, the so-called $3+1$ scheme, the new mass eigenstate ν_4 is assumed to be weakly mixed with the active neutrino flavors $(\nu_e, \nu_\mu, \nu_\tau)$ and it is separated from the standard mass eigenstates (ν_1, ν_2, ν_3) by a large $O(\mathrm{eV}^2)$ splitting, giving rise to the hierarchical pattern $|\Delta m^2_{21}| \ll |\Delta m^2_{31}| \ll |\Delta m^2_{41}|$. The 3+1 scheme involves six mixing angles and three (Dirac) CP-violating phases (see sec. 2.3.1). In this scheme, the mixing can be parameterized as, $U = \tilde{R}_{34} R_{24} \tilde{R}_{14} R_{23} \tilde{R}_{13} R_{12}\,,$ where, R_{ij} ($\tilde{R}_{ij}$) is a real (complex) rotation in the (i,j) plane. The details of the parameterization of U can be seen in sec. 2.6. Hence, in case of discovery of a sterile neutrino, we would face the formidable challenge of identifying six more properties namely, 3 mixing angles (θ_{14}, θ_{24}, and θ_{34}), 2 CP-phases (δ_{14} and δ_{34}), and the sign of Δm^2_{41}, in addition to those involved in the standard 3-flavor framework.

The $3+1$ scheme naturally predicts sizable effects at the short-baselines, where the oscillating factor $\Delta_{41} \equiv \Delta m^2_{41} L/4E$ (L being the baseline and E the neutrino energy) is of order one, and one expects an oscillating behavior with the characteristic L/E dependency. As a result, the SBL experiments are the best place to look for the sign and magnitude of the Δm^2_{41}, and for the magnitude of the new mixing angles originated due to the mixing between the standard three mass eigenstates (ν_1, ν_2, ν_3) and the new mass eigenstate ν_4. However, it must be emphasized that sterile neutrinos are observable in other (non-short-baseline) types of experiments where they may manifest in a more subtle way. For example, in the solar sector, a non zero-value of the electron neutrino mixing with ν_4 (parameterized by the matrix element U_{e4}) can be felt as a small deviation of the unitarity of the (ν_1, ν_2, ν_3) sub-system [93, 94] (see also [95]). In the atmospheric sector, as first evidenced in [96], at very high [O(TeV)] energies one expects a novel MSW resonance, which may reveal as a distortion of the zenith angle distribution. To this regard we mention the dedicated analysis underway in the IceCube collaboration whose preliminary results have been shown very recently in [97]. Complementary information on sterile neutrino mixing using atmospheric neutrinos has been also extracted from Super-Kamiokande [98].

Sterile neutrino oscillations can also influence the long-baseline (LBL) accelerator experiments [3]. We recall that these setups, when working in the $\nu_\mu \to \nu_e$ (and $\bar{\nu}_\mu \to \bar{\nu}_e$) appearance channel, can probe the 3-flavor CP-violating phenomena encoded by the CP-phase $\delta_{\rm CP}$. Their sensitivity is related to the fact that at long distances the $\nu_\mu \to \nu_e$ transition probability develops a small interference term (which is completely negligible at SBL) between the oscillations induced by the atmospheric splitting and those driven by the (much smaller) solar splitting. As first evidenced in [104], in the presence of a sterile neutrino, a new interference term appears in the transition probability, which depends on one additional CP-phase[4]. Notably, the size of the new non-standard 4-flavor interference term is expected to be similar to that of the standard 3-flavor interference term. Therefore, the sensitivity to the new interference term can disclose the possibility to explore the new enlarged CP-violation (CPV) sector, which involves two additional CP-phases. It should be stressed that both in the 3-flavor [5] and 4-flavor [6] schemes, the CP-phases cannot be

---

[3] In this thesis we have mainly focused on the $\nu_\mu(\bar{\nu}_\mu) \to \nu_e(\bar{\nu}_e)$ channels even though we have also added the events in our analysis coming from $\nu_\mu(\bar{\nu}_\mu) \to \nu_\mu(\bar{\nu}_\mu)$ channels. However, information on sterile neutrinos can also be obtained from the LBL disappearance $\nu_\mu \to \nu_\mu$ searches and from the neutral current data. See the analysis performed by MINOS [99, 100], NOνA [101]. Also the appearance $\nu_\mu \to \nu_\tau$ channel can provide information, albeit currently the low statistics limits the sensitivity. See the analysis performed by OPERA [102, 103].

[4] This is true in vacuum. According to the parameterization used in [104], this CP-phase is δ_{14}. However in presence of matter, this interference term depends on one more extra CP-phase namely δ_{34} which may have significant impact on the physics analysis [see chapter 7].

[5] In 3ν framework, the oscillation picture at the SBL experiments basically boils down to the 2ν framework, and as a result of that SBL experiments are not sensitive to CPV.

[6] In the 3+1 scheme with one light eV-scale sterile neutrino, the oscillation picture at the SBL experiments also boils down to the 2-flavor scheme, and therefore, one cannot observe CPV. However when more sterile neutrinos come into play the SBL experiments can be sensitive to CPV. In this regard it is worthy to note that the SBL experiments can access only a restricted number of the CP-phases involved in the model, while the LBL ones are sensitive to all of them. For example, in the 3+2 scheme, the SBL experiments are sensitive to one CP-phase over a total of five CP-phases.

observed in SBL experiments because of the negligible values the two standard oscillating frequencies. As a whole, we see that the SBL setups are sensitive to the new mass-squared splitting and new mixing angles, where as the LBL setups are sensitive to the CP phases. Therefore, in the eventuality of discovery of a light sterile neutrino (or, of any scheme involving more than one sterile neutrino), the LBL setups would play a complementary role to the SBL experiments due to their unique sensitivity to the new CP-phases.

It is now interesting to ask if there exists any extra mass eigenstate(s) in Nature then does it affect the standard expectations of the so-called standard 3-flavor phenomena like MH, CPV and octant discovery which are expected to be well addressed by the LBL experiments in near future. Therefore, in view of the potential discovery of a light eV-scale sterile neutrino at the SBL experiments, a reassessment of the performance of the planned LBL projects appears to be mandatory. To accomplish that goal, few attempts have already been made in the literature and as a consequence, few interesting outcomes have emerged out of those attempts. For example, 4-flavor analysis[7] [104, 107] of the latest data collected by the two currently running LBL experiments T2K and NOνA[8] have already given some weak hints on the new CP-phases involved in the 3+1 scheme, and have also evidenced the fragility of the present (weak) indication in favor of the normal hierarchy, which emerges in the standard 3-flavor framework. In addition, in [107] it has been pointed out that the statistical significance of the current indications concerning the standard CP-phase δ_{CP} and the neutrino mass hierarchy is modified (reduced) in the presence of sterile neutrinos. Now in case of octant issue, most of the octant sensitivity studies have been performed within the 3-flavor framework (for recent works see [18, 58, 112, 113, 114, 115]). As a result there is a lack of knowledge about the situation in presence of 3+1 scheme. Therefore, it is timely and interesting to investigate such interesting features in LBL setups assuming full exposure of each experiment.

---

[7] Such analysis are performed for realistic values of the new active-sterile mixing angles as indicated by the global 3+1 fits [105, 106].

[8] In principle (see the 4-flavor analysis performed in [108]), the new CP-phases can impact also the $\nu_\mu \to \nu_e$ searches of ICARUS [109, 110] and OPERA [111]. However, the very low statistics prevents to extract any information on the CP-phases.

Let us now turn our focus into another new physics, namely long-range force (LRF). As long as this new force is concerned, it arrises as a consequence of the addition of an extra $U(1)'$ gauge boson along with the standard $SU(2)_L \otimes U(1)_Y$ gauge group[9]. If the mass of this new gauge boson is light enough then the range of the force induced by it may have terrestrial range and the force is known is long-range force. The concept of LRF in particle physics was first introduced by Yang-Lee [76] and Okun [77]. According to their proposal, composition dependent long-range force can be natural consequence of gauging the baryon number or lepton number and that force can be probed in the classic Etovos type of experiment [78]. It was noticed [79, 80, 81] long ago that there are three leptonic combinations of $U(1)'$ symmetries possible with minimal matter content, namely $L_e - L_\mu$, $L_e - L_\tau$, and $L_\mu - L_\tau$, which can be gauged in an anomaly free way and the gauge bosons associated with these flavor-dependent symmetries can be very light and neutral, leading to new non-universal flavor-diagonal neutral current (FDNC) interactions of the neutrinos which can give rise to non-trivial three-neutrino mixing effects in terrestrial experiments, and could affect the neutrino propagation through matter [116, 117, 118, 119, 120]. Now the question is, can we constrain/discover these long-range FDNC interactions in upcoming long-baseline neutrino experiments? If this LRF exists in Nature, can it become fatal in our attempts to resolve the remaining unknowns in neutrino oscillation?

With all these keeping in mind, in this thesis we present a detailed and prospective study of the physics potential of the two currently running LBL setups T2K [121, 122] and NOνA [123, 124], and two future generation highly sophisticated experiments DUNE [125, 126] and LBNO [127, 128] in presence of an eV-scale sterile neutrino[10] and long-range force, taking into account the future full exposure of each experiment.

---

[9] details of theoretical description is given in appendix A.

[10] Old works on sterile neutrinos at LBL can be found in [129, 130, 131, 132, 133, 134, 135, 136, 137]. More recent studies focusing on the future LBNE/DUNE experiment [125] have been recently performed in [138, 139, 140]. In principle, the CERN-Pyhäsalmi baseline of 2290 km actively studied under the umbrella of the LBNO collaboration [141, 142] can also be very sensitive to these issues. The same is also true for the future T2HK experiment [143, 144], which is a bigger version of T2K.

This thesis is organized as follows.

In chapter 2, we lay the foundation of our discussions by introducing the basic understanding of neutrino oscillations starting from 2-flavor framework followed by the 3-flavor and 4-flavor framework respectively. In chapter 3, we extend our discussions by introducing some experimental motivations for choosing an eV-scale sterile neutrino in our analysis. Here we devote few sections for the discussion of different anomalies (for example, LSND, Gallium, MiniBoone, and reactor anomalies) observed in different experiments. Before going into the discussions of experimental setups, analysis details, and obtained results in the next few chapters, in chapter 4, we give a detail discussion on the current status of the oscillation parameters involving in 3-flavor as well as in 3+1 framework. Following that, in chapter 5, we give the experimental details of all the LBL setups like DUNE, LBNO, T2K, and NOνA, and also we present the details of the simulation method used for all the numerical analyses presented in this thesis.

In chapter 6, we explore the physics potential of T2K and NOνA in presence of an eV-scale light sterile neutrino assuming an expected full exposure regime of each experiment. In section 6.1, we present a detailed discussion on the behavior of the 4-flavor $\nu_\mu \to \nu_e$ and $\bar{\nu}_\mu \to \bar{\nu}_e$ transition probabilities. For the first time we extend the bi-probability and bi-events representation, commonly used in the 3-flavor framework, to the more general 3+1 scheme. Following that, the next few sections are devoted for the presentation of the results of the sensitivity study of T2K and NOνA. Specifically, we elaborate the details of CPV discovery followed by the CP-reconstruction capability, and MH discovery potential of these two experiments. Finally we summarize our findings.

In chapter 7, we investigate the impact of an eV-scale sterile neutrino at the more sensitive next-generation LBL facility DUNE. In section 7.1, we start our discussion by introducing the theoretical framework and present a detailed discussion on the behavior of the 4-flavor $\nu_\mu \to \nu_e$ transition probabilities in vacuum and also in matter. In section 7.2, we describe the details of the statistical method used for all the analyses. In section 7.3, we make some important considerations at the level of the bi-probability and bi-events plots and at the level of the energy spectrum, and then we present the results of the sensitivity study of the mass hierarchy in the 3+1 scheme. In section 7.4, we discuss the results concerning the CPV discovery potential and the capability of reconstruction of the CP-phases. Finally we summarize our results.

In chapter 8, we explore the impact of eV-scale sterile neutrino on the measurement of octant of θ_{23}. In section 8.1, we start our discussion with the details of theoretical framework for understanding the octant issue in 3-flavor as well as in 4-flavor framework. In section 8.2, we then present all the numerical results. There we first discuss the bi-events plot and then present the octant sensitivity plots of distinguishing one octant from another in presence of 3ν as well as 3+1 scenario. Finally in section 8.3, we summarize all our results.

In chapter 9, we start section 9.1 with a discussion on flavor-dependent LRF and how it arises from abelian gauged $L_e - L_{\mu,\tau}$ symmetry. This is followed by a brief discussion on the current constraints on the effective gauge couplings $\alpha_{e\mu,e\tau}$ of the $L_e - L_{\mu,\tau}$ symmetry from various neutrino oscillation experiments. In section 9.2, we study in detail the three-flavor oscillation picture in presence of long-range potential. We derive the compact analytical expressions for the effective oscillation parameters in case of the $L_e - L_\mu$ symmetry. Next, we demonstrate the accuracy of our approximate analytical probability expressions by comparing it with the exact numerical results. We also discuss some salient features of the neutrino and antineutrino appearance and disappearance probabilities (calculated numerically) for the DUNE and LBNO baselines in the presence of long-range potential. At the beginning of section 9.3, we study the impact of the long-range potential due to $L_e - L_\mu$ symmetry on the expected event spectra and total event rates for the DUNE and LBNO experiments. In section 9.4, we describe our simulation strategy. Next, we derive the expected constraints on $\alpha_{e\mu}$ from DUNE and LBNO in section 9.5.1, and estimate the discovery reach for $\alpha_{e\mu}$ in section 9.5.2. In section 9.5.3, we study the possibility of CP-violation search in presence of LRF. Section 9.5.4 is devoted to assess the impact of LRF on mass hierarchy measurements. Finally, we summarize our results in section 9.6.

In chapter 10, we make conclusions of our findings and comment about the future outlooks. At the very end in appendix A, we present the detail derivation of the long-range potential arising because of the inclusion of an extra $U(1)_{L_e-L_\mu}$ gauge group on top of SM gauge group.

Chapter 2

Brief description of the theory of Neutrino Oscillation in 3+1 framework

2.1 A brief history of neutrino

In 1930, a new elusive particle was first postulated by Pauli in order to explain the energy, momentum, and spin angular momentum conservation in β-decay :

$$n \rightarrow p + e^- + \bar{\nu}_e \tag{2.1}$$

Later this new particle ν_e was named as "neutrino" by Fermi who developed the theory of β-decay. Experimental detection of neutrinos by the use of beta-capture was first proposed by Wang Gangchang in 1942 [145]. Later, in 1956, the detection of electron antineutrino was first confirmed in the Cowan-Reines neutrino experiment [146], for which Fredrick Reines was awarded with the Nobel Prize in 1995. However the effect of neutrino oscillation was first recorded in Ray Davis's Homestake Experiment in 1960, which confirmed a clear deficit of solar neutrino flux as compared to the Standard Solar Model prediction. This is known as solar neutrino problem. Using an analogy with the Kaon oscillation [147], in 1957, Bruno Pontecorvo proposed a theoretical framework of neutrino-antineutrino transitions based on simple quantum mechanical idea. Although such transitions have not been observed yet, but the idea gave a good starting point for the foundation of the theory of neutrino flavor oscillation which was developed by Maki, Nakagawa, and Sakata in 1962 [148]. Later in 1967, it was more elaborated by Pontecorvo[149]. According to that theory, neutrino flavor eigenstates (ν_e, ν_μ, ν_τ) are the linear super position of three mass eigenstates and these flavor eigenstates convert from one flavor to another while traveling from one space point to another space point.

In the beginning of 1998, Super-Kamiokande collaboration [150] first reported the evidence of atmospheric neutrino oscillation, which led to the solution of the long-standing atmospheric neutrino puzzle. They showed that the ratio of the muon to electron atmospheric neutrino events coming from the opposite side of the Earth were different. After a very careful analysis, they came to the conclusion that almost half of the muon neutrinos changes to tau neutrinos while passing through the Earth. Similarly in 2001, Sudbury Neutrino Observatory collaboration [151] reported the quantitative measurement of how many of the ν_es' coming from the Sun, change flavor to ν_μ and how many to ν_τ, which ultimately solved the solar neutrino puzzle. These revolutionary results have been awarded recently with the 2015 Nobel Prize [13]. All these experimental evidences of neutrino oscillation not only have confirmed that neutrinos are massive but also they have brought us into the field of precision era.

Field	$SU(3)_C \otimes SU(2)_L \otimes U(1)_Y$	Spin	Weak Isospin I^3	Electric charge Q	Color charge
$L_e \equiv (\nu_e\,,\, e^-)_L^T$	$(1,2,-1)$	$1/2$	$(1/2\,,\,-1/2)^T$	$(0\,,\,-1)^T$	None
$L_\mu \equiv (\nu_\mu\,,\, \mu^-)_L^T$	$(1,2,-1)$	$1/2$	$(1/2\,,\,-1/2)^T$	$(0\,,\,-1)^T$	None
$L_\tau \equiv (\nu_\tau\,,\, \tau^-)_L^T$	$(1,2,-1)$	$1/2$	$(1/2\,,\,-1/2)^T$	$(0\,,\,-1)^T$	None
$E_R \equiv (e_R,\, \mu_R,\, \tau_R)$	$(1,1,-2)$	$1/2$	0	-1	None
$N_S \equiv (\nu_s, ...)$	$(1,1,0)$	$1/2$	0	0	None

Table 2.1: Quantum numbers of leptons in SM framework. Here, $Q = I^3 + Y/2$. Y is the hypercharge quantum number. ν_s is defined as sterile neutrino. The exact number of sterile neutrino types is not known if it exists in Nature.

It is now worth mentioning that all the neutrinos ($\nu_e, \ \nu_\mu, \ \nu_\tau$) confirmed by the experiments are known as active neutrinos. However many theoretical models and SBL experiment anomalies (for details, please see Chapter 3) prefer to the existence of another kind of neutrino, which we call sterile neutrino. They are the hypothetical particles with right-handed chirality, do not take part directly in any kind of SM interactions except gravitational interaction. Their masses may have any values ranging from sub-eV to 10^{15} GeV. In Table 2.1, we give the details of the quantum numbers of the active and sterile neutrinos in SM framework.

2.2 Two flavor neutrino oscillation framework:

Before going into the four flavor neutrino oscillation framework, we start our discussion from the very basic effective two flavor neutrino oscillation. The underlying mechanism of neutrino oscillation is based on simple quantum mechanics. Here first we discuss the two flavor neutrino oscillation in vacuum before going into more general case of N-flavors.

We know that the time evolution of a stationary state $|\psi_k\rangle$ with energy E_k is written as

$$|\psi_k(t)\rangle = e^{-iE_k t}\,|\psi_k\rangle\,. \tag{2.2}$$

Where, the state vectors at different times simply differ by an overall complex phase factor.

In a similar fashion, the time evolution equation for two stationary neutrino mass eigenstates $|\nu_1\rangle$ and $|\nu_2\rangle$ with energy eigenvalues E_1 and E_2 respectively in vacuum is given by

$$i\frac{d}{dt}\begin{pmatrix}|\nu_1\rangle \\ |\nu_2\rangle\end{pmatrix} = \begin{pmatrix}E_1 & 0 \\ 0 & E_2\end{pmatrix}\begin{pmatrix}|\nu_1\rangle \\ |\nu_2\rangle\end{pmatrix}. \tag{2.3}$$

So, by definition the mass eigenstates evolve in time without mixing. However if there is mixing, the eigenstates are known as flavor eigenstates which are produced in weak interactions. The flavor eigenstates are related to the mass eigenstates as

$$\begin{pmatrix} |\nu_e\rangle \\ |\nu_\mu\rangle \end{pmatrix} = \begin{pmatrix} \cos\theta & \sin\theta \\ -\sin\theta & \cos\theta \end{pmatrix} \begin{pmatrix} |\nu_1\rangle \\ |\nu_2\rangle \end{pmatrix}. \tag{2.4}$$

After a time t,

$$|\nu_\mu(t)\rangle = -\sin\theta\, e^{-iE_1t}\, |\nu_1\rangle + \cos\theta\, e^{-iE_2t}\, |\nu_2\rangle\,. \tag{2.5}$$

Now the probability of the state $|\nu_\mu(t)\rangle$ appearing as ν_e is

$$P(\nu_\mu \to \nu_e) = \left|\langle\nu_e|\nu_\mu(t)\rangle\right|^2. \tag{2.6}$$

Let us now calculate $\langle\nu_e|\nu_\mu(t)\rangle$.

$$\begin{aligned} \langle\nu_e|\nu_\mu(t)\rangle &= (\cos\theta\,\langle\nu_1| + \sin\theta\,\langle\nu_2|)\left(-\sin\theta\, e^{-iE_1t}\,|\nu_1\rangle + \cos\theta\, e^{-iE_2t}\,|\nu_2\rangle\right) \\ &= -\sin\theta\cos\theta e^{-iE_1t} + \sin\theta\cos\theta e^{-iE_2t} \\ &= \sin\theta\cos\theta\left(e^{-iE_2t} - e^{-iE_1t}\right). \end{aligned} \tag{2.7}$$

So,

$$\left|\langle\nu_e|\nu_\mu(t)\rangle\right|^2 = 2\sin^2\theta\cos^2\theta\,[1-\cos(E_2-E_1)t]\,. \tag{2.8}$$

Using Eq. (2.6), we can write down

$$P(\nu_\mu \to \nu_e) = \sin^2 2\theta\, \sin^2\frac{(E_2-E_1)t}{2}. \tag{2.9}$$

If we assume the same momentum for the two highly relativistic neutrinos, then

$$E_1 = \sqrt{p^2 + m_1^2} \approx p + \frac{m_1^2}{2p}, \tag{2.10}$$

$$E_2 = \sqrt{p^2 + m_2^2} \approx p + \frac{m_2^2}{2p}. \tag{2.11}$$

Now we can rewrite the Eq. (2.9) as

$$P(\nu_\mu \to \nu_e) = \sin^2 2\theta \, \sin^2 \left(\frac{\Delta m^2 t}{4p} \right). \tag{2.12}$$

For highly relativistic neutrinos, assuming $p \approx E \gg m_k \, (k = 1,2)$ and $t \approx L$ in natural unit system, the above equation can be written as

$$P(\nu_\mu \to \nu_e) = \sin^2 2\theta \, \sin^2 \left(\frac{\Delta m^2 L}{4E} \right). \tag{2.13}$$

Now, expressing Δm^2 in eV^2, L in $\mathrm{m} \, (\mathrm{km})$ and E in $\mathrm{MeV} \, (\mathrm{GeV})$ respectively, the above equation can be written as

$$P(\nu_\mu \to \nu_e) = \sin^2 2\theta \, \sin^2 \left(\frac{1.27 \, \Delta m^2 L}{E} \right). \tag{2.14}$$

2.3 N-flavor neutrino oscillation probability:

From the above discussion it is clear that for one flavor of neutrino oscillating into another, at least one neutrino flavor must have some finite mass. Different experimental evidence proves that neutrino changes its flavor during oscillation and there are at least three flavors whose existence have also been proved experimentally. So to make the discussion more general, we present here the theoretical framework for N-flavor neutrino oscillation. In N-flavor framework, the flavor eigenstates ($|\nu_\alpha\rangle$) are related to the mass eigenstates ($|\nu_i\rangle$) by the following equation:

$$|\nu_\alpha\rangle = \sum_{i=1}^{N} U_{\alpha i}^* |\nu_i\rangle. \tag{2.15}$$

In general, U is the $N \times N$ complex unitary matrix. Now after a time t,

$$|\nu_\alpha(t)\rangle = \sum_i U^*_{\alpha i} e^{-iE_i t} |\nu_i\rangle \tag{2.16}$$

E_i is the energy of the ith mass eigenstate $|\nu_i\rangle$. The probability of oscillating the flavor eigenstate $|\nu_\alpha(t)\rangle$ into $|\nu_\beta\rangle$ is given by

$$\begin{aligned} P(\nu_\alpha \to \nu_\beta) &= \left|\langle \nu_\beta | \nu_\alpha(t)\rangle\right|^2 \\ &= \left| \sum_i \sum_j U^*_{\alpha i} U_{\beta j} e^{-iE_i t} \langle \nu_j | \nu_i \rangle \right|^2 \\ &= \left| \sum_i U^*_{\alpha i} U_{\beta i} e^{-iE_i t} \right|^2, \end{aligned} \tag{2.17}$$

which after a few steps straight forward calculation can be written as

$$\begin{aligned} P(\nu_\alpha \to \nu_\beta) = \sum_i |U_{\alpha i}|^2 |U_{\beta i}|^2 + 2\sum_{i>j} Re\left(U^*_{\alpha i} U_{\alpha j} U_{\beta i} U^*_{\beta j}\right) \\ -4\sum_{i>j} Re\left(U^*_{\alpha i} U_{\alpha j} U_{\beta i} U^*_{\beta j}\right) \sin^2 \frac{(E_i - E_j)t}{2} \\ +2\sum_{i>j} Im\left(U^*_{\alpha i} U_{\alpha j} U_{\beta i} U^*_{\beta j}\right) \sin(E_i - E_j)t. \end{aligned} \tag{2.18}$$

Now using the unitarity relation,

$$\sum_{i=1}^{N} U^*_{\alpha i} U_{\beta i} = \delta_{\alpha\beta}, \tag{2.19}$$

Eq. (2.18) can be written as,

$$\begin{aligned} P(\nu_\alpha \to \nu_\beta) = \delta_{\alpha\beta} - 4\sum_{i>j} Re\left(U^*_{\alpha i} U_{\alpha j} U_{\beta i} U^*_{\beta j}\right) \sin^2 \frac{(E_i - E_j)t}{2} \\ +2\sum_{i>j} Im\left(U^*_{\alpha i} U_{\alpha j} U_{\beta i} U^*_{\beta j}\right) \sin(E_i - E_j)t. \end{aligned} \tag{2.20}$$

Using the relation $(E_i - E_j) = \frac{m_i^2 - m_j^2}{2E} = \frac{\Delta m_{ij}^2}{2E}$, and replacing '$t$' by '$L$', we get

$$P(\nu_\alpha \to \nu_\beta) = \delta_{\alpha\beta} - 4\sum_{i>j} Re\left(U_{\alpha i}^* U_{\alpha j} U_{\beta i} U_{\beta j}^*\right) \sin^2\left(\frac{\Delta m_{ij}^2 L}{4E}\right) + 2\sum_{i>j} Im\left(U_{\alpha i}^* U_{\alpha j} U_{\beta i} U_{\beta j}^*\right) \sin 2\left(\frac{\Delta m_{ij}^2 L}{4E}\right). \tag{2.21}$$

This is the well known standard N-flavor oscillation probability expression.

2.3.1 Number of mixing angles and phases in case of active-sterile mixing:

In general, for a N number of massive lepton families, mixing is expressed by a $N \times N$ complex unitary matrix, which has $\frac{N(N-1)}{2}$ number of mixing angles, $\frac{(N-1)(N-2)}{2}$ number of Dirac CP-phases and $(N-1)$ number of Majorana phases. As an example for 3ν families, one has three mixing angles, one Dirac CP-phase, and two Majorana CP-phases.

However this does not hold good always, specially in presence of sterile neutrinos. For example, if there exists one sterile neutrino, then N becomes 4. In that case, there are six mixing angles, three Dirac CP-phases, and three Majorana CP-phases. In case of two sterile neutrinos, there are ten mixing angles, six Dirac CP-phases, and four Majorana CP-phases. Mixing angles can be written as,

$$\theta_{12}, \theta_{13}, \theta_{14}, \theta_{15}, \theta_{23}, \theta_{24}, \theta_{25}, \theta_{34}, \theta_{35}, \theta_{45}. \tag{2.22}$$

However, since sterile neutrinos only interact through active-sterile mixing, θ_{45} is not a physically observable quantity.

As discussed in [152], in general, in case of $N_s = (N-3)$ number of sterile neutrinos there should be $3(N-2) = 3(N_s+1)$ number of mixing angles, $(2N-5) = (2N_s+1)$ number of Dirac CP-phases, and $(N-1) = (N_s+2)$ number of Majorana CP-phases.

So for $N_s = 1$, number of mixing angles is six, number of Dirac CP-phases is three, and number of Majorana CP-phases is three. Similarly, for $N_s = 2$, number of mixing angles is nine, number of Dirac CP-phases is five, and number of Majorana CP-phases is four. These results perfectly agree with physically observable scenarios.

2.4 Three flavor neutrino oscillation framework:

2.4.1 Three flavor oscillation in vacuum

Let us now turn our discussion into the most widely accepted three flavor neutrino oscillation framework which can describe almost all the experimental data available so far. From the discussion of sec. 2.3.1, it is clear that in 3ν framework, there are three mixing angles and one Dirac CP-phase. Since Majorana phases do not come into oscillation picture, we do not explicitly write them in the parameterization. According to the standard parameterization as followed in case of three flavor quark mixing matrix [153, 154], the unitary matrix U is parameterized as

$$\begin{aligned} U &= R(\theta_{23})R(\theta_{13},\delta_{\rm CP})R(\theta_{12}) \\ &= \begin{pmatrix} 1 & 0 & 0 \\ 0 & c_{23} & s_{23} \\ 0 & -s_{23} & c_{23} \end{pmatrix} \begin{pmatrix} c_{13} & 0 & s_{13}e^{-i\delta_{\rm CP}} \\ 0 & 1 & 0 \\ -s_{13}e^{i\delta_{\rm CP}} & 0 & c_{13} \end{pmatrix} \begin{pmatrix} c_{12} & s_{12} & 0 \\ -s_{12} & c_{12} & 0 \\ 0 & 0 & 1 \end{pmatrix} \\ &= \begin{pmatrix} c_{12}\,c_{13} & s_{12}\,c_{13} & s_{13}\,e^{-i\delta_{\rm CP}} \\ -s_{12}\,c_{23} - c_{12}\,s_{23}\,s_{13}\,e^{i\delta_{\rm CP}} & c_{12}\,c_{23} - s_{12}\,s_{23}\,s_{13}\,e^{i\delta_{\rm CP}} & s_{23}\,c_{13} \\ s_{12}\,s_{23} - c_{12}\,c_{23}\,s_{13}\,e^{i\delta_{\rm CP}} & -c_{12}\,s_{23} - s_{12}\,c_{23}\,s_{13}\,e^{i\delta_{\rm CP}} & c_{23}\,c_{13} \end{pmatrix}. \end{aligned} \tag{2.23}$$

Here $R(\theta_{ij},\delta_{\rm CP})$ is the orthogonal 3×3 rotation matrix in the ij-plane which depends on the mixing angle θ_{ij} and the Dirac-type CP violating phase $\delta_{\rm CP}$, whereas $R(\theta_{ij})$ is the function of mixing angle θ_{ij} only. Here $c_{ij} \equiv \cos\theta_{ij}$, $s_{ij} \equiv \sin\theta_{ij}$. U is known as Pontecorvo-Maki-Nakagawa-Sakata (PMNS) matrix [147, 148, 155]. For 3-flavor framework,

$$|\nu_\alpha\rangle = \sum_{i=1}^{3} U^*_{\alpha i}|\nu_i\rangle, \tag{2.24}$$

where $\alpha = e^-, \mu^-, \tau^-$ and $i = 1, 2, 3$.

Following [156], the 3-flavor $\nu_\mu \to \nu_e$ appearance and $\nu_\mu \to \nu_\mu$ survival probability expressions in vacuum upto second order in α and $\sin\theta_{13}$ can be written as

$$\begin{aligned} P(\nu_\mu \to \nu_e) = {} & \alpha^2 \sin^2 2\theta_{12}\, c_{23}^2 \Delta^2 + 4 s_{13}^2 s_{23}^2 \sin^2\Delta \\ & + 2 s_{13} \sin 2\theta_{12} \sin 2\theta_{23} \,(\alpha\Delta) \sin\Delta \cos(\Delta + \delta_{\rm CP}), \end{aligned} \tag{2.25}$$

$$\begin{aligned} P(\nu_\mu \to \nu_\mu) = {} & 1 - \sin^2 2\theta_{23} \sin^2\Delta + (\alpha\Delta)\, c_{12}^2 \sin^2 2\theta_{23} \sin 2\Delta \\ & - \alpha^2\Delta^2 \left[\sin^2 2\theta_{12}\, c_{23}^2 + c_{12}^2 \sin^2 2\theta_{23} \left(\cos 2\Delta - s_{12}^2\right)\right] \\ & + 4 s_{13}^2 s_{23}^2 \cos 2\theta_{23} \sin^2\Delta - 2\,(\alpha\Delta)\, s_{13} \sin 2\theta_{12}\, s_{23}^2 \sin 2\theta_{23} \cos\delta_{\rm CP} \sin 2\Delta, \end{aligned} \tag{2.26}$$

where $\alpha = \frac{\Delta m^2_{21}}{\Delta m^2_{31}}$ and $\Delta = \frac{\Delta m^2_{31} L}{4E}$. Using Eq. (2.21) for full 3-flavor probability or Eq. (2.25) for approximated probability, we can see that if PMNS matrix is not real then

$$P\left(\nu_e \longrightarrow \nu_\mu\right) \neq P\left(\nu_\mu \longrightarrow \nu_e\right). \tag{2.27}$$

Also we know,

$$\left(\nu_e \longrightarrow \nu_\mu\right) \xrightarrow{\hat{C}\hat{P}} \left(\bar{\nu}_e \longrightarrow \bar{\nu}_\mu\right). \tag{2.28}$$

Again under CPT,

$$\left(\nu_e \longrightarrow \nu_\mu\right) \xrightarrow{\hat{C}\hat{P}\hat{T}} \left(\bar{\nu}_\mu \longrightarrow \bar{\nu}_e\right). \tag{2.29}$$

Similarly,

$$\left(\nu_\mu \longrightarrow \nu_e\right) \xrightarrow{\hat{C}\hat{P}\hat{T}} \left(\bar{\nu}_e \longrightarrow \bar{\nu}_\mu\right). \tag{2.30}$$

So from Eq. (2.27), we can write,

$$P\left(\nu_e \longrightarrow \nu_\mu\right) \neq P\left(\bar{\nu}_e \longrightarrow \bar{\nu}_\mu\right). \tag{2.31}$$

That is CP is violated in neutrino oscillation and this is known as intrinsic CP-violation in lepton sector. Also one important point we should keep in mind that to observe CP-violation in neutrino oscillation, we should concentrate on the appearance channel $(\alpha \neq \beta)$ only not on the disappearance channel. This is because the disappearance channel does not contain the imaginary part and as a result the difference between the neutrino and antineutrino survival channels cancel each other.

So if, CP is not conserved, the oscillation probabilities for neutrinos are different from those for antineutrinos. The CP-odd asymmetries are defined as

$$\Delta P_{\alpha\beta} \equiv P\left(\nu_\alpha \to \nu_\beta ; L\right) - P\left(\bar{\nu}_\alpha \to \bar{\nu}_\beta ; L\right). \tag{2.32}$$

From CPT invariance we find that $\Delta P_{\alpha\beta} = -\Delta P_{\beta\alpha}$. From the Eq. (2.21), it is quite easy to find that

$$\Delta P_{e\mu} = \Delta P_{\mu\tau} = \Delta P_{\tau e} = 4J_{cp} \times \left[\sin\left(\frac{\Delta m^2_{21} t}{2E}\right) + \sin\left(\frac{\Delta m^2_{32} t}{2E}\right) + \sin\left(\frac{\Delta m^2_{31} t}{2E}\right)\right]. \tag{2.33}$$

Where, $J_{cp} = \frac{1}{8}\cos\theta_{13}\sin 2\theta_{12}\sin 2\theta_{13}\sin 2\theta_{23}\sin\delta_{\text{CP}}$ is known as Jarlskog invariant.

For observing CP-odd asymmetry, following few important points can be noted as,

- It vanishes if any of the mixing angles $\theta_{12}, \theta_{13}, \theta_{23}$ is zero or 90^0.
- If any mass square difference is zero, then $\Delta P_{\alpha\beta}$ becomes zero.
- δ_{CP} must have the values other than 0 or, $\pm 180^0$.

2.5 Neutrino Propagation in Matter

When the flavor eigenstates $(\nu_e, \nu_\mu, or\, \nu_\tau)$ of the neutrinos propagate through matter they interact with the matter constituents (electrons, protons and neutrons) very weakly through hard scattering and coherent forward elastic scattering. These interactions can be classified into two ways: one is charged current (CC) and another one is neutral current

(NC) interaction. CC interactions are mediated by the $W^{\pm}$ gauge bosons and NC interactions are mediated by the Z^0 gauge boson as shown in Fig. 2.1. The potential contribution of neutral current interactions mediated by Z^0 bosons is same for all the three flavors and thus leading to an overall phase and does not contribute to the probability calculation. The only contribution comes from the charged current interaction between ν_e and e^- mediated by $W^{\pm}$ gauge bosons. For neutrinos, CC potential have the form, $V_{CC} = \sqrt{2} G_F N_e$, and the NC potential have the form $V_{NC} = -G_F N_n/\sqrt{2}$, where G_F is the Fermi coupling constant, N_e and N_n are the electron and neutron number densities of matter respectively. We can write the CC potential in terms of matter density (ρ) as,

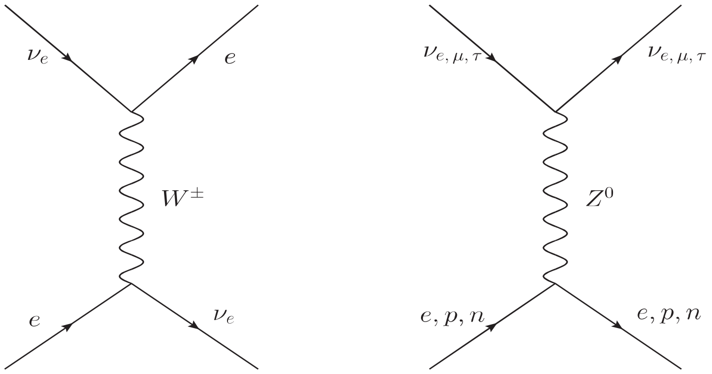

Figure 2.1: Left figure corresponds to the charged current interaction (CC). Right figure corresponds to the neutral current (NC) interaction of active neutrinos.

$$V_{CC} \simeq 7.6 \times (\frac{N_e}{N_p + N_n}) \times (\frac{\rho}{10^{14} gm/cc}) \text{ eV}. \tag{2.34}$$

In an electrically neutral, isoscalar medium, $N_e = N_p = N_n$. So,

$$V_{CC} \simeq 7.6 \times 0.5 \times (\frac{\rho}{10^{14} gm/cc}) \text{ eV}. \tag{2.35}$$

For antineutrinos, $V_{CC} \rightarrow -V_{CC}$ and $V_{NC} \rightarrow -V_{NC}$.

2.5.1 Two flavor oscillation in Matter

In two flavor framework in vacuum, the time evolution Schrodinger equation in mass basis is given by,

$$i\frac{d}{dt}\begin{pmatrix}|\nu_1\rangle \\ |\nu_2\rangle\end{pmatrix} = \begin{pmatrix}\frac{m_1^2}{2E} & 0 \\ 0 & \frac{m_2^2}{2E}\end{pmatrix}\begin{pmatrix}|\nu_1\rangle \\ |\nu_2\rangle\end{pmatrix}, \tag{2.36}$$

where m_1 and m_2 are the masses of the two mass eigenstates $|\nu_1\rangle$ and $|\nu_2\rangle$ respectively. Now this above equation in flavor basis gets modified in presence of matter as,

$$i\frac{d}{dt}\begin{pmatrix}|\nu_\alpha\rangle \\ |\nu_\beta\rangle\end{pmatrix} = \frac{1}{2E}\left[U\begin{pmatrix}m_1^2 & 0 \\ 0 & m_2^2\end{pmatrix}U^\dagger + \begin{pmatrix}a & 0 \\ 0 & 0\end{pmatrix}\right]\begin{pmatrix}|\nu_\alpha\rangle \\ |\nu_\beta\rangle\end{pmatrix}, \tag{2.37}$$

with, $U = \begin{pmatrix}\cos\theta & \sin\theta \\ -\sin\theta & \cos\theta\end{pmatrix}$.

Hence,

$$i\frac{d}{dt}\begin{pmatrix}|\nu_\alpha\rangle \\ |\nu_\beta\rangle\end{pmatrix} = \frac{1}{2E}\begin{pmatrix}m_1^2\cos^2\theta + m_2^2\sin^2\theta + a & (m_2^2 - m_1^2)\sin\theta\cos\theta \\ (m_2^2 - m_1^2)\sin\theta\cos\theta & m_1^2\sin^2\theta + m_2^2\cos^2\theta\end{pmatrix}\begin{pmatrix}|\nu_\alpha\rangle \\ |\nu_\beta\rangle\end{pmatrix}, \tag{2.38}$$

where $a = 2\sqrt{2}G_F N_e E \equiv 2V_{CC}E$. Here we assume that $\alpha = e^-$ and $\beta = \mu^-$. For antineutrinos, $a \to -a$.

Now if we go to the mass basis then we see,

$$i\frac{d}{dt}\begin{pmatrix}|\nu_1\rangle \\ |\nu_2\rangle\end{pmatrix} = \frac{1}{2E}\begin{pmatrix}m_1^2 + a\cos^2\theta & a\sin\theta\cos\theta \\ a\sin\theta\cos\theta & m_2^2 + a\sin^2\theta\end{pmatrix}\begin{pmatrix}|\nu_1\rangle \\ |\nu_2\rangle\end{pmatrix}. \tag{2.39}$$

That is the mass matrix is no longer diagonal now. To make this mass matrix diagonal, the mass eigenvalues in presence of matter becomes

$$m^2_{1m,2m} = \frac{1}{2}\left[(m_1^2 + m_2^2 + a) \pm \sqrt{(a - \Delta m^2 \cos 2\theta)^2 + (\Delta m^2 \sin 2\theta)^2}\right]. \tag{2.40}$$

Hence,

$$\Delta m^2_m = (m^2_{2m} - m^2_{1m}) = \sqrt{(a - \Delta m^2 \cos 2\theta)^2 + (\Delta m^2 \sin 2\theta)^2}. \tag{2.41}$$

We can also calculate the oscillation probability in matter directly with the new mass eigenstates. Let the mass eigenstates in matter is connected to the flavor eigenstates by an unitary matrix,

$$U_m = \begin{pmatrix} \cos\theta_m & \sin\theta_m \\ -\sin\theta_m & \cos\theta_m \end{pmatrix}. \tag{2.42}$$

So, the time evolution equation in flavor basis is written as

$$\begin{aligned} i\frac{d}{dt}\begin{pmatrix} |\nu_\alpha\rangle \\ |\nu_\beta\rangle \end{pmatrix} &= \frac{1}{2E} U_m \begin{pmatrix} m^2_{1m} & 0 \\ 0 & m^2_{2m} \end{pmatrix} U_m^\dagger \begin{pmatrix} |\nu_\alpha\rangle \\ |\nu_\beta\rangle \end{pmatrix} \\ &= \frac{1}{2E}\begin{pmatrix} m^2_{1m}\cos^2\theta_m + m^2_{2m}\sin^2\theta_m & (m^2_{2m} - m^2_{1m})\sin\theta_m\cos\theta_m \\ (m^2_{2m} - m^2_{1m})\sin\theta_m\cos\theta_m & m^2_{1m}\sin^2\theta_m + m^2_{2m}\cos^2\theta_m \end{pmatrix}\begin{pmatrix} |\nu_\alpha\rangle \\ |\nu_\beta\rangle \end{pmatrix}. \end{aligned} \tag{2.43}$$

Comparing Eq. (2.38) and Eq. (2.43), we can write

$$\begin{aligned} \Delta m^2_m \sin 2\theta_m &= \Delta m^2 \sin 2\theta \\ \text{or,} \qquad \sin 2\theta_m &= \frac{\Delta m^2 \sin 2\theta}{\Delta m^2_m}. \end{aligned} \tag{2.44}$$

So the mixing angle in matter is related to the vacuum mixing angle as,

$$\sin 2\theta_m = \frac{\Delta m^2 \sin 2\theta}{\sqrt{(a - \Delta m^2 \cos 2\theta)^2 + (\Delta m^2 \sin 2\theta)^2}}. \tag{2.45}$$

Now just like the Eq. (2.14), the oscillation probability in matter becomes

$$P_m\left(\nu_\mu \to \nu_e\right) = \sin^2 2\theta_m \sin^2\left(1.27\frac{\Delta m_m^2 L}{E}\right). \tag{2.46}$$

We can now draw some important conclusions which are given below:

- If $a = 0$, then we get the vacuum result.
- If $\Delta m^2 = 0$, then $P_m = 0$, whatever may be the potential.
- If the matter potential is very dense that is $a \to \infty$, then also $P_m = 0$.
- If $\Delta m^2 \to -\Delta m^2$, then mixing angle in matter changes and oscillation probability will be different. So matter oscillation effects can be useful to probe the nature of the hierarchy.

2.5.2 MSW resonance

Most striking feature of matter effects is the resonance enhancement of the oscillation probabilities in comparison to the vacuum case. This famous mechanism is known as MSW resonance [63, 157].

From Eq. (2.46), it is clear that probability will be maximum if, $\sin^2 2\theta_m = 1$. Then it follows from Eq. (2.45) that $a = \Delta m^2 \cos 2\theta$. This is known as Resonance condition.

For the resonance condition to be satisfied, mixing in matter should be maximal $\left(\theta_m = 45^0\right)$, no matter how small the mixing angle θ is in vacuum. If one choose $\Delta m^2 > 0$ for the resonance of neutrino oscillation then $\Delta m^2 < 0$ is the resonance condition for antineutrino oscillation.

2.5.3 Three flavor oscillation in matter

In presence of matter, the time evolution Schrodinger equation in 3ν flavor basis is written as

$$i\frac{d}{dt}\begin{pmatrix}|\nu_e\rangle\\|\nu_\mu\rangle\\|\nu_\tau\rangle\end{pmatrix}=\left[\frac{1}{2E}U\begin{pmatrix}m_1^2&0&0\\0&m_2^2&0\\0&0&m_3^2\end{pmatrix}U^\dagger+\begin{pmatrix}V_{CC}+V_{NC}&0&0\\0&V_{NC}&0\\0&0&V_{NC}\end{pmatrix}\right]\begin{pmatrix}|\nu_e\rangle\\|\nu_\mu\rangle\\|\nu_\tau\rangle\end{pmatrix}.$$

Now, after solving the above equation, the 3-flavor $\nu_\mu\to\nu_e$ appearance and $\nu_\mu\to\nu_\mu$ survival probability expressions [156] in matter upto second order in α and $\sin\theta_{13}$ can be written as

$$\begin{aligned}P(\nu_\mu\to\nu_e)&=\alpha^2\sin^2 2\theta_{12}\,c_{23}^2\,\frac{\sin^2 A\Delta}{A^2}+4\,s_{13}^2 s_{23}^2\,\frac{\sin^2(A-1)\Delta}{(A-1)^2}\\&\quad+2\,\alpha\,s_{13}\sin2\theta_{12}\sin2\theta_{23}\cos(\Delta+\delta_{\rm CP})\,\frac{\sin A\Delta}{A}\,\frac{\sin(A-1)\Delta}{(A-1)}.\end{aligned}\tag{2.47}$$

$$\begin{aligned}&P(\nu_\mu\to\nu_\mu)=\\&1-\sin^2 2\theta_{23}\sin^2\Delta+(\alpha\Delta)\,c_{12}^2\sin^2 2\theta_{23}\sin2\Delta\\&+\alpha^2\sin^2 2\theta_{12}\,c_{23}^2\,\frac{\sin^2 A\Delta}{A^2}-(\alpha\Delta)^2 c_{12}^4\sin^2 2\theta_{23}\cos2\Delta-4\,s_{13}^2 s_{23}^2\,\frac{\sin^2(A-1)\Delta}{(A-1)^2}\\&+\frac{1}{2A}\alpha^2\sin^2 2\theta_{12}\sin^2 2\theta_{23}\left(\sin\Delta\,\frac{\sin A\Delta}{A}\cos(A-1)\Delta-\frac{\Delta}{2}\sin2\Delta\right)\\&-\frac{2}{A-1}s_{13}^2\sin^2 2\theta_{23}\left(\sin\Delta\cos A\Delta\,\frac{\sin(A-1)\Delta}{(A-1)}-\frac{A\Delta}{2}\sin2\Delta\right)\\&-2\,\alpha\,s_{13}\sin2\theta_{12}\sin2\theta_{23}\cos\delta_{\rm CP}\cos\Delta\,\frac{\sin A\Delta}{A}\,\frac{\sin(A-1)\Delta}{(A-1)}\\&+\frac{2}{A-1}\alpha\,s_{13}\sin2\theta_{12}\sin2\theta_{23}\cos2\theta_{23}\cos\delta_{\rm CP}\sin\Delta\left(A\sin\Delta-\frac{\sin A\Delta}{A}\cos(A-1)\Delta\right).\end{aligned}\tag{2.48}$$

Here, $\Delta=\frac{\Delta m_{31}^2 L}{4E}$, and $A=\frac{2\sqrt{2}G_F N_e E}{\Delta m_{31}^2}$. For neutrino and inverted ordering, $\Delta\to-\Delta$ and $A\to-A$. For antineutrino and normal ordering, $\delta_{\rm CP}\to-\delta_{\rm CP}$, and $A\to-A$. Similarly for antineutrino and inverted ordering $\delta_{\rm CP}\to-\delta_{\rm CP}$, $\Delta\to-\Delta$.

2.6 Neutrino oscillations in 3+1 framework

In 3+1 framework, there exists an extra mass eigenstate $|\nu_4\rangle$ of mass m_4 on top of three mass eigenstates $|\nu_1\rangle$, $|\nu_2\rangle$, and $|\nu_3\rangle$ with masses m_1, m_2, and m_3 respectively in 3ν framework. We call this extra mass eigenstate "sterile" neutrino. In this framework, the time evolution Schrodinger equation for the flavor basis in vacuum becomes,

$$i\frac{d}{dt}\begin{pmatrix} |\nu_e\rangle \\ |\nu_\mu\rangle \\ |\nu_\tau\rangle \\ |\nu_s\rangle \end{pmatrix} = \frac{1}{2E}\left[U \begin{pmatrix} m_1^2 & 0 & 0 & 0 \\ 0 & m_2^2 & 0 & 0 \\ 0 & 0 & m_3^2 & 0 \\ 0 & 0 & 0 & m_4^2 \end{pmatrix} U^\dagger \right] \begin{pmatrix} |\nu_e\rangle \\ |\nu_\mu\rangle \\ |\nu_\tau\rangle \\ |\nu_s\rangle \end{pmatrix}. \tag{2.49}$$

Here U is the 4×4 unitary matrix. As from the discussion of calculation of number of mixing angles and number of CP-phases in sec. 2.3.1, it has total six mixing angles $(\theta_{12}, \theta_{13}, \theta_{23}, \theta_{14}, \theta_{24}, \theta_{34})$ and three Dirac-type phases and three Majorana-type phases. However Majorana phases do not come into oscillation picture.

So, a convenient parameterization of U can be,

$$U = R(\theta_{34}, \delta_{34})R(\theta_{24})R(\theta_{14}, \delta_{14})R(\theta_{23})R(\theta_{13}, \delta_{13})R(\theta_{12}), \tag{2.50}$$

where $R(\theta_{ij}, \delta_{ij})$ is the orthogonal 4×4 rotation matrix in the ij-plane, which depends on the mixing angle θ_{ij} and the Dirac-type CP violating phase δ_{ij}, whereas $R(\theta_{ij})$ is the function of mixing angle θ_{ij} only. The new rotation matrices in the 3+1 scheme are expressed in the following fashion:

$$R(\theta_{14}, \delta_{14}) = \begin{pmatrix} c_{14} & 0 & 0 & s_{14}e^{-i\delta_{14}} \\ 0 & 1 & 0 & 0 \\ 0 & 0 & 1 & 0 \\ -s_{14}e^{i\delta_{14}} & 0 & 0 & c_{14} \end{pmatrix}, R(\theta_{24}) = \begin{pmatrix} 1 & 0 & 0 & 0 \\ 0 & c_{24} & 0 & s_{24} \\ 0 & 0 & 1 & 0 \\ 0 & -s_{24} & 0 & c_{24} \end{pmatrix},$$

and,

$$R(\theta_{34},\delta_{34}) = \begin{pmatrix} 1 & 0 & 0 & 0 \\ 0 & 1 & 0 & 0 \\ 0 & 0 & c_{34} & s_{34}e^{-i\delta_{34}} \\ 0 & 0 & -s_{34}e^{i\delta_{34}} & c_{34} \end{pmatrix}.$$

It is also important to note here that in 3ν framework we denoted Dirac-type CP-phase as $\delta_{\rm CP}$, whereas, here we denote $\delta_{\rm CP}$ as δ_{13} just for symbolic convenience in 4ν framework.

This parameterization in Eq. (2.50) has the following properties: i) When the active-sterile mixing angles are zero ($\theta_{14} = \theta_{24} = \theta_{34} = 0$), it returns to the 3-flavor matrix in its common parameterization. ii) With the leftmost positioning of the matrix $R(\theta_{34},\delta_{34})$, the vacuum $\nu_\mu \to \nu_e$ conversion probability is independent of θ_{34} and it's associated CP-phase δ_{34} (see [104]). iii) For small values of θ_{13} and of the active-sterile mixing angles, one has $|U_{e3}|^2 \simeq s_{13}^2$, $|U_{e4}|^2 = s_{14}^2$, $|U_{\mu 4}|^2 \simeq s_{24}^2$ and $|U_{\tau 4}|^2 \simeq s_{34}^2$, with an immediate physical interpretation of the new mixing angles.

The matrix elements of this 4×4 mixing matrix as a function of mixing angles and phases are listed below:

$$\begin{aligned}
&U_{e1} = c_{12}\,c_{13}\,c_{14}, \quad U_{e2} = s_{12}\,c_{13}\,c_{14}, \quad U_{e3} = s_{13}\,c_{14}\,e^{-i\delta_{13}}, \quad U_{e4} = s_{14}\,e^{-i\delta_{14}} \\
&U_{\mu 1} = c_{12}\left(-c_{24}\,s_{13}\,s_{23}\,e^{i\delta_{13}} - c_{13}\,s_{14}\,s_{24}\,e^{i\delta_{14}}\right) - s_{12}\,c_{23}\,c_{24} \\
&U_{\mu 2} = s_{12}\left(-c_{24}\,s_{13}\,s_{23}\,e^{i\delta_{13}} - c_{13}\,s_{14}\,s_{24}\,e^{i\delta_{14}}\right) + c_{12}\,c_{23}\,c_{24} \\
&U_{\mu 3} = c_{13}\,s_{23}\,c_{24} - s_{13}\,s_{14}\,s_{24}\,e^{-i(\delta_{13}-\delta_{14})} \\
&U_{\mu 4} = c_{14}\,s_{24} \\
&U_{\tau 1} = -s_{12}\left(-s_{23}\,c_{34} - c_{23}\,s_{24}\,s_{34}\,e^{-i\delta_{34}}\right) \\
&\qquad + c_{12}\left(-c_{13}\,c_{24}\,s_{14}\,s_{34}\,e^{i(\delta_{14}-\delta_{34})} - s_{13}e^{i\delta_{13}}\left(c_{23}\,c_{34} - e^{-i\delta_{34}}\,s_{23}\,s_{24}\,s_{34}\right)\right) \\
&U_{\tau 2} = c_{12}\left(-s_{23}\,c_{34} - c_{23}\,s_{24}\,s_{34}\,e^{-i\delta_{34}}\right) \\
&\qquad + s_{12}\left(-c_{13}\,c_{24}\,s_{14}\,s_{34}\,e^{i(\delta_{14}-\delta_{34})} - s_{13}e^{i\delta_{13}}\left(c_{23}\,c_{34} - e^{-i\delta_{34}}\,s_{23}\,s_{24}\,s_{34}\right)\right) \\
&U_{\tau 3} = -c_{24}\,s_{13}\,s_{14}\,s_{34}\,e^{-i(\delta_{13}-\delta_{14}+\delta_{34})} + c_{13}\left(c_{23}\,c_{34} - s_{23}\,s_{24}\,s_{34}\,e^{-i\delta_{34}}\right) \\
&U_{\tau 4} = c_{14}\,c_{24}\,s_{34}\,e^{-i\delta_{34}} \\
&U_{s1} = -s_{12}\left(-c_{23}\,c_{34}\,s_{24} + s_{23}\,s_{34}\,e^{i\delta_{34}}\right) \\
&\qquad + c_{12}\left(-c_{13}\,c_{24}\,c_{34}\,s_{14}\,e^{i\delta_{14}} - s_{13}e^{i\delta_{13}}\left(-s_{23}\,s_{24}\,c_{34} - e^{i\delta_{34}}\,c_{23}\,s_{34}\right)\right) \\
&U_{s2} = c_{12}\left(-c_{23}\,c_{34}\,s_{24} + s_{23}\,s_{34}\,e^{i\delta_{34}}\right) \\
&\qquad + s_{12}\left(-c_{13}\,c_{24}\,c_{34}\,s_{14}\,e^{i\delta_{14}} - s_{13}e^{i\delta_{13}}\left(-s_{23}\,s_{24}\,c_{34} - e^{i\delta_{34}}\,c_{23}\,s_{34}\right)\right) \\
&U_{s3} = -c_{24}\,c_{34}\,s_{13}\,s_{14}\,e^{-i(\delta_{13}-\delta_{14})} + c_{13}\left(-c_{34}\,s_{23}\,s_{24} - c_{23}\,s_{34}\,e^{i\delta_{34}}\right) \\
&U_{s4} = c_{14}\,c_{24}\,c_{34}
\end{aligned} \tag{2.51}$$

2.6.1 Appearance probability ($\nu_\mu \to \nu_e$) in 3+1 scheme

Using Eq. (2.21), we can write,

$$P_{\mu e} = -4 \sum_{i>j} Re \left(U^*_{\mu i} U_{\mu j} U_{ei} U^*_{ej} \right) \sin^2 \left(\frac{\Delta m^2_{ij} L}{4E} \right) \\ + 2 \sum_{i>j} Im \left(U^*_{\mu i} U_{\mu j} U_{ei} U^*_{ej} \right) \sin 2 \left(\frac{\Delta m^2_{ij} L}{4E} \right).$$

Expanding the imaginary part, we can write,

$$\begin{aligned} P^{Im}_{\mu e} = \; & 2 \left[Im \left(U^*_{\mu 2} U_{\mu 1} U_{e2} U^*_{e1} \right) \sin 2 \left(\frac{\Delta m^2_{21} L}{4E} \right) + Im \left(U^*_{\mu 3} U_{\mu 1} U_{e3} U^*_{e1} \right) \sin 2 \left(\frac{\Delta m^2_{31} L}{4E} \right) \right. \\ & + \; Im \left(U^*_{\mu 4} U_{\mu 1} U_{e4} U^*_{e1} \right) \sin 2 \left(\frac{\Delta m^2_{41} L}{4E} \right) + Im \left(U^*_{\mu 3} U_{\mu 2} U_{e3} U^*_{e2} \right) \sin 2 \left(\frac{\Delta m^2_{32} L}{4E} \right) \\ & \left. + \; Im \left(U^*_{\mu 4} U_{\mu 2} U_{e4} U^*_{e2} \right) \sin 2 \left(\frac{\Delta m^2_{42} L}{4E} \right) + Im \left(U^*_{\mu 4} U_{\mu 3} U_{e4} U^*_{e3} \right) \sin 2 \left(\frac{\Delta m^2_{43} L}{4E} \right) \right]. \end{aligned} \tag{2.52}$$

Now, if the new mass-squared difference Δm^2_{41} is of the order of 1 eV^2 which is much larger than that of the solar and atmospheric mass-squared differences involving three active neutrinos, then $\Delta m^2_{41} \simeq \Delta m^2_{42} \simeq \Delta m^2_{43}$. Therefore, we can consider all these new mass-squared differences to be equal to Δm^2_{41} in the above equation. Also for SBL experiments, typically we have $L/E \sim 1\,\mathrm{m/MeV}$. As a result, for this choice of L/E and for the three active neutrinos, the combination $\frac{\Delta m^2_{ij} L}{4E} \ll 1$, for $i, j\,(i > j) = 1, 2, 3$, so that all the terms involving the sine functions of these arguments in the above equation are very small and they can be dropped. Under these circumstances, the above Eq. (2.52) can be approximated as

$$P^{Im}_{\mu e} \simeq 2\, Im \left[U^*_{\mu 4} U_{e4} \left(U_{\mu 1} U^*_{e1} + U_{\mu 2} U^*_{e2} + U_{\mu 3} U^*_{e3} \right) \right] \sin 2 \left(\frac{\Delta m^2_{41} L}{4E} \right). \tag{2.53}$$

Now from the unitarity relation $U\,U^\dagger = \mathbb{1}$, we can write

$$U_{\mu 1} U^*_{e1} + U_{\mu 2} U^*_{e2} + U_{\mu 3} U^*_{e3} + U_{\mu 4} U^*_{e4} = 0. \tag{2.54}$$

So the above Eq. (2.53) boils down to

$$P^{Im}_{\mu e} = -2\, Im\left[\left|U_{\mu 4}\right|^2 \left|U_{e4}\right|^2\right] \sin 2\left(\frac{\Delta m^2_{41} L}{4E}\right) = 0. \tag{2.55}$$

Let us now expand the real part as

$$\begin{aligned} P^{Re}_{\mu e} = -4 \Bigg[& Re\left(U^*_{\mu 2} U_{\mu 1} U_{e2} U^*_{e1}\right) \sin^2\left(\frac{\Delta m^2_{21} L}{4E}\right) + Re\left(U^*_{\mu 3} U_{\mu 1} U_{e3} U^*_{e1}\right) \sin^2\left(\frac{\Delta m^2_{31} L}{4E}\right) \\ + & Re\left(U^*_{\mu 4} U_{\mu 1} U_{e4} U^*_{e1}\right) \sin^2\left(\frac{\Delta m^2_{41} L}{4E}\right) + Re\left(U^*_{\mu 3} U_{\mu 2} U_{e3} U^*_{e2}\right) \sin^2\left(\frac{\Delta m^2_{32} L}{4E}\right) \\ + & Re\left(U^*_{\mu 4} U_{\mu 2} U_{e4} U^*_{e2}\right) \sin^2\left(\frac{\Delta m^2_{42} L}{4E}\right) + Re\left(U^*_{\mu 4} U_{\mu 3} U_{e4} U^*_{e3}\right) \sin^2\left(\frac{\Delta m^2_{43} L}{4E}\right)\Bigg]. \end{aligned} \tag{2.56}$$

Using the same approximations and unitarity relation used above we can write,

$$P^{Re}_{\mu e} = 4\, \left|U_{\mu 4}\right|^2 \left|U_{e4}\right|^2 \sin^2\left(\frac{\Delta m^2_{41} L}{4E}\right). \tag{2.57}$$

Adding Eq. (2.55) and Eq. (2.57) we get the appearance probability

$$\begin{aligned} P_{\mu e} \simeq P^{Re}_{\mu e} + P^{Im}_{\mu e} &= 4\, \left|U_{\mu 4}\right|^2 \left|U_{e4}\right|^2 \sin^2\left(\frac{\Delta m^2_{41} L}{4E}\right) \\ &= \sin^2 2\theta_{\mu e} \sin^2\left(\frac{\Delta m^2_{41} L}{4E}\right). \end{aligned} \tag{2.58}$$

Here we have defined, $\sin^2 2\theta_{\mu e} = 4\left|U_{e4}\right|^2 \left|U_{\mu 4}\right|^2$. This expression of appearance probability is valid for both neutrino and antineutrino in SBL experiments. For example, LSND [158, 159] looks at the electron antineutrino appearance search, MiniBooNE [160, 161, 162] was operated in both neutrino and antineutrino appearance mode, whereas, NOMAD [163] looks at the electron neutrino appearance search.

Let us now calculate the appearance probability in long-baseline experiments like T2K, T2HK, NOνA, MINOS, and DUNE which is our main thrust in this thesis. To explain most of our numerical results, we have used the expression of 4ν vacuum ν_e appearance probability as given below. As shown in [104], the 4ν vacuum ν_e appearance probability in long-baseline can be approximately written as

$$\begin{aligned}
P_{\mu e}^{4\nu} \simeq & \,(1 - s_{14}^2 - s_{24}^2)\, P_{\mu e}^{3\nu} \\
& + 4 \sin\theta_{14} \sin\theta_{24} \sin\theta_{13} \sin\theta_{23} \sin\Delta \sin(\Delta + \delta_{13} - \delta_{14}) \\
& - 4 \sin\theta_{14} \sin\theta_{24} \cos\theta_{23} \sin\theta_{12} \cos\theta_{12}\, (\alpha\Delta) \sin\delta_{14} \\
& + \frac{1}{2} \sin^2 2\theta_{\mu e},
\end{aligned} \tag{2.59}$$

with, $\alpha = \frac{\Delta m_{21}^2}{\Delta m_{31}^2}$, and $\Delta = \frac{\Delta m_{31}^2 L}{4E}$. The above equation can be approximately written as

$$P_{\mu e}^{4\nu} \simeq \mathrm{P}^{\mathrm{ATM}} + \mathrm{P}^{\mathrm{SOL}} + \mathrm{P}_{\mathrm{I}}^{\mathrm{INT}} + \mathrm{P}_{\mathrm{II}}^{\mathrm{INT}} + \mathrm{P}_{\mathrm{III}}^{\mathrm{INT}} + \mathrm{P}^{\mathrm{STR}}. \tag{2.60}$$

Where the sum of first three terms $\mathrm{P}^{\mathrm{ATM}}$, $\mathrm{P}^{\mathrm{SOL}}$ and $\mathrm{P}_{\mathrm{I}}^{\mathrm{INT}}$ represent the 3ν vacuum transition probability $P_{\mu e}^{3\nu}$ with a suppressed factor $(1 - s_{14}^2 - s_{24}^2)$. The term $\mathrm{P}_{\mathrm{II}}^{\mathrm{INT}}$ corresponds to the interference between the atmospheric and the sterile frequency, whereas the term $\mathrm{P}_{\mathrm{III}}^{\mathrm{INT}}$ can be ascribed to the interference between the solar and sterile frequency. Sterile frequency does not appear in these expressions as it gets averaged out due to very fast oscillation induce by itself. The last term $\mathrm{P}^{\mathrm{STR}}$ is purely 4-flavor contribution.

The analysis of short-baseline (SBL) [105, 106] anomalies indicates that $\sin\theta_{14}$ and $\sin\theta_{24}$ have the very similar size to $\sin\theta_{13}$ (say, order ε). For the purpose of our works, we assume

$$\sin\theta_{14} \sim \sin\theta_{24} \sim \sin\theta_{13} \sim \varepsilon, \text{ and } \alpha \sim \varepsilon^2. \tag{2.61}$$

We have defined $\sin 2\theta_{\mu e}$ as

$$\sin^2 2\theta_{\mu e} = 4\,|U_{e4}|^2 |U_{\mu 4}|^2. \tag{2.62}$$

To make our analytical understanding more clear, we assume

$$\sin 2\theta_{\mu e} = 2|U_{e4}||U_{\mu 4}| \approx 2 s_{14} s_{24}. \tag{2.63}$$

Now for particular case, if $s^2_{14} = s^2_{24}$, we can write

$$s^2_{14} + s^2_{24} \approx 2\,s^2_{14} \approx 2\,s_{14}\,s_{24} \approx \sin 2\theta_{\mu e}. \tag{2.64}$$

As a result we can express each term of Eq. (2.59) as a function of $\sin 2\theta_{\mu e}$ which helps us to realize the strength of each term. So, the Eq. (2.59) is written as

$$\begin{aligned} P^{4\nu}_{\mu e} \simeq\, & (1 - \sin 2\theta_{\mu e})\, P^{3\nu}_{\mu e} \\ & + \; 2\,\sin 2\theta_{\mu e}\,\sin\theta_{13}\,\sin\theta_{23}\,\sin\Delta\,\sin(\Delta + \delta_{13} - \delta_{14}) \\ & - \; 2\sin 2\theta_{\mu e}\,\cos\theta_{23}\,\sin\theta_{12}\,\cos\theta_{12}\,(\alpha\,\Delta)\,\sin\delta_{14} \\ & + \; \frac{1}{2}\sin^2 2\theta_{\mu e}. \end{aligned} \tag{2.65}$$

In Fig. 1 of [104], the running behavior of each term as a function of $\sin 2\theta_{\mu e}$ has been shown. Following that we get to know that in the SBL constraint on $\sin 2\theta_{\mu e}$, the only relevant contributions come from the three terms $\mathrm{P}^{\mathrm{ATM}}$, $\mathrm{P}^{\mathrm{INT}}_{\mathrm{I}}$, and $\mathrm{P}^{\mathrm{INT}}_{\mathrm{II}}$. Other terms have very negligible contributions.

So neglecting the poorly contributing terms, the 4-flavor transition probability can be approximately written as

$$P^{4\nu}_{\mu e} \simeq \mathrm{P}^{\mathrm{ATM}} + \mathrm{P}^{\mathrm{INT}}_{\mathrm{I}} + \mathrm{P}^{\mathrm{INT}}_{\mathrm{II}}, \tag{2.66}$$

where, these three terms are approximately given as

$$\mathrm{P}^{\mathrm{ATM}} \simeq 4\sin^2\theta_{13}\sin^2\theta_{23}\sin^2\Delta. \tag{2.67}$$

$$\mathrm{P}^{\mathrm{INT}}_{\mathrm{I}} \simeq 8 s_{12} c_{12} s_{13} s_{23} c_{23} (\alpha\Delta) \sin\Delta \cos(\Delta + \delta_{13}). \tag{2.68}$$

$$\mathrm{P}^{\mathrm{INT}}_{\mathrm{II}} \simeq 8 s_{14} s_{24} s_{13} s_{23}\,\sin\Delta\,\sin(\Delta + \delta_{13} - \delta_{14}). \tag{2.69}$$

It should be noted that for antineutrino, the sign before the CP-phases δ_{13} and δ_{14} will be opposite to that of Eq. (2.68) and Eq. (2.69) respectively. It is also worth to mention here that the terms $\mathrm{P}^{\mathrm{ATM}}$, $\mathrm{P}^{\mathrm{INT}}_{\mathrm{I}}$, and $\mathrm{P}^{\mathrm{INT}}_{\mathrm{II}}$ are of the order of ε^2, ε^3, and ε^3 respectively.

2.6.2 Survival probability ($\nu_\mu \rightarrow \nu_\mu$) in 3+1 scheme

Using Eq. 2.21, we can write

$$P_{\mu\mu} = 1 - 4\sum_{i>j} Re\left(U^*_{\mu i}U_{\mu j}U_{\mu i}U^*_{\mu j}\right)\sin^2\left(\frac{\Delta m^2_{ij}L}{4E}\right) + 2\sum_{i>j} Im\left(U^*_{\mu i}U_{\mu j}U_{\mu i}U^*_{\mu j}\right)\sin 2\left(\frac{\Delta m^2_{ij}L}{4E}\right). \tag{2.70}$$

Since, $Im\left(\left|U_{\mu i}\right|^2\left|U_{\mu j}\right|^2\right) = 0$, we can rewrite the above equation as

$$P_{\mu\mu} = 1 - 4\sum_{i>j} Re\left(U^*_{\mu i}U_{\mu j}U_{\mu i}U^*_{\mu j}\right)\sin^2\left(\frac{\Delta m^2_{ij}L}{4E}\right). \tag{2.71}$$

Now, expanding it we get,

$$\begin{aligned} P_{\mu\mu} = \; & 1 - 4\Bigg[\left|U_{\mu 2}\right|^2\left|U_{\mu 1}\right|^2\sin^2\left(\frac{\Delta m^2_{21}L}{4E}\right) + \left|U_{\mu 3}\right|^2\left|U_{\mu 1}\right|^2\sin^2\left(\frac{\Delta m^2_{31}L}{4E}\right) \\ & + \left|U_{\mu 4}\right|^2\left|U_{\mu 1}\right|^2\sin^2\left(\frac{\Delta m^2_{41}L}{4E}\right) + \left|U_{\mu 3}\right|^2\left|U_{\mu 2}\right|^2\sin^2\left(\frac{\Delta m^2_{32}L}{4E}\right) \\ & + \left|U_{\mu 4}\right|^2\left|U_{\mu 2}\right|^2\sin^2\left(\frac{\Delta m^2_{42}L}{4E}\right) + \left|U_{\mu 4}\right|^2\left|U_{\mu 3}\right|^2\sin^2\left(\frac{\Delta m^2_{43}L}{4E}\right)\Bigg]. \end{aligned} \tag{2.72}$$

Now for T2K, NOνA, MINOS, IceCube and other long-baseline experiments, the following approximations are made:

$$\frac{\Delta m^2_{41}L}{4E} \simeq \frac{\Delta m^2_{42}L}{4E} \simeq \frac{\Delta m^2_{43}L}{4E} \text{ and } \frac{\Delta m^2_{32}L}{4E} \simeq \frac{\Delta m^2_{31}L}{4E}, \tag{2.73}$$

and, solar term is neglected. We also use the unitarity relation,

$$\sum_{k=1}^{4}\left|U_{\mu k}\right|^2 = 1. \tag{2.74}$$

So, from Eq. (2.72), we can write

$$
\begin{aligned}
P_{\mu\mu} \simeq\ & 1-4\left(1-\left|U_{\mu 3}\right|^2-\left|U_{\mu 4}\right|^2\right)\left|U_{\mu 3}\right|^2 \sin^2\left(\frac{\Delta m_{31}^2 L}{4E}\right) \\
& -4\left(1-\left|U_{\mu 4}\right|^2\right)\left|U_{\mu 4}\right|^2 \sin^2\left(\frac{\Delta m_{41}^2 L}{4E}\right) \qquad (2.75) \\
\simeq\ & 1-4\left(1-\left|U_{\mu 3}\right|^2-\left|U_{\mu 4}\right|^2\right)\left|U_{\mu 3}\right|^2 \sin^2\left(\frac{\Delta m_{31}^2 L}{4E}\right) \\
& -\sin^2 2\theta_{\mu\mu} \sin^2\left(\frac{\Delta m_{41}^2 L}{4E}\right), \qquad (2.76)
\end{aligned}
$$

where,

$$
\sin^2 2\theta_{\mu\mu} = 4\left|U_{\mu 4}\right|^2\left(1-\left|U_{\mu 4}\right|^2\right). \tag{2.77}
$$

By using all the above approximations, we notice that the survival probability can be expressed in terms of two matrix elements $U_{\mu 3}$ and $U_{\mu 4}$. We can further simplify the survival probability expression using some approximations. The sensitivity towards the CP-phases is very poor in this channel in vacuum. So we can safely put $\delta_{13} = \delta_{14} = 0$. Also from the reactor analysis, constraint on the mixing angle θ_{14} is very very stringent [164, 165]. As a consequence, we can assume, $\sin\theta_{14} \to 0$ and $\cos\theta_{14} \to 1$. With all these, the survival probability in vacuum can be written as,

$$
P_{\mu\mu} \simeq = 1-\cos^4\theta_{24}\sin^2 2\theta_{23}\sin^2\left(\frac{\Delta m_{31}^2 L}{4E}\right)-\sin^2 2\theta_{24}\sin^2\left(\frac{\Delta m_{41}^2 L}{4E}\right). \tag{2.78}
$$

From this expression it is clear that the long-baseline experiments [166, 167] are primarily sensitive to the matrix element $U_{\mu 4}$, i.e., to the mixing angle θ_{24} in the limit $\theta_{14} \to 0$ and can shed light on the magnitude of θ_{24} by looking at the survival channel. All the probability expressions derived above are useful for the far detector analysis only and also in vacuum. However the situation is much more complicated in presence of terrestrial matter effect which we will discuss in the next section.

Let us now calculate the ν_e survival probability used particularly in the reactor experiments [164, 165]. This is written as,

$$\begin{aligned}
P_{ee} = {} & 1-4\Bigg[|U_{e2}|^2|U_{e1}|^2\sin^2\left(\frac{\Delta m^2_{21}L}{4E}\right)+|U_{e3}|^2|U_{e1}|^2\sin^2\left(\frac{\Delta m^2_{31}L}{4E}\right) \\
& +|U_{e4}|^2|U_{e1}|^2\sin^2\left(\frac{\Delta m^2_{41}L}{4E}\right)+|U_{e3}|^2|U_{e2}|^2\sin^2\left(\frac{\Delta m^2_{32}L}{4E}\right) \\
& +|U_{e4}|^2|U_{e2}|^2\sin^2\left(\frac{\Delta m^2_{42}L}{4E}\right)+|U_{e4}|^2|U_{e3}|^2\sin^2\left(\frac{\Delta m^2_{43}L}{4E}\right)\Bigg]. \qquad (2.79)
\end{aligned}$$

Reactor experiments look for electron antineutrino disappearance channel from electron antineutrino source [1]. Due to very short-baseline nature of these experiments that is for very small L/E, we can neglect the terms related to Δm^2_{21}, Δm^2_{31} and Δm^2_{32}. So we can rewrite the Eq. (2.79) as

$$\begin{aligned}
P_{ee} = {} & 1-4\Bigg[|U_{e4}|^2|U_{e1}|^2\sin^2\left(\frac{\Delta m^2_{41}L}{4E}\right) \\
& +|U_{e4}|^2|U_{e2}|^2\sin^2\left(\frac{\Delta m^2_{42}L}{4E}\right)+|U_{e4}|^2|U_{e3}|^2\sin^2\left(\frac{\Delta m^2_{43}L}{4E}\right)\Bigg]. \qquad (2.80)
\end{aligned}$$

Again for $\frac{\Delta m^2_{41}L}{4E} \simeq \frac{\Delta m^2_{42}L}{4E} \simeq \frac{\Delta m^2_{43}L}{4E}$ and using the unitarity condition $\sum_{k=1}^{4}|U_{ek}|^2 = 1$, the above equation simplifies as,

$$P_{ee} = 1-4\left(1-|U_{e4}|^2\right)|U_{e4}|^2\sin^2\left(\frac{\Delta m^2_{41}L}{4E}\right), \qquad (2.81)$$

$$P_{ee} = 1-\sin^2 2\theta_{ee}\sin^2\left(\frac{\Delta m^2_{41}L}{4E}\right), \qquad (2.82)$$

where, $\sin^2 2\theta_{ee} = 4|U_{e4}|^2\left(1-|U_{e4}|^2\right)$. Putting the value of U_{e4} from Eq. (2.51), we can show,

$$P_{ee} = 1-\sin^2 2\theta_{14}\sin^2\left(\frac{\Delta m^2_{41}L}{4E}\right). \qquad (2.83)$$

So the reactor experiments are primarily sensitive to the matrix element U_{e4}, i.e., to the mixing angle θ_{14}.

---

[1] Accelerator based long-baseline experiment T2K [168] has also constrained $\sin^2 2\theta_{14}$ using electron antineutrino disappearance events observed in near detector.

2.7 Neutrino oscillations in 3+1 framework in presence of matter

In the previous section we have described the details of the vacuum appearance and survival oscillation probabilities in 3+1 framework. Here, we discuss the matter induced neutrino oscillations in 3+1 framework following the exact approach presented in [104].

In the presence of matter, the Hamiltonian in flavor basis is written as,

$$H = UKU^{\dagger} + V\,, \tag{2.84}$$

where K denotes the diagonal matrix containing the wave numbers

$$K = \text{diag}(0, k_{21}, k_{31}, k_{41})\,, \tag{2.85}$$

with $k_{i1} = \Delta m^2_{i1}/2E\,(i = 2,3,4)$ and V is given as

$$V = \text{diag}(V_{CC}, 0, 0, -V_{NC})\,, \tag{2.86}$$

where,

$$V_{CC} \;=\; \sqrt{2}G_F N_e \tag{2.87}$$

is the charged-current interaction matter potential of the electron neutrinos. N_e is the electron number density of Earth matter, and

$$V_{NC} \;=\; -\frac{G_F N_n}{\sqrt{2}} \tag{2.88}$$

is the neutral-current interaction matter potential (common to all the active neutrino species). N_n is the neutron number density of matter. For later convenience, we introduce a positive-definite ratio "r" as

$$r = -\frac{V_{NC}}{V_{CC}} = \frac{1}{2}\frac{N_n}{N_e}\,. \tag{2.89}$$

In an electrically neutral, isoscalar medium like Earth matter, $N_e \simeq N_p \simeq N_n$, which results $r \simeq 0.5$. In order to simplify the analytical calculation with matter effects, it is convenient to go to a new basis

$$\bar{\nu} = \bar{U}^{\dagger} \nu \,, \tag{2.90}$$

where

$$\bar{U} = R_{34}(\theta_{34}, \delta_{34}) R_{24}(\theta_{24}, 0) R_{14}(\theta_{14}, \delta_{14}) \tag{2.91}$$

is the 4×4 mixing matrix involving the active-sterile rotations. So, the mixing matrix U defined in Eq. (2.50) can be written as

$$U = \bar{U} U_{3\nu} \,, \tag{2.92}$$

where $U_{3\nu}$ is the 4×4 matrix involving the rotations related to (1,2,3) sub-block, that is,

$$U_{3\nu} = R(\theta_{23}, 0) R(\theta_{13}, \delta_{13}) R(\theta_{12}, 0) \tag{2.93}$$

In the new basis, the Hamiltonian becomes

$$\bar{H} = \bar{H}^{\mathrm{kin}} + \bar{H}^{\mathrm{dyn}} = U_{3\nu} K U_{3\nu}^{\dagger} + \bar{U}^{\dagger} V \bar{U} \,, \tag{2.94}$$

where the first term is the kinematic contribution describing the neutrino oscillations in vacuum, and the second one represents a nonstandard dynamical term describes the matter interactions. Now, $|k_{41}|$ is much bigger than $|k_{21}|$ and $|k_{31}|$. Indeed, it can be seen from Eq. (2.94) that, (4,4) entry of $\bar{H}$ is much bigger than all the other elements and the fourth eigenvalue of $\bar{H}$ is much larger than the other three ones. As a result the fourth eigenstate $\bar{\nu}_s$ evolves independently of the others. So we can write down the 4×4 Hamiltonian as effective 3×3 Hamiltonian by extracting the submatrix with indices $(1,2,3)$ from $\bar{H}$, i.e.,

$$\bar{H}_{3\nu} = \bar{H}_{3\nu}^{\mathrm{kin}} + \bar{H}_{3\nu}^{\mathrm{dyn}} \tag{2.95}$$

governing the evolution of the $(\bar{\nu}_e, \bar{\nu}_\mu, \bar{\nu}_\tau)$ system, where the dynamical part is given as

$$\bar{H}_{3\nu}^{\text{dyn}} = V_{CC} \begin{bmatrix} |\bar{U}_{e1}|^2 + r|\bar{U}_{s1}|^2 & r\bar{U}_{s1}^* \bar{U}_{s2} & r\bar{U}_{s1}^* \bar{U}_{s3} \\ \dagger & r|\bar{U}_{s2}|^2 & r\bar{U}_{s2}^* \bar{U}_{s3} \\ \dagger & \dagger & r|\bar{U}_{s3}|^2 \end{bmatrix}, \tag{2.96}$$

The sign † represents the complex conjugate of the element with the same two indices inverted. In the above equation we have used the relations $\bar{U}_{e2} = \bar{U}_{e3} = \bar{U}_{\mu 3} = 0$. Now expanding the small mixing angles θ_{i4} $(i = 1, 2, 3)$ upto first order, Eq. (2.96) can be written as,

$$\bar{H}_{3\nu}^{\text{dyn}} \approx V_{\text{CC}} \begin{bmatrix} 1-(1-r)s_{14}^2 & r\tilde{s}_{14} s_{24} & r\tilde{s}_{14} \tilde{s}_{34}^* \\ \dagger & r s_{24}^2 & r s_{24} \tilde{s}_{34}^* \\ \dagger & \dagger & r s_{34}^2 \end{bmatrix}. \tag{2.97}$$

We notice that if we put the new mixing angles θ_{14}, θ_{24}, and θ_{34} to be zero then one recovers the (diagonal) standard 3-flavor MSW Hamiltonian. In general, in the 4-flavor case, the Hamiltonian in Eq. (2.97) encodes both diagonal and off-diagonal perturbations.

Let us now give the scattering matrix in the new basis $\bar{\nu}$ for further calculation of oscillation probabilities.

$$\bar{S} \equiv e^{-i\bar{H}L} \approx \begin{pmatrix} e^{-i\bar{H}_{3\nu}L} & 0 \\ 0 & e^{-ik_{41}L} \end{pmatrix}, \tag{2.98}$$

which can be rotated to the original flavor basis by using the unitary transformation such as

$$S = \bar{U}\bar{S}\bar{U}^\dagger. \tag{2.99}$$

Now after calculating the S-matrix elements it is straight forward to calculate the oscillation probability. For example, a source flavor ν_α is related to the final flavor ν_β after traversing a distance L is given by,

$$\nu_\beta(L) = S_{\beta\alpha}\nu_\alpha(0), \tag{2.100}$$

and the 4-flavor oscillation probability is given by,

$$P_{\alpha\beta}^{4\nu} \equiv P^{4\nu}(\nu_\alpha \to \nu_\beta; L) = |S_{\beta\alpha}|^2 \,. \tag{2.101}$$

Now using the relations $\bar{U}_{e2} = \bar{U}_{e3} = \bar{U}_{\mu 3} = 0$, one can easily calculate the two S-matrix elements relevant for appearance ($\nu_\mu \to \nu_e$) and survival ($\nu_\mu \to \nu_\mu$) probability which are given as,

$$\begin{aligned} S_{e\mu} &= \bar{U}_{e1}\left[\bar{U}_{\mu 1}^{*}\bar{S}_{ee} + \bar{U}_{\mu 2}^{*}\bar{S}_{e\mu}\right] + \bar{U}_{e4}\bar{U}_{\mu 4}^{*}\bar{S}_{ss}\,, &(2.102)\\ S_{\mu\mu} &= \bar{U}_{\mu 1}^{*}\left[\bar{U}_{\mu 1}\bar{S}_{ee} + \bar{U}_{\mu 2}\bar{S}_{\mu e}\right] + \bar{U}_{\mu 2}^{*}\left[\bar{U}_{\mu 1}\bar{S}_{e\mu} + \bar{U}_{\mu 2}\bar{S}_{\mu\mu}\right] + |\bar{U}_{\mu 4}|^2\bar{S}_{ss}\,, &(2.103) \end{aligned}$$

where the five relevant matrix elements of the matrix $\bar{U}$ are given by

$$\begin{aligned} \bar{U}_{e1} &= c_{14} \\ \bar{U}_{\mu 1} &= s_{14}s_{24}e^{i\delta_{14}} \\ \bar{U}_{\mu 2} &= c_{24} \\ \bar{U}_{e4} &= s_{14}e^{-i\delta_{14}} \\ \bar{U}_{\mu 4} &= c_{14}s_{24}\,. \end{aligned} \tag{2.104}$$

It is very clear from Eq. (2.102) and Eq. (2.103) that in vacuum, both $S_{e\mu}$ and $S_{\mu\mu}$ are independent of the mixing angle θ_{34} and the associated CP-phase δ_{34}, whereas in matter they are dependent on θ_{34} and δ_{34} through the matrix elements $\bar{S}_{ee}$, $\bar{S}_{e\mu}$, $\bar{S}_{\mu e}$ and $\bar{S}_{\mu\mu}$.

Due to very fast oscillations induce by the term $\bar{S}_{ss} = e^{-ik_{41}L}$, one should consider average value of the square of the sine or cosine functions associated with the large mass-squared difference Δm_{41}^2 while calculating the oscillation probabilities. Although for numerical analysis those terms get averaged out automatically by the finite energy resolution of the detector.

As an example let us now calculate the 4ν appearance probability in presence of matter following [104].

$$\begin{aligned} P^{4\nu}_{\mu e} \equiv |S_{e\mu}|^2 = & |\bar{U}_{e1}|^2 \, |\bar{U}_{\mu 1}|^2 \, |\bar{S}_{ee}|^2 \\ & + |\bar{U}_{e1}|^2 \, |\bar{U}_{\mu 2}|^2 \, |\bar{S}_{e\mu}|^2 \\ & + 2 \, |\bar{U}_{e1}|^2 \, \mathrm{Re} \, [\bar{U}^*_{\mu 1} \, \bar{U}_{\mu 2} \, \bar{S}_{ee} \, \bar{S}^*_{e\mu}] \\ & + |\bar{U}_{e4}|^2 \, |\bar{U}_{\mu 4}|^2 \, . \end{aligned} \tag{2.105}$$

Now using the explicit form of the matrix elements given in Eq. 2.104, we can simplify the probability expression as

$$\begin{aligned} P^{4\nu}_{\mu e} = & \, c^2_{14} \, s^2_{14} \, s^2_{24} \, \bar{P}^{3\nu}_{ee} \\ & + c^2_{14} \, c^2_{24} \, \bar{P}^{3\nu}_{\mu e} \\ & - 2 \, c^2_{14} \, c_{24} \, s_{14} \, s_{24} \, \mathrm{Re} \, (e^{-i\delta_{14}} \, \bar{S}_{ee} \, \bar{S}^*_{e\mu}) \\ & + c^2_{14} \, s^2_{14} \, s^2_{24} \, , \end{aligned} \tag{2.106}$$

with $\bar{P}^{3\nu}_{ee} = |\bar{S}_{ee}|^2$ and $\bar{P}^{3\nu}_{\mu e} = |\bar{S}_{e\mu}|^2$.

Now for small mixing angles of θ_{14} and θ_{24}, we can further simplify the above equation as

$$\begin{aligned} P^{4\nu}_{\mu e} = & \, (1 - s^2_{14} - s^2_{24}) \, \bar{P}^{3\nu}_{\mu e} \\ & - 2 \, s_{14} \, s_{24} \, \mathrm{Re} \, (e^{-i\delta_{14}} \, \bar{S}_{ee} \, \bar{S}^*_{e\mu}) \\ & + s^2_{14} \, s^2_{24} \, (1 + \bar{P}^{3\nu}_{ee}) \end{aligned} \tag{2.107}$$

In a similar fashion, we can also calculate the survival probability $P^{4\nu}_{\mu\mu}$ by squaring the modulous of the S-matrix element $S_{\mu\mu}$, i.e.,

$$P^{4\nu}_{\mu\mu} = |S_{\mu\mu}|^2 . \tag{2.108}$$

All the above calculations presented in this chapter are very very useful in providing a very good understanding of the oscillation physics of neutrinos in two-flavor, three-flavor, and four-flavor framework both in vacuum as well as in presence of matter. In addition understanding the numerical results also becomes much easier with the help of these analytical expressions.

Chapter 3

Experimental Motivations of the existence of eV-Scale Sterile Neutrino

3.1 Short-baseline anomalies and indication of the eV-scale sterile neutrino:

In this section we discuss a number of experimentally observed anomalies like reactor anomaly, Gallium anomaly, LSND anomaly, and MiniBooNE anomaly which indicate in favour of the existence of one (at least) additional mass eigenstate ν_4 with one eV-scale order mass-squared difference (Δm^2). This new extra mass eigenstate is known as "sterile neutrino". Let us now discuss these anomalies one by one.

3.1.1 Gallium anomaly

Gallium anomaly [169, 170, 171, 172] is a short-baseline anomaly related to the deficit of ν_e survival events in the Gallium detector of two radioactive source experiments GALLEX [173, 174, 175] and SAGE [169, 176, 177, 178]. These two experiments were designed to detect solar neutrino oscillation. Now in order to optimize these experiments, two artificial radioactive sources ^{51}Cr and ^{37}Ar were used which produce electron neutrinos through the electron capture process

$$e^- + {}^{51}Cr \rightarrow {}^{51}Cr + \nu_e, \quad e^- + {}^{37}Ar \rightarrow {}^{37}Cl + \nu_e\,. \tag{3.1}$$

These electron neutrinos were observed through the process

$$\nu_e + {}^{71}Ga \rightarrow {}^{71}Ge + e^-\,, \tag{3.2}$$

where the threshold of detecting neutrino was 0.233 MeV. The germanium-71 produced in this reaction was first chemically extracted and then it was converted to germane (${}^{71}GeH_4$). Its decay was then detected in the counters where one decay corresponds to detection of one neutrino. The ratio of the observed (N_{exp}) and the calculated (N_{cal}) production rate of Ge-71 was found 0.84 ± 0.05 which is a deficit with a nominal 2.7σ statistical significance as can be seen from the figure. One of the possible reasons may be that ν_e is oscillating into sterile state and evading the detection process in the detector. Since the two experiments have average baseline $< L >_{GALLEX} = 1.9$m and $< L >_{SAGE} = 0.6$m respectively and average energy is of the order of KeV-scale, the Gallium anomaly can be explained by the neutrino oscillation generated by the mass-squared difference

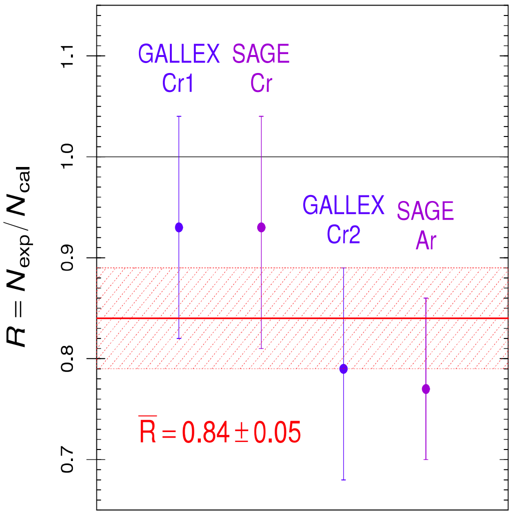

Figure 3.1: Ratio of the observed (N_{exp}) and the calculated (N_{cal}) electron neutrino events in two experiments GALLEX and SAGE. The horizontal red line corresponds to the average ratio $\bar{R}$ with the red band shows the uncertainty. This figure has been taken from [84].

$$\Delta m^2 \geq 1\ \mathrm{eV}^2. \tag{3.3}$$

3.1.2 LSND anomaly

It is an excess of $\bar{\nu}_e$ events in $\bar{\nu}_\mu$ beam. LSND (Liquid Scintillator Neutrino Detector) experiment [158, 159] was dedicatedly designed to search for the $\bar{\nu}_\mu \rightarrow \bar{\nu}_e$ oscillation with high sensitivity. The oscillation length of this experiment was 30 m and the $\bar{\nu}_e$ events traversed a distance of 30 m before they were detected in the liquid scintillator detector in the energy range $20 \lesssim E_e \lesssim 60$ MeV for the energy E_e of the detected positron. $\bar{\nu}_\mu$ neutrinos were produced from the μ^+ decay at rest and they oscillated to $\bar{\nu}_e$ while traversing from source to detector and detected through the inverse neutron decay process

$$\mu^+ \rightarrow e^+ + \nu_e + \bar{\nu}_\mu, \;\; \bar{\nu}_e + p \rightarrow n + e^+. \tag{3.4}$$

The data obtained from the experiment reported an excess $\bar{\nu}_e$ events over the background

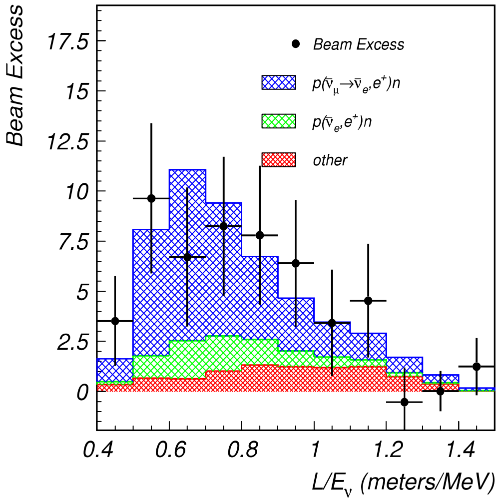

Figure 3.2: Electron antineutrino access in LSND. This figure has been taken from [159].

as shown in Fig. 3.2. The statistical significance of this excessive events is about 3.8σ. One of the best possible reasons may be that some of the $\bar{\nu}_\mu$ neutrinos convert into sterile states and then again come back as $\bar{\nu}_e$ flavor leading to an excess as discussed above. Now in order to have such kind of oscillation in this experiment, new mass-squared difference should be

$$\Delta m^2 \geq 0.1 \text{ eV}^2. \tag{3.5}$$

However it should be noted that the KARMEN [179, 180] with baseline 18 m and almost same energy range did not confirm the same result as LSND but could not exclude the entire allowed region in $(\sin^2 2\theta,\ \Delta m^2)$ plane constrained by LSND.

3.1.3 MiniBooNE anomaly

In order to test the LSND results, MiniBooNE experiment was designed in Fermilab with a baseline of 540 m. The experiment was operated in both neutrino [160] and antineutrino mode [161, 162], and the collected data have been fitted by the effective two neutrino model. The result shows that the oscillations obtained in $\nu_\mu \to \nu_e$ and $\bar{\nu}_\mu \to \bar{\nu}_e$ channel can be explained by the new mass-squared difference in the range $0.01\text{eV}^2 \leq \Delta m^2 \leq 1\text{eV}^2$ and the allowed region in $(\sin^2 2\theta,\ \Delta m^2)$ plane is consistent with the region given by LSND result. However, in the low energy regime the data is not consistent with the fit for both neutrino and antineutrino events, whereas in the high energy region data gives consistent result as shown in Fig. 3.3. The overall statistical significance of excess of MiniBooNE events is 3.4σ for neutrino mode and 2.8σ for antineutrino mode. To understand the physics behind this kind of excess, MicroBooNE experiment has been designed and it is expected to provide us accurate information in coming days.

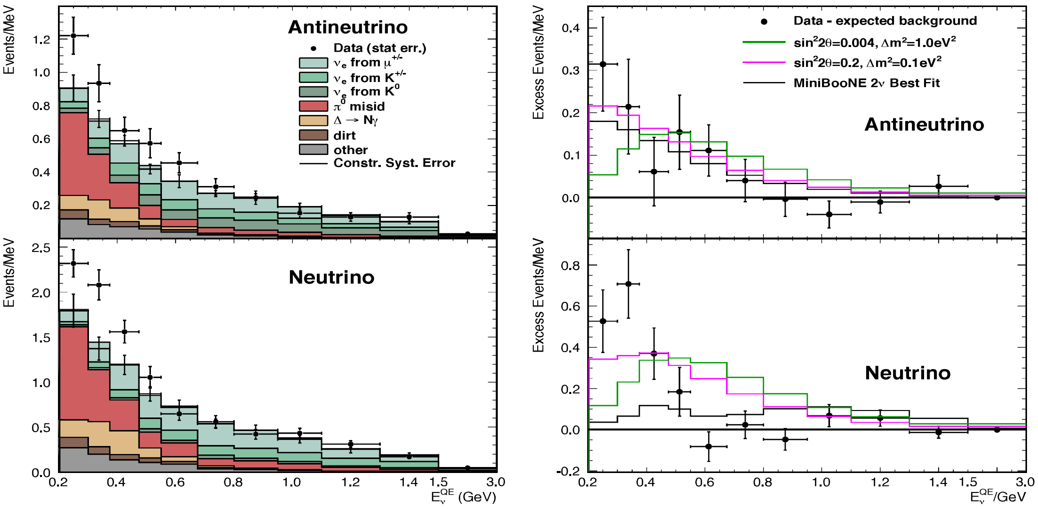

Figure 3.3: Electron neutrino and antineutrino access in MiniBooNE. This figure has been taken from [162].

3.1.4 Reactor antineutrino anomaly

New analysis of reactor electron antineutrino flux [181] predicts 3% higher flux than the earlier existing calculation. As a result one should expect more events in the detector. But a deficit of $\bar{\nu}_e$ events has been observed in comparison with the events expected from the calculation of the reactor antineutrino fluxes . This is known as reactor antineutrino anomaly [182, 183, 184]. It has been observed by many reactor based short-baseline experiments like Daya Bay [185, 186, 187], RENO [188], Double Chooz [189]. However the statistical significance of the deficiency depends on the estimated uncertainties of the calculated reactor antineutrino fluxes, and the situation has become more complicated specially after the discovery of a 5 MeV bump in antineutrino reconstructed energy spectrum observed by all the above three reactor experiments. In reactor experiments, the electron antineutrinos are detected in the liquid scintillator detector through the process,

$$\bar{\nu}_e + p \rightarrow n + e^+, \tag{3.6}$$

and the energy threshold for the detection of neutrino is 1.8 MeV. The average ratio $\bar{R}$ of the observed events (N_{exp}) and the calculated events (N_{cal}) have been found as 0.934 ± 0.024 [183] as can be seen in Fig. 3.4.

Now it may happen that some of the $\bar{\nu}_e$ neutrinos are oscillating into the sterile states and as a result we see a deficit of $\bar{\nu}_e$ events in the detector. Like other anomalies as discussed above, reactor antineutrino anomaly can also be explained by the neutrino oscillation generated by the additional mass-squared difference if,

$$\Delta m^2 \geq 0.5\,\mathrm{eV}^2. \tag{3.7}$$

So all the anomalies discussed above stimulate us to think about the physics beyond the standard model and all of them hint towards the existence of a new mass-squared difference of the order of eV^2 as one of best possible solutions and this Δm^2 is much much greater than the magnitude of the two already known solar ($\Delta m^2_{21} \sim 10^{-5}\,\mathrm{eV}^2$) and atmospheric ($|\Delta m^2_{31}| \sim 10^{-3}\,\mathrm{eV}^2$) mass-squared splittings.

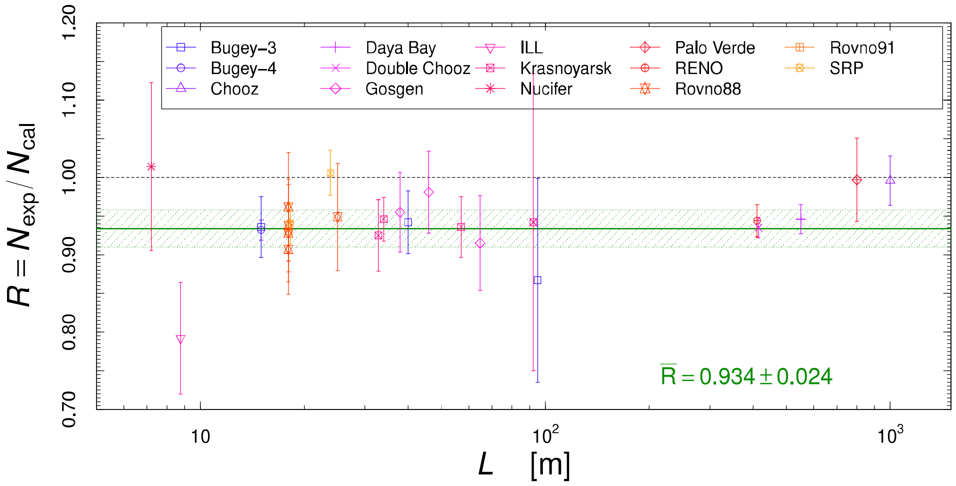

Figure 3.4: Figure shows the ratio R of the observed events and the calculated events of different reactor experiments as a function reactor detector distance (L). Error bars are the uncertainties associated with different experiments. The horizontal black dotted line denotes the expected ratio. The horizontal green band shows the average ratio ($\bar{R}$) and its uncertainty. This figure has been taken from [183].

Chapter 4

Current status of the oscillation parameters in 3ν and 3+1 frameworks

Tremendous efforts and invaluable contributions from the neutrino oscillation experiments in the atmospheric, accelerator, reactor, and solar sector over the last few decades have established the existence of three flavor framework of neutrinos beyond any doubt. As already discussed earlier, it involves two independent mass-squared splittings (atmospheric splitting $|\Delta m^2_{31}| = |m^2_3 - m^2_1|$ or $|\Delta m^2_{32}| = |m^2_3 - m^2_2|$, and solar splitting, $\Delta m^2_{21} = m^2_2 - m^2_1$), three mixing angles ($\theta_{12}$, θ_{13}, θ_{23}), and one CP-phase $\delta_{\mathrm{CP}}(\equiv \delta_{13})$. All these parameters have been measured quite precisely except θ_{23} and CP-phase δ_{CP}. The solar neutrino oscillation data, and the reactor based KamLAND experiment data [190, 191, 192, 193] which are sensitive to the same oscillation channel, have measured θ_{12} and Δm^2_{21} with a good precision as evident from Fig. 4.1. It is worth to mention here that there is a mild tension between the measurements of Δm^2_{21} by KamLAND which prefers the best fit value: $7.6 \times 10^{-5}\,\mathrm{eV}^2$, and by solar neutrino data which prefers the best fit value: $4.96 \times 10^{-5}\,\mathrm{eV}^2$, leading to a discrepancy at the 2σ level. However, the global analysis of all these oscillation data [193] prefers the best fit value of Δm^2_{21} close to the value preferred by the KamLAND data. Now, based on atmospheric neutrino oscillation, Super-Kamiokande [194] has measured another two parameters, namely $\sin^2 2\theta_{23}$ and $|\Delta m^2_{32}|$. Accelerator based long-baseline experiment MINOS [195] has also constrained the $\sin^2\theta_{23}$ and $|\Delta m^2_{32}|$ parameter space as can be seen from the red dashed curve of the left panel of Fig. 4.2. The reactor experiments Daya Bay [196], RENO [197], Double

Chooz [16] have measured θ_{13} mixing angle very precisely. With the recent data based on 1230 days of operation, Daya Bay [198] have given a very precise measurement on $\sin^2 2\theta_{13}$ (0.0841 $\pm$ 0.0027 (stat.) $\pm$ 0.0019 (syst.)) as shown in the right panel of Fig. 4.2. However despite all these utmost efforts there are two fundamental oscillation parameters still remain poorly determined, namely θ_{23} and the CP phase $\delta_{\rm CP}$. Very recent result from the NOνA experiment [26] hints towards the non-maximal θ_{23} with two nearly degenerate solutions as can be seen from the left panel of Fig.(4.2): one is $\theta_{23} < \pi/4$, known as lower octant (LO), and the other one is $\theta_{23} > \pi/4$, called higher octant (HO). In addition, although the sign of Δm^2_{21} ($m^2_2 - m^2_1$) is known to be positive, but the sign of Δm^2_{31} or Δm^2_{32} remains unknown and this is known as mass hierarchy (MH) problem (see Fig. (4.3)). It can be either positive ($m_1 < m_2 < m_3$), known as normal hierarchy (NH) or it can be negative ($m_3 < m_1 < m_2$), denoted as inverted hierarchy (IH). Now regarding the CP phase $\delta_{\rm CP}$, it is worthwhile to mention that a preliminary analysis with all its latest data combining with the reactor antineutrino measurements, T2K [202] excludes the CP conserving phases at 95% C.L for both the choices of mass hierarchies (NH or IH) as can be seen from Fig. (4.4).

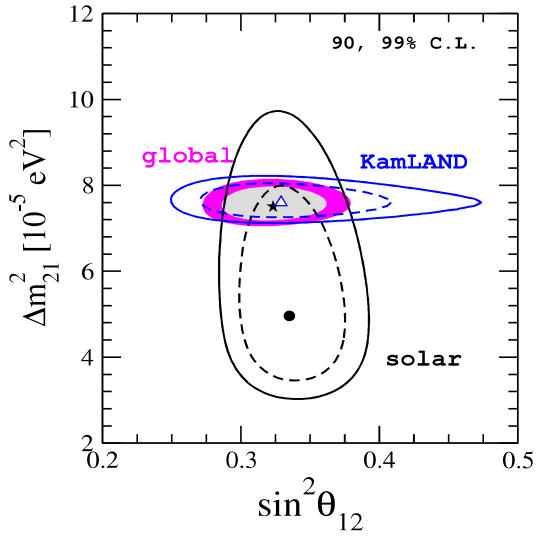

Figure 4.1: 90% and 99% C.L. allowed region in $\sin^2\theta_{12}$ and Δm^2_{21} plane constrained by solar (black lines), KamLAND (blue lines), and global (colored regions) data. This figure has been taken from [193].

Lack of sufficient data has so far been the biggest obstacle to making any firm statement regarding these unknown issues. Accelerator based ongoing and upcoming long-baseline experiments like T2K [121, 122], NOνA [123, 124], DUNE [125, 126],

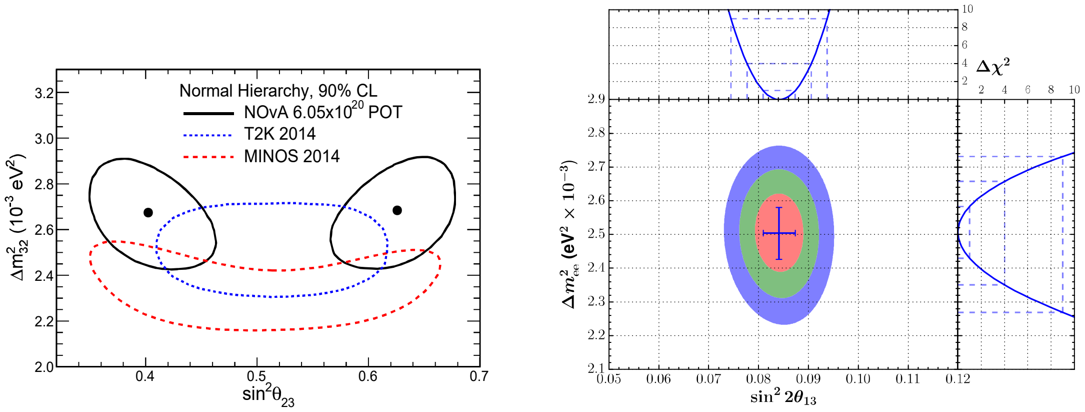

Figure 4.2: (a) 90% C.L. allowed region of $\sin^2\theta_{23}$ and Δm^2_{32}. Black dots denote the best fit values obtained by NOνA. Blue and red dashed curves correspond to T2K [199] and MINOS [195] allowed contours respectively. This figure has been taken from [26]. (b) Allowed region in $\sin^2 2\theta_{13}$ and Δm^2_{ee} plane constrained by Daya Bay data. Here, $\Delta m^2_{ee} \simeq \cos^2\theta_{12}\,|\Delta m^2_{31}| + \sin^2\theta_{12}\,|\Delta m^2_{32}|$ [200]. The color shaded regions correspond to 1σ (red), 2σ (green), and 3σ (blue) confidence regions at 2 d.o.f. The top and right panels depict the $\Delta\chi^2$ profile along $\sin^2 2\theta_{13}$ and Δm^2_{ee} axes respectively. This figure has been taken from [198].

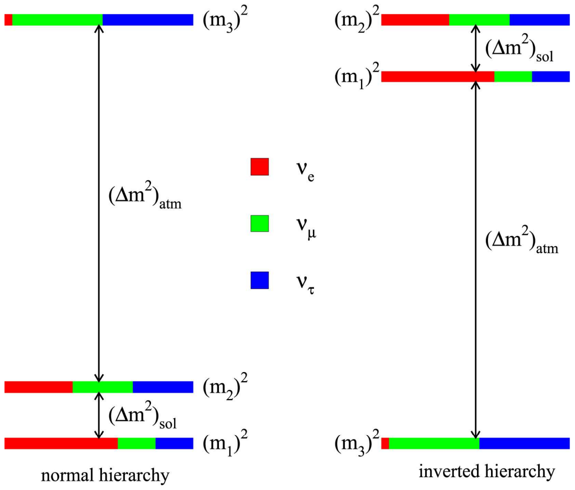

Figure 4.3: Two possible neutrino mass ordering. This figure has been taken from [201].

and T2HK [143, 144] are expected to provide very precise measurement on the parameters θ_{23}, Δm^2_{31} (with correct sign), and CP phase $\delta_{\rm CP}$. Although all these individual sectors give independent measurements of different oscillation parameters, it is highly needed to make full 3-flavor analysis combining all the data available so far from all those sectors mentioned above. In that perspective, global fit analyses [23, 24, 25] of neutrino and antineutrino oscillation data do that job. All of these analyses agree quite well with each other. From the very recent analysis [25], the current status of the 3ν oscillation parameters is shown in the Table 4.1.

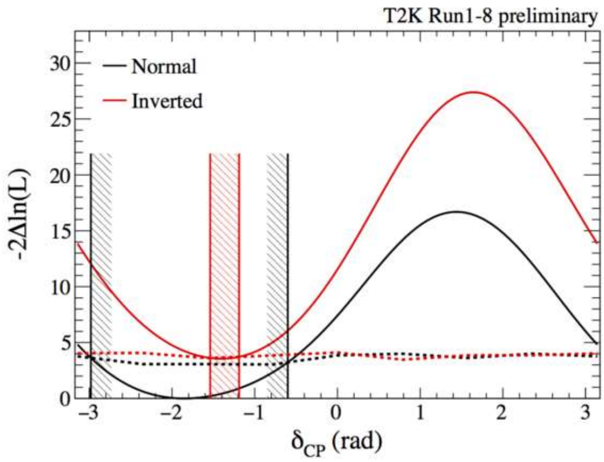

Figure 4.4: -2ΔlnL (equivalent to $\Delta\chi^2$) vs $\delta_{\rm CP}$ is shown for normal hierarchy (black curve) and inverted hierarchy (red curve). Black (red) vertical lines correspond to 95% C.L. allowed region of CP violating phases for NH (IH) cases. This figure has been taken from [202].

Parameter	**Best fit value**	**3σ range**
$\sin^2\theta_{12}$	0.320	0.273-0.379
$\sin^2\theta_{13}$ (NH)	0.021	0.019-0.024
$\sin^2\theta_{13}$ (IH)	0.022	0.020-0.024
$\sin^2\theta_{23}$ (NH)	0.547	0.445-0.599
$\sin^2\theta_{23}$ (IH)	0.551	0.453-0.598
$\delta_{\rm CP}/^\circ$ (NH)	218	157-349
$\delta_{\rm CP}/^\circ$ (IH)	281	202-349
$\frac{\Delta m^2_{21}}{10^{-5}\,{\rm eV}^2}$	7.55	7.05-8.14
$\frac{\lvert\Delta m^2_{31}\rvert}{10^{-3}\,{\rm eV}^2}$ (NH)	2.50	2.41-2.60
$\frac{\lvert\Delta m^2_{31}\rvert}{10^{-3}\,{\rm eV}^2}$ (IH)	2.42	2.31-2.51

Table 4.1: Current status of the oscillation parameters [25] in 3ν framework.

Let us now discuss the current status of the oscillation parameters involved in 3+1 framework. As already discussed earlier, in presence of a sterile neutrino, there exists three more mixing angles (θ_{14}, θ_{24}, and θ_{34}), two more CP-phases (δ_{14} and δ_{34} according to our parameterization) and one large mass-squared splitting Δm^2_{41} in addition to those involved in the standard 3-flavor framework. Very recent results from IceCube [166], Daya Bay [164], MINOS [167] collaboration have placed new constraints on active-sterile mixing angles. Using the electron antineutrino disappearance measurements, short-baseline reactor experiment Daya Bay along with Bugey-3 data [165] has provided an upper bound on $\sin^2 2\theta_{14}$ which is $\simeq 0.06$ at 90% C.L. around the best fit value of $\Delta m^2_{41} \simeq 1.75\,\text{eV}^2$ [203] as can be seen from Fig. 4.5. Extracting further information suggests that $\theta_{14} \lesssim 7°$ or so. Using the muon neutrino and antineutrino disappearance

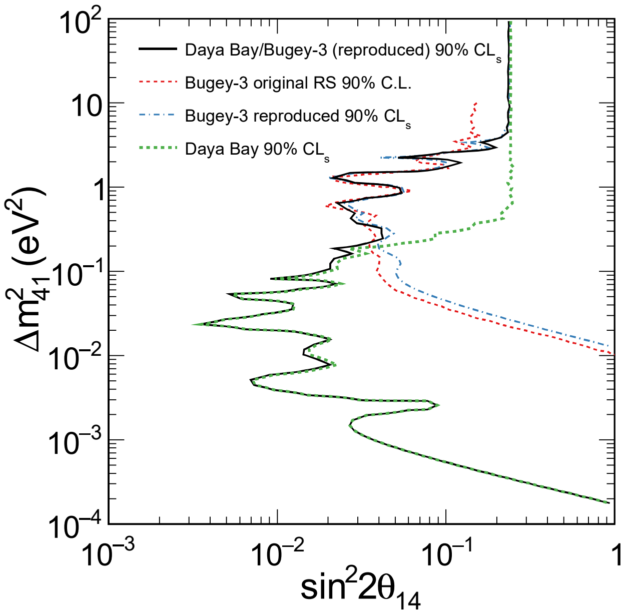

Figure 4.5: Figure shows the 90% C.L. allowed space of $\sin^2 2\theta_{14}$ and Δm^2_{41} plane with different combination of data set. Regions to the right of the curves are excluded. This figure has been taken from [165].

measurements, IceCube [166] collaboration result suggests a new upper limit of $\simeq 0.06$ on $\sin^2 2\theta_{24}$ at 90% C.L. around $\Delta m^2_{41} \simeq 1.75\,\text{eV}^2$, which means that θ_{24} is constrained to be smaller than 7° or so. However this is the most conservative exclusion limit on θ_{24} where $\theta_{34} = 0$ has been assumed in the analysis. Similarly, MINOS [165, 167] collaboration has put an upper bound of $\simeq 0.03$ on $|U_{\mu 4}|^2$ (see Eq. 2.51) that is on $\sin^2\theta_{24}$ (with the approximation of $\theta_{14} = 0$) at 90% C.L around $\Delta m^2_{41} \simeq 1.75\,\text{eV}^2$ which is equivalent to $\theta_{24} \lesssim 10°$ (see Fig. 4.6). In this analysis, θ_{34} has been marginalized, and $\theta_{14} = 0$ has been considered because of its very negligible effect on the ν_μ survival channel of interest.

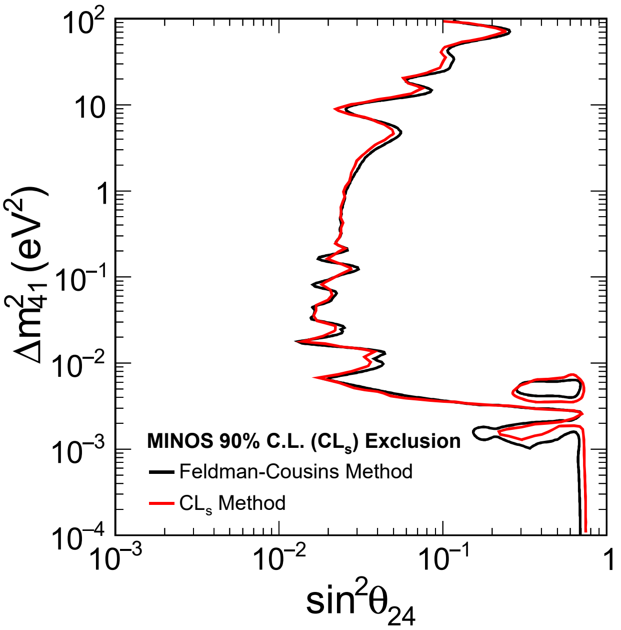

Figure 4.6: Figure shows the 90% C.L. allowed space of $\sin^2\theta_{24}$ and Δm^2_{41} plane with MINOS data. Regions to the right of the curves are excluded. This figure has been taken from [165].

In addition to the information on $|U_{\mu 4}|^2$, MINOS and IceCube data also shed some light on the another active-sterile mixing matrix element $|U_{\tau 4}|^2$ (see Eq. 2.51) that is on the mixing angle θ_{34}. Sensitivity to this mixing angle basically comes from the neutral current event sample in case of MINOS [167] and from the matter effect of high energy neutrinos propagating through Earth in case of IceCube [96, 204, 205, 206, 207, 208, 209, 210]. Analysis of atmospheric neutrino data of Super-Kamiokande [98] has put an upper limit of $|U_{\tau 4}|^2 < 0.18$ at 90% C.L. for $\Delta m^2_{41} > 0.1\,\text{eV}^2$. MINOS [167] data also has constrained $\sin^2\theta_{34}$ at 90% C.L. which is < 0.2 for $\Delta m^2_{41} = 0.5\,\text{eV}^2$. Again, using three years of IceCube DeepCore data [211], a new limit of $|U_{\tau 4}|^2 < 0.15$ has been obtained at 90% C.L. for $\Delta m^2_{41} = 1\,\text{eV}^2$ (see Fig. 4.7).

Similar to the 3ν global analysis, there have also been few 3+1 global analyses [106, 183, 203, 213] performed in the very recent past combining all the data available so far in the atmospheric, accelerator, reactor, and solar sector. Very recently, updated 3+1 global analysis [183] of short-baseline neutrino oscillation data have provided a clear overview on the current status of the active-sterile mixing parameters as shown in the Table 4.2. The most important point to note from this analysis is that, the inclusion of IceCube [166] and MINOS [167] data have helped a lot to put a stringent constraint on

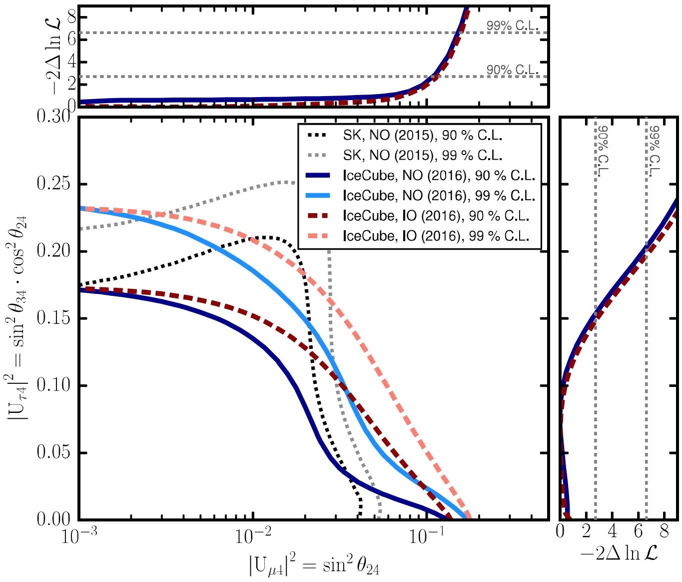

Figure 4.7: Middle big panel of the figure shows the 90% and 99% C.L. allowed parameter space in the plane $\left[|U_{\mu4}|^2,\, |U_{\tau4}|^2\right]$ for different data set and mass ordering. Regions to the right of the curves are excluded. The top and right panels are the likelihood projection on the active-sterile mixing matrix elements $|U_{\mu4}|^2$ and $|U_{\tau4}|^2$ respectively. All these results have been obtained for $\Delta m^2_{41} = 1.0\,\text{eV}^2$. This figure has been taken from [211].

Parameter	Best fit value	3σ range
$\lvert U_{e4}\rvert^2$	0.020	0.0098-0.031
$\lvert U_{\mu4}\rvert^2$	0.015	0.0060-0.026
$\lvert U_{\tau4}\rvert^2$	-	$\lesssim 0.039$
$\Delta m^2_{41}\,/\,\text{eV}^2$	1.70	$\lesssim$ 148 [212]

Table 4.2: Current status of the active-sterile mixing oscillation parameters [183] in 3+1 framework.

$|U_{\tau4}|^2\,(< 0.014)$, and $\theta_{34}\,(< 7^\circ)$ at 90% C.L. respectively for any values of Δm^2_{41}. However, it has been shown that the main contribution in constraining the allowed region of $|U_{\tau4}|^2$ for $\Delta m^2_{41} \lesssim 1.5\,\text{eV}^2$ comes from the IceCube than the MINOS data. It is worth to mention that currently the constraint on the CP phase δ_{14} [214] is very weak, in fact any value in between $-\pi$ to π is allowed at 3σ C.L. Similarly at present we also have no concrete information regarding the CP phase δ_{34} which may possess any value within its allowed range $[-\pi,\, \pi]$.

Now following all the above mentioned recent past global analyses more or less, for the purpose of the works [215, 216, 217] presented in this thesis, we have used the following benchmark values of the oscillation parameters as shown in the Table 4.3. However for the work [218] presented also in this thesis, we have used slightly different set of parameter values as shown in the Table 9.2 of chapter 9.

Parameter	**True value**	**Marginalization Range**
$\sin^2\theta_{12}$	0.304	Not marginalized
$\sin^2 2\theta_{13}$	0.085	Not marginalized
$\sin^2\theta_{23}$	0.42, 0.50, 0.58	[0.34, 0.68]
$\sin^2\theta_{14}$	0.025	Not marginalized
$\sin^2\theta_{24}$	0.025	Not marginalized
$\sin^2\theta_{34}$	0, 0.025, 0.25	Not marginalized
$\delta_{13}/^\circ$	[- 180, 180]	[- 180, 180]
$\delta_{14}/^\circ$	[- 180, 180]	[- 180, 180]
$\delta_{34}/^\circ$	[- 180, 180]	[- 180, 180]
$\frac{\Delta m^2_{21}}{10^{-5}\,\text{eV}^2}$	7.50	Not marginalized
$\frac{\Delta m^2_{31}}{10^{-3}\,\text{eV}^2}$ (NH)	(2.475)	Not marginalized
$\frac{\Delta m^2_{31}}{10^{-3}\,\text{eV}^2}$ (IH)	- 2.4	Not marginalized
$\frac{\Delta m^2_{41}}{\text{eV}^2}$	1.0	Not marginalized

Table 4.3: Parameter values/ranges used in the numerical calculations. The second column reports the true values of the oscillation parameters used to simulate the "observed" data set. The third column depicts the range over which $\sin^2\theta_{23}$, $\delta_{13}(\equiv\delta_{\text{CP}})$, δ_{14}, and δ_{34} are varied while minimizing the χ^2 to obtain the final results.

Chapter 5

Brief description of the Experimental setups and definition of χ^2

In order to assess the physics potential of the long-baseline (LBL) experiments, we have performed all the numerical simulations using GLoBES [219, 220] software along with its extra tools [221]. Here, in section 5.1, we give a brief description of all the LBL experiments which have been simulated for our present study. In section 5.2, we present the definition of χ^2 used to get a quantitative measurement of the sensitivity of the standard and new physics scenario. Finally in section 5.3, we present a very useful relation between the proton beam power, proton energy, and number of protons on target. This relationship carries a high value as it gives an overall idea about the potential of an experiment.

5.1 LBL experiments

5.1.1 DUNE:

DUNE is a future-generation highly sophisticated long-baseline neutrino oscillation experiment having 1300 km baseline from Fermilab to South Dakota in USA. It is expected to play an important role in the future neutrino roadmap to unravel the fundamental properties of neutrino [125, 126, 222, 223, 224, 225, 226, 227, 228, 229]. To accomplish its broad and rich physics objectives as a world-class facility, it is needed to develop three major components: a) an intense ($\sim$ megawatt), wide-band neutrino beam at Fermilab,

b) a fine-grained, high-precision near neutrino detector just downstream of the neutrino source, and c) a massive ($\sim$ 40 kt) liquid argon time-projection chamber (LArTPC) far detector housed deep underground at the Sanford Underground Research Facility (SURF) in Lead, South Dakota. The LArTPC technology is quite effective for uniform and high accuracy imaging of massive active volumes [230]. One of the merits of a LArTPC is that it works like a totally active calorimeter where one can detect the energy deposited by all final-state particles, providing an excellent energy resolution over a wide range of energies inevitable to study the first and second oscillation maxima. We assume a fiducial mass of 35 kt for the far detector in our simulation, and consider the detector properties which are given in Table 1 of Ref. [141]. As far as the neutrino beam specifications are concerned, we consider a proton beam power of 708 kW in its initial phase with a proton energy of 120 GeV which can deliver 6×10^{20} protons on target in 200 days per calendar year. We have used the fluxes which were estimated assuming a decay pipe length of 200 m and 200 kA horn current [231]. In our simulation, we consider a total run time of ten years which is equivalent to a total exposure of 248 kt $\cdot$ MW $\cdot$ year, equally shared between neutrino and antineutrino mode. We take the reconstructed neutrino and anti-neutrino energy range to be 0.5 GeV to 10 GeV. To incorporate the systematic uncertainties, we consider an uncorrelated 5% normalization error and no calibration error on signal, 5% normalization error and no calibration error on background for both the appearance and disappearance channels to analyze the prospective data from the DUNE experiment. We consider the same set of systematics for both the neutrino and antineutrino channels which are also uncorrelated. For both ν_e and $\bar{\nu}_e$ appearance channels, the backgrounds mainly arise from three different sources: *a*) the intrinsic $\nu_e/\bar{\nu}_e$ contamination of the beam, *b*) the number of muon events which will be misidentified as electron events, and c) the neutral current events. Our assumptions on various components of the DUNE set-up are slightly different compared to what have been considered for the Conceptual Design Report (CDR) in Ref. [125][1]. It has been shown in Ref. [125] that considering the CDR reference beam design and with an exposure of 1320 kt $\cdot$ MW $\cdot$ year, CPV can be determined for 75% of $\delta_{\rm CP}$ values at 3σ confidence level. We have checked that similar coverage in $\delta_{\rm CP}$ values for establishing CPV can be achieved with our assumptions on the DUNE setup if we consider

---

[1] But, needless to mention, these assumptions on the beam fluxes, various detector characteristics, and systematic uncertainties are preliminary, and are expected to evolve with time as our understanding about the key components of the DUNE experiment is going to be refined/improved with the help of ongoing R&D efforts.

the same amount of exposure and the same oscillation parameters. Lastly it is worthy to say that we take the neutrino interaction cross-sections from Refs. [232, 233], where the authors gave the cross-section for water and isoscalar targets. So, to obtain cross-sections for LAr, we have scaled the inclusive charged current cross-sections of water by a factor of 1.06 for neutrino, and 0.94 for anti-neutrino [234, 235].

5.1.2 LBNO:

In Europe, the proposed LBNO experiment [127, 128, 141, 236] offers an interesting possibility to address the fundamental unsolved issues in neutrino oscillation physics using a baseline of 2290 km between CERN and Pyhäsalmi mine in Finland which enables us to cover a wide range of L/E choices, mandatory to resolve parameter degeneracies. The Pyhäsalmi mine will house a giant 70 kt LArTPC as a far detector which will observe the neutrinos produced in a conventional wide-band beam facility at CERN. The fluxes that we use in our simulation have been computed assuming an exposure of 1.5×10^{20} protons on target in 200 days per calendar year (with 80% efficiency of the accelerator) from the SPS accelerator at 400 GeV with a beam power of 750 kW [237]. For LBNO also, we assume five years of neutrino run and five years of anti-neutrino run. We consider the same detector properties as that of DUNE following the reference [141].

5.1.3 T2K:

In this section, we briefly mention the key experimental features of the currently running T2K [121, 122] experiment that go into carrying out the simulation. The T2K experiment in Japan is collecting the data since 2010. Neutrinos are being produced at the J-PARC accelerator facility in Tokai, and are being observed in the 22.5 kton (fiducial) Super-Kamiokande water Čerenkov detector at Kamioka, at a distance of 295 km from the source at an off-axis angle of 2.5° [122]. Due to the off-axis nature of the beam [238], it peaks sharply at the first oscillation maximum of 0.6 GeV. Another major benefit of using the off-axis technique is that it helps to reduce the intrinsic ν_e contamination in the beam and also the background coming from neutral current events, improving the signal-to-background ratio by great extent. As a result, the T2K experiment has already been able to provide an important breakthrough to establish the three-flavor paradigm by observing the θ_{13}-driven appearance signal in $\nu_\mu \to \nu_e$ oscillation channel [239]. In May 2014, T2K started its operation in the antineutrino mode, and after collecting 10% of their expected antineutrino data set, they announced the first appearance results in the antineutrino channel [240, 241], clearly taking a first step towards probing the CP asymmetry in a direct fashion. A very recent preliminary analysis of T2K data prefers the strong possibility of maximal CP-violation in the lepton sector. In our study, we consider the full projected exposure of 7.8×10^{21} protons on target (P.O.T.) generated by a proton beam of power 750 kW and proton energy of 30 GeV. We also assume that the T2K experiment would use half of its full exposure in the neutrino mode which is 3.9×10^{21} P.O.T. and the remaining half would be used during antineutrino run. We follow the recent publication by the T2K collaboration [242] in great detail to simulate the signal and background event spectra and their total rates to obtain our final results. Following the same reference [242], we assume an uncorrelated 5% normalization error on signal and 10% normalization error on background for both the appearance and disappearance channels to analyze the prospective data from the T2K experiment. We use the same set of systematics for both the neutrino and antineutrino channels which are also uncorrelated.

5.1.4 NOνA:

The US-based long-baseline experiment NOνA is also a long-baseline off-axis experiment already taking data. It uses a 14 kton liquid scintillator far detector at Ash River, Minnesota to detect the oscillated NuMI[2] muon neutrino beam produced at Fermilab [124, 243, 244, 245]. The NOνA far detector is placed 810 km away from the source at an off-axis angle of 14 mrad (0.8°) with respect to the beam line, and sees a narrow-band beam which peaks around 2 GeV. Based on the exposure of 2.74×10^{20} p.o.t., recently, the NOνA experiment has released their first ν_e appearance data providing a solid evidence of $\nu_\mu \to \nu_e$ oscillation over a baseline of 810 km which is the longest baseline in operation now [123, 246, 247, 248]. In this work, we take the full projected exposure of 3.6×10^{21} p.o.t. which the NOνA experiment aims to use during their full running time with a NuMI beam power of 700 kW and 120 GeV proton energy [124]. In our simulation, we assume that NOνA would also use 50% of its full exposure in the neutrino mode which is 1.8×10^{21} p.o.t. and the remaining 50% would be utilized to collect the data in

---

[2] Neutrinos at the Main Injector.

the anti-neutrino mode. Following references [58, 244, 249], we estimate the signal and background event spectra and their total rates in our calculations. We use a simplified systematic treatment for NOνA: an uncorrelated 5% normalization uncertainty on signal and 10% normalization uncertainty on background for both the appearance and disappearance channels. This is true for both the neutrino and antineutrino modes which are also assumed to be uncorrelated.

5.2 Definition of χ^2 function

In this section, we give a brief description of the statistical method used to analyse the mock data. For the purpose of analysing the data, we use the following Poissonian χ^2 function based on the techniques discussed in Refs. [250, 251],

$$\chi^2\,(\omega^{\text{true}},\lambda^{\text{true}}\,;\,\omega^{\text{test}},\lambda^{\text{test}},\xi_s,\xi_b) = \min_{\{\xi_s,\xi_b\}}\left[2\sum_{i=1}^{n}(\tilde{y}_i - x_i - x_i \ln\frac{\tilde{y}_i}{x_i}) + \frac{\xi_s^2}{\sigma_{\xi_s}^2} + \frac{\xi_b^2}{\sigma_{\xi_b}^2}\right]\,, \quad (5.1)$$

where n is the total number of reconstructed energy bins of neutrino/antineutrino and

$$\tilde{y}_i(\{\omega^{\text{test}},\lambda^{\text{test}}\},\{\xi_s,\xi_b\}) = N_i^{pr}(\{\omega^{\text{test}},\lambda^{\text{test}}\})[1+\pi^s\xi_s] + N_i^b(\{\omega^{\text{test}},\lambda^{\text{test}}\})[1+\pi^b\xi_b]\,. \quad (5.2)$$

$N_i^{pr}(\{\omega^{\text{test}},\lambda^{\text{test}}\})$ is the predicted number of signal events in the i-th energy bin for a test set of oscillation parameters $\omega^{\text{test}}\,(\theta_{12},\theta_{13},\theta_{23},\delta_{\text{CP}},\Delta m^2_{21},\Delta m^2_{31})$ and a test set of new physics parameters λ^{test} (= 0, for SM). $N_i^b(\{\omega^{\text{test}},\lambda^{\text{test}}\})$ is the number of background events in the i-th bin where the charged current backgrounds are dependent on ω^{test} and λ^{test}, and the neutral current backgrounds do not depend on the parameters ω^{test} and λ^{test}. The quantities π^s and π^b in Eq. (5.2) are the systematic errors on the signal and background respectively. It is worth to note that π^s and π^b takes different values for different experimental setups. The systematic errors π^s and π^b are implemented with the nuisance parameters ξ_s and ξ_b which are known with some accuracy σ_{ξ_s} and σ_{ξ_b}. The terms $\xi_s^2/\sigma_{\xi_s}^2$ and $\xi_b^2/\sigma_{\xi_b}^2$ are called “pulls” due to the systematic error on signal and background respectively. We incorporate the data in Eq. (5.1) through the variable $x_i = N_i^{obs} + N_i^b$, where $N_i^{obs}(\omega^{\text{true}},\lambda^{\text{true}})$ is the number of observed charged current signal events in the i-th energy bin and $N_i^b(\omega^{\text{true}},\lambda^{\text{true}})$ is the background as mentioned earlier. Here ω^{true} and λ^{true}

are the true set of oscillation parameters and new physics parameters respectively. To estimate the total χ^2, we add the χ^2 contributions coming from all the relevant channels in a given experiment and this is given as,

$$\chi^2_{\text{total}} = \sum_{channel} \chi^2\,(\omega^{\text{true}}, \lambda^{\text{true}}; \omega^{\text{test}}, \lambda^{\text{test}}, \xi_s, \xi_b), \tag{5.3}$$

which, for the purpose of our work can be explicitly written as,

$$\chi^2_{\text{total}} = \chi^2_{\nu_\mu \to \nu_e} + \chi^2_{\nu_\mu \to \nu_\mu} + \chi^2_{\bar{\nu}_\mu \to \bar{\nu}_e} + \chi^2_{\bar{\nu}_\mu \to \bar{\nu}_\mu}\,. \tag{5.4}$$

Here, we assume that all these channels are completely uncorrelated, all the energy bins in a given channel are fully correlated, and the systematic errors on signal and background are fully uncorrelated. Finally, χ^2_{total} is marginalized in the fit over the free oscillation parameters to obtain $\Delta\chi^2_{\text{min}}$, that is

$$\Delta\chi^2_{\text{min}} = \min_{\{\omega,\lambda\}} \left[\sum_{channel} \chi^2\,(\omega, \lambda, \xi_s, \xi_b) \right]. \tag{5.5}$$

ω and λ may be anything "true" or "test". We should keep in mind that in this work we have not used any "pulls" (or commonly known as "prior") on any one of the standard oscillation parameters including matter density. It is also to be noted that we have not used any prior on any new physics parameter assuming that the LBL experiments will be able to determine them precisely or they will give stringent constraint on that parameters. For completeness we give the mathematical expression of prior below:

$$\chi^2_{\text{prior}} = \left(\frac{\omega^{\text{test}} - \omega^{\text{true}}}{\sigma(\omega^{\text{true}})} \right)^2 + \left(\frac{\rho^{\text{test}} - \rho^{\text{true}}}{\sigma(\rho^{\text{true}})} \right)^2 + \text{if any (on } \lambda). \tag{5.6}$$

Where, $\sigma(\omega^{\text{true}})$ is the 1σ uncertainty on the best-fit value of the oscillation parameter ω^{true}. In case of matter density, ρ^{true} is set to 1, i.e., 5% uncertainty corresponds to $\sigma(\rho^{\text{true}}) = 0.05$.

5.3 Calculation of P.O.T. in LBL experiments

Let us now calculate the protons on target (P.O.T.) in long-baseline experiments. All the LBL experiments used in this thesis are superbeam experiments. Basically, superbeam is the intense neutrino beam produced by the accelerated high energy protons. These high energy protons first hit a target and produce $\pi^{\pm}$. These pions after decaying produce muon-neutrinos (ν_μ) or muon-antineutrinos ($\bar{\nu}_\mu$). These muon-neutrinos (antineutrinos) oscillate while traveling from source to detector. So we see that the more is the P.O.T. bigger is the production of ν_μ or $\bar{\nu}_\mu$.

Now the number of P.O.T. (say, x) depends on the average proton energy 'E_p' (GeV) and the average proton beam power 'W' (MW) per operational year.

Let, one operational year = 't' second. So, the number of protons deposited on the target in 'y' year is given as

$$\begin{aligned} x &= \frac{W \times 10^6 \times y \times t}{E_p \times 10^9 \times 1.6 \times 10^{-19}} \\ &= \frac{W \times y \times t \times 10^{16}}{1.6 \times E_p}. \end{aligned} \tag{5.7}$$

Let us now take few examples which are related to the numerical simulations used in this thesis.

5.3.1 DUNE:

Beam power, W = 708 kW,
Proton energy, E_p = 120 GeV,
Number of operational days in 1 yr. = 200,
So, $t \simeq 1.7 \times 10^7$ seconds,
So the number of P.O.T. in 1 year is

$$\begin{aligned} x &= \frac{W \times y \times t \times 10^{16}}{1.6 \times E_p} \\ &\simeq \frac{0.7 \times 1 \times 1.7 \times 10^7 \times 10^{16}}{1.6 \times 120} \\ &\simeq 6 \times 10^{20}. \end{aligned} \tag{5.8}$$

For 10 years, total P.O.T. is $x \simeq 6 \times 10^{21}$.

5.3.2 LBNO:

Beam power, $W = 750$ kW,

Proton energy, $E_p = 400$ GeV,

Number of operational days in 1 yr. = 200,

With 80% efficiency, $t \simeq 1.3 \times 10^7$ seconds,

So the number of P.O.T. in 1 year is

$$\begin{aligned} x &= \frac{W \times y \times t \times 10^{16}}{1.6 \times E_p} \\ &\simeq \frac{0.75 \times 1 \times 1.3 \times 10^7 \times 10^{16}}{1.6 \times 400} \\ &\simeq 1.5 \times 10^{20}. \end{aligned} \tag{5.9}$$

For 10 years, total P.O.T. is $x \simeq 1.5 \times 10^{21}$.

5.3.3 T2K:

Beam power, $W = 750$ kW,

Proton energy, $E_p = 30$ GeV,

For T2K, operational time in 1 year is, $t \simeq 10^7$ seconds,

So the number of P.O.T. in 1 year is

$$\begin{aligned} x &= \frac{W \times y \times t \times 10^{16}}{1.6 \times E_p} \\ &\simeq \frac{0.75 \times 1 \times 10^7 \times 10^{16}}{1.6 \times 30} \\ &\simeq 1.56 \times 10^{21}. \end{aligned} \tag{5.10}$$

For 5 years, total P.O.T. is $x \simeq 7.8 \times 10^{21}$.

5.3.4 NOνA:

Beam power, $W = 700$ kW,

Proton energy, $E_p = 120$ GeV,

For NOνA, operational time in 1 year is, $t \simeq 1.7 \times 10^7$ seconds,

So the number of P.O.T. in 1 year is

$$\begin{aligned} x &= \frac{W \times y \times t \times 10^{16}}{1.6 \times E_p} \\ &\simeq \frac{0.7 \times 1 \times 1.7 \times 10^7 \times 10^{16}}{1.6 \times 120} \\ &\simeq 6 \times 10^{20}. \end{aligned} \tag{5.11}$$

For 6 years, total P.O.T. is $x \simeq 3.6 \times 10^{21}$.

Chapter 6

Discovery Potential of T2K and NOνA in the presence of a Light Sterile Neutrino

In this chapter we study the impact of one light sterile neutrino on the prospective data expected to come from the two presently running long-baseline experiments T2K [121, 122] and NOνA [124, 243, 244, 252] after they accumulate their full planned exposure. Introducing for the first time, the bi-probability representation in the 4-flavor framework, commonly used in the 3-flavor scenario, we present a detailed discussion of the behavior of the $\nu_\mu \to \nu_e$ and $\bar{\nu}_\mu \to \bar{\nu}_e$ transition probabilities in the 3+1 scheme. We also perform a detailed sensitivity study of these two experiments (both in the stand-alone and combined modes) to assess their discovery reach in the presence of a light sterile neutrino. We find that the performance of both these experiments in claiming the discovery of the CP-violation induced by the standard CP-phase $\delta_{13} \equiv \delta_{\mathrm{CP}}$, and the neutrino mass hierarchy get substantially deteriorated. Finally, we estimate the discovery potential of total CP-violation (i.e., induced simultaneously by the two CP-phases δ_{13} and δ_{14}), and the capability of the two experiments of reconstructing the true values of such CP-phases. The details of all the analyses and the respective results have been discussed in the next few sections.

This chapter is organized as follows. In section 6.1, we present a detailed discussion of the behavior of the 4-flavor $\nu_\mu \to \nu_e$ and $\bar{\nu}_\mu \to \bar{\nu}_e$ transition probabilities. For the first time we extend the bi-probability representation, commonly used in the 3-flavor framework, to the more general 3+1 scheme. Section 6.2 deals with the experimental details and also discusses the bi-events plots. In section 6.3, we describe the details of the statistical method that we use for the analysis. Section 6.4 is devoted to the presentation of the results of the sensitivity study of T2K and NOνA. Finally in section 6.5 we summarize our results.

6.1 Conversion probability in the 3+1 scheme

6.1.1 Theoretical framework

As discussed in section 2.6, the presence of a sterile neutrino ν_s, the mixing among the flavor and the mass eigenstates is described by a 4×4 matrix. A convenient parameterization of the mixing matrix is

$$U = \tilde{R}_{34} R_{24} \tilde{R}_{14} R_{23} \tilde{R}_{13} R_{12} \,, \tag{6.1}$$

where R_{ij} ($\tilde{R}_{ij}$) are real (complex) 4×4 rotations in the (i, j) plane containing the 2×2 submatrix

$$R^{2\times2}_{ij} = \begin{pmatrix} c_{ij} & s_{ij} \\ -s_{ij} & c_{ij} \end{pmatrix} \quad \tilde{R}^{2\times2}_{ij} = \begin{pmatrix} c_{ij} & \tilde{s}_{ij} \\ -\tilde{s}^{*}_{ij} & c_{ij} \end{pmatrix} , \tag{6.2}$$

in the (i, j) sub-block, with

$$c_{ij} \equiv \cos\theta_{ij} \qquad s_{ij} \equiv \sin\theta_{ij} \qquad \tilde{s}_{ij} \equiv s_{ij} e^{-i\delta_{ij}} . \tag{6.3}$$

6.1.2 Analytical Expressions in Vacuum and Matter

Let us now consider the transition probability relevant for T2K and NOνA. From the discussion of section 2.6.1, we know that the $\nu_\mu \to \nu_e$ conversion probability in presence of a sterile neutrino can be approximately written as the sum of three contributions

$$P^{4\nu}_{\mu e} \simeq P^{\rm ATM} + P^{\rm INT}_{\rm I} + P^{\rm INT}_{\rm II} . \tag{6.4}$$

The first (positive-definite) term is driven by the atmospheric frequency and it gives the leading contribution to the probability. The second and third terms are related to the interference of two distinct frequencies and can assume both positive and negative values. The first of the two interference terms is connected to the standard solar-atmospheric interference, while the second one is driven by the atmospheric-sterile interference. The conversion probability depends on the three small mixing angles θ_{13}, θ_{14}, θ_{24}, whose best estimates, derived from the global 3-flavor (for θ_{13}) analyses [22, 253, 254] and from the 3+1 fits [105, 106] (for θ_{14} and θ_{24}), turn out to be very similar and we have approximately $s_{13} \sim s_{14} \sim s_{24} \sim 0.15$ (see table 4.3). Therefore, it is meaningful to treat all such three mixing angles as small quantities of the same order ε. Another small quantity involved in the transition probability is the ratio of the solar and the atmospheric mass-squared splitting $\alpha \equiv \Delta m^2_{21}/\Delta m^2_{31} \simeq \pm 0.03$, which can be assumed to be of order ε^2. Keeping terms up to the third order, in vacuum, one finds

$$P^{\mathrm{ATM}} \simeq 4 s^2_{23} s^2_{13} \sin^2\Delta\,, \tag{6.5}$$

$$P^{\mathrm{INT}}_{\mathrm{I}} \simeq 8 s_{13} s_{12} c_{12} s_{23} c_{23} (\alpha\Delta) \sin\Delta \cos(\Delta + \delta_{13})\,, \tag{6.6}$$

$$P^{\mathrm{INT}}_{\mathrm{II}} \simeq 4 s_{14} s_{24} s_{13} s_{23} \sin\Delta \sin(\Delta + \delta_{13} - \delta_{14})\,, \tag{6.7}$$

where $\Delta \equiv \Delta m^2_{31} L/4E$ is the atmospheric oscillating factor, which depends on the baseline L and the neutrino energy E. The two LBL experiments under consideration, T2K and NOνA, make use of an off-axis configuration, which leads to a narrow-band sharply-peaked energy spectrum of the emitted neutrinos. In theory, the off-axis angle should be tuned exactly to match (at the peak energy) the condition $\Delta \sim \pi/2$, corresponding to the first oscillation maximum. In practice this condition holds only approximately. In T2K, the neutrino flux is peaked at $E = 0.6$ GeV and the condition $\Delta = \pi/2$ is exactly matched. In NOνA, the peak of flux is located at $E = 2$ GeV, while the oscillations maximum is at $E = 1.5$ GeV. In the following, when discussing the behavior of the conversion probability we will choose the peak value for both experiments, i.e. we will use $E = 0.6$ GeV for T2K and $E = 2$ GeV for NOνA. This will allow a better understanding of the subsequent discussion at the events level presented in section 6.2. In fact, in both experiments the total rate keeps the leading contribution from the energies close to the peak. Also, it should be stressed that the sensitivity to the spectral distortions is quite limited (due to systematic errors and the limited statistics) and the total rate suffices to understand the basic feature of the numerical results, albeit our analysis includes a full treatment of the spectrum (see section 6.2).

The presence of matter slightly modifies the transition probability through the MSW effect, which introduces a dependency on the ratio

$$v = \frac{V_{CC}}{k} \equiv \frac{2V_{CC}E}{\Delta m^2_{31}}\,, \tag{6.8}$$

where,

$$V_{CC} = \sqrt{2}G_F N_e \tag{6.9}$$

is the constant matter potential along the neutrino trajectory in the earth crust. Both in T2K and in NOνA the value of v is relatively small, being $v \sim 0.05$ in T2K, and $v \sim 0.17$ in NOνA, where we have taken as a benchmark value the peak energy ($E = 0.6$ GeV in T2K, $E = 2$ GeV in NOνA). Therefore, v can be treated as a small parameter of order ε. The $\nu_\mu \to \nu_e$ conversion probability in matter can be obtained (see the appendix in [104] and the works [255, 256, 257]) by performing, in the leading term of the vacuum probability, the following substitution

$$P_m^{\rm ATM} \simeq (1+2v)P^{\rm ATM}\,, \tag{6.10}$$

which incorporates the (third order) corrections due to matter effects. It can be shown that the two interference terms acquire corrections which are of the fourth order. In this work, we will limit the expansion at the third order in ε. Therefore, the interference terms will have the vacuum expression. It is also important to mention here that in presence of matter probability expression becomes dependent of the mixing angle θ_{34} with the phase δ_{34} associated with it. However the corrections are of fourth order and beyond. So it does not come in the probability expressions [1]. Before closing this section we recall that a swap in the neutrino mass hierarchy is parametrized by the replacements

$$\Delta \to -\Delta, \qquad \alpha \to -\alpha, \qquad v \to -v. \tag{6.11}$$

Due to the change of sign of v in Eq. (6.10), the transition probability (which acquires

---

[1] In this point it is also worth to mention that in the numerical analysis we have considered full four flavor probability with matter effect. However due to small matter effect in T2K and NOνA, we have put $\theta_{34} = \delta_{34} = 0$, because of fourth order or beyond corrections which has negligible effect.

the dominant contribution from the atmospheric term) tend to increase (decrease) with respect to the vacuum case in the NH (IH) case. NOνA is expected to be more sensitive than T2K to the MH because of the larger value of the ratio v. Finally, we recall that the

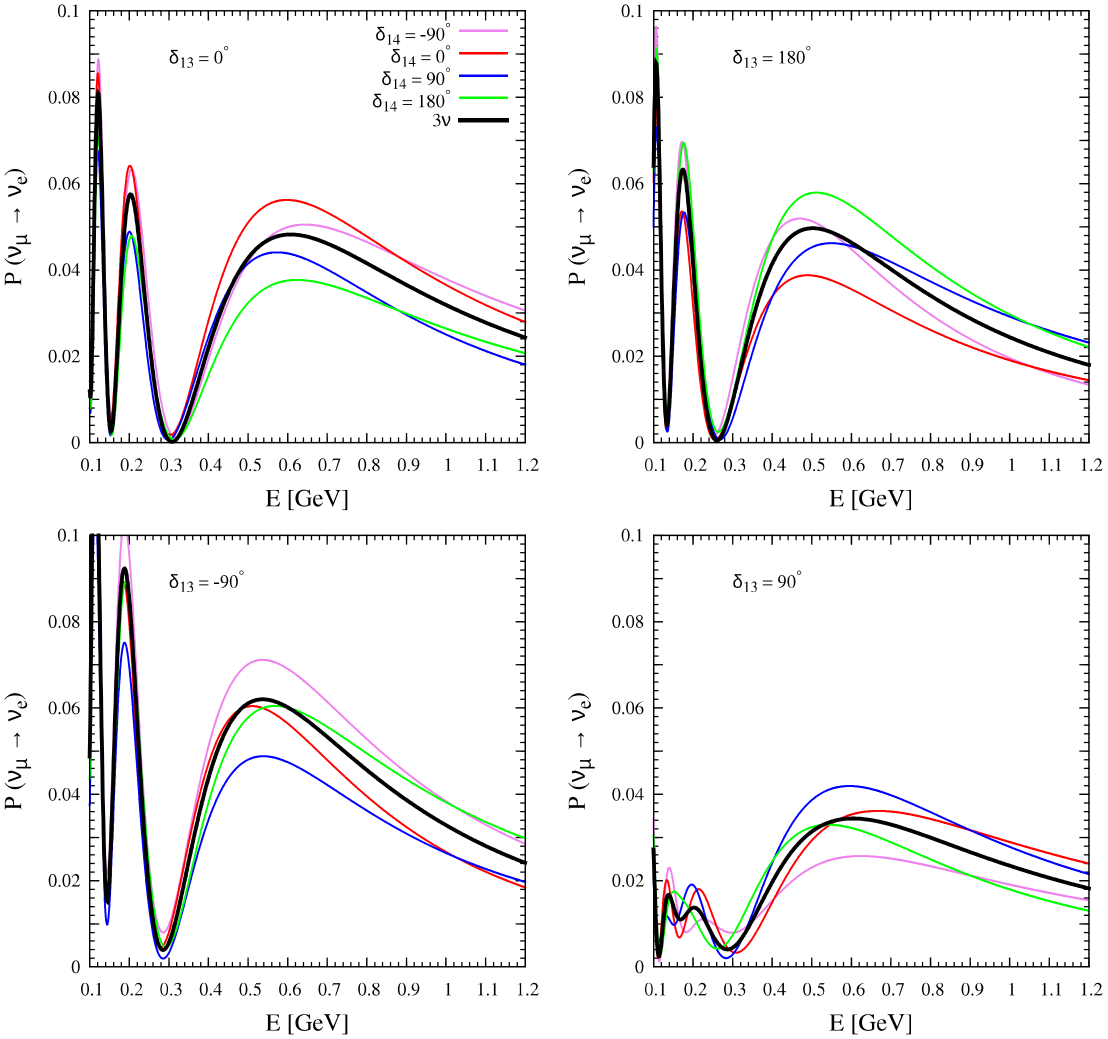

Figure 6.1: $\nu_\mu \rightarrow \nu_e$ transition probability as a function of neutrino energy for T2K after performing the averaging over the fast oscillations.

transition probability for antineutrinos is obtained from that of neutrinos with a change in the sign of the MSW potential V and of all the CP-phases. This, for a given choice of the MH, corresponds to the substitutions

$$\delta_{13} \rightarrow -\delta_{13}, \qquad \delta_{14} \rightarrow -\delta_{14}, \qquad v \rightarrow -v. \tag{6.12}$$

In the NH case $v > 0$ for neutrinos and $v < 0$ for antineutrinos. According to Eq. (6.10), in the NH case the leading contribution to the transition probability will increase (decrease) for neutrinos (antineutrinos). In the IH case the opposite conclusion holds. Figures 6.1

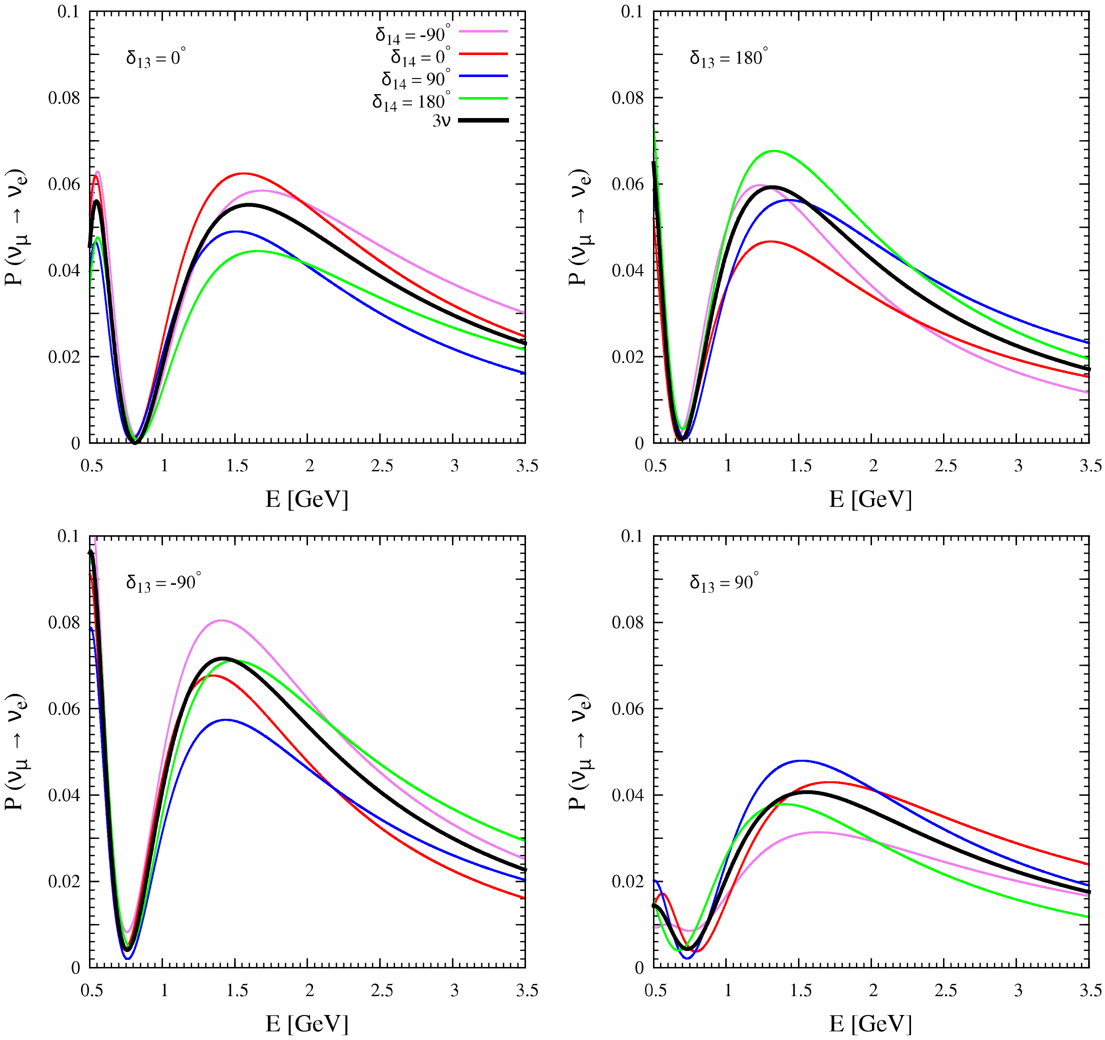

Figure 6.2: $\nu_\mu \to \nu_e$ transition probability as a function of neutrino energy for NOνA after performing the averaging over the fast oscillations.

and 6.2 show the transition probability for neutrinos as a function of the energy for both experiments T2K and NOνA. In both figures we have assumed normal hierarchy and we have taken the mass-squared difference $\Delta m^2_{41} = 1$ eV^2 and fixed the mixing angle θ_{13} and the two mixing angles θ_{14} and θ_{24} at the benchmark values indicated in the second column of Table 4.3, where we also report all the other mass-mixing parameters involved in the calculations. For such high values of the mass-squared splitting, the oscillating factor Δ_{14} is very large and the sterile-induced oscillations are completely averaged out by the finite energy resolution of the detector. Hence, we report the transition probability obtained after that such an averaging process has been taken into account. In each plot of Figs. 6.1 and 6.2, the value of the standard CP-phase δ_{13} is kept fixed at the value displayed in the legend, while the new phase δ_{14} assumes four representative values. In each panel, the 3-flavor probability is represented by a thick black line, while the four 3+1 cases are displayed by thin colored lines. The magenta curve corresponds to $\delta_{14} = -\pi/2$, the blue one to $\delta_{14} = \pi/2$, the red one to $\delta_{14} = 0$ and the green one to $\delta_{14} = \pi$. For clarity, we will adopt such color convention in all the figures presented in this chapter. From Figs. 6.1 and 6.2 it clearly emerges that the impact of the 4-flavor corrections induced by a non-zero value of the mixing angles θ_{14} and θ_{24} is sizable. Their amplitude and shape depend on the particular value of the new CP-phase δ_{14}. The plots show that the most evident effect of the 4-flavor corrections is a change in the overall normalization of the transition probability with respect to the standard 3-flavor case. In addition, an appreciably different energy dependence is also present, which reflects the different dependency from the L/E ratio of the standard interference term [Eq. (6.6)] and the non-standard one [Eq. (6.7)]. The changes induced in the overall normalization are as big as the modifications induced by varying δ_{13} (compare the excursion of the black curves between different panels with the excursion of the colored curve in a given panel). This confirms the analytical estimates made in the previous section.

6.1.3 Bi-Probability Plots

In the 3-flavor framework, the behavior of the transition probability is often represented with the CP-phase trajectory diagrams in bi-probability space, first introduced in [55]. Such plots, commonly dubbed as bi-probability plots, represent the parametric curves of the two transition probabilities ($\nu_\mu \to \nu_e$ and $\bar{\nu}_\mu \to \bar{\nu}_e$) where the varying parameter is the CP-phase δ_{13}. Since the two transition probabilities are cyclic functions of the phase δ_{13}, the resulting contours form a closed curve. This representation is particularly advantageous as it gives a bird-eye view of the salient features of a given experimental setups, in particular its sensitivity to MH and CPV. Here we attempt to generalize the bi-probability representation to the more general 4-flavor scheme. This makes sense because also in the 4-flavor scheme the probability remains a cyclic function of the (more numerous) CP-phases. Also in this case, as we will show, this representation is very useful for the interpretation of the numerical results. In the following we first recall the basic features of the bi-probability plots in the standard 3-flavor framework, then we generalize our study to the 4-flavor scheme.

The 3-flavor case

In the 3-flavor case the neutrino and antineutrino transition probabilities can be written as

$$\begin{aligned} P &= P_0 + A(\cos\Delta\cos\delta_{13} - \sin\Delta\sin\delta_{13}) && (6.13) \\ \bar{P} &= \bar{P}_0 + \bar{A}(\cos\Delta\cos\delta_{13} + \sin\Delta\sin\delta_{13})\,. && (6.14) \end{aligned}$$

In general, due to the presence of matter effects one has $P_0 \neq \bar{P}_0$ and $A \neq \bar{A}$. As discussed in the previous section the matter effects shift[2] P_0 by an amount proportional to the small parameter $v = 2VE/\Delta m^2_{31}$, which is of order $O(\varepsilon)$. Therefore, since P_0 in vacuum is $O(\varepsilon^2)$, the absolute shift of P_0 is $O(\varepsilon^3)$, which is thus comparable with the amplitude ($A \simeq \bar{A}$) of the interference term. The amplitude of the interference term is also modified with respect to the vacuum case, its relative change being proportional to v. Since the amplitude A is of order $O(\varepsilon^3)$, the corrections are of order $O(\varepsilon^4)$. Therefore, truncating the expansion of the probability at the third order corresponds to consider $A = \bar{A}$, with

$$A \simeq 8 s_{13} s_{12} c_{12} s_{23} c_{23} (\alpha\Delta) \sin\Delta\,. \tag{6.15}$$

The relations (6.13)-(6.14) represent the parametric equations of an ellipse of center $(P_0, \bar{P}_0)$. Under the assumption $A = \bar{A}$, as already shown in [55], the major (minor) axis of the ellipse is proportional to $\sin\Delta$ ($\cos\Delta$) and has an inclination of $-\pi/4$ ($\pi/4$). To see this one can perform a counter-clockwise rotation R of the parametric curve around its center $(P_0, \bar{P}_0)$ by the angle $\omega = \pi/4$

$$R = \begin{bmatrix} \cos\omega & -\sin\omega \\ \sin\omega & \cos\omega \end{bmatrix} = \frac{1}{\sqrt{2}} \begin{bmatrix} 1 & -1 \\ 1 & 1 \end{bmatrix}, \tag{6.16}$$

obtaining for the rotated probabilities

$$\begin{aligned} P' &= P_0 - \sqrt{2}A\sin\Delta\sin\delta_{13} && (6.17) \\ \bar{P}' &= \bar{P}_0 + \sqrt{2}A\cos\Delta\cos\delta_{13}\,. && (6.18) \end{aligned}$$

---

[2] P_0 and $\bar{P}_0$ can be identified with $P^{\rm ATM}_m$ of Eq. (6.10), where the sign of the adimensional quantity v related to the matter effects (for a fixed choice of the mass hierarchy) is opposite for neutrinos and antineutrinos.

From these relations one arrives at the equation of an ellipse in the canonical form

$$\frac{(P'-P_0)^2}{a^2}+\frac{(\bar{P}'-P_0)^2}{b^2}=1\,, \tag{6.19}$$

with the two semi-axes having lengths

$$a = \sqrt{2}A\sin\Delta\,, \tag{6.20}$$

$$b = \sqrt{2}A\cos\Delta\,. \tag{6.21}$$

The combination of signs in the parametric equations (6.17)-(6.18) implies that for the NH case the “chirality” of the ellipse is positive, i.e. the trajectory winds in the counter-clockwise sense as the phase δ_{13} increases. The chirality is opposite (negative) in the IH case since the coefficient A changes its sign under a swap of the mass hierarchy [see Eq. (6.15)].

The energy spectrum of the neutrino beams employed in typical LBL experiments is peaked around the first oscillation maximum, where $\Delta \sim \pi/2$ and therefore one expects $a \gg b$, i.e. the major axis much bigger than the minor one. This feature is particularly pronounced in T2K since, as already remarked in the previous section, the peak energy ($E = 0.6\,\mathrm{GeV}$) almost exactly matches the condition $\Delta = \pi/2$. In this case the ellipse becomes almost degenerate with a line. This behavior can be observed in Fig. 6.3, where in all four panels the two black curves correspond to the 3-flavor limit for the two cases of NH (solid line) and IH (dashed line). The colored curves correspond to four representative 4-flavor cases that will be discussed later. In the NOνA experiment, at the peak energy ($E = 2\,\mathrm{GeV}$) we have $\Delta = 0.4\pi$ and the ratio of the major over the minor axis is given by $a/b = \tan\Delta \sim 3$, as one can appreciate from the plots in Fig. 6.4, where again like for T2K, we display the two cases of NH (black solid line) and IH (black dashed line).

The bi-probability representation is particularly useful because it neatly shows that the presence of matter effects tend to split the two ellipses corresponding to the two mass hierarchies, thus giving a qualitative bird-eye view of the sensitivity of a given experiment to the MH. In addition, the ellipse curves show pictorially the effect of the genuine (or intrinsic) CPV due to $\sin\delta_{13}$, disentangling it from the fake (or extrinsic) CPV induced by the matter effects. In particular, for $\delta_{13} = (-\pi/2, \pi/2)$ the representative point in the bi-probability space (respectively a circle and a square) lies on the intercepts of the ellipse with the major axis and one has the maximal (intrinsic) CPV. Conversely, the effect from the CP conserving $\cos\delta_{13}$ term is proportional to the length of the minor axis. For $\delta_{13} = (0, \pi)$ the representative point on the ellipse (respectively a triangle and an asterisk) basically coincide.

From the comparison of Fig. 6.3 and Fig. 6.4, it emerges that the splitting between the NH and IH curves is less pronounced in T2K than in NOνA. This is a consequence of the fact that, as already discussed in the previous section, the matter effects are larger in the second experiment. It is useful to recall [see Eq. (6.10)] that the matter effects induce modifications proportional to the dimensionless quantity $v = 2VE/\Delta m^2_{31}$, which is $v \simeq 0.05$ at the T2K peak energy and $v \simeq 0.17$ at the NOνA peak energy.

The 4-flavor case

In the 3+1 scheme the transition probabilities have the general form

$$P = P_0 + A\cos(\Delta + \delta_{13}) + B\sin(\Delta - \delta_{14} + \delta_{13}) , \tag{6.22}$$

$$\bar{P} = \bar{P}_0 + \bar{A}\cos(\Delta - \delta_{13}) + \bar{B}\sin(\Delta + \delta_{14} - \delta_{13}) , \tag{6.23}$$

where, neglecting $O(\varepsilon^4)$ corrections, we have

$$A \simeq \bar{A} \simeq S_A \frac{\alpha}{|\alpha|} \Delta \sin\Delta , \tag{6.24}$$

$$B \simeq \bar{B} \simeq S_B \sin\Delta . \tag{6.25}$$

We have introduced the two (positive definite) auxiliary quantities

$$S_A = 8 s_{13} s_{12} c_{12} s_{23} c_{23} |\alpha| , \tag{6.26}$$

$$S_B = 4 s_{14} s_{24} s_{13} s_{23} , \tag{6.27}$$

which, for the specific values of the mixing angles under consideration (see the second Table of 4.3) yield

$$S_A \simeq 0.8 \times 10^{-2} , \tag{6.28}$$

$$S_B \simeq 10^{-2} . \tag{6.29}$$

In the expression of the coefficients A and B in Eqs. (6.24)-(6.25) we have left evident the dependency from the oscillation factor Δ and from the sign of the ratio α. This will be useful when discussing the role of the neutrino mass hierarchy. We note that, under a swap of the MH (implying $\Delta \to -\Delta$ and $\alpha \to -\alpha$), both coefficients A and B change sign and therefore their product AB remains unaltered and positive definite. The equations (6.22)-(6.23) can be re-expressed in the form

$$P = P_0 + C\cos\delta_{13} + D\sin\delta_{13} \tag{6.30}$$

$$\bar{P} = \bar{P}_0 + \bar{C}\cos\delta_{13} + \bar{D}\sin\delta_{13}\,, \tag{6.31}$$

where the new coefficients $C, D, \bar{C}, \bar{D}$ depend on Δ and on the CP-phase δ_{14} as follows

$$C = +A\cos\Delta + B\sin(\Delta - \delta_{14})\,, \tag{6.32}$$

$$D = -A\sin\Delta + B\cos(\Delta - \delta_{14})\,, \tag{6.33}$$

$$\bar{C} = +\bar{A}\cos\Delta + \bar{B}\sin(\Delta + \delta_{14})\,, \tag{6.34}$$

$$\bar{D} = +\bar{A}\sin\Delta - \bar{B}\cos(\Delta + \delta_{14})\,. \tag{6.35}$$

By eliminating the CP-phase δ_{13} from the expressions (6.30)-(6.31), one easily arrives at the equation of an ellipse.[3] However, the situation is more involved with respect to the 3-flavor case, because the geometrical properties of the 4-flavor ellipse (length and inclination of the two axes) depend not only on Δ but also on the new CP-phase δ_{14}.

Figures 6.3 and 6.4 represent the 4-flavor ellipses obtained respectively for T2K (at the energy $E = 0.6\,\mathrm{GeV}$) and NOνA (at the energy $E = 2.0\,\mathrm{GeV}$) for four fixed values of the phase δ_{14}. In each panel the solid (dashed) curve represents the NH (IH) case. From the figures it is evident that the properties of the ellipses depend on: i) the particular experiment (due to the different value of the oscillation factor Δ); ii) the value of the phase δ_{14}; iii) the neutrino mass hierarchy (only in NOνA).

We can understand the basic behavior of a 4-flavor ellipse using the following relation for its inclination,[4] valid under the assumption that the perturbations induced by the matter

---

[3] If one makes explicit the dependency on δ_{14} (instead of δ_{13}) and treats δ_{14} as the varying parameter one still obtains a (different) ellipse. In this case, the center of the ellipse depends on the value of δ_{13}.

[4] For the derivation one has to write the equation of the ellipse by eliminating the parameter δ_{13} and than use the general formulae available in textbooks.

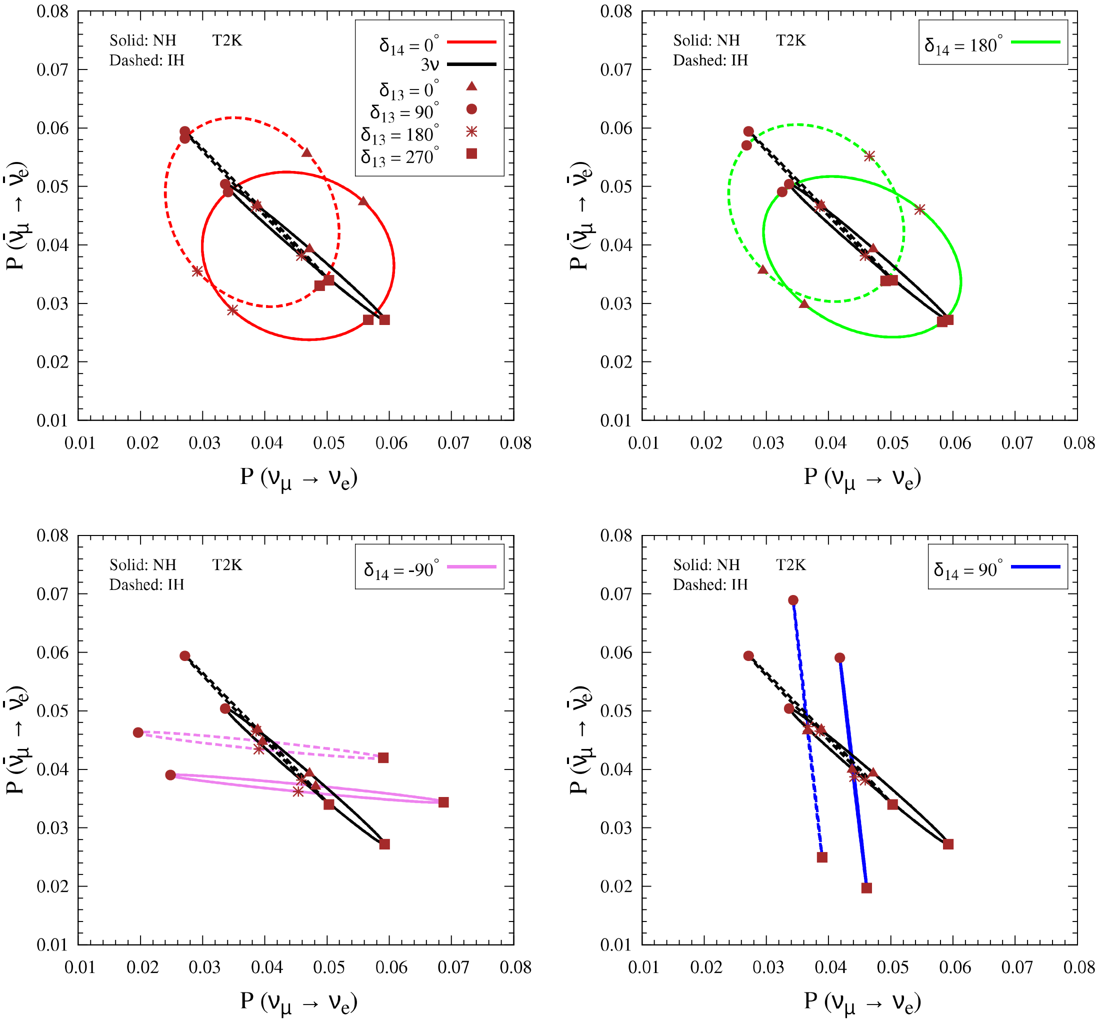

Figure 6.3: Bi-probability plots for T2K for four fixed values of δ_{14} and neutrino energy 0.6 GeV. In each panel, we also show the 3-flavor ellipses for the sake of comparison. In both the 3-flavor and 4-flavor ellipses, the running parameter is the CP-phase δ_{13} varying in the range $[-\pi, \pi]$. The solid (dashed) curves refer to NH (IH).

effects on the interference terms are negligible (i.e. $A = \bar{A}$ and $B = \bar{B}$),

$$\tan 2\omega = \frac{(B^2 - A^2)\cos 2\Delta - 2AB \sin 2\Delta \cos \delta_{14}}{2AB \sin \delta_{14}}, \tag{6.36}$$

which, making use of the definitions of A and B in Eqs. (6.24)-(6.25), and in particular of the invariance of the (positive) sign of the product AB, becomes

$$\tan 2\omega = \frac{(S_B^2 - S_A^2 \Delta^2)\cos 2\Delta - 2S_A S_B |\Delta| \sin 2\Delta \cos \delta_{14}}{2S_A S_B |\Delta| \sin \delta_{14}}. \tag{6.37}$$

The angle $\omega \in]-\pi/4, \pi/4[$ represents the inclination (with respect to the axis of the

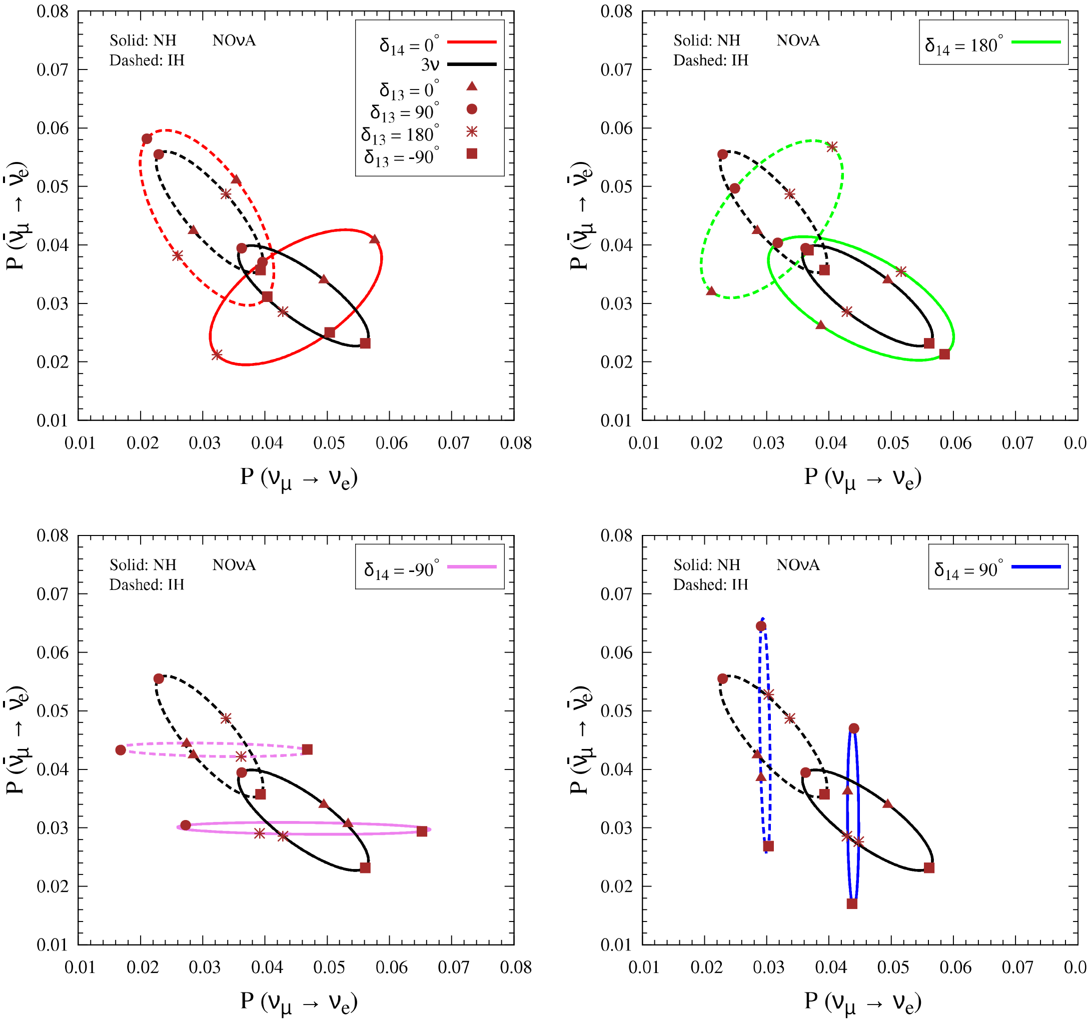

Figure 6.4: Bi-probability plots for NOνA for four fixed values of δ_{14} and neutrino energy of 2 GeV. In each panel, we also show the 3-flavor ellipses for the sake of comparison. In both the 3-flavor and 4-flavor ellipses, the running parameter is the CP-phase δ_{13} varying in the range $[-\pi, \pi]$. The solid (dashed) curves refer to NH (IH).

abscissas) of the major (minor) axis depending on the negative (positive) sign of the denominator in Eq. (6.37) (i.e. the sign of $\sin\delta_{14}$ since the product AB is positive definite). In the limit $\sin\delta_{14} \to 0$ the inclination of the major axis is $|\omega| = \pi/4$. In this case, the sign of ω can be determined by looking at the sign of the numerator in Eq. (6.37). If the numerator is positive, one has $\omega = -\pi/4$, if it is negative one has $\omega = \pi/4$.

In T2K we have $\Delta \simeq \pi/2$ and Eq. (6.37) takes the simpler form

$$\tan 2\omega = \frac{S_A^2 \Delta^2 - S_B^2}{2 S_A S_B |\Delta| \sin\delta_{14}} \simeq \frac{0.22}{\sin\delta_{14}}\,. \tag{6.38}$$

This result is independent of the mass hierarchy and therefore the inclination of the ellipses will be identical in the two cases of NH and IH. This is confirmed by Fig. 6.3. Indeed, in each panel the solid ellipse has almost the same orientation of the dashed one. The very small difference in the inclinations is due to the matter effects [O(ε^4)] that we are neglecting at the level of the interference terms. The matter effects are instead retained at the level of the leading terms P_0 and $\bar{P}_0$ where they induce O(ε^3) corrections. As a result the centers of the ellipses are shifted in opposite directions (with respect to the vacuum case) for the two cases of NH and IH. We also observe that the centers of the 4-flavor ellipses almost coincide with those of the 3-flavor ones since, as discussed in section 6.1 [see Eq. (6.10)], the matter effects enter in a similar way in the two schemes. The very small differences in the location of the centers of the 3-flavor and 4-flavor ellipses is imputable to corrections of order O(ε^4), which are neglected in our treatment. For the two values $\delta_{14} = (0, \pi)$, the inclination of the major axis is $\omega = -\pi/4$ since the numerator in Eq. (6.38) is positive in both cases. This is confirmed by the first (red curves) and second (green curves) panel of Fig. 6.3. For $\delta_{14} = \pm\pi/2$, one has $\tan 2\omega = \pm 0.22$, approximately corresponding to $\omega \simeq \pm 0.11$ (or $\pm 6^0$). In the case $\delta_{14} = -\pi/2$, the sign of the denominator in Eq. (6.38) is negative and the inclination of -6^0 is that of the major axis. In the case $\delta_{14} = \pi/2$, the sign of the denominator in Eq. (6.38) is positive and the inclination of $+6^0$ is that of the minor axis. This behavior is corroborated by the third panel (magenta curves) and fourth panel (blue curves) of Fig. 6.3. In NOνA we have $\Delta \simeq 0.4\pi$ and Eq. (6.37) takes the form

$$\tan 2\omega = k_1 \frac{1 \mp k_2 \cos\delta_{14}}{\sin\delta_{14}}\,. \tag{6.39}$$

where the two constants k_1, k_2 are given by

$$k_1 \simeq 3.85 \times 10^{-3}\,, \tag{6.40}$$

$$k_2 \simeq 1.53 \times 10^{2}\,. \tag{6.41}$$

The minus (plus) sign in Eq. (6.39) refers to the case of NH (IH). So at the NOνA peak energy, which corresponds to a value of Δ different from $\pi/2$, differently from T2K, we expect a dependency of the orientation of the ellipse from the mass hierarchy. For the two values $\delta_{14} = (0, \pi)$ the denominator goes to zero so the absolute inclination of the ellipses is $|\omega| = \pi/4$. The sign of ω is determined by the sign of the numerator, which in the normal hierarchy case is negative for $\delta_{14} = 0$ and positive for $\delta_{14} = \pi$. Therefore, in the NH case the inclination of the major axis is $\pi/4$ for $\delta_{14} = 0$ and $-\pi/4$ for $\delta_{14} = \pi$. In the IH case the situation is reversed, since the sign in the numerator in Eq. (6.39) is opposite. This behavior is basically confirmed by the first two panels of Fig. 6.4. Coming now to the two cases $\delta_{14} = \pm\pi/2$, one has $\tan 2\omega = k_1/\sin\delta_{14}$, which is a relation independent of the neutrino mass hierarchy. Due to the small value of the coefficient k_1, the value of ω is approximately zero. The inclination refers to the major (minor) axis for $\delta_{14} = -\pi/2$ ($\delta_{14} = \pi/2$). This behavior is confirmed by the numerical results displayed in the third and fourth panel in Fig. 6.4.

Hence, one can see that for both experiments the relatively simple formulae illustrated above allow us to explain analytically all the properties of the ellipses displayed in Figs. 6.3 and 6.4, which are obtained by a full numerical calculation. In the case of T2K the formula for the inclination of the ellipse is accurate at the level of less than one degree. In NOνA the accuracy, in some cases, is at the level of a few degrees, due to the larger impact of the fourth order corrections related to matter effects. For clarity, in Table 6.1 we report the approximated properties of the ellipses for the 3-flavor and the 4-flavor cases.

	δ_{14}(true)	MH	Chirality	Inclination (T2K)	Inclination (NOνA)
3ν		NH	+	-45^0	-45^0
		IH	-	-45^0	-45^0
4ν	0^0	NH	+	-45^0	$+45^0$
		IH	+	-45^0	-45^0
	180^0	NH	-	-45^0	-45^0
		IH	-	-45^0	$+45^0$
	-90^0	NH	+	-6^0	0^0
		IH	+	-6^0	0^0
	90^0	NH	-	-84^0	-90^0
		IH	-	-84^0	-90^0

Table 6.1: Geometrical properties of the ellipses for the 3-flavor and 4-flavor schemes. The first column reports the value of the CP-phase δ_{14} (not defined in the 3-flavor case). The second column reports the neutrino mass hierarchy. The third column reports the chirality of the ellipse (which is the same for T2K and NOνA). The plus (minus) sign means that the trajectory winds in the counter-clockwise (clockwise) sense as the phase δ_{13} increases. The fourth and fifth columns report the inclination of the major axis of the ellipse for T2K and NOνA, respectively. The values of the inclinations are those found with the third order expansion of the transition probabilities.

The bi-probability plots shown in Figs. 6.3 and 6.4 are obtained for fixed values of the

CP-phase δ_{14}. Since the value of δ_{14} is unknown, it is interesting to ask what happens if one superimposes all the (theoretically infinite) ellipses corresponding to all the possible choices of δ_{14}. The result of this exercise is shown in figure 6.5, which has been produced by drawing the convolution of all the ellipses[5] obtained with a dense grid for the parameter δ_{14} in its range of variability $[-\pi, \pi]$. Alternatively, Fig. 6.5 may be seen as a dense scatter plot obtained by varying simultaneously both CP-phases δ_{13} and δ_{14}. This plot provides a bird-eye view of the degree of separation of the two neutrino mass hierarchies in the 3+1 scheme. We see that a separation persists also in such an enlarged scheme. This means that there will exist some combinations of the two CP-phases δ_{13} and δ_{14} (corresponding to those points which do not lie in the superposition area of the blue and orange regions) for which it will be possible to distinguish between the two hierarchies at some non-zero confidence level. The numerical analysis of the section 6.4 will allow us to determine such specific combinations of the two CP-phases and the exact confidence level of the separation of the two hierarchies.

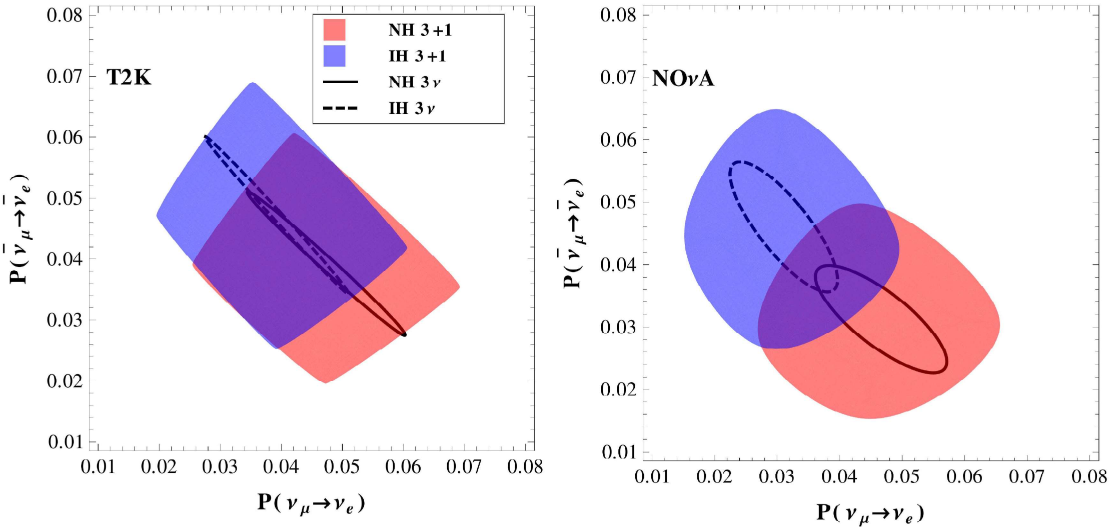

Figure 6.5: The colored shaded blobs represent the convolution of the bi-probability graphs for T2K (left panel) and NOνA (right panel) in the 3+1 scheme. The blobs are obtained by superimposing several ellipses, each corresponding to a different value of the CP-phase δ_{14} taken in its range of variability $[-\pi, \pi]$. The black curves show the 3-flavor ellipses as a benchmark. In both the 3-flavor and 4-flavor cases, the running parameter on the ellipses is the CP-phase δ_{13}.

---

[5] A similar plot has been shown in [258] for the experiment NOνA to visualize the impact of new CP-phases potentially related to non-standard neutrino interactions.

6.2 Discussion at the events level

All the experimental features of these two experiments T2K and NOνA has been discussed in details in section 5.1. Here we discuss the event spectra and the bi-events plots in details.

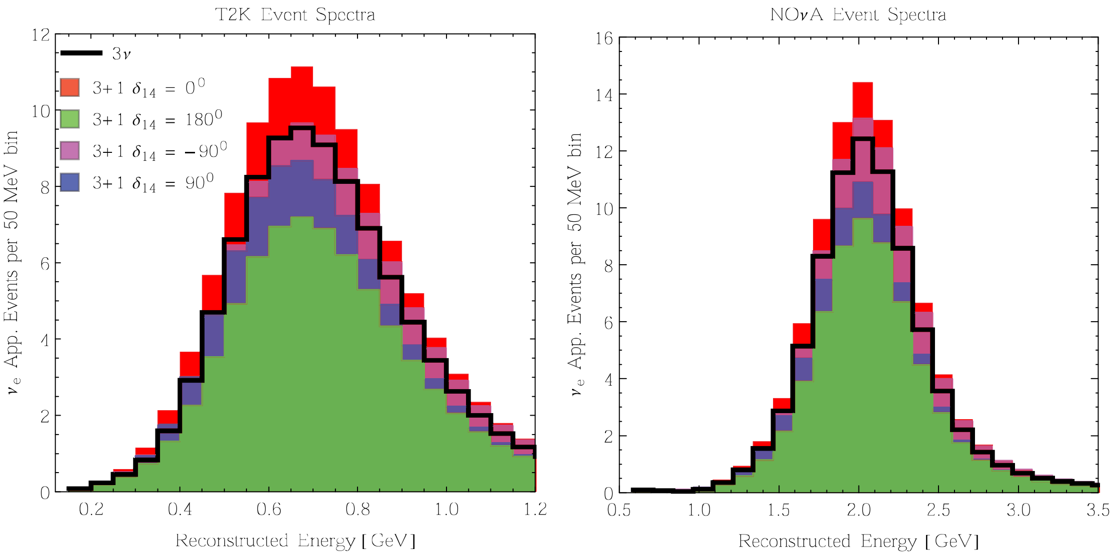

Figure 6.6: Expected signal event spectra in the ν_e appearance channel as a function of the reconstructed neutrino energy. The left (right) panel refers for T2K (NOνA). The black line corresponds to the 3-flavor case. The colored histograms refer to the 3+1 scheme for the four different values of δ_{14} indicated in the legend. In all cases (both 3-flavor and 4-flavor) we have set $\delta_{13} = 0$.

6.2.1 Event spectra

We devote this section to discuss the expected event spectra in 3ν and 3+1 schemes for both the T2K and NOνA setups using their full projected exposures as mentioned in the previous section. The number of expected appearance electron events[6] in the i-th energy bin in the detector is estimated using the following well known expression

$$N_i = \frac{T\, n_n\, \varepsilon}{4\pi L^2} \int_0^{E_{\max}} dE \int_{E_{A_i}^{\min}}^{E_{A_i}^{\max}} dE_A\, \phi(E)\, \sigma_{\nu_e}(E)\, R(E, E_A)\, P_{\mu e}(E)\,, \tag{6.42}$$

---

[6] We can calculate the number of positron events using Eq. (6.42), by taking into account appropriate oscillation probability and cross-section. The same strategy can be applied to estimate $\mu^{\pm}$ events.

where $\phi(E)$ is the neutrino flux, T is the total running time, n_n is the number of target nucleons in the detector, ε is the detector efficiency, σ_{ν_e} is the neutrino interaction cross-section, and $R(E,E_A)$ is the Gaußian energy resolution function of the detector. The quantities E and E_A are the true and reconstructed (anti-)neutrino energies respectively, and L is the baseline. In Fig. 6.6, we show the expected signal event spectra for the ν_e appearance channel as a function of reconstructed neutrino energy for both the experiments under consideration. As expected due to their off-axis nature, we see a narrow peak in the projected event spectrum around 0.6 GeV for the T2K experiment (see the left panel), and for the NOνA experiment (see the right panel), the events mainly occur around 2 GeV where the flux is maximum. In both panels, the thick black lines correspond to the 3ν case assuming $\delta_{13} = 0°$. The other colored histograms (red, green, magenta, and blue) are drawn in the 3+1 scheme assuming different values of δ_{14} which are mentioned in the figure legends. Next, we discuss the bi-events plots to get more physics insight.

6.2.2 Bi-events plots

The bi-probability plots presented in section 6.1.3 give a very clear idea of the behavior of the transition probability at the specific value of the energy corresponding to the peak of the spectrum and allow us to approximately predict the behavior of a given off-axis experiment, since the dominant contribution to the total rate comes from the energies close to the peak. In this section we present, for completeness, also the bi-events plots, where on the two axes it is represented the theoretical value of number of events (ν_e on the x-axis, $\bar{\nu}_e$ on the y-axis) expected in a given experiment. Such plots provide a more precise information on the behavior of a given experiment, because the event rates take into account the complete energy spectrum and provide the information on the statistics involved in the experiment. Figure 6.7 shows the bi-events plots for T2K, where we have used the same contour style convention of the bi-probability plots. We still have elliptical curves, since we are just replacing the coefficients in the parametric equations (6.32)-(6.35) with appropriate weighted averages. A quick comparison of the T2K bi-events plot in Fig. 6.7 with the corresponding bi-probability one (Fig. 6.3) shows that the geometrical properties of the ellipses are slightly different from those obtained for the probabilities. Apart from an obvious deformation factor due to the different scale used for the events, we can appreciate other differences, which are introduced by the contribution of several

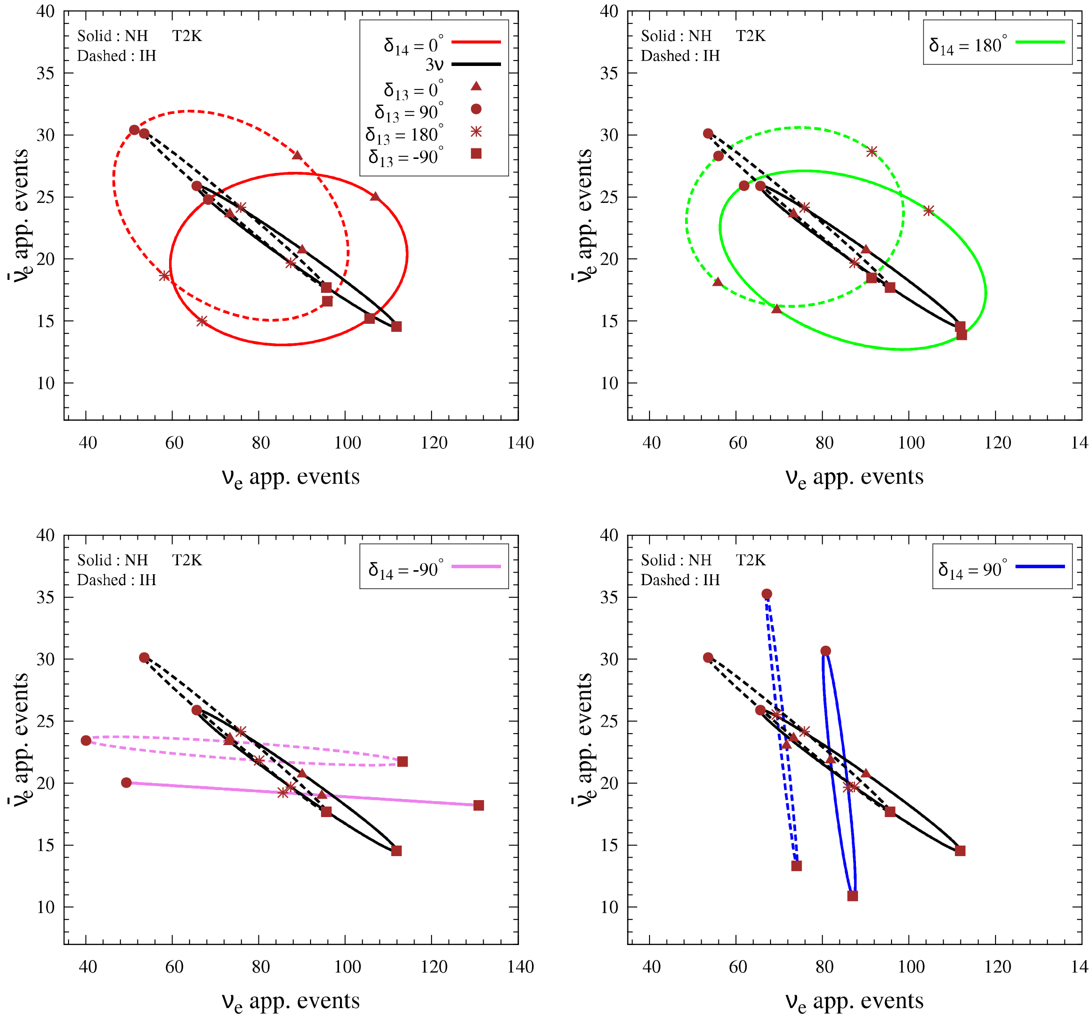

Figure 6.7: Bi-events plots for T2K for four fixed values of the CP-phase δ_{14}. In each panel, we also show the 3-flavor ellipses for the sake of comparison. In both the 3-flavor and 4-flavor ellipses, the running parameter is the CP-phase δ_{13} varying in the range $[-\pi, \pi]$. The solid (dashed) curves refer to NH (IH). We have assumed that half of the full T2K exposure will be used in the neutrino mode and the other half in the antineutrino mode.

energies in the integration. In particular, appreciable differences are now visible between the two cases of NH and IH. Most importantly, figure 6.7 gives a clear feeling on the number of events expected in the experiment T2K.

Figure 6.8 shows the bi-events plots for NOνA. The comparison with the corresponding bi-probability plot in Fig. 6.4 shows that the geometrical properties of the ellipses are quite similar to those obtained for the probabilities. This is due to the fact the the energy spectrum of NOνA is more sharp than the T2K one (see Fig. 6.6). As a consequence the peak energy is more important in determining the global behavior of the total rate.

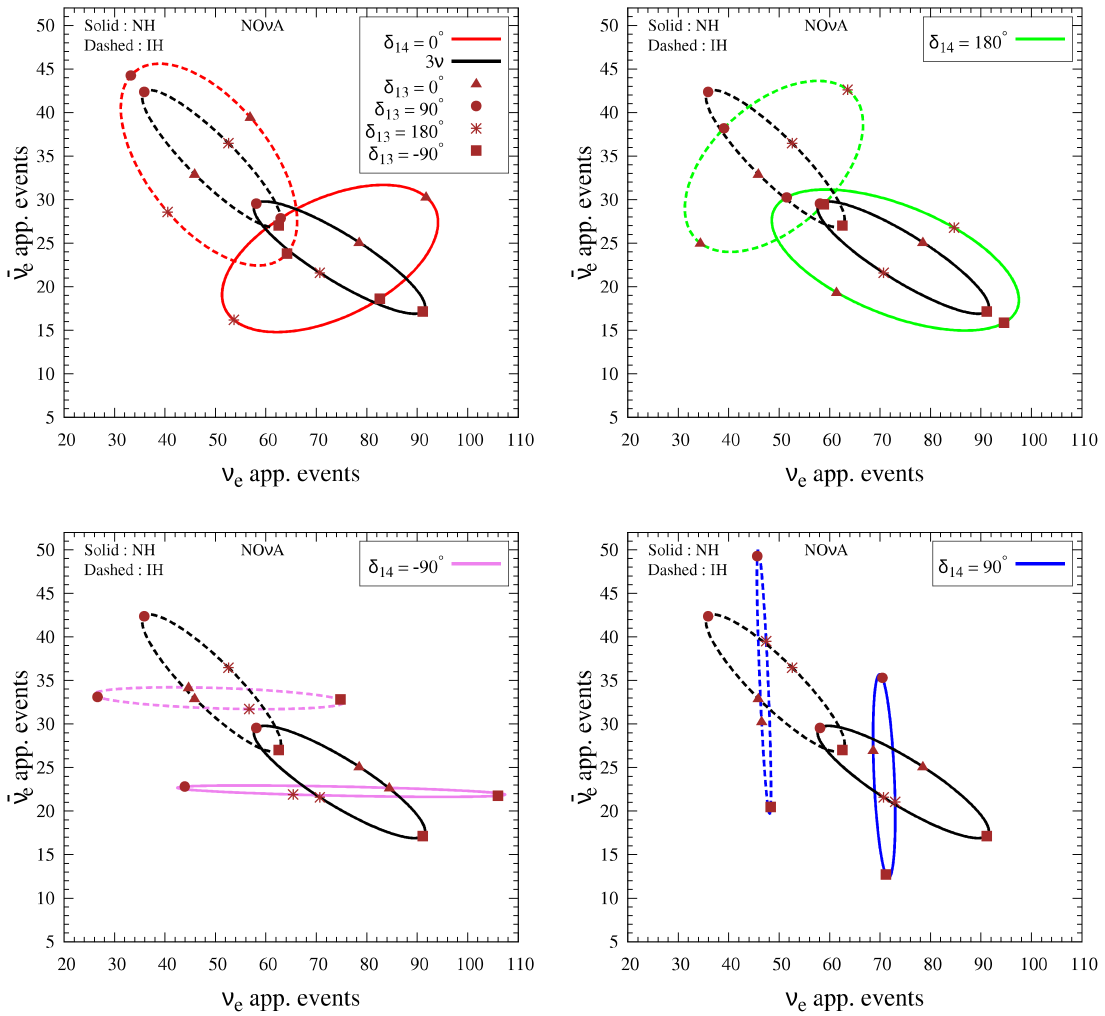

Figure 6.8: Bi-events plots for NOνA for four fixed values of δ_{14}. In each panel, we also show the 3-flavor ellipses for the sake of comparison. In both the 3-flavor and 4-flavor ellipses, the running parameter is the CP-phase δ_{13} varying in the range $[-\pi, \pi]$. The solid (dashed) curves refer to NH (IH). We have assumed that half of the full NOνA exposure will be used in the neutrino mode and the other half in the antineutrino mode.

Finally, in Fig. 6.9 we show the convolution plot in the bi-event space, which gives a visual information on the degree of separation of the two neutrino mass hierarchies.

6.3 Details of the Statistical Method

This section deals with the numerical technique and analysis procedure which we follow to compute our main results. We use the GLoBES software [219, 220] along with its new physics tools to obtain our results. We include the 4-flavor effects both in the $\nu_\mu \to \nu_e$

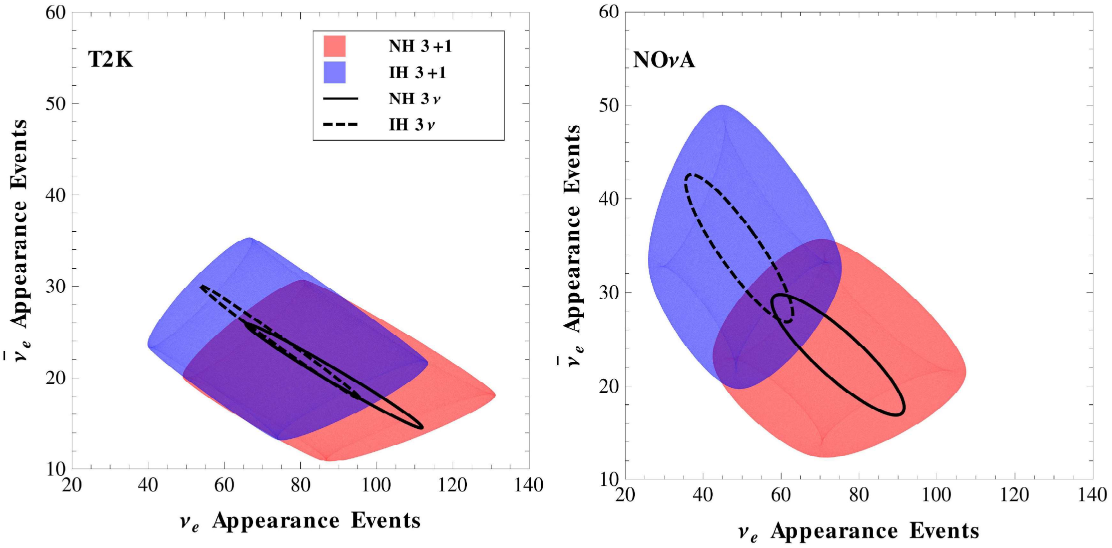

Figure 6.9: The colored shaded blobs represent the convolution of the bi-events graphs for T2K (left panel) and NOνA (right panel) in the 3+1 scheme. The blobs are obtained by superimposing several ellipses, each corresponding to a different value of the CP-phase δ_{14} taken in its range of variability $[-\pi, \pi]$. The black curves show the 3-flavor ellipses as a benchmark. In both the 3-flavor and 4-flavor cases, the running parameter on the ellipses is the CP-phase δ_{13} in the range $[-\pi, \pi]$. For both T2K and NOνA we have assumed that half of the full exposure will be used in the neutrino mode and the other half in the antineutrino mode.

appearance channel and in the $\nu_\mu \to \nu_\mu$ disappearance channel. We have found that, for the $\nu_\mu \to \nu_\mu$ disappearance channel, the survival probability is very close to the 3-flavor case, in agreement with the analytical considerations made in [104]. We consider the true value of $\sin^2 2\theta_{13}$ to be 0.085 (see Table 4.3) to generate the data and keep it fixed in the fit expecting that the Daya Bay experiment would be able to measure θ_{13} with a very high-precision ($\sim$ 3% relative precision at 1σ C.L.) by the end of 2017 [187]. As far as the atmospheric mass-squared splitting is concerned, we take the true value of $\Delta m^2_{32} = 2.4 \times 10^{-3}$ eV^2 (-2.4×10^{-3} eV^2) for NH (IH). Accordingly, we take Δm^2_{31} = 2.475×10^{-3} eV^2 (-2.4×10^{-3} eV^2) for NH (IH). We also do not marginalize over this parameter in the fit since the present precision on this parameter is already quite good [254], and the future data from the running T2K and NOνA experiments would certainly improve this further [242, 259]. This should remain true also in the presence of sterile neutrino oscillations because the value of Δm^2_{31} is extracted from the $\nu_\mu \to \nu_\mu$ searches which, for the small values of the mixing angles θ_{14} and θ_{24} considered in the present analysis (see Table 4.3), are almost unaffected by the 4-flavor effects. For θ_{23}, we consider the maximal mixing ($\pi/4$) as the true choice, and in the fit, we marginalize over the range given in Table 4.3. We marginalize over both the choices of hierarchy in the fit for all the analyses, except for the mass hierarchy discovery studies where our aim is to exclude the wrong hierarchy in the fit. We vary the true value of δ_{13} in its allowed range of $[-\pi, \pi]$, and it has been marginalized over its full range in the fit if the performance indicator demands so. We take the line-averaged constant Earth matter density[7] of 2.8 g/cm^3 for both the baselines.

We take the mass-squared splitting $\Delta m^2_{41} = 1\,\mathrm{eV}^2$, which is the value currently suggested by the SBL anomalies. However, we stress that our results would remain unaltered for different choices of such parameter, provided that $\Delta m^2_{41} \gtrsim 0.1\,\mathrm{eV}^2$. For such values, the fast oscillations induced by the new large frequency get completely averaged because of the finite resolution of the detector. For the same reason, the LBL setups are insensitive to the sign of Δm^2_{41} and we can safely assume positive sign for it. Concerning the active-sterile mixing angles, we take the true value of 0.025 for both the $\sin^2\theta_{14}$ and $\sin^2\theta_{24}$ and keep them fixed in the fit. These values are close to the best fit obtained by the global 3+ fits [105]. We vary the true value of δ_{14} in its allowed range of $[-\pi, \pi]$, and it has been marginalized over its full range in the fit as needed. We assume $\sin^2\theta_{34} = 0$ (and, as a consequence δ_{34} does not come in the parameterization) in all the simulations.[8] In our analysis, we do not explicitly consider the near detectors of T2K and NOνA which may shed some light on θ_{14} and θ_{24}, but certainly, the near detector data are not sensitive to the CP-phases which is the main thrust of this work. In our simulation, we have performed a full spectral analysis using the binned events spectra for both experiments. In the statistical analysis, as discussed in the section 5.2, we have used the Poissonian $\Delta\chi^2$. Apart from the neutrino oscillation parameters marginalization as described above, $\Delta\chi^2$ is also marginalized over the uncorrelated systematic uncertainties (as mentioned in section 5.1 in the experimental description of T2K and NOνA.) using the method of pulls. When showing the results, we display the $1, 2, 3\sigma$ confidence levels for 1 d.o.f. using the relation n$\sigma \equiv \sqrt{\Delta\chi^2}$. In [261], it was shown that the above relation is valid in the frequentist method of hypothesis testing.

---

[7] The line-averaged constant Earth matter density has been computed using the Preliminary Reference Earth Model (PREM) [260].

[8] We recall that the vacuum $\nu_\mu \to \nu_e$ transition probability is independent of θ_{34} (and δ_{34}). In matter, a tiny dependence appears which is more appreciable in NOνA than in T2K (see the appendix of [104] for a detailed discussion).

6.4 Results of the Sensitivity Study

6.4.1 CP-violation Searches in the Presence of Sterile Neutrinos

In this section we explore the impact of sterile neutrinos in the CPV searches of T2K and NOνA. As a first step we consider the discovery potential of the CPV induced by the standard 3-flavor CP-phase δ_{13}, which is proportional to $\sin\delta_{13}$. The discovery potential is defined as the confidence level at which one can reject the test hypothesis of no CP-violation, i.e. the cases $\delta_{13} = 0$ and $\delta_{13} = \pi$. We have taken the best fit values of all the parameters at the values specified in the second column of Table 4.3. In the 3-flavor scheme, we marginalize over θ_{23} and over the hierarchy. In the 3+1 scheme, in addition, we marginalize over the unknown value of δ_{14}.

In Figure 6.10 we display the results of the numerical analysis. The upper panels refer to T2K, the middle ones to NOνA, and the lower ones to their combination. In the left (right) panels, we consider NH (IH) as the true hierarchy choice. In each panel, we present the results obtained for the 3-flavor case (black solid curve) and for the 3+1 scheme, in which case we select four different values of the true value of δ_{14} (while its test value is left free to vary and is marginalized away). The values of the phase δ_{14} and the colors of the corresponding curves are the same of the previous plots. The 3-flavor sensitivities (black curves) are in agreement withthose shown in the official analyses [242]. We see that for all values of the new CP-phase δ_{14} the discovery potential of the two experiments decreases with respect to that of the 3-flavor case. The loss of sensitivity is imputable to the degeneracy between the two CP-phases δ_{13} and δ_{14}. Similar to the 3-flavor case, the discovery potential has a maximum for $\delta_{13} = -90^0$ ($\delta_{13} = 90^0$) for NH (IH). Abrupt changes in the sensitivity are evident in the range $[45^0, 135^0]$ for the NH case and in the range $[-135^0, -45^0]$ for the IH case. This behavior can be traced to the degeneracy among the two CP-phases and the mass hierarchy. In fact, in these ranges the best fit is obtained for the false hierarchy. In the bi-events plots these ranges correspond to points where the ellipses of the two hierarchies tend to overlap.

Until now we have considered only four selected values of the CP-phase δ_{14}. It is interesting to see what happens for a generic choice of such a parameter. To this purpose we have generalized the analysis by treating δ_{14} as a free parameter. In Fig. 6.11 we show the iso-contour lines of the discovery potential of the CP-violation induced by δ_{13} as a function of the true values of the two phases δ_{13} and δ_{14}. Inside the red regions the discovery potential is larger than 2σ. Inside the beige regions it is larger than 1σ. The plots refer to the combination T2K + NOνA for the two cases of NH (left) and IH (right). One can easily check that horizontal cuts of the contour plots made in correspondence of the four particular values of the phase δ_{14} considered in Fig. 6.10 return the 1σ and 2σ intervals derivable from the last two panels of Fig. 6.10. In the 3+1 scheme also the new CP-phase δ_{14} can be a source of CP-violation. Hence it is interesting to determine the discovery potential of the CPV induced by $\sin\delta_{14}$ alone and the *total* CP-violation induced simultaneously by $\sin\delta_{13}$ and $\sin\delta_{14}$. Our numerical analysis shows that the discovery potential of non-zero $\sin\delta_{14}$ is always below the 2σ level so we do not show the corresponding plot. Instead in Fig. 6.12 we show the results for the *total* CPV discovery since it is appreciably different (larger) from that induced by $\sin\delta_{13}$ alone. The plots refer to the combination T2K + NOνA for the two cases of NH (left) and IH (right). Inside the small green regions the discovery potential is larger than 3σ. Inside the red regions it is larger than 2σ. Inside the beige regions it is larger than 1σ. As expected the regions in Fig. 6.12 contain as sub-regions those of Fig. 6.11 where the sole CPV induced by $\sin\delta_{13}$ is considered. In Fig. 6.12 we can recognize nine white regions where the discovery potential is below 1σ. We stress that these nine regions correspond to four physical regions because both CP-phases are cyclic variables. Geometrically one can view the square represented in Fig. 6.12 as an unwrapped torus, provided one takes into account that the upper edge is connected with the lower edge, and that left edge with the right one[9]. These four regions contain the points where the total CPV is zero i.e. $\sin\delta_{13} = \sin\delta_{14} = 0$. This condition is verified for the four (inequivalent) CP-conserving cases $[\delta_{13}, \delta_{14}] = [0,0]$, $[\pi,0]$, $[0,\pi]$, $[\pi,\pi]$ and all the other five combinations obtainable by a change of sign of one of (or both) the phases equal to π.

6.4.2 Reconstruction of the CP phases

The CP-violation discovery potential tells us how much one experiment will be able to rule out the case of CP conservation given a positive observation of CPV corresponding

---

[9] Formally one can see that the square is homeomorphic to the torus. Topologically the torus can be seen as the quotient space of the square.

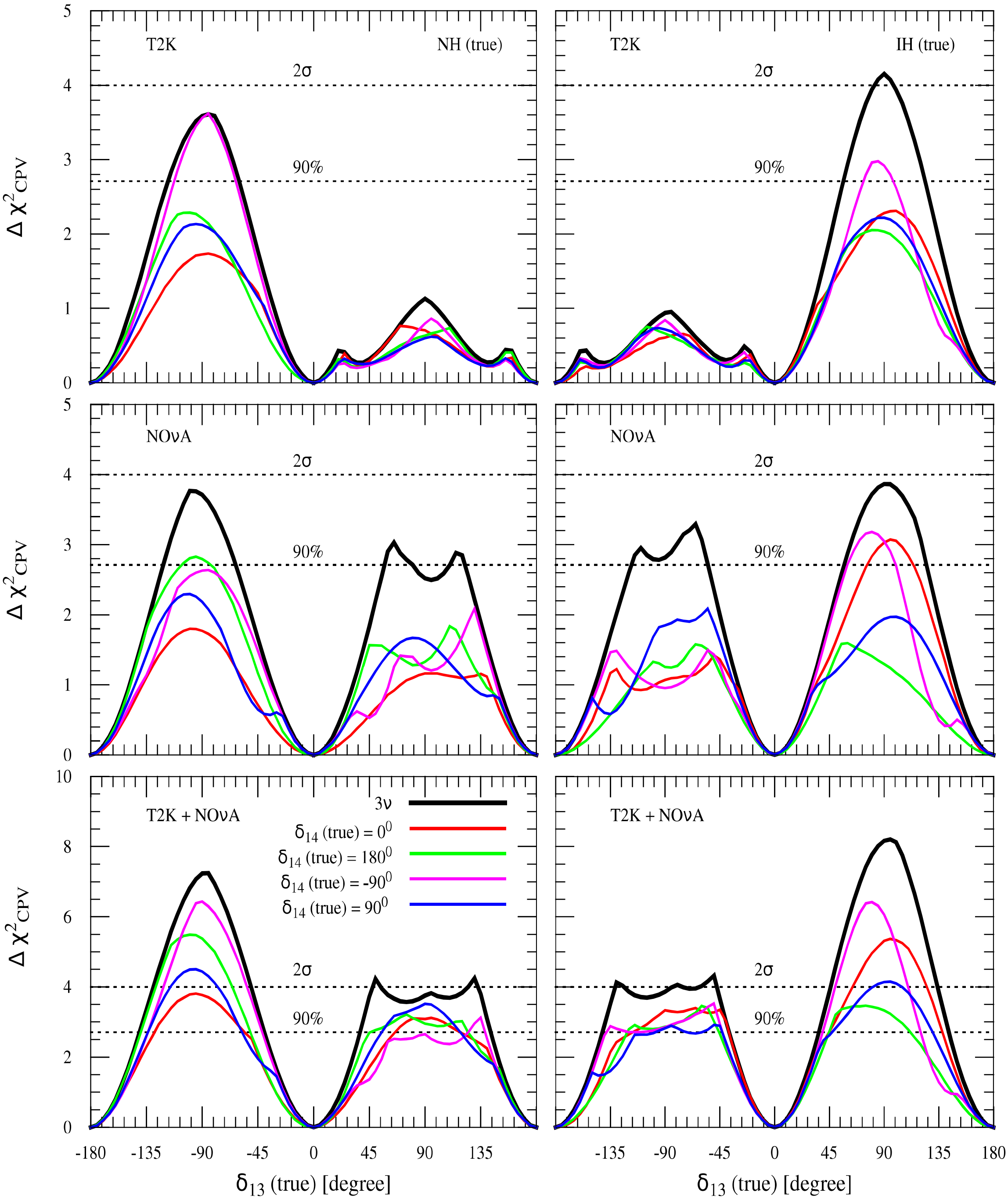

Figure 6.10: Discovery potential of CP-violation induced by $\sin\delta_{13}$. Upper panels refer to T2K. Middle panels to NOνA. Lower panels to T2K and NOνA combined. In the left (right) panels, we consider NH (IH) as the true hierarchy choice. In each panel, the black curve corresponds to the 3-flavor case. The colored curves are obtained in the 3+1 scheme for four different true values of δ_{14}. We marginalize over θ_{23} and δ_{14} over their allowed ranges in the fit, and also over the hierarchy.

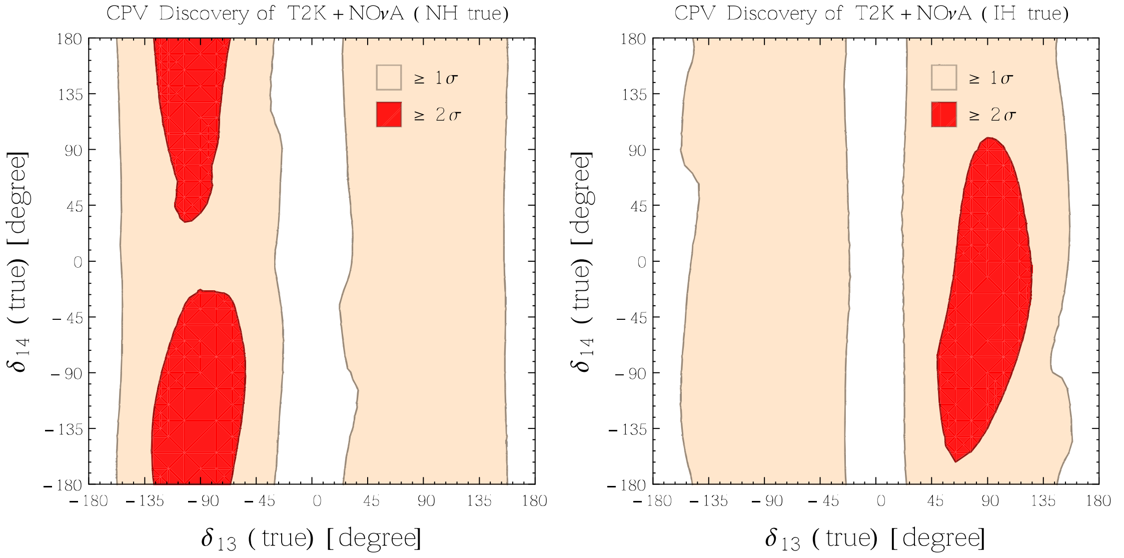

Figure 6.11: Discovery potential of CP-violation induced by $\sin\delta_{13}$ in the 3+1 scheme for the T2K + NOνA combined setup. Inside the red regions the discovery potential is $\geq 2\sigma$. Inside the beige regions it is $\geq 1\sigma$.

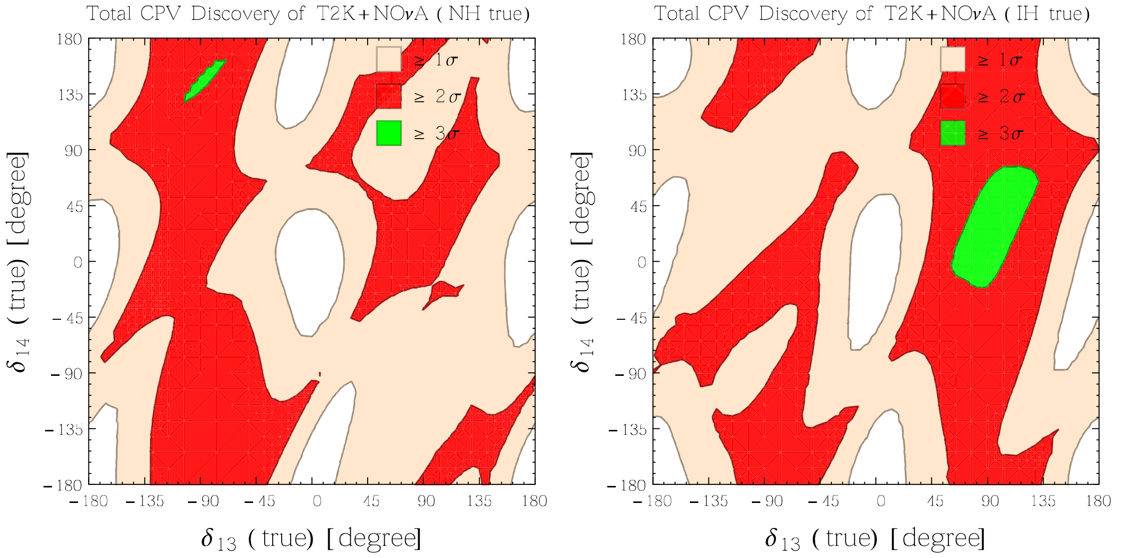

Figure 6.12: Discovery potential of total CP-violation (induced simultaneously by $\sin\delta_{13}$ and $\sin\delta_{14}$) in the 3+1 scheme for the T2K + NOνA combined setup. Inside the green regions the discovery potential is $\geq 3\sigma$. Inside the red regions it is $\geq 2\sigma$. Inside the beige regions it is $\geq 1\sigma$.

to a true value of the phases δ_{13} and δ_{14}. While this is certainly a very important feature, a complementary information is provided by the capability of reconstructing the values of the two CP-phases, independent of the amount of CP-violation (if any). Figure 6.13 gives a quantitative answer to such a different kind of question. The four plots represent the regions reconstructed around four representative points in the plane $[\delta_{13}, \delta_{14}]$. In all cases we have taken the NH as the true hierarchy in the data and then marginalized over NH and IH in theory. Similar results (not shown) were obtained for the IH case. The two upper panels refer to the CP-conserving cases $[0,0]$ and $[\pi,\pi]$ respectively. The third and fourth panels refer to the two (maximally) CP-violating cases $[-\pi/2,-\pi/2]$ and $[\pi/2,\pi/2]$. The two confidence levels refer to 1σ and 2σ (1 d.o.f.). We see that in all cases we obtain a unique reconstructed region at the 1σ level. Note that this is true also in the second panel, because the four corners of the square form a connected region due to the cyclic properties of the two CP-phases. At the 2σ level we obtain a unique region only in the case $[-\pi/2,-\pi/2]$ (bottom left). Small spurious islands start to appear in the other cases. We have checked that these islands disappear if one assumes the prior knowledge of the correct mass hierarchy. In all cases the typical 1σ uncertainty is about 40^0 (50^0) for δ_{13} (δ_{14}). As recently shown in the 4-flavor analysis performed in [107], the present data seem to indicate a slight preference for the combination $[\delta_{13},\delta_{14}] = [-\pi/2,-\pi/2]$. If this trend gets confirmed in a few years (assuming the existence of a sterile neutrino), the picture should resemble that of the left bottom panel of Fig. 6.13.

6.4.3 Impact of Sterile Neutrinos on Mass Hierarchy Measurements

In this section we assess the discovery potential of the neutrino mass hierarchy. This is defined as the confidence level at which one can exclude the false (or wrong) test hierarchy given a data set generated with the true hierarchy. We have taken the best fit values of all the parameters as given in Table 4.3. In the test model, we have marginalized over δ_{13} and θ_{23} within their full 3σ range. In the 3+1 scheme we have also marginalized over the CP-phase δ_{14}. In Fig. 6.14 we show the discovery potential of excluding the wrong hierarchy as a function of the true value of δ_{13}. The upper panels refer to T2K, the middle ones to NOνA, and the lower ones to their combination. In the left (right) panels, we consider NH (IH) as the true hierarchy choice. In each panel, we give the results for the 3-flavor case (thick black curve) and for the 3+1 scheme (colored curves) for four different values of the true δ_{14} (that is -90^0, 90^0, 0^0 and 180^0). The color convention is the same adopted in the rest of the chapter.

We observe that in T2K (upper panels) the discovery potential is quite limited both in the 3-flavor framework and in the 3+1 scheme. This is due to the fact that the matter

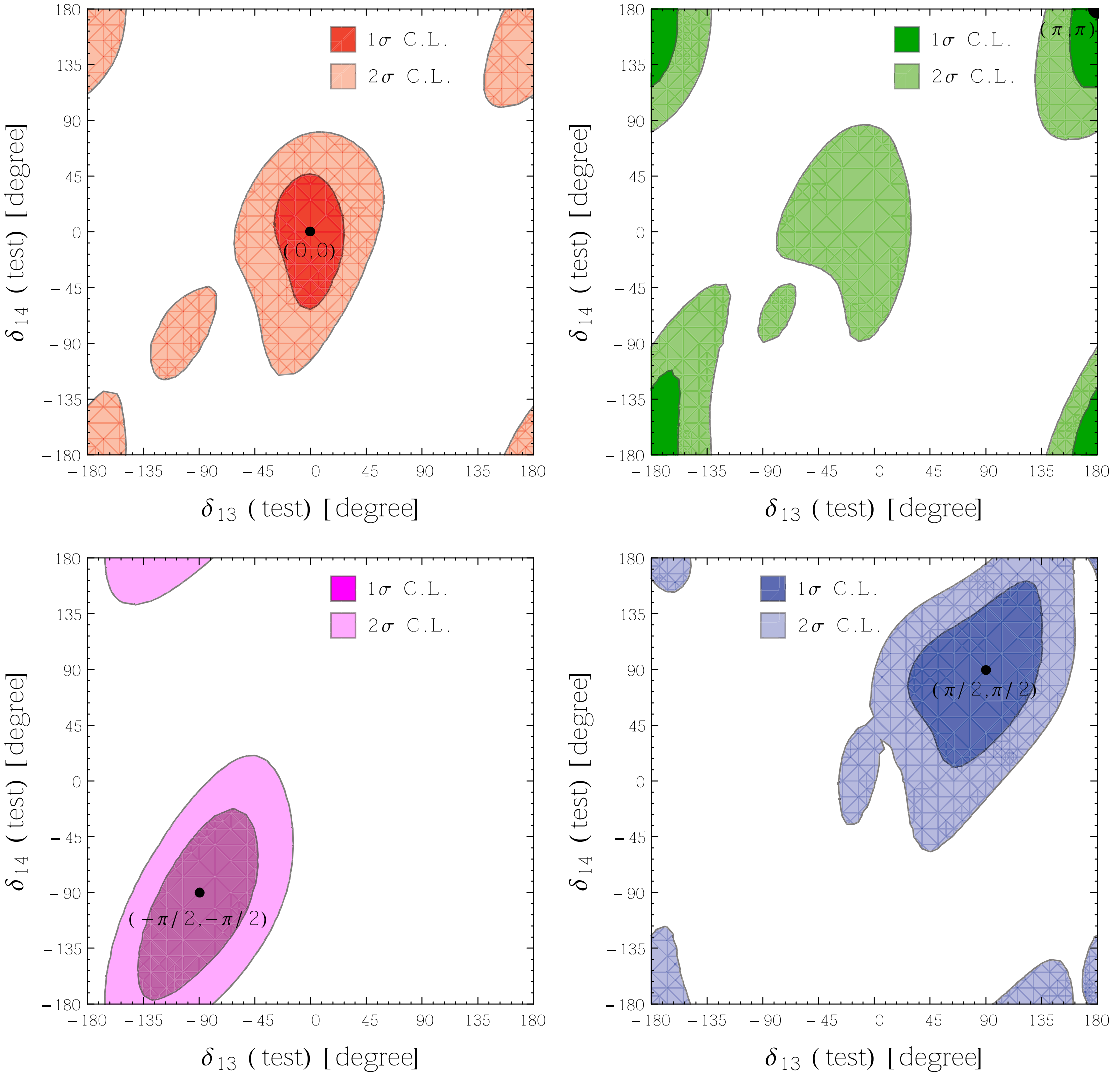

Figure 6.13: Reconstructed regions for the two CP-phases δ_{13} and δ_{14} for the T2K + NOνA combined setup, for the four choices of their true values indicated in each panel. The NH is taken as the true hierarchy, while we have marginalized over the two possible hierarchies in the test model. The contours refer to 1σ and 2σ levels.

effects are small in T2K. Comparing the results of the 3+1 scheme (colored curves) with those of the 3-flavor one (black curve) we observe that, apart for the case $\delta_{14} = -90^0$ for NH ($\delta_{14} = 90^0$ for IH), in all the other cases the discovery potential is smaller than the 3-flavor one. The overall behavior of the 4-flavor curves is similar to that of the 3-flavor one. In particular, the sensitivity presents a maximum at $\delta_{13} = -90^0$ for NH. This similar behavior can be understood by observing that in the bi-events plots the point $\delta_{13} = -90^0$ (the squares in the four panels of Fig. 6.7) always provides the maximal separation from the cloud generated by the convolution of all the possible IH ellipses (see Fig. 6.9). A similar observation can be done for the specular case of $\delta_{13} = +90^0$ and IH.

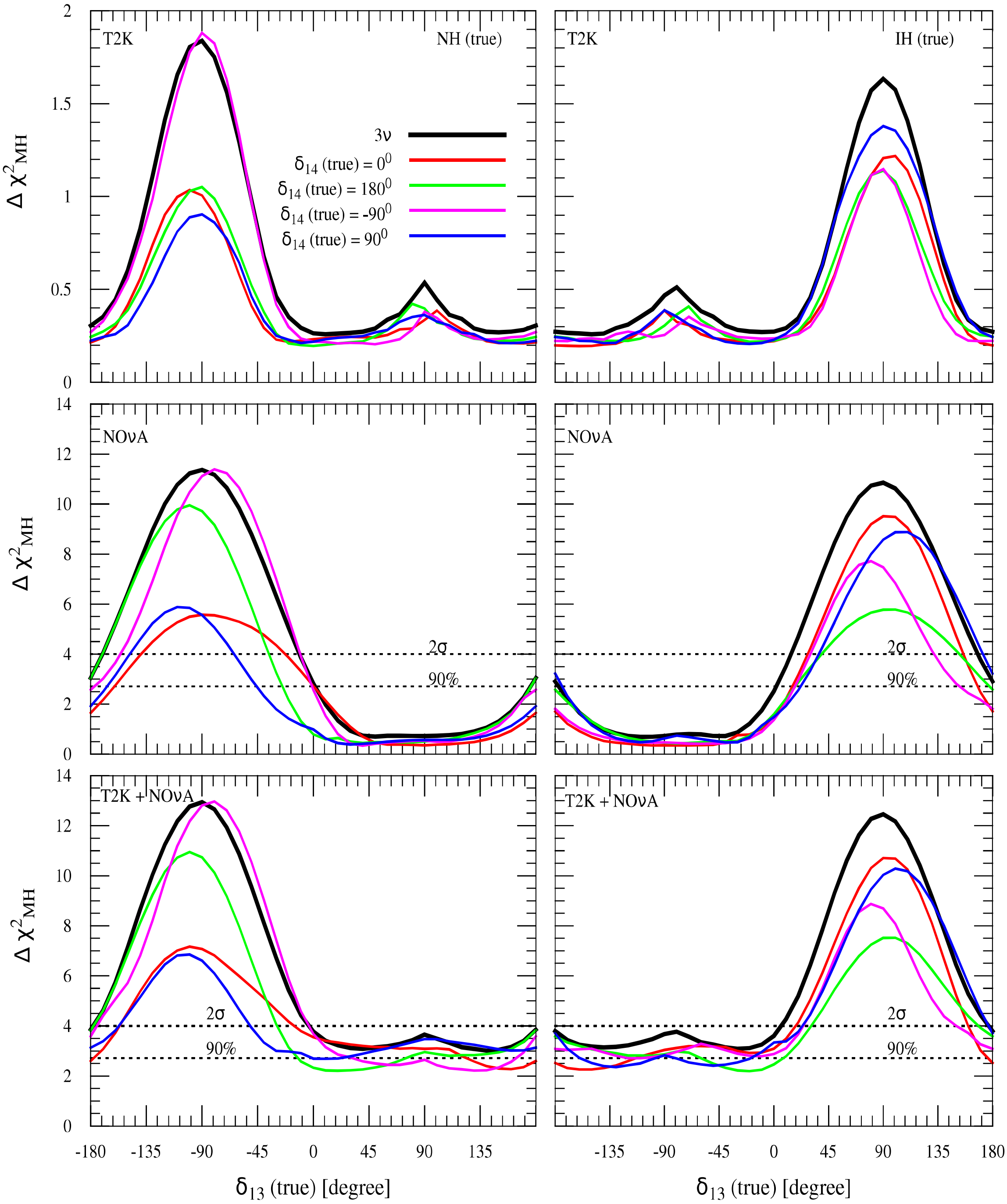

Figure 6.14: Discovery potential for excluding the wrong hierarchy as a function of true δ_{13}. Upper panels are for T2K. Middle panels are for NOνA. Lower panels are for T2K and NOνA combined. In the left (right) panels, we consider NH (IH) as true hierarchy choice. In each panel, we give the results for the 3-flavor case (black line) and for the 3+1 scheme for four different values of true δ_{14}.

Concerning NOνA (middle panels) we can make the following observations. Similarly to T2K the maximal discovery potential is obtained for $\delta_{13} = -90^0$ for NH and $\delta_{13} =$

90^0 for IH. For such two values the representative points on the ellipse (the squares for NH and the circles for IH in Fig. 6.8) always provide the maximal separation from the convolution of all the ellipses of the opposite MH (see again Fig. 6.9). However, there are also important differences with respect to T2K. First of all, we observe that the maximal discovery potential is much larger than that of T2K. This is imputable to the fact that the matter effects are much bigger in NOνA (see the discussion in section 6.1). Second, we can see that in the NH case (left middle panel) there is a good sensitivity not only for $\delta_{14} = -90^0$ (magenta curve) but also for $\delta_{14} = 180^0$ (green curve). In the IH case (right middle panel) there is a good sensitivity for $\delta_{14} = 90^0$ (blue curve) and $\delta_{14} = 0^0$ (red curve). This different behavior with respect to T2K can be traced to the fact that in NOνA the peak energy is not centered exactly at the first oscillation maximum but at $\Delta = 0.4\pi$. Finally, we notice that the combination of the two experiments (lower panels) is dominated by NOνA.

The study of the discovery potential of the neutrino mass hierarchy can be generalized to the case in which the CP-phase δ_{14} can assume any value in its variability range. Figure 6.15 shows the results of such more general analysis, where we have treated δ_{14} as a free parameter. We display the iso-contour lines of the discovery potential as a function of the true values of the two phases δ_{13} and δ_{14}. Inside the red regions the discovery potential is larger than 3σ. Inside the blue regions it is larger than 2σ. The plots refer to the combination T2K + NOνA for the two cases of NH (left) and IH (right). One can easily check that horizontal cuts of the contour plots made in correspondence of the four particular values of the phase δ_{14} considered in Fig. 6.14 return the 1σ and 2σ intervals derivable from the last two panels of Fig. 6.14.

6.5 Summary

We have considered the impact of an eV-scale light sterile neutrino on the prospective data expected to come from the two long-baseline experiments T2K and NOνA after they accumulate their full planned exposure. In section 6.1, we have presented a detailed discussion of the behavior of the 4-flavor $\nu_\mu \to \nu_e$ and $\bar{\nu}_\mu \to \bar{\nu}_e$ transition probabilities, extending for the first time the bi-probability representation, commonly used in the 3-flavor framework, to the 3+1 scheme. In section 6.2, we have extended our discussion

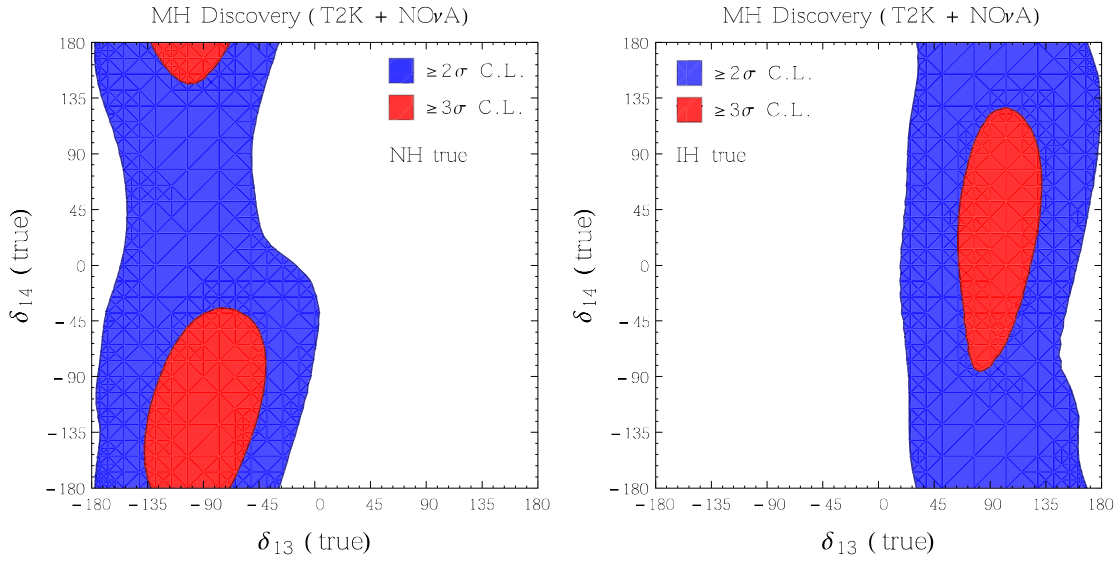

Figure 6.15: Discovery potential for excluding the wrong hierarchy for the combination of T2K and NOνA as a a function of the two CP-phases δ_{13} and δ_{14}. Inside the red regions the discovery potential is $\geq 3\sigma$. Inside the blue regions it is $\geq 2\sigma$.

from probability level to event level by introducing the energy spectra and bi-event plots for both T2K and NOνA. These bi-event plots give a beautiful visual view of the physics potential of an experiment from the perspective of understanding the mass hierarchy, and CP-violation which are the main thrust of this chapter.

In section 6.4 we have performed a comprehensive sensitivity study of the two experiments (taken alone and in combination) in order to assess their discovery potential in the presence of a sterile neutrino species. We have considered realistic benchmark values of the 3+1 mass-mixing parameters as inferred from the existing global short-baseline fits. We found that the performance of both the experiments in claiming the discovery of the CP-violation induced by the standard CP-phase $\delta_{13} \equiv \delta_{\text{CP}}$, and the neutrino mass hierarchy get substantially deteriorated. The degree of loss of sensitivity depends on the value of the unknown CP-phase δ_{14}. We have also assessed the discovery potential of total CP-violation (i.e., induced simultaneously by the two CP-phases δ_{13} and δ_{14}) and the capability of the two experiments of reconstructing the true values of such CP-phases. The typical (1σ level) uncertainty on the reconstructed phases is approximately 40^0 for δ_{13} and 50^0 for δ_{14}.

Chapter 7

Physics Reach of DUNE with a Light Sterile Neutrino

In this chapter we investigate the implications of one light eV-scale sterile neutrino on the physics potential of the proposed long-baseline experiment DUNE [125, 126] assuming future full exposure of data. DUNE is a highly sophisticated future generation experiment and it is well known that it can address few vital fundamental unknown issues in three flavor framework like MH determination, CPV discovery, octant of θ_{23}, and many others in high confidence level. However it becomes highly interesting and curious when we ask that what happens to these unknown issues in presence of a sterile neutrino. Here we have addressed two of the above issues namely MH and CP sensitivity in details. If the future short-baseline experiments confirm the existence of active-sterile oscillations, and the new mixing angles $(\theta_{14}, \theta_{24}, \theta_{34})$ turn out to be comparable to θ_{13}, then it can have significant impact on mass hierarchy (MH) and CP-violation (CPV) searches at DUNE. We find that both the MH sensitivity, and CPV discovery sensitivity induced by $\delta_{13} \equiv \delta_{\rm CP}$ get substantially deteriorated in comparison to three flavor expectation. It gets further deteriorated if θ_{34} is large ($\sim 30^0$). We have also studied the CPV discovery induced by other two phases δ_{14} and δ_{34}. We find that the sensitivity to the CPV generated by the new phase δ_{14} can reach 3σ for an appreciable fraction of its true values. Interestingly, θ_{34} and its associated phase δ_{34} can influence both the ν_e appearance and ν_μ disappearance channels via matter effects which for DUNE are pronounced. Hence, δ_{34} can also contribute to CPV provided θ_{34} is large. Finally, we investigate the capability of reconstructing the two phases δ_{13} and δ_{14}. The details of all the analyses and the respective results have been discussed in the next few sections.

This chapter is structured as follows. In section 7.1, we introduce the theoretical framework and present a detailed discussion of the behavior of the 4-flavor $\nu_\mu \to \nu_e$ transition probabilities both in vacuum and in matter. In section 7.2, we describe the details of the DUNE setup and of the statistical analysis. In section 7.3, we make some important considerations at the level of the bi-probability and bi-events plots and at the level of the energy spectrum, and then we present the results of the sensitivity study of the mass hierarchy in the 3+1 scheme. Section 7.4 is devoted to the results concerning the CPV discovery potential and the capability of reconstruction of the CP-phases. Finally, we draw our conclusions in section 7.5.

7.1 Transition probability in the 3+1 scheme

7.1.1 Theoretical framework

As discussed in section 2.6, in the presence of a sterile neutrino ν_s, the mixing among the flavor and the mass eigenstates is described by a 4×4 matrix. A convenient parameterization of the mixing matrix is

$$U = \tilde{R}_{34} R_{24} \tilde{R}_{14} R_{23} \tilde{R}_{13} R_{12}\,, \tag{7.1}$$

where R_{ij} ($\tilde{R}_{ij}$) are real (complex) 4×4 rotations in the (i,j) plane containing the 2×2 submatrix

$$R_{ij}^{2\times2} = \begin{pmatrix} c_{ij} & s_{ij} \\ -s_{ij} & c_{ij} \end{pmatrix} \quad \tilde{R}_{ij}^{2\times2} = \begin{pmatrix} c_{ij} & \tilde{s}_{ij} \\ -\tilde{s}_{ij}^* & c_{ij} \end{pmatrix}\,, \tag{7.2}$$

in the (i,j) sub-block, with

$$c_{ij} \equiv \cos\theta_{ij} \qquad s_{ij} \equiv \sin\theta_{ij} \qquad \tilde{s}_{ij} \equiv s_{ij} e^{-i\delta_{ij}}\,. \tag{7.3}$$

7.1.2 Transition probability in Vacuum

In the DUNE setup the matter effects play an important role. However, for the sake of clearness, before discussing the flavor conversion in the presence of matter we give a brief sketch of the basic formulae in vacuum. This will help the reader to grasp some new qualitative features, which emerge solely in the presence to matter. As discussed in section 2.6.1, the $\nu_\mu \to \nu_e$ conversion probability can be approximately written as the sum of three contributions

$$P^{4\nu}_{\mu e} \simeq P^{\rm ATM} + P^{\rm INT}_{\rm I} + P^{\rm INT}_{\rm II}\,. \tag{7.4}$$

The first (positive-definite) term is related to the atmospheric frequency and it gives the leading contribution to the probability. The second and third terms are driven by the interference of two distinct frequencies and can have both positive and negative sign. The first of the two interference terms is driven by the standard solar-atmospheric interference, while the second one is related to the atmospheric-sterile interference. The transition probability depends on the three small mixing angles θ_{13}, θ_{14}, θ_{24}, whose best estimates, derived from the global 3-flavor analyses [23, 22, 254] (for θ_{13}) and from the 3+1 fits [105, 106] (for θ_{14} and θ_{24}), turn out to be very similar and we have approximately $s_{13} \sim s_{14} \sim s_{24} \sim 0.15$ (see Table 4.3). Therefore, it is meaningful to treat all such three mixing angles as small quantities of the same order ε. Another small quantity entering the transition probability is the ratio of the solar over the atmospheric mass-squared splitting $\alpha \equiv \Delta m^2_{21}/\Delta m^2_{31} \simeq \pm 0.03$, which can be assumed to be of order ε^2. Keeping terms up to the third order, in vacuum, one finds [104]

$$P^{\rm ATM} \simeq 4 s^2_{23} s^2_{13} \sin^2\Delta\,, \tag{7.5}$$

$$P^{\rm INT}_{\rm I} \simeq 8 s_{13} s_{12} c_{12} s_{23} c_{23} (\alpha\Delta) \sin\Delta \cos(\Delta + \delta_{13})\,, \tag{7.6}$$

$$P^{\rm INT}_{\rm II} \simeq 4 s_{14} s_{24} s_{13} s_{23} \sin\Delta \sin(\Delta + \delta_{13} - \delta_{14})\,, \tag{7.7}$$

where $\Delta \equiv \Delta m^2_{31} L/4E$ is the atmospheric oscillating factor, which depends on the baseline L and on the neutrino energy E. It is important to note that the vacuum expression of the transition probability does not depend on the third mixing angle θ_{34} and on the associated CP-phase δ_{34}. As we will discuss in the next section, this is no more true in the presence of matter, where such a dependency emerges.

7.1.3 Transition probability in Matter

The details of the oscillation probabilities in 3+1 scheme in presence of matter have been discussed in section 2.7. Using Eq. (2.95), we can write,

$$\bar{H}_{3\nu} = \bar{H}_{3\nu}^{\mathrm{kin}} + \bar{H}_{3\nu}^{\mathrm{dyn}} \tag{7.8}$$

governing the evolution of the $(\bar{\nu}_e, \bar{\nu}_\mu, \bar{\nu}_\tau)$ system. We should note here that the bar sign on top of neutrino denotes the new basis of the system. Now the dynamical part has the form

$$\bar{H}_{3\nu}^{\mathrm{dyn}} = V_{CC} \begin{bmatrix} |\bar{U}_{e1}|^2 + r|\bar{U}_{s1}|^2 & r\bar{U}_{s1}^*\bar{U}_{s2} & r\bar{U}_{s1}^*\bar{U}_{s3} \\ \dagger & r|\bar{U}_{s2}|^2 & r\bar{U}_{s2}^*\bar{U}_{s3} \\ \dagger & \dagger & r|\bar{U}_{s3}|^2 \end{bmatrix}, \tag{7.9}$$

where we have indicated with † the complex conjugate of the element with the same two indices inverted. In deriving Eq. (7.9) we have used the relations $\bar{U}_{e2} = \bar{U}_{e3} = \bar{U}_{\mu 3} = 0$. Considering the explicit expressions of the elements of $\bar{U}$ (see sec. 2.7), and taking their first-order expansion in the small mixing angles θ_{i4} $(i = 1,2,3)$, Eq. (7.9) takes the form

$$\bar{H}_{3\nu}^{\mathrm{dyn}} \approx V_{\mathrm{CC}} \begin{bmatrix} 1-(1-r)s_{14}^2 & r\tilde{s}_{14}s_{24} & r\tilde{s}_{14}\tilde{s}_{34}^* \\ \dagger & rs_{24}^2 & rs_{24}\tilde{s}_{34}^* \\ \dagger & \dagger & rs_{34}^2 \end{bmatrix}. \tag{7.10}$$

From Eq. (7.10), we see that for vanishing sterile neutrino angles ($\theta_{14} = \theta_{24} = \theta_{34} = 0$) one recovers the (diagonal) standard 3-flavor MSW Hamiltonian. In general, in the 4-flavor case, the Hamiltonian in Eq. (7.10) encodes both diagonal and off-diagonal perturbations. We can observe that these corrections are formally equivalent to non-standard neutrino interactions (NSI)[1]

$$\bar{H}_{3\nu}^{\mathrm{dyn}} \approx V_{\mathrm{CC}} \begin{bmatrix} 1+\varepsilon_{ee} & \varepsilon_{e\mu} & \varepsilon_{e\tau} \\ \dagger & \varepsilon_{\mu\mu} & \varepsilon_{\mu\tau} \\ \dagger & \dagger & \varepsilon_{\tau\tau} \end{bmatrix}. \tag{7.11}$$

---

[1] We stress that this is only a formal analogy. The real NSI are mediated by heavy particles. In contrast, in the case of sterile neutrinos there is no heavy mediator and the NSI-like structure of the Hamiltonian is merely related to the fact that we are working in the new basis introduced in Eq. (2.90), which is rotated with respect to the original flavor basis and is particularly convenient to handle the problem under consideration. It is worthwhile to mention that a similar analogy has been noticed concerning the solar neutrino transitions in the presence of sterile species [93].

This formal analogy is helpful in understanding the sensitivity to the new dynamical effects implied by the sterile neutrinos. It is well known that in the $\nu_\mu \to \nu_e$ channel, which is relevant to the present discussion, the NSI that play the most important role are $\varepsilon_{e\mu}$ and $\varepsilon_{e\tau}$. If one assumes that the three new mixing angles have the same value $s_{14}^2 = s_{24}^2 = s_{34}^2 = 0.025$, all the corrections in Eq. (7.11) are very small ($|\varepsilon_{\alpha\beta}| \simeq 0.01$) and they have a negligible impact. In this case, the dynamics is almost equivalent to that of the standard 3-flavor case. However, if one allows the third mixing angle to assume values close to its upper bound ($\theta_{34} \sim 30^0$), the elements of the third column of the Hamiltonian in Eq. (7.11) can be appreciably larger ($|\varepsilon_{e\tau}| \simeq |\varepsilon_{\mu\tau}| \simeq 0.04$ and $|\varepsilon_{\tau\tau}| \simeq 0.13$). In this last case, one may expect an appreciable dependency of the transition probability on the mixing angle θ_{34} and on the associated CP-phase δ_{34}. Therefore, in contrast to the vacuum case, in matter, the transition probability is sensitive to these two additional parameters. This behavior has been already pointed out in the analytical treatment presented in [104] (see sec. 2.7), and successively noticed in the numerical simulations performed in [140]. It represents an interesting feature, because in favorable circumstances (i.e., a large value of θ_{34}), the $\nu_\mu \to \nu_e$ channel may be sensitive not only to the two CP-phases δ_{13} and δ_{14} but also to the CP-phase δ_{34}. Hence, the $\nu_\mu \to \nu_e$ searches may provide full access to the rich CPV structure of the 3+1 scheme. In order to illustrate the peculiar role of the third mixing angle, in our numerical study we will consider the following three benchmark cases: $\theta_{34} = 0$, $\theta_{34} = 9^0$ (i.e., equal to the other two mixing angles θ_{14} and θ_{24}) and $\theta_{34} = 30^0$ (which is a value close to its current upper bound). For clarity, we report these values in the second column of Table 4.3.

For the sake of completeness we report the exact expression of the 4-flavor transition probability using Eq. 2.105,

$$\begin{aligned} P_{\mu e}^{4\nu} &= c_{14}^2 s_{24}^2 s_{14}^2 \bar{P}_{ee}^{3\nu} \\ &+ c_{14}^2 c_{24}^2 \bar{P}_{\mu e}^{3\nu} \\ &- 2c_{14}^2 c_{24} s_{14} s_{24} \mathrm{Re}(e^{-i\delta_{14}} \bar{S}_{ee} \bar{S}_{e\mu}^*) \\ &+ c_{14}^2 s_{14}^2 s_{24}^2 \,. \end{aligned} \tag{7.12}$$

This expression is completely general, except for the assumption of averaged oscillations, and connects the 4-flavor transition probability to the amplitudes of the effective 3-flavor system governed by the effective Hamiltonian in Eq. (7.8). We have defined $\bar{P}^{3\nu}_{ee} \equiv |\bar{S}_{ee}|^2$ and $\bar{P}^{3\nu}_{\mu e} \equiv |\bar{S}_{e\mu}|^2$, where $\bar{S}_{ee}$ and $\bar{S}_{e\mu}$ are the transition elements of the evolution operator in the rotated basis (for a detailed derivation see section 2.7). Note that, in matter, a dependency of the transition probability on the mixing angle θ_{34} and on its associated CP-phase δ_{34} arises through $\bar{S}_{ee}$ and $\bar{S}_{e\mu}$. For a vanishing value of all the three mixing angles $\theta_{14}, \theta_{24}, \theta_{34}$, Eq. (7.12) returns the 3-flavor limit. For small values of the two mixing angles θ_{14} and θ_{24}, Eq. (7.12) takes the form

$$\begin{aligned} P^{4\nu}_{\mu e} &\simeq (1 - s^2_{14} - s^2_{24})\bar{P}^{3\nu}_{\mu e} \\ &- 2 s_{14} s_{24} \mathrm{Re}(e^{-i\delta_{14}} \bar{S}_{ee} \bar{S}^*_{e\mu}) \\ &+ s^2_{14} s^2_{24} (1 + \bar{P}^{3\nu}_{ee})\,. \end{aligned} \tag{7.13}$$

The first term in Eq. (7.13), apart from a pre-factor close to one, is the three-flavor transition probability modified according to the non-standard dynamics encoded by Eq. (7.10). This modified 3-flavor probability, in vacuum, returns the standard transition probability, which contains the well-known interference term between the atmospheric and solar oscillations of Eq. (7.6). The second term in Eq. (7.13) has kinematical origin (i.e., it is non-zero also in vacuum) and originates from the interference of the new large frequency introduced by the fourth mass eigenstate with the atmospheric and solar splittings. As shown in [104], only the interference with the atmospheric splitting is appreciable and, in vacuum, the second term of Eq. (7.13) returns Eq. (7.7). The last term in Eq. (7.13) is of the fourth order and has negligible impact.

7.2 Statistical Method used for Numerical Analysis

All the experimental features of DUNE has been discussed in details in section 5.1. Now the experimental sensitivities presented in this work are estimated using the GLoBES software [219, 220] along with its new physics tools. We incorporate the 4-flavor effects both in the $\nu_\mu \to \nu_e$ appearance channel, and in the $\nu_\mu \to \nu_\mu$ disappearance channel. The same is also true for the anti-neutrino mode. We take the neutrino interaction cross-sections from Refs. [232, 233], where the authors gave the cross-section for water and isoscalar targets. To obtain cross-sections for LAr, we have scaled the inclusive charged current cross-sections of water by a factor of 1.06 for neutrino, and 0.94 for anti-neutrino [234, 235]. The details of the statistical method that we follow in the present work, are exactly similar to what have been described in section 6.3. The only difference that we have in the present chapter is that, we have also analyzed the cases where the active-sterile mixing angle θ_{34} and its associated CP-phase δ_{34} are non-zero, since the impact of these parameters can be significant for the DUNE baseline as can be seen from our sensitivity results which we present in the next sections. Table 4.3 shows the true values of the oscillation parameters and their marginalization ranges which we consider in our simulation. For non-zero $\sin^2\theta_{34}$, we take the true values of 0.025 and 0.25 which are well within its allowed range [105, 106]. We vary the true value of δ_{34} in its allowed range of $[-\pi, \pi]$, and it has been marginalized over its full range in the fit as needed. We consider the mass-squared splitting $\Delta m^2_{41} = 1\,\text{eV}^2$, which is the value currently suggested by the SBL anomalies. However, our results would be unchanged for different choices of this parameter, provided that $\Delta m^2_{41} \gtrsim 0.1\,\text{eV}^2$. For such values, the very fast oscillations driven by the new large mass-squared splittng are completely averaged by the finite resolution of the detector. For the same reason, DUNE is insensitive to the sgn(Δm^2_{41}) and we can safely assume a definite (positive) sign for it. For the 2-3 mixing angle, we consider the maximal mixing ($\pi/4$) as the true value, and in the fit, we marginalize over the range given in Table 4.3. We marginalize over both the choices of hierarchy in the fit for all the analyses, except for the mass hierarchy discovery studies where our goal is to exclude the wrong hierarchy in the fit. We take the line-averaged constant Earth matter density[2] of 2.87 g/cm^3 for the DUNE baseline. In our calculation, we do not explicitly consider the near detector of DUNE which may provide some information on θ_{14} and θ_{24}, but certainly, the near detector data are not sensitive to the CP-phases in which we are interested. In our simulation, we have performed a full spectral analysis using the binned events spectra for the DUNE setup. In the numerical analysis, the Poissonian $\Delta\chi^2$ (see section 5.2 for definition) is marginalized over the uncorrelated systematic uncertainties (as mentioned in section 5.1 in the experimental description of DUNE.) using the method of pulls. To present the results, we display the $1, 2, 3\sigma$ confidence levels for 1 d.o.f. using the relation $\text{N}\sigma \equiv \sqrt{\Delta\chi^2}$. In [261], it was demonstrated that the above relation is valid in the frequentist method of hypothesis testing.

---

[2] The line-averaged constant Earth matter density has been computed using the Preliminary Reference Earth Model (PREM) [260].

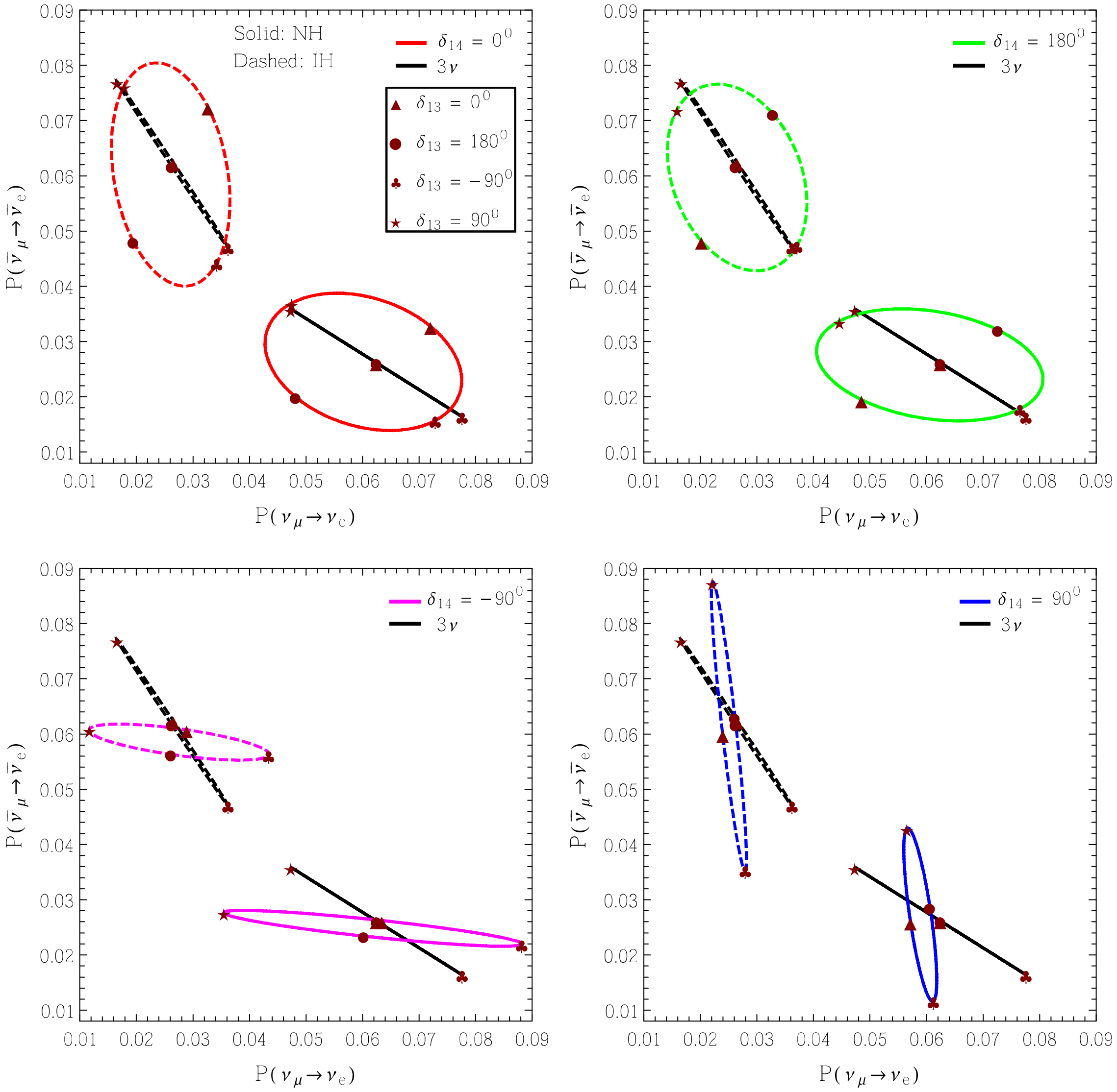

Figure 7.1: Bi-probability plots corresponding to the first oscillation maximum (E = 2.54 GeV) obtained for four fixed values of δ_{14}. In each panel, we also show the 3-flavor ellipses for the sake of comparison. In both the 3-flavor and 4-flavor ellipses, the running parameter is the CP-phase δ_{13} varying in the range $[-\pi, \pi]$. The solid (dashed) curves refer to NH (IH). We have assumed $\theta_{34} = 0^0$.

7.3 Mass hierarchy discovery potential in the 3+1 scheme

In this section we discuss the sensitivity of DUNE to the neutrino mass hierarchy. As a first step we provide a description at the level of the transition probability and at the level of signal events aided by bi-probability and bi-event plots. Second, we highlight the role of the spectral shape information in the hierarchy discrimination. Finally, we present the results of the full numerical analysis.

7.3.1 Discussion at the level of bi-probability and bi-events plots

In the 3-flavor framework, the behavior of the transition probability is often represented with the CP-phase trajectory diagrams in bi-probability space, first introduced in [55]. In the recent work [215], such representation has been extended to the 3+1 scheme. This representation is particularly advantageous as it gives a bird-eye view of the salient features of a given experimental setup, in particular its sensitivity to the MH. In Figure 7.1, we show the bi-probability plots corresponding to the first oscillation maximum ($E = 2.54\,\mathrm{GeV}$) obtained for four values of δ_{14}. In each panel, we also show the 3-flavor ellipses (black curves) for the sake of comparison. In both the 3-flavor and 4-flavor ellipses, the running parameter is the CP-phase δ_{13} varying in the range $[-\pi, \pi]$. The solid (dashed) curves refer to NH (IH). In the 3-flavor case the ellipses are basically degenerate with a line, because at the first oscillation maximum only terms proportional to $\sin\delta_{13}$ survive in the transition probability. In contrast, in the 4-flavor case, there are both terms proportional to $\cos\delta_{13}$ and $\sin\delta_{13}$ (see [215] for details). The orientation and the lengths of the two axes of the ellipses depend on the particular value of δ_{14}. In all plots of Fig. 7.1, $\theta_{34} = 0^0$ has been assumed. In the most general case, when θ_{34} is non-zero, the geometrical properties of the ellipses sensibly depends also on the third CP-phase δ_{34}. Such a dependency is more pronounced when θ_{34} is large. From the four bi-probability plots shown in Fig. 7.1, one can already envisage that the separation of the two mass hierarchies tends to decrease in the 3+1 scheme. In fact, for particular values of the CP-phases, the minimal distance between the NH and IH ellipses decreases with respect to the 3-flavor case. The overall picture can be visualised by introducing the convoluted bi-probability plots shown in Fig. 7.2. These plots are generated by superimposing several ellipses corresponding to all the possible choices of δ_{14} and δ_{34}. In the left panel it is assumed $\theta_{34} = 0$ and δ_{34} is irrelevant. The right panel is generated with $\theta_{34} = 30^0$ and also the phase δ_{34} is relevant. The graphs in Fig. 7.2 may be also seen as dense scatter plots obtained by varying simultaneously the CP-phases δ_{13}, δ_{14} (and δ_{34} in the right panel). Fig. 7.2 provides a bird-eye view of the degree of separation of the two neutrino mass hierarchies in the 3+1 scheme. From the right panel, we can see that for $\theta_{34} = 30^0$ there is even a small region of the bi-probability space where the two hierarchies overlap. One may ask what happens when the integrated spectrum (and not the probability at the first oscillation maximum) is taken into account.

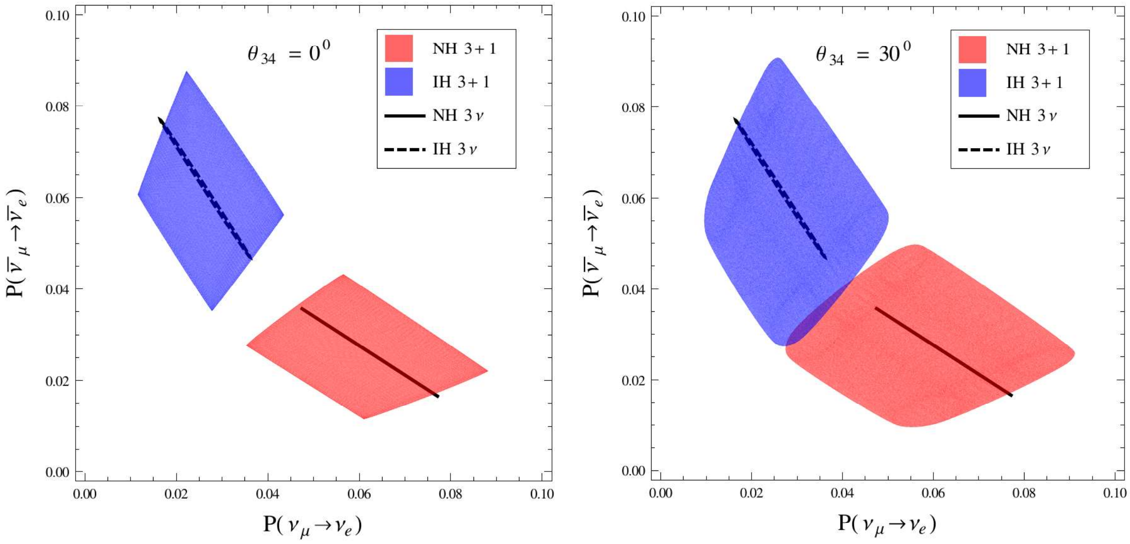

Figure 7.2: The colored shaded blobs represent the convolution of the bi-probability graphs for DUNE in the 3+1 scheme. The left panel corresponds to the case $\theta_{34} = 0$, while the right panel corresponds to the case $\theta_{34} = 30^0$. The blobs in the left panel are obtained by superimposing several ellipses, each corresponding to a different value of the CP-phase δ_{14} taken in its range of variability $[-\pi, \pi]$. In the right panel also the CP-phase δ_{34} is allowed to vary. The black curves show the 3-flavor ellipses as a benchmark. In both the 3-flavor and 4-flavor cases, the running parameter on the ellipses is the CP-phase δ_{13}.

Fig. 7.3, which represents the convolution plots at the level of the total events, quantitatively answers this question. In Fig. 7.3, we introduce the bi-event plots, in which the two axes represent the total number of ν_e (x-axis) and $\bar{\nu}_e$ (y-axis) events[3]. In both panels, the 3-flavor case is represented by the black ellipses, which are obtained varying the CP-phase δ_{13} in the range $[-\pi, \pi]$. In the 3+1 scheme, there are more CP-phases and the bi-event plot becomes a blob. In particular in the left panel, where we have taken $\theta_{34} = 0$, we vary the two phases δ_{13} and δ_{14} in the range $[-\pi, \pi]$. In addition, in the right panel, which corresponds to $\theta_{34} = 30^0$, we also vary the phase δ_{34} in the same range. The 3+1 blobs can be seen as a convolution of an infinite ensemble of ellipses having different orientations or, alternatively, as a scatter plot obtained by varying simultaneously the CP-phases δ_{13}, δ_{14} (and also δ_{34} in the right panel). One can see that the distance between the blobs corresponding to the two hierarchies tends to further decrease. In particular, as evident from the right panel of Fig. 7.3, for $\theta_{34} = 30^0$ there is a sizable region where the two hierarchies overlap. For each point of this region there are two possible choices of

---

[3] In the 3+1 scheme, these kind of plots were introduced for the first time in Ref. [215] in the context of T2K and NOνA.

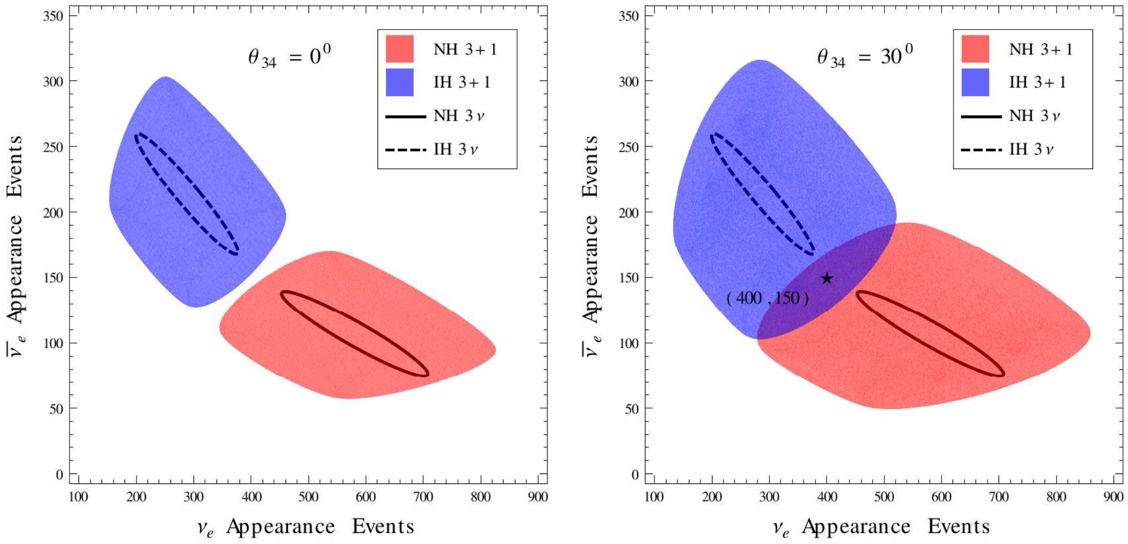

Figure 7.3: The colored shaded blobs represent the convolution of the bi-events graphs for DUNE in the 3+1 scheme. The left panel corresponds to the case $\theta_{34} = 0$, while the right panel corresponds to the case $\theta_{34} = 30^0$. The blobs in the left panel are obtained by superimposing several ellipses, each corresponding to a different value of the CP-phase δ_{14} taken in its range of variability $[-\pi, \pi]$. In the right panel also the CP-phase δ_{34} is allowed to vary. The black curves show the 3-flavor ellipses as a benchmark. In both the 3-flavor and 4-flavor cases, the running parameter on the ellipses is the CP-phase δ_{13}.

the three CP-phases (one choice corresponding to NH and the other one to IH). In these cases there is a complete degeneracy between the two hierarchies at the level of the total number of (both neutrino and antineutrino) events and the total events information cannot distinguish among NH and IH. The star in the right panel of Fig. 7.3, corresponding to 400 ν_e and 150 $\bar{\nu}_e$ events for both NH and IH, is a representative degenerate case, which we intend to discuss in more detail in the following subsection.

7.3.2 Role of the energy spectrum

The DUNE experiment employs a wide-band energy spectrum, whose shape brings additional information to that given by the total number of events. Therefore, even when there is a complete degeneracy at the level of the total number of events, it is possible to distinguish the two hierarchies at some confidence level. Figure 7.4 serves to illustrate this point. It represents the expected signal event spectrum of DUNE for the ν_e (left panel) and $\bar{\nu}_e$ (right panel) appearance channels as a function of the reconstructed neutrino energy. The red (blue) histogram corresponds to the case of NH (IH). All the spectra are

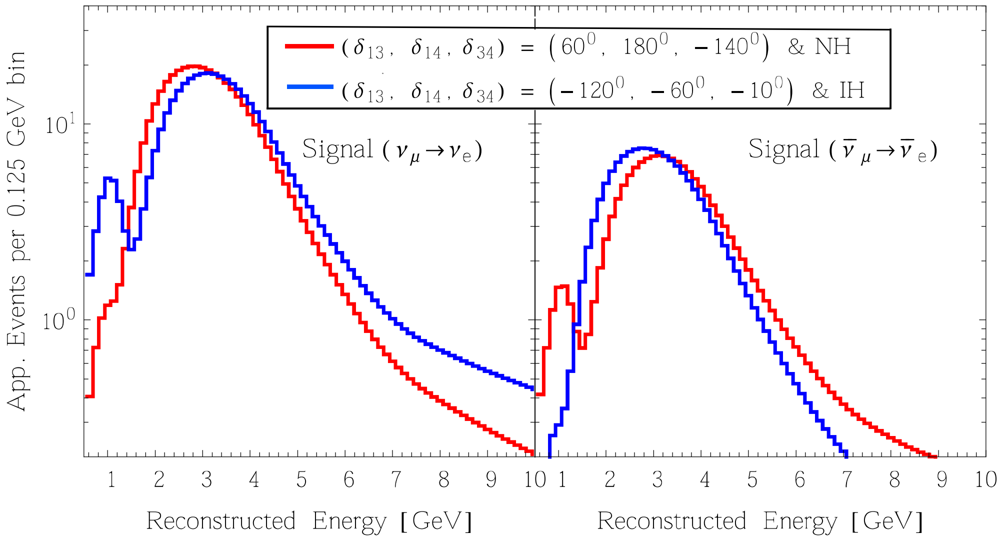

Figure 7.4: Expected signal event spectrum of DUNE for the ν_e (left panel) and $\bar{\nu}_e$ (right panel) appearance channel as a function of the reconstructed neutrino energy. The red (blue) histogram corresponds to the case of NH (IH). All the spectra are obtained for $\theta_{34} = 30^0$. For the values of the three CP-phases $(\delta_{13}, \delta_{14}, \delta_{34})$ indicated in the legend, which are different for NH and IH, the number of neutrino and antineutrino events are identical for the two hierarchies. This behavior can be visualized in the right panel of the convoluted bi-events plot shown in Fig. 7.3, where the two choices of parameters correspond to the same point (indicated by a star). In this particular case, the distinction between the two mass hierarchies relies solely upon the difference in the shape of the energy spectrum.

obtained for $\theta_{34} = 30^0$. For the values of the three CP-phases $(\delta_{13}, \delta_{14}, \delta_{34})$ indicated in the legend, which are different for the two hierarchies, the number of neutrino and antineutrino events are identical for the two hierarchies. This fact can be visualised in the right panel of the convoluted bi-events plot shown in Fig. 7.3, where the two choices of parameters correspond to the same point (indicated by a star). In this particular case, the distinction between the two mass hierarchies relies solely upon the difference in the shape of the energy spectrum, which, as one can appreciate in Fig. 7.4, is sizable. Therefore, we expect a good discrimination potential also for those points which are completely degenerate at the event level. This will be confirmed by the numerical simulation presented in the following, where we find that the pure-shape information is able to guarantee a minimal 4σ level separation between the two mass hierarchies. This point makes it evident that a deep understanding of the systematic uncertainties affecting the shape of the spectrum should be considered as an important intermediate target of DUNE and of the other new-generation wide-band LBL experiments.

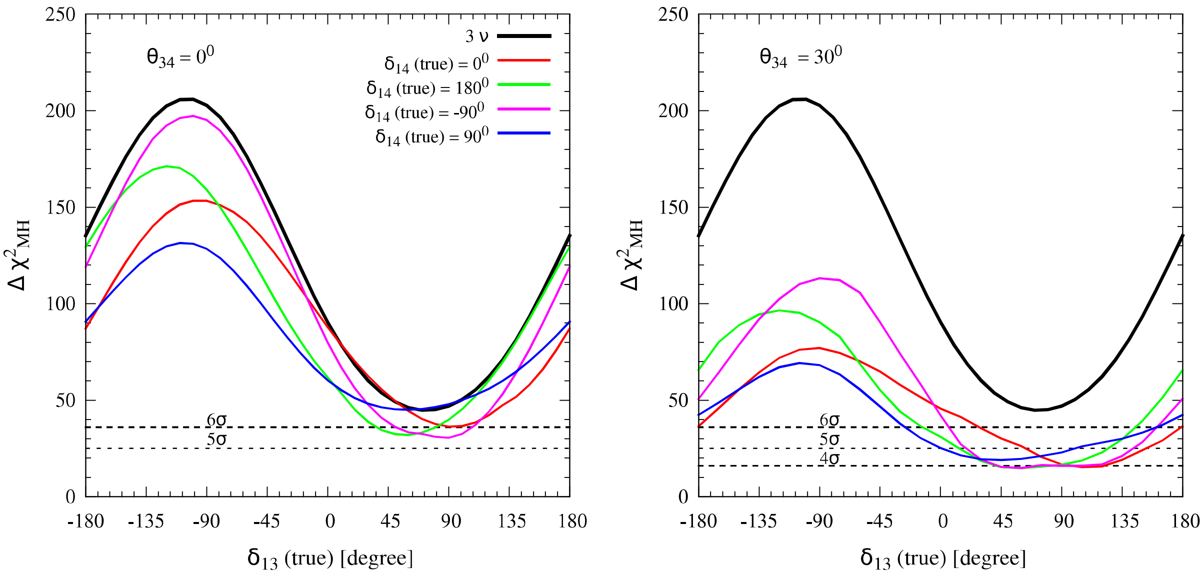

Figure 7.5: Discovery potential for excluding the wrong hierarchy (IH) as a function of true δ_{13}. In both panels we have fixed $\theta_{14} = \theta_{24} = 9^0$. The left (right) panel refers to $\theta_{34} = 0$ ($\theta_{34} = 30^0$). In each panel, we give the results for the 3-flavor case (black line) and for the 3+1 scheme for four different values of true δ_{14}. In the right panel the CP-phase δ_{34} has been marginalized over its full allowed range.

7.3.3 Numerical Results

In our numerical analysis we calculate the DUNE discovery potential of the neutrino mass hierarchy. This is defined as the confidence level at which one can exclude the false (or wrong) test hierarchy given a data set generated with the true hierarchy. We have taken the best fit values of all the parameters as given in Table 4.3. In the 3-flavor scheme, we have marginalized over δ_{13} and θ_{23} within their full 3σ range. In the 3+1 scheme, we have also marginalized over the CP-phase δ_{14} (and δ_{34} if $\theta_{34} \neq 0$). In Fig. 7.5, we show the discovery potential of excluding the wrong hierarchy as a function of the true value of δ_{13} considering NH as the true hierarchy choice. In each panel, we give the results for the 3-flavor case with the help of thick black curve. In both the panels, for the 3+1 scheme (colored curves), we have taken $\theta_{14} = \theta_{24} = 9^0$ while generating the data and also in the fit. In the left panel, we consider $\theta_{34} = 0$ both in data and also in fit, and give the results for four different values of the true δ_{14} (-90^0, 90^0, 0^0, and 180^0) while marginalizing over test δ_{14} in its entire range of $[-\pi, \pi]$ in the fit. In the right panel, we show the same considering the true and test $\theta_{34} = 30^0$, and therefore, we marginalize over both test δ_{14} and test δ_{34} in their entire ranges of $[-\pi, \pi]$ in the fit. In the right panel, we also marginalize over true choices of unknown δ_{34} in its full range of $[-\pi, \pi]$ in the data. In the left panel (corresponding to $\theta_{34} = 0$), we observe that the qualitative behavior of the 3+1 curves are similar to the 3-flavor case. In particular, there is a maximum around $\delta_{13} \sim -90^0$, and a minimum around $\delta_{13} \sim 90^0$. The opposite is true for the IH (not shown). It is evident that in general, there is a deterioration of the discovery potential for all values of the new CP-phase δ_{14}. However, even in the region around the minimum, the sensitivity never drops below 5σ confidence level. In the right panel (corresponding to $\theta_{34} = 30^0$), the situation is qualitatively similar, but the sensitivity deteriorates more[4] compared to the left panel. In particular, in the range $\delta_{13} \in [45^0, 135^0]$, the sensitivity can drop down to 4σ confidence level. This range corresponds to the region of the space spanned by the three CP-phases, where there is basically a complete degeneracy at the level of the total number of events (in both neutrino and antineutrino channels), and the distinction between NH and IH is totally entrusted to the energy spectrum. A concrete example of this kind has been provided in the previous subsection. To this regard, it is important to underline the fundamental difference between the experiments (like DUNE) that make use of an on-axis broad-band neutrino beam, and those using an off-axis configuration (T2K and NOνA). In this last case, there is basically no spectral information and, as a consequence, there are regions of the parameters space where the MH discovery potential is almost zero (see for example Fig. 14 in [215]). In a nutshell, in the off-axis configuration, one has basically only the events counting at disposal, while in the on-axis case, there is the extra information coming from the spectral shape. Needless to say, the precondition to take advantage of this additional information is a good understanding of all the ingredients that enter the calculation of the event spectrum, and a refined treatment of the related systematic uncertainties.

7.4 CP-violation searches in the 3+1 scheme

In this section, we explore the impact of sterile neutrinos in the CPV searches of DUNE. In the 3+1 scheme, there are three CP-phases, all of which can contribute to CPV. We first

---

[4] We have checked that for the case $\theta_{34} = 9^0$, the results are intermediate between those found in the two cases $\theta_{34} = 0$ and $\theta_{34} = 30^0$ shown in Fig. 7.5. In particular, the minimal sensitivity is approximately 5σ.

discuss the discovery potential of the CPV induced by the standard 3-flavor CP-phase $\delta_{13} = \delta$. We will show that, in general, it tends to deteriorate in the 3+1 scheme with respect to the 3-flavor case. Then, we treat the sensitivity to the CPV induced by the other two CP-phases δ_{14} and δ_{34}. Finally, we assess the capability of reconstructing the two phases δ_{13} and δ_{14}.

7.4.1 CP-violation discovery potential

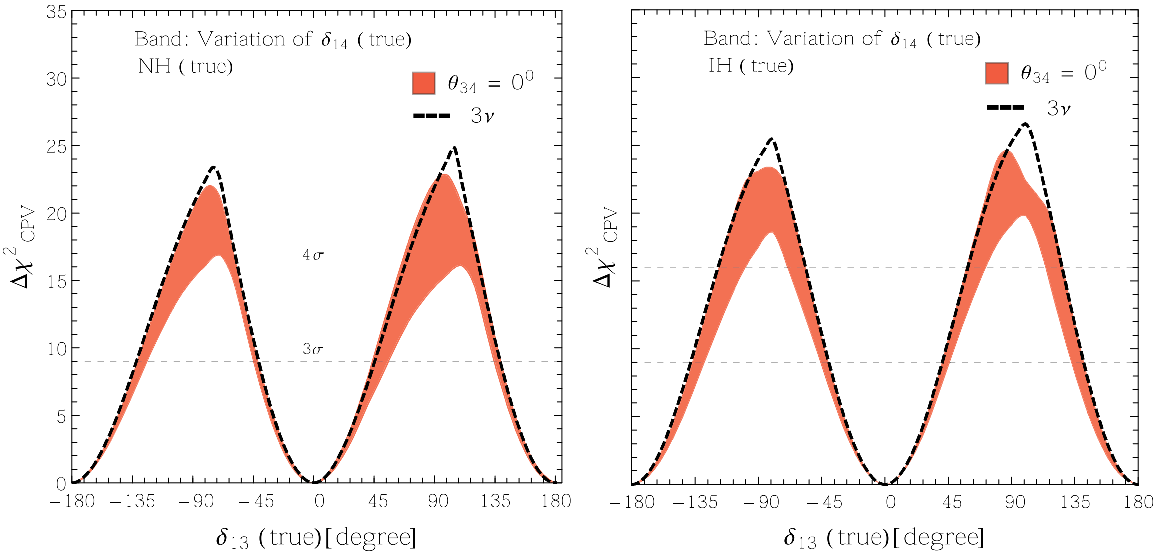

Figure 7.6: DUNE discovery potential of the CPV induced by δ_{13}. The left (right) panel refers to true NH (IH). In both panels, the black dashed curve corresponds to the 3-flavor case. In 3+1 scenario, we fix the true and test values of $\theta_{14} = \theta_{24} = 9^0$, and we take the true and test θ_{34} to be 0^0 in both the panels. In both the panels, the red bands are obtained in the 3+1 scheme by varying the unknown true δ_{14} in its entire range of $[-\pi, \pi]$ in the data while marginalizing over test δ_{14} in the same range. Both in 3ν and 3+1 schemes, we marginalize over test θ_{23} and over both the choices of test hierarchy.

The discovery potential of CPV induced by a given true δ_{13} is defined as the confidence level at which one can reject the test hypothesis of no CPV i.e. the cases test $\delta_{13} = 0$ and test $\delta_{13} = \pi$ in the fit from that given true δ_{13}. In Fig. 7.6, we report the discovery potential of CPV induced by δ_{13}. We show it as a function of the true value of δ_{13}. The left (right) panel refers to true NH (IH). As far as the standard oscillation parameters are concerned, we marginalize over test $\sin^2\theta_{23}$ in the range 0.34 to 0.68, and over both the choices of hierarchy in the fit for both 3ν and 3+1 cases. In both the panels, the black dashed curves correspond to the 3-flavor case. In 3+1 scenario, we fix the true and test values of θ_{14} and θ_{24} to be 9^0, and we take the true and test θ_{34} to be 0^0 in both the panels, and therefore, δ_{34} becomes irrelevant. In both the panels, the red bands are obtained in the 3+1 scheme by varying the unknown true δ_{14} in its entire range of $[-\pi, \pi]$ in the data while marginalizing over test δ_{14} in the same range. Figure 7.6 shows that the discovery potential can be deteriorated in the 3+1 scheme as compared to the 3-flavor framework. In particular, around $\delta_{13} \sim \pm\, 90^0$, where the discovery potential attains the maximal value, the discovery potential can decrease from $\sim 5\sigma$ C.L. (3-flavor case) to $\sim 4\sigma$ C.L. (3+1 case). In the 3+1 scheme, one expects CPV to come also from the two new phases δ_{14} and δ_{34}. In the second and third panels of Fig. 7.7, we display the discovery potential of the CPV induced by such two phases. In the first panel, for the sake of comparison, we report the CPV discovery potential induced by the standard CP-phase δ_{13} so that one can have a global view of the sensitivities. The thinner (magenta) bands correspond to the case in which all the three new mixing angles have the identical true and test values $\theta_{14} = \theta_{24} = \theta_{34} = 9^0$. The thicker (green) bands correspond to the case in which true and test $\theta_{14} = \theta_{24} = 9^0$, and true and test $\theta_{34} = 30^0$. In each panel, the bands have been obtained by varying the true values of the two undisplayed CP-phases in their allowed

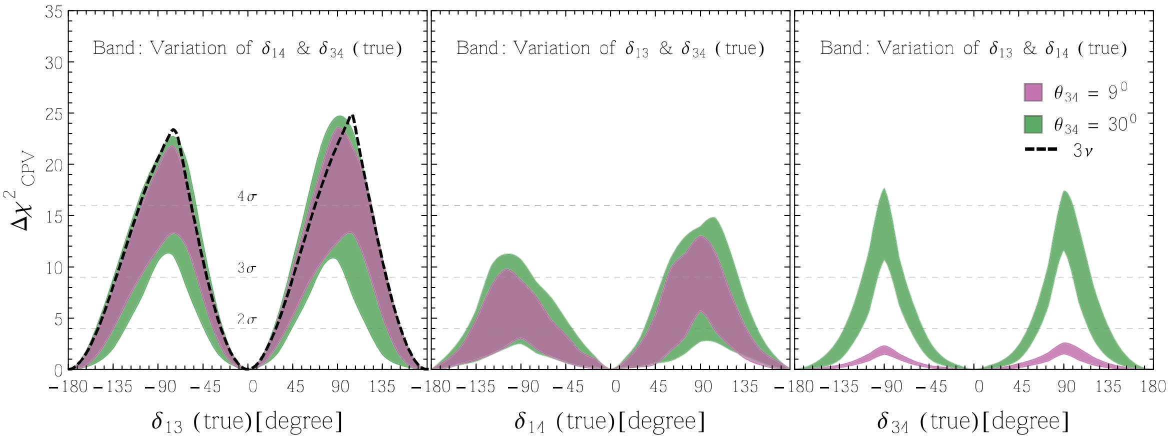

Figure 7.7: The bands displayed in the left, middle and right panels represent the discovery potential of the CPV induced, respectively, by δ_{13}, δ_{14} and δ_{34} in the 3+1 scheme. The thinner (magenta) bands correspond to the case in which all the three new mixing angles have the identical true and test value $\theta_{14} = \theta_{24} = \theta_{34} = 9^0$. The thicker (green) bands correspond to the case in which true and test $\theta_{14} = \theta_{24} = 9^0$, and true and test $\theta_{34} = 30^0$. In each panel, the bands have been obtained by varying the true values of the two undisplayed CP-phases in their allowed ranges of $[-\pi, \pi]$ in the data while marginalizing over their test values in the same range in the fit. The left panel also reports the 3-flavor curve (black dashed line) for the sake of comparison. In all cases, we marginalize over hierarchy with NH as true choice.

ranges of $[-\pi, \pi]$ in the data while marginalizing over their test values in the same range in the fit. From the comparison of the three panels, we can see that if all the three mixing angles have the same value $\theta_{14} = \theta_{24} = \theta_{34} = 9^0$ (see the magenta bands), there is a clear hierarchy in the sensitivity to the three CP-phases. The standard phase δ_{13} comes first, δ_{14} comes next, and δ_{34} is the last one, inducing a negligible amount of CPV. In particular, we see that, in the less optimistic cases, corresponding to the lower border of the bands, only the standard CP-phase δ_{13} can give rise to a signal stronger than 3σ for an appreciable fraction of the true values of the phase. This fraction decreases if θ_{34} increases (compare the red band in the left panel of Fig. 7.6 with the two bands in the left panel of Fig. 7.7). In Table 7.1, for completeness, we report such a fraction for the three values of $\theta_{34} = 0^0, 9^0$, and 30^0 as well as for the 3-flavor case. In the same table, we also report as a benchmark the "guaranteed" discovery potential for the particular value $\delta_{13} = -90^0$. Concerning the second CP-phase δ_{14} (see the middle panel), the discovery potential spans over a wide band. In favorable cases, one may observe a signal above the 3σ level. However, the lower border of the band is always below the $\sim 2\sigma$ confidence level. This implies that there is not a guaranteed discovery potential at the 3σ confidence level for such a phase. Finally, let us come to the third CP-phase δ_{34}, shown in the right panel. We see that if the mixing angle θ_{34} is very big, the sensitivity can be appreciable. Also, we note that the shape of the band is rather different from that obtained for the other two CP-phases. This different behavior can be understood by observing that in this case, the $\nu_\mu \to \nu_\mu$ disappearance channel also contributes to the sensitivity. In fact, it is well known that the ν_μ survival probability has a pronounced sensitivity to the NSI-like coupling $\varepsilon_{\mu\tau}$. From the expression of the Hamiltonian in Eq. (7.10), one can see that $\varepsilon_{\mu\tau} = rs_{24}\tilde{s}^*_{34}$, hence a sensitivity to the ν_μ survival probability to the CP-phase δ_{34} is expected[5]. In order to make this point more clear, in Fig. 7.8 we display the partial contributions to the CPV induced by δ_{34} deriving from the $\nu_\mu \to \nu_e$ channel, the $\nu_\mu \to \nu_\mu$ channel and from their combination. In this plot we have fixed the test value of θ_{23} at its true (maximal) value because the $\nu_\mu \to \nu_e$ channel, when taken alone, has a limited sensitivity to this parameter. Finally, we remark that the $\nu_\mu \to \nu_\mu$ channel has almost no role in the sensitivity to the

---

[5] It should be noted that the ν_μ survival probability depends only on the real part of the new dynamical NSI-like coupling $\text{Re}(\varepsilon_{\mu\tau}) = \text{Re}(rs_{24}\tilde{s}^*_{34}) = rs_{24}s_{34}\cos\delta_{34}$. This implies that the sensitivity to δ_{34} is attained only via terms proportional to $\cos\delta_{34}$. This feature is reflected in the particular shape of the blue band in Fig. 7.8, which is symmetrical under a reflection around $\delta_{34} = 0^0$, i.e., under the transformation $\delta_{34} \to -\delta_{34}$. It is worth noticing that while the $\cos\delta_{34}$ term does not give rise to manifest CPV, its measurement allows one to establish the existence of CPV indirectly.

other two CP-phases δ_{13} and δ_{14}, as we have explicitly verified numerically.

	θ_{34}	Nσ_{min} [δ_{13}(true) = -90^0]	CPV coverage (3σ)
3ν		4.5	50.0%
3+1	0^0	3.9	43.2%
	9^0	3.4	32.0%
	30^0	3.3	16.0%

Table 7.1: Discovery potential and coverage for the CPV induced by δ_{13} for four benchmark models in the NH case. The first column reports the scheme under consideration. The second column reports the value of θ_{34} (not relevant for the 3ν scheme). The third column reports the discovery potential (in units of standard deviations) for the particular value $\delta_{13} = -90^0$. The fourth column reports the coverage at the 3σ level. Note that in the 3+1 scheme, the figures reported in the third (fourth) columns represent the minimal "guaranteed" discovery potential (coverage) as derivable from the lower border of the corresponding band in the left panel of Figs. 7.6 and 7.7.

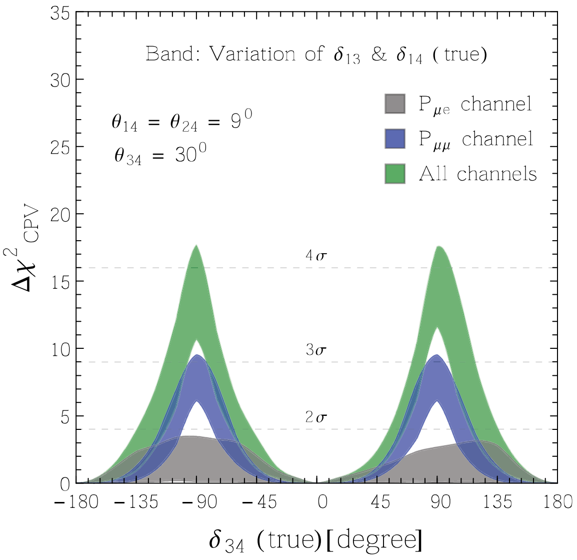

Figure 7.8: Partial contributions to the sensitivity to the CPV induced by the phase δ_{34} deriving from different channels and from their combination. The gray band is the contribution from ν_e and $\bar{\nu}_e$ appearance, the blue band refers to the ν_μ and $\bar{\nu}_\mu$ disappearance, and the green band is the global sensitivity obtained including all channels. The three new mixing angles have been fixed to $\theta_{14} = \theta_{24} = 9^0$ and $\theta_{34} = 30^0$. The mixing angle θ_{23} has been fixed to be maximal (both true and test value). We marginalize over hierarchy with NH as true choice.

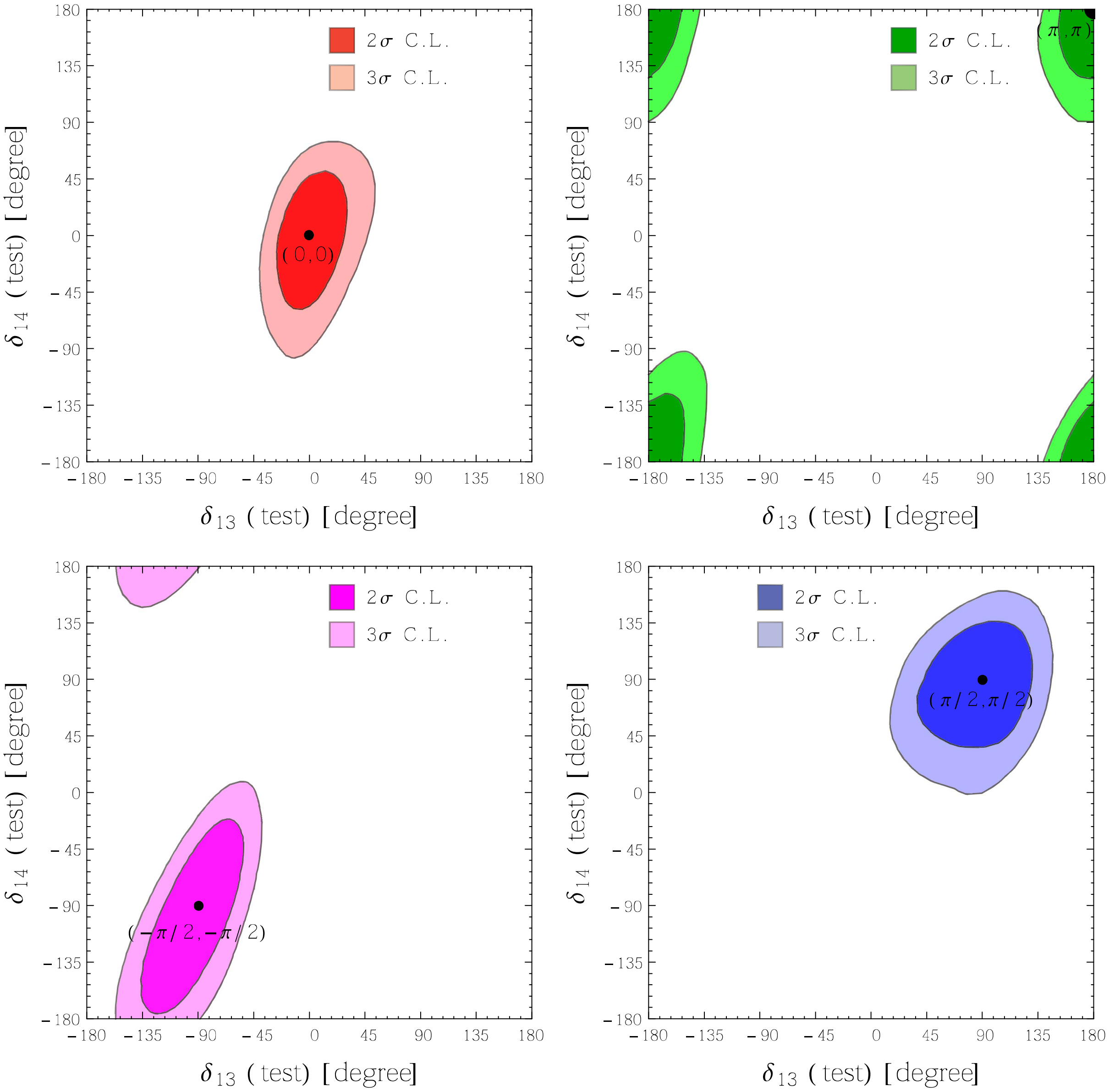

Figure 7.9: Reconstructed regions for the two CP-phases δ_{13} and δ_{14} for the four choices of their true values indicated in each panel. The NH is taken as the true hierarchy, while we have marginalized over the two possible hierarchies in the test model. The contours refer to 2σ and 3σ levels. We have fixed the values θ_{34} (true) = 0^0.

7.4.2 Reconstruction of the CP-phases

In the previous subsection, we have focused our attention on the discovery potential of the CPV arising from the three CP-phases involved in the 3+1 scheme. However, we deem it important to pursue the exploration of the CP-phases independently of the amount of CPV (if any) that they may generate. In principle, any value of the CP-phases is plausible, including the CP-conserving cases. According to this point of view, one should try to

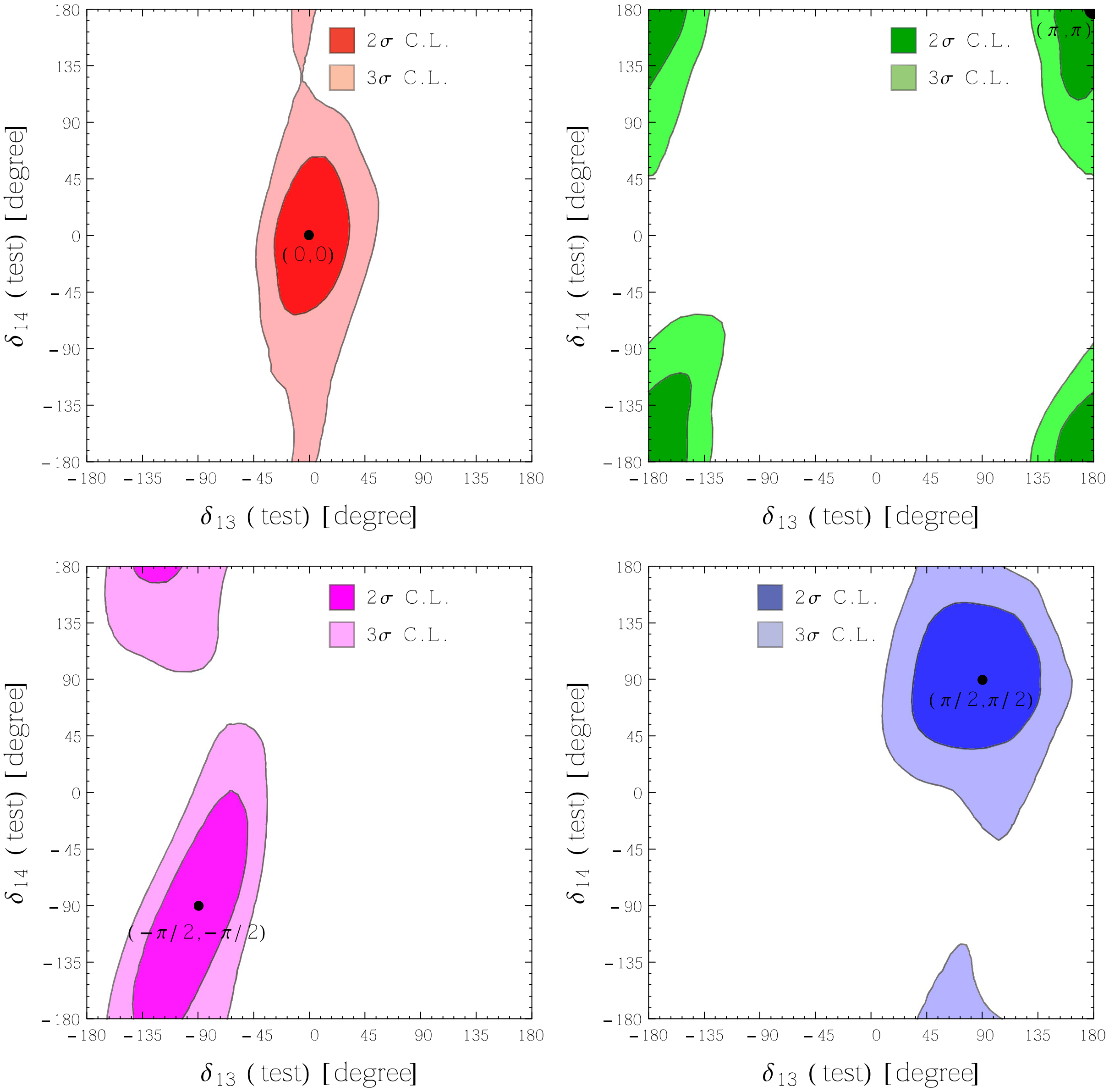

Figure 7.10: Reconstructed regions for the two CP-phases δ_{13} and δ_{14} for the four choices of their true values indicated in each panel. The NH is taken as the true hierarchy, while we have marginalized over the two possible hierarchies in the test model. The contours refer to 2σ and 3σ confidence levels. We have fixed θ_{34} (true) = 30^0, and have marginalized over δ_{34} (both true and test values) over its range of variability.

answer the following question: what is the capability of reconstructing the true values of the CP-phases. In the following, we address this issue, confining our study to the two CP-phases δ_{13} and δ_{14}, to which one expects to have a more pronounced sensitivity.

In Fig. 7.9, we have performed this exercise under the assumption that true and test values of $\theta_{34} = 0$, and therefore, the third CP-phase δ_{34} becomes irrelevant. In each panel, we show the regions reconstructed around the representative true values of δ_{13} and δ_{14}. In all cases, we have taken the NH as the true hierarchy in the data, and then marginalized over both NH and IH in theory. However, we find that the marginalization procedure never selects the wrong hierarchy. Hence, there is no degeneracy between mass hierarchy and the CP-phases. Similar results (not shown) are obtained for the IH case. The two upper panels refer to two representative CP-conserving scenarios $[0,0]$ and $[\pi,\pi]$. The third and fourth panels refer to two representative CP-violating cases $[-\pi/2,-\pi/2]$ and $[\pi/2,\pi/2]$. The two confidence levels correspond to 2σ and 3σ (1 d.o.f.). We see that in all cases we obtain a unique reconstructed region at the 3σ level[6]. The typical 1σ level uncertainty on the reconstructed CP-phases is approximately 20^0 (30^0) for δ_{13} (δ_{14}). The regions in Fig. 7.9 should be compared with the analogous ones obtained with the combination of the prospective data of T2K and NOνA (see Fig. 13 in [215]). From such a comparison, one can see that DUNE is much more effective in the reconstruction of the CP-phases. In fact, in the combination of T2K and NOνA, a good reconstruction is possible only at the 1σ confidence level, and in favorable cases, at the 2σ level. At higher confidence levels, the reconstruction capability basically disappears. In DUNE, the situation is much improved. This is imputable both to the higher statistics and to the spectral shape information attainable from the wide-band neutrino flux.

We close our discussion on the CP-phases by showing the impact of θ_{34} and of the ignorance of the related CP-phase δ_{34} on the reconstruction of the two CP-phases δ_{13} and δ_{14}. Figure 7.10 is analogous to Fig. 7.9, but now, we assume $\theta_{34} = 30^0$ both in data and in theory. In this case, the transition probability depends also on the third CP-phase δ_{34}. Since it is unknown, one has to marginalize over the true and test values of this CP-phase while reconstructing the other two phases. As evident from all panels of Fig. 7.10, the quality of the reconstruction deteriorates. In particular, the uncertainty on δ_{14} increases roughly by two times (from $\sim 30^0$ to $\sim 60^0$), while that on δ_{13} remains basically unchanged (still around $\sim 25^0$). Hence, the reconstruction of the standard CP-phase δ_{13} is more robust than that of new CP-phase δ_{14} with respect to the perturbations induced by a large value of the mixing angle θ_{34}. This behavior can be traced to the fact that, differently from δ_{13}, the two new CP-phases δ_{14} and δ_{34} both enter at the dynamical level [see Eqs. (7.10-7.11)], and in particular, in the NSI-like matrix element $\varepsilon_{e\tau} \propto \tilde{s}_{14}\tilde{s}^*_{34}$. Therefore, one may expect a certain degree of degeneracy among the two new CP-phases,

---

[6] Note that this is true also in the second panel, because the four corners of the square form a connected region due to the cyclic nature of the two CP-phases.

which in the marginalization process over the undisplayed CP-phase δ_{34}, translates into a deterioration in the reconstruction of δ_{14}.

7.5 Summary

In this chapter we have investigated the impact of one light eV-scale sterile neutrino on the prospective data expected to be collected at the planned long-baseline experiment DUNE. In section 7.1, we discuss the details of theoretical framework of vacuum and matter oscillation probability in 3+1 scheme which gives us a very good analytical understanding to explain the numerical simulations. After discussing the statistical method in section 7.2 we have discussed the bi-probability and bi-event plots in section 7.3.1. From figure 7.3 we see that for large value of θ_{34} there is an overlap between the two blobs which creates a clear degeneracy between NH and IH. However this type of degeneracy can be lifted easily using the broad band nature of the DUNE spectrum which is clearly visible in fig. 7.4 in section 7.3.2. In section 7.3.3 we have presented the numerical results concerning the neutrino mass hierarchy. We have found that the discovery potential of the neutrino mass hierarchy (MH) remains above 5σ confidence level if all the three new mixing angles are relatively small ($\theta_{14} = \theta_{24} = \theta_{34} = 9^0$). In contrast, if the third mixing angle θ_{34} is taken at its upper limit ($\theta_{34} = 30^0$), the MH sensitivity can drop to 4σ confidence level. Our analysis has clearly shown that the spectral information attainable from the wide-band spectrum employed by DUNE is crucial to preserve a good sensitivity to the MH also in the 3+1 scheme.

In section 7.4.1, we have also assessed the sensitivity to the CPV induced both by the standard CP-phase $\delta_{13} \equiv \delta_{\rm CP}$, and by the new CP-phases (δ_{14} and δ_{34} in our parameterization). We have found that the performance of DUNE in claiming the discovery of CPV induced by δ_{13} gets deteriorated as compared to the 3-flavor case. In particular, the maximal sensitivity (reached around $\delta_{13} \sim \pm 90^0$) decreases from 5σ to 4σ confidence level if all the three new mixing angles are small ($\theta_{14} = \theta_{24} = \theta_{34} = 9^0$), and can drop almost to 3σ confidence level if $\theta_{34} = 30^0$. The sensitivity to the CPV induced by the new CP-phase δ_{14} can reach 3σ C.L. for an appreciable fraction of its true values, but never reaches 4σ confidence level. The sensitivity to the third CP-phase δ_{34}, which arises exclusively through matter effects, is appreciable only if θ_{34} is large. Interestingly, we have found that the sensitivity to δ_{34} stems from both the ν_e appearance and ν_μ disappearance channels.

In section 7.4.2, we have finally investigated the capability of DUNE in reconstructing the true values of the two CP-phases δ_{13} and δ_{14}. The typical 1σ level uncertainty on the reconstructed CP-phase δ_{13} (δ_{14}) is approximately 20^0 (30^0) provided $\theta_{34} = 0$. But, in case of large θ_{34}, the reconstruction of δ_{14} (but not that of δ_{13}) becomes poor. So, finally, we can conclude that the results presented in this chapter clearly demonstrates that in the presence of a light eV-scale sterile neutrino, the proposed LBL experiments such as DUNE would be quite sensitive to the new CP-phases associated to the sterile state, and therefore, would play a complementary role to the SBL experiments.

Chapter 8

Octant of θ_{23} in danger with a light sterile neutrino

Present global fits [22, 23, 24, 25] of world neutrino data and also the recent result from the running LBL experiment NOνA [26] hint towards non-maximal θ_{23} with two nearly degenerate solutions, one in the lower octant ($\theta_{23} < \pi/4$), and the other in the higher octant ($\theta_{23} > \pi/4$). This octant ambiguity of θ_{23} is one of the fundamental issues in the neutrino sector, and its resolution is a crucial goal of next-generation long-baseline (LBL) experiments. In this chapter, we address the impact of a light eV-scale sterile neutrino towards such a measurement, taking the Deep Underground Neutrino Experiment (DUNE) as a case study. In the so-called 3+1 scheme involving three active and one sterile neutrinos, the $\nu_\mu \to \nu_e$ transition probability probed in the LBL experiments acquires a new interference term via active-sterile oscillations. We find that this interference term can mimic a swap of the θ_{23} octant, even if one uses the information from both neutrino and antineutrino channels. As a consequence, for unfavorable combinations of the CP-phases in the 4-flavor scheme, the sensitivity to the octant of θ_{23} can be completely lost, and this may have serious implications for our understanding of neutrinos from both the experimental and theoretical perspectives. The details of all the analyses and the respective results have been discussed in the next few sections.

This chapter is structured as follows. In section 8.1, we start our discussion with the details of theoretical framework for understanding the octant issue in 3-flavor as well as in 4-flavor framework. In section 8.2, we then present all the numerical results. There we first discuss the bi-events plot and then present the octant sensitivity plots in certain confidence levels. Finally in section 8.3, we summarize all our results.

8.1 Theoretical framework

As discussed in section 2.4.1, following [156], the 3-flavor $\nu_\mu \to \nu_e$ appearance and $\nu_\mu \to \nu_\mu$ survival probability expressions in vacuum upto second order in α and $\sin\theta_{13}$ can be written as,

$$\begin{aligned} P(\nu_\mu \to \nu_e) &= \alpha^2 \sin^2 2\theta_{12}\, c_{23}^2 \Delta^2 + 4 s_{13}^2 s_{23}^2 \sin^2\Delta \\ &\quad + 2 s_{13} \sin 2\theta_{12} \sin 2\theta_{12}\, (\alpha\Delta) \sin\Delta \cos(\Delta + \delta_{\rm CP})\,. \qquad (8.1) \\ P(\nu_\mu \to \nu_\mu) &= 1 - \sin^2 2\theta_{23} \sin^2\Delta + (\alpha\Delta)\, c_{12}^2 \sin^2 2\theta_{23} \sin 2\Delta \\ &\quad + \alpha^2\Delta^2 \left[\sin^2 2\theta_{12}\, c_{23}^2 + c_{12}^2 \sin^2 2\theta_{23} \left(\cos 2\Delta - s_{12}^2\right)\right] \\ &\quad + 4 s_{13}^2 s_{23}^2 \cos 2\theta_{23} \sin^2\Delta - 2\,(\alpha\Delta)\, s_{13} \sin 2\theta_{12}\, s_{23}^2 \sin 2\theta_{23} \cos\delta_{\rm CP} \sin 2\Delta. \qquad (8.2) \end{aligned}$$

Where, $\alpha = \frac{\Delta m_{21}^2}{\Delta m_{31}^2}$ and $\Delta = \frac{\Delta m_{31}^2 L}{4E}$.

For the time being, let us assume a very simplified case where the survival probability can be written as,

$$P(\nu_\mu \to \nu_\mu) \simeq 1 - \sin^2 2\theta_{23} \sin^2\Delta. \qquad (8.3)$$

From this expression it is clear that,

$$P_{\mu\mu}(\theta_{23}) = P_{\mu\mu}(\pi/2 - \theta_{23}). \qquad (8.4)$$

So there exists two solutions, one is $< 45^0$, known as lower octant (LO), and other one is $> 45^0$, known as higher octant (HO). This is known as “octant degeneracy” or sometime “octant ambiguity”.

Let us now concentrate on the appearance probability in Eq. 8.1, where we see that

$$P_{\mu e} \propto \sin^2\theta_{23}, \text{ but not } \propto \sin^2 2\theta_{23}. \qquad (8.5)$$

That is even in most simplified case,

$$P_{\mu e}(\theta_{23}) \neq P_{\mu e}(\pi/2-\theta_{23}). \tag{8.6}$$

So to distinguish between the two octants we must need to add the information coming from the appearance channel. However in principle the appearance channel is enough to discriminate between the two octants but due to small statistics in this channel in LBL experiments, we also need the information coming from disappearance channel as it provides huge statistics which actually help to get good sensitivity to resolve the octant ambiguity. As a result both the channels play complementary role with each other. Below, we describe the more details about the octant issue in 3+1 scheme.

Following the discussions pursued in the previous chapters, we already know that in the 3+1 scheme, a fourth mass eigenstate ν_4 is introduced and the mixing is described by a 4×4 matrix

$$U = \tilde{R}_{34}R_{24}\tilde{R}_{14}R_{23}\tilde{R}_{13}R_{12}\,, \tag{8.7}$$

where R_{ij} ($\tilde{R}_{ij}$) is a real (complex) rotation in the (i,j) plane.

Let us now come to the transition probability relevant for the LBL experiment DUNE. Matter effects have a sizable impact in DUNE, and confer a high sensitivity to the MH. However, for simplicity, we neglect them in the considerations below, because they are basically irrelevant for the physical process that we want to highlight. We stress that in the numerical simulations we properly include the matter effects assuming a line-averaged constant density of 2.87 g/cm^3 based on the PREM profile of Earth crust. In section 2.6.1, we have already discussed that the $\nu_\mu \to \nu_e$ conversion probability in presence of a sterile neutrino can be approximately written as the sum of three contributions

$$P^{4\nu}_{\mu e} \simeq P^{\rm ATM} + P^{\rm INT}_{\rm I} + P^{\rm INT}_{\rm II}\,. \tag{8.8}$$

which in vacuum take the form

$$\begin{aligned}
P^{\rm ATM} &\simeq 4s_{23}^2 s_{13}^2 \sin^2\Delta\,, && (8.9)\\
P^{\rm INT}_{\rm I} &\simeq 8s_{13}s_{12}c_{12}s_{23}c_{23}(\alpha\Delta)\sin\Delta\cos(\Delta\pm\delta_{13})\,, && (8.10)\\
P^{\rm INT}_{\rm II} &\simeq 4s_{14}s_{24}s_{13}s_{23}\sin\Delta\sin(\Delta\pm\delta_{13}\mp\delta_{14})\,, && (8.11)
\end{aligned}$$

where $\Delta \equiv \Delta m^2_{31} L/4E$ is the atmospheric oscillating frequency depending on the baseline L and the neutrino energy E, and $\alpha \equiv \Delta m^2_{21}/\Delta m^2_{31}$. The double sign in front of the CP-phases reflects the fact that it is opposite for neutrinos (upper sign) and antineutrinos (lower sign). The first term P^{ATM}, which is positive definite and independent of the CP-phases, gives the leading contribution to the probability. The term $P^{\mathrm{INT}}_{\mathrm{I}}$ is related to the interference of the oscillations driven by the solar and atmospheric frequencies. This term, apart from higher order corrections, coincides with the standard interference term, which renders the 3-flavor transition probability sensitive to the CP-phase $\delta_{\mathrm{CP}} \equiv \delta_{13}$. The term $P^{\mathrm{INT}}_{\mathrm{II}}$ is a genuine 4-flavor effect, and is driven by the interference between the atmospheric frequency and the large frequency related to the new mass eigenstate [104]. This term does not manifest an explicit dependency on $\Delta m^2_{41} \equiv m^2_4 - m^2_1$ because the related oscillations are very fast and get averaged out by the finite energy resolution of the detector. We now observe that, as can be inferred from the latest 3-flavor global analyses [22, 23, 262] and from the global 3+1 fits [105, 106], the three small mixing angles have similar size $s_{13} \sim s_{14} \sim s_{24} \simeq 0.15$, and therefore they can all be assumed of the same order ε, while the ratio $\alpha \simeq \pm 0.03$ is of order ε^2. This implies that

$$P_0 \sim \varepsilon^2\,, \qquad P_1 \sim \varepsilon^3\,, \qquad P_2 \sim \varepsilon^3\,. \tag{8.12}$$

Now let us come to the θ_{23} octant issue. In general, we can re-express the atmospheric mixing angle as

$$\theta_{23} = \frac{\pi}{4} \pm \eta\,. \tag{8.13}$$

where η is a positive-definite angle and the positive (negative) sign corresponds to HO (LO). The current 3-flavor global fits [22, 23, 262] suggest that θ_{23} can deviate by no more than $\sim 6^0$ from maximal mixing. Equivalently, $\sin^2\theta_{23}$ must lie in the range $\sim [0.4, 0.6]$. This implies that η is confined to relatively small values ($\eta \lesssim 0.1$), and can be considered of the same order of magnitude (ε) of s_{13}, s_{14} and s_{24}. Therefore, it is legitimate to use the expansion

$$s^2_{23} = \frac{1}{2}(1 \pm \sin 2\eta\,) \simeq \frac{1}{2} \pm \eta\,. \tag{8.14}$$

An experiment can be sensitive to the octant if, despite the freedom introduced by the unknown CP-phases, there is still a difference between the probabilities in the two octants, i.e.

$$\Delta P \equiv P^{\rm HO}_{\mu e}(\delta^{\rm HO}_{13}, \delta^{\rm HO}_{14}) - P^{\rm LO}_{\mu e}(\delta^{\rm LO}_{13}, \delta^{\rm LO}_{14}) \neq 0\,. \tag{8.15}$$

In Eq. (8.15) we must think to one of the two octants as the true choice (used to simulate data) and the other one as the test parameter (used to simulate the theoretical model). For example, if for definiteness we fix the LO as the true choice, then for a given combination of $(\delta^{\rm LO}_{13}, \delta^{\rm LO}_{14})$ there can be sensitivity to the octant if $\Delta P \neq 0$ in the hypothesis that $(\delta^{\rm HO}_{13}, \delta^{\rm HO}_{14})$ are both unknown and free to vary in the range $[-\pi, \pi]$. According to Eq. (8.8), we can split ΔP in the sum of three terms

$$\Delta P = \Delta P_0 + \Delta P_1 + \Delta P_2\,. \tag{8.16}$$

The first term is positive-definite, does not depend on the CP-phases and is given by

$$\Delta P_0 \simeq 8\eta s^2_{13} \sin^2\Delta\,. \tag{8.17}$$

The second and third terms depend on the CP-phases and can have both positive or negative values. Their expressions are given by

$$\begin{aligned} \Delta P_1 &= A\big[\cos(\Delta \pm \phi^{\rm HO}) - \cos(\Delta \pm \phi^{\rm LO})\big]\,, && (8.18)\\ \Delta P_2 &= B\big[\sin(\Delta \pm \psi^{\rm HO}) - \sin(\Delta \pm \psi^{\rm LO})\big]\,, && (8.19) \end{aligned}$$

where for compactness, we have introduced the amplitudes[1]

$$\begin{aligned} A &= 4 s_{13} s_{12} c_{12} (\alpha\Delta) \sin\Delta\,, && (8.20)\\ B &= 2\sqrt{2} s_{14} s_{24} s_{13} \sin\Delta\,, && (8.21) \end{aligned}$$

---

[1] In the expressions of A and B we are neglecting terms proportional to powers of η, which would give rise to negligible (at least fourth order in ε) corrections.

and the auxiliary CP-phases

$$\phi = \delta_{13}\,, \tag{8.22}$$

$$\psi = \delta_{13} - \delta_{14}\,, \tag{8.23}$$

with the appropriate superscripts (LO or HO). If we adopt as a benchmark value $\sin^2\theta_{23} = 0.42\,(0.58)$ for LO (HO), i.e. $\eta = 0.08$, at the first oscillation maximum ($\Delta = \pi/2$), we have

$$\Delta P_0 \simeq 0.014\,, \quad |A| \simeq 0.013\,, \quad |B| \simeq 0.010\,. \tag{8.24}$$

These numbers give a feeling of the (similar) size of the three terms involved in Eq. (8.16). It is clear that an experiment can be sensitive to the octant only if the positive-definite difference ΔP_0 cannot be completely compensated by a negative contribution coming from the sum of ΔP_1 and ΔP_2.

Now, we recall what happens in the 3-flavor framework, when the last term ΔP_2 in Eq. (8.16) is absent. In this case, if one considers only the neutrino channel there are unfavorable combinations of the two CP-phases $\delta_{13}^{\rm LO}$ and $\delta_{13}^{\rm HO}$ for which $\Delta P = 0$ and there is no sensitivity to the octant. On the other hand, as recently recognized in [58, 59], the octant-δ_{13} degeneracy can be lifted if one exploits also the antineutrino channel. This fact can be understood from Fig. 8.1, which represents the bi-event plot for the DUNE experiment. In such a plot, the ellipses refer to the 3-flavor case, while the colored blobs represent the 3+1 scheme. We take $\sin^2\theta_{23} = 0.42\,(0.58)$ as a benchmark value for the LO (HO) octant. First, we notice that in DUNE the MH is not an issue because there is a clear separation between NH and IH, which is basically guaranteed by the presence of matter effects[2]. So we can fix the attention on one of the two hierarchies, for example the NH. We observe, that the (black) ellipse corresponding to the LO is well separated from the (yellow) HO ellipse. This separation is a synergistic effect of the fact that we are considering *both* neutrino and antineutrino events. Finally, let us come to the 3+1 scheme. In this case the third term in Eq. (8.16) is active. It depends on the additional CP-phase δ_{14}, so its sign can been chosen independently of that of the second term. This circum-

---

[2] The small overlap between NH and IH blobs in Fig. 8.1 for the LO case can be removed using the spectral information available in DUNE (see [216]).

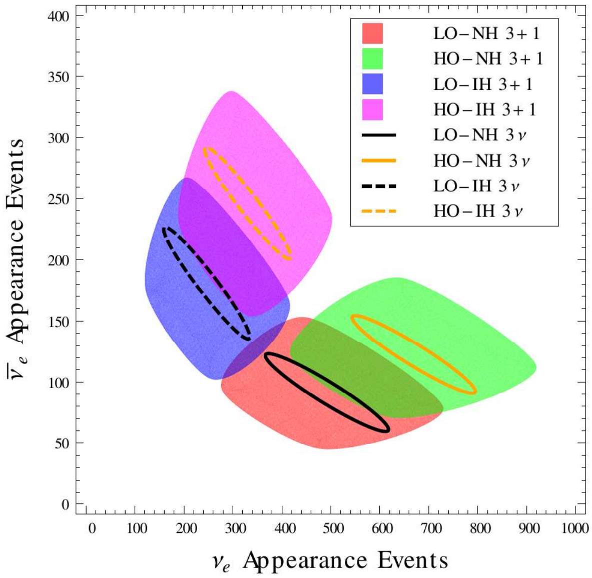

Figure 8.1: Bi-event plot corresponding to the DUNE setup. The ellipses represent the 3-flavor case, while the colored blobs correspond to the 3+1 scheme (see the legend). We take $\sin^2\theta_{23} = 0.42\,(0.58)$ as benchmark value for the LO (HO). In the 3-flavor ellipses, the running parameter is δ_{13} varying in the range $[-\pi,\pi]$. In the 4-flavor blobs there are two running parameters, δ_{13} and δ_{14}, both varying in their allowed ranges $[-\pi,\pi]$. In the 3+1 case we have assumed $\theta_{34} = 0^0$.

stance gives more freedom in the 3+1 scheme and there is more space for degeneracy. The bi-event plot in Fig. 8.1 confirms such a basic expectation. The graph now becomes a blob, which can be seen as a convolution of an ensemble of ellipses (see [215, 216]), and the separation between LO and HO is lost even if one considers both neutrino and antineutrino events.

8.2 Numerical results

In our simulations, we use the GLoBES software [219, 220]. For DUNE, we consider a total exposure of 248 kt · MW · year, shared equally between neutrino and antineutrino modes. For the details of the DUNE setup, and of the statistical analysis, we follow the discussion in section 5.1 and 5.2. The best fit values of all the relevant oscillation parameters have been taken from Table 4.3. Figure 8.2 displays the discovery potential for identifying the true octant as a function of true δ_{13}. The left (right) panel refers to the true choice LO-NH (HO-NH). In both panels, for comparison, we show the results for the 3-flavor case (represented by the black curve). Concerning the 3+1 scheme, we draw the curves corresponding to four representative values of true δ_{14} $(0^0, 180^0, -90^0, 90^0)$. In the 3ν case we marginalize over mass hierarchy (MH), $(\sin^2\theta_{23}, \delta_{13})$ (test) with the restriction that θ_{23}(test) lies in opposite octant with respect to the true choice of the octant of θ_{23}. In the 3+1 scheme, we fix $\theta_{14} = \theta_{24} = 9^0$ and $\theta_{34} = 0$, and we marginalize over $(\theta_{23}, \delta_{13}, \delta_{14})$ (test). In 3+1 case also we marginalize over the MH. However, we have checked that the minimum of $\Delta\chi^2$ is never reached in the wrong hierarchy. This confirms that MH is not a source of degeneracy in the determination of the octant.

The 3-flavor curves have been already discussed in the literature (see for example [18, 58, 115]). Nonetheless, we deem it useful to make the following remarks: i) a good θ_{23} octant sensitivity for all values of δ_{13} (true) can be achieved with equal neutrino and antineutrino runs [58], ii) the spectral information plays an important role in distinguishing between the two octants for unfavorable choices of true hierarchy and δ_{13}, and iii) always the sensitivity is higher for LO compared to HO irrespective of the hierarchy choice. For the first time, during this work, we realized that this last issue of asymmetric sensitivity between LO and HO is related to a synergistic effect of the $\nu_\mu \to \nu_\mu$ and $\nu_\mu \to \nu_e$ channels. Basically, the $\nu_\mu \to \nu_\mu$ channel fixes the test value of θ_{23} in the octant opposite to its true value. However, such a test value is not exactly equal to its octant symmetric choice (i.e., $\theta_{23}^{\text{test}} \neq \pi/2 - \theta_{23}^{\text{true}}$). This happens because the $\nu_\mu \to \nu_\mu$ survival probability contains higher order octant-sensitive terms, which can been probed in high-statistics experiments like DUNE. We find that these corrections always go in the direction of increasing (decreasing) the difference $|\sin^2\theta_{23}^{\text{test}} - \sin^2\theta_{23}^{\text{true}}|$ by $\sim 15\%$ with respect to its default value $|0.58 - 0.42| = 0.16$ in the LO (HO) case. Since the leading term of the $\nu_\mu \to \nu_e$ appearance channel is sensitive to this difference, the performance is enhanced (suppressed) in the LO (HO) case.

Fig. 8.2 shows that in the 3+1 scheme there exist unfavorable combinations of δ_{13} (true) and δ_{14} (true) for which the octant sensitivity falls below the 2σ level. We have verified that for such combinations the spectra corresponding to the two octants are almost indistinguishable both for neutrinos and antineutrinos. Therefore, even a broad-band experiment such as DUNE cannot break the degeneracy introduced by a sterile neutrino.

So far, we have considered two true values of $\sin^2\theta_{23} = 0.42$ (LO) and 0.58 (HO) (see Fig. 8.2). However, it is interesting to ask how things change if different choices are made

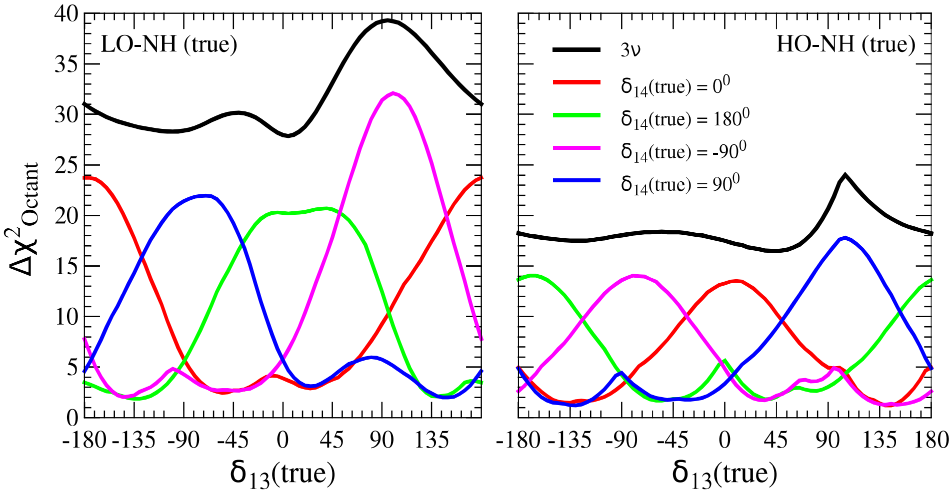

Figure 8.2: Discovery potential for excluding the wrong octant as a function of true δ_{13} assuming LO-NH (left panel) and HO-NH (right panel) as the true choice. We take $\sin^2\theta_{23} = 0.42\,(0.58)$ as benchmark value for the LO (HO). In each panel, we present the results for the 3-flavor case (black line), and for the 3+1 scheme considering four different values of true δ_{14} (colored lines). In the 3ν case, we marginalize away $(\theta_{23}, \delta_{13})$ (test). In the 3+1 scheme, we fix $\theta_{14} = \theta_{24} = 9^0$, $\theta_{34} = 0$, and marginalize over $(\theta_{23}, \delta_{13}, \delta_{14})$ (test).

for the true value of θ_{23}. Figure 8.3 answers this question. It represents the discovery potential for identifying the true octant in the plane $[\sin^2\theta_{23}, \delta_{13}]$ (true) assuming NH as true choice. The left (right) panel corresponds to the 3ν (3+1) scheme. In the 3+1 case we marginalize away also the CP-phase δ_{14} (true) (in addition to all the test parameters) since it is unknown. Hence, the outcome of this procedure determines the minimal guaranteed sensitivity, i.e. the one corresponding to the worst case scenario. The solid blue, dashed magenta, and dotted black curves correspond, respectively, to 2σ, 3σ and 4σ confidence levels (1 d.o.f.). The comparison of the two panels gives a bird-eye view of the situation. It is clear that, in the 3+1 scheme, no minimal sensitivity is guaranteed in the entire plane. We have checked that similar conclusions are valid also in the case of IH as true MH.

Note added

It is important to mention that, the IceCube [166], Daya Bay [164], and MINOS [167] Collaborations reported new constraints on active-sterile mixing which is slightly different from the constraints used to produce the above results in this chapter. The new upper

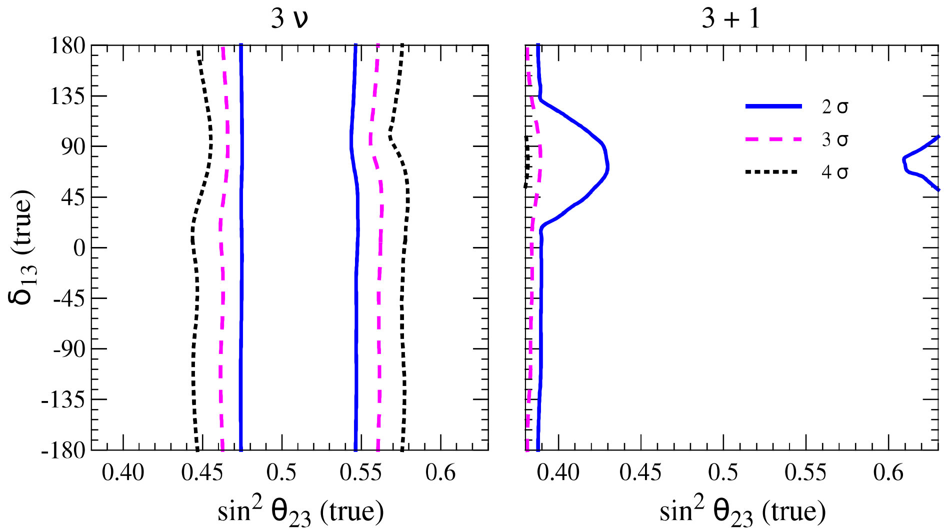

Figure 8.3: Discovery potential for excluding the wrong octant in $(\sin^2\theta_{23}, \delta_{13})$ (true) plane assuming NH as true choice. The left (right) panel corresponds to the 3ν (3+1) case. In the 3-flavor case, we marginalize away $(\theta_{23}, \delta_{13})$ (test). In the 3+1 case, in addition, we marginalize over δ_{14} (true) and δ_{14} (test) fixing $\theta_{14} = \theta_{24} = 9^0$ and $\theta_{34} = 0$. The solid blue, dashed magenta, and dotted black curves correspond, respectively, to the 2σ, 3σ, and 4σ confidence levels (1 d.o.f.).

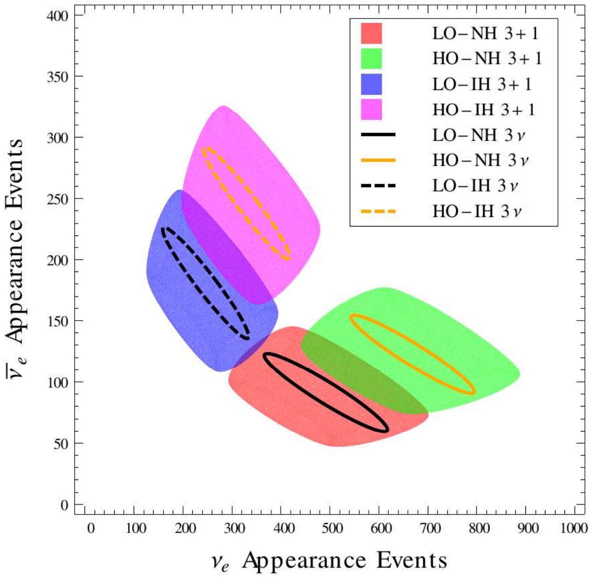

Figure 8.4: Bi-event plot corresponding to the DUNE setup. The ellipses represent the 3-flavor case, while the colored blobs correspond to the 3+1 scheme (see the legend). Every other details are same as Fig. 8.1 except the fact that here we have considered $\theta_{14} = 7^0$, $\theta_{24} = 9^0$, $\theta_{34} = 0$ in the 3+1 case.

limit from the IceCube Collaboration [166] on $\sin^2 2\theta_{24}$ around the current best-fit Δm^2_{41} $\simeq 1.75$ eV^2 [203] is $\simeq 0.2$ at 99% confidence level, which means that θ_{24} is constrained to

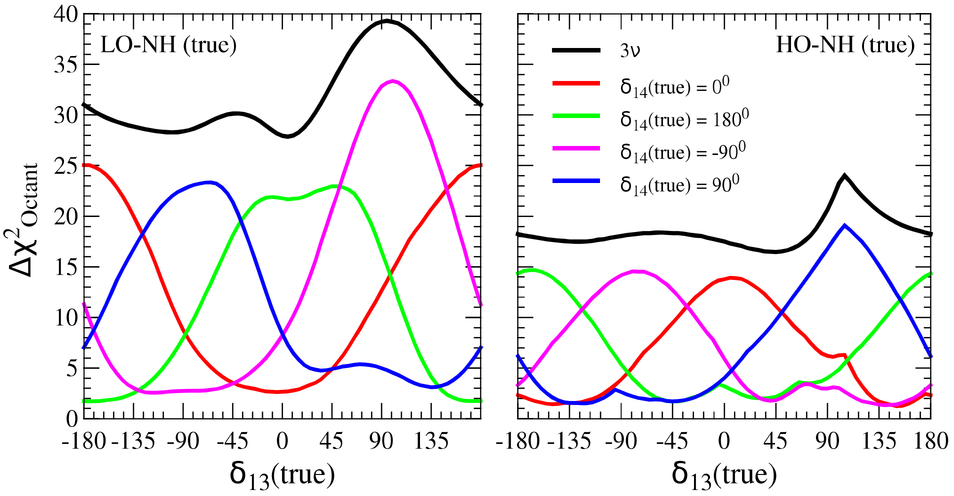

Figure 8.5: Discovery potential for excluding the wrong octant as a function of true δ_{13} assuming LO-NH (left panel) and HO-NH (right panel) as the true choice. Every other details are same as Fig. 8.2 except the fact that we fix here $\theta_{14} = 7^0$, $\theta_{24} = 9^0$, $\theta_{34} = 0$, and marginalize over $(\theta_{23}, \delta_{13}, \delta_{14})$ (test).

be smaller than 13° or so. The MINOS Collaboration placed a new upper limit of $\simeq 0.03$ on $\sin^2\theta_{24}$ around $\Delta m^2_{41} \simeq 1.75$ eV^2 at 90% C.L. [165, 167] suggesting that the upper limit on θ_{24} is around 10°. Therefore, the benchmark value $\theta_{24} = 9°$ which we have considered in our work is compatible with these new limits. The combined analysis of the Daya Bay and Bugey-3 data provides a new constraint [165] on $\sin^2 2\theta_{14}$ which is $\simeq 0.06$ at 90% confidence level around $\Delta m^2_{41} \simeq 1.75$ eV^2. This implies that θ_{14} is smaller than 7° or so, which is pretty close to the benchmark value of $\theta_{14} = 9°$ that we have considered in our analysis. However for completeness, we show here two new figures Fig. 8.4 and Fig. 8.5 as similar to the figures Fig. 8.1 and Fig. 8.2 respectively. We see that our results remain almost unaltered even if we take $\theta_{14} = 7°$ and $\theta_{24} = 9°$ instead of our benchmark choice of $\theta_{14} = \theta_{24} = 9°$. Hence, we can safely conclude that the sensitivity towards the octant of θ_{23} can be completely lost even in light of the new constraints on the active-sterile mixing that were reported recently.

8.3 Summary

In this chapter, we have addressed for the first time the impact of a light eV-scale sterile neutrino in identifying the octant of the mixing angle θ_{23} at the next generation LBL experiment DUNE. We have shown that in the 3+1 scheme, the new recently identified interference term [104] that enters the $\nu_\mu \to \nu_e$ transition probability can perfectly mimic a swap of the θ_{23} octant, even when we use the information from both the neutrino and antineutrino channels. As a consequence, the sensitivity to the octant of θ_{23} can be completely lost in the presence of active-sterile oscillations. It remains to be seen if other kinds of experiments, in particular those using atmospheric neutrinos, can lift or at least alleviate the degeneracy that we have found in the context of LBL experiments. Our educated guess is that this would prove to be very difficult since obtaining a satisfying θ_{23} octant sensitivity with atmospheric neutrinos is a very hard task already in the 3-flavor framework, and in the enlarged 3+1 scheme, the situation should naturally worsen.

Chapter 9

Exploring Flavor-Dependent Long-Range Forces in Long-Baseline Neutrino Oscillation Experiments

The Standard Model gauge group can be extended with minimal matter content by introducing anomaly free $U(1)$ symmetry, such as $L_e - L_\mu$ or $L_e - L_\tau$. If the neutral gauge boson corresponding to this abelian symmetry is ultra-light, then it will give rise to flavor-dependent long-range leptonic force, which can have significant impact on neutrino oscillations. For an instance, the electrons inside the Sun can generate a flavor-dependent long-range potential at the Earth surface, which can suppress the $\nu_\mu \to \nu_e$ appearance probability in terrestrial experiments. The sign of this potential is opposite for antineutrinos, and affects the oscillations of (anti-)neutrinos in different fashion. This feature invokes fake CP-asymmetry like the SM matter effect and can severely affect the leptonic CP-violation searches in long-baseline experiments. In this chapter, we study in detail the possible impacts of these long-range flavor-diagonal neutral current interactions due to $L_e - L_\mu$ symmetry on the CP-violation discovery as well as on the mass hierarchy determination, taking DUNE and LBNO as two potential LBL experiments. We also ask a legitimate question that if there is no signal received in these experiments then would these experiments be able to give a stringent bound on this new physics coupling parameter. In this regard, we find that DUNE (LBNO) can place stringent constraint on the effective gauge coupling $\alpha_{e\mu} < 1.9 \times 10^{-53}$ (7.8×10^{-54}) at 90% C.L., which is almost

30 (70) times better than the existing bound from the Super-Kamiokande experiment. We also observe that if $\alpha_{e\mu} \geq 2 \times 10^{-52}$, the CP-violation discovery reach of these future facilities vanishes completely. The mass hierarchy measurement remains robust in DUNE (LBNO) if $\alpha_{e\mu} < 5 \times 10^{-52}$ (10^{-52}). The details of all the analysis and the respective results have been discussed in the next few sections.

This chapter is organized as follows. We start section 9.1 with a discussion on flavor-dependent LRF and how it arises from abelian gauged $L_e - L_{\mu,\tau}$ symmetry. Then, we discuss the strength of the long-range potential $V_{e\mu/e\tau}$ at the Earth surface generated by the electrons inside the Sun. This is followed by a brief discussion on the current constraints that we have on the effective gauge couplings $\alpha_{e\mu,e\tau}$ of the $L_e - L_{\mu,\tau}$ symmetry from various neutrino oscillation experiments. In section 9.2, we study in detail the three-flavor oscillation picture in presence of long-range potential. We derive the compact analytical expressions for the effective oscillation parameters in case of the $L_e - L_\mu$ symmetry, and also present a simple expression for the resonance energy, where 1-3 mixing angle in matter becomes 45° in the presence of long-range potential. Next, we demonstrate the accuracy of our approximate analytical probability expressions by comparing it with the exact numerical results. We also discuss some salient features of the appearance and disappearance probabilities (calculated numerically) for the Fermilab-Homestake and CERN-Pyhäsalmi baselines in the presence of long-range potential towards the end of this section for both neutrino and antineutrino case. At the beginning of section 9.3, we study the impact of the long-range potential due to $L_e - L_\mu$ symmetry on the expected event spectra and total event rates for the DUNE and LBNO experiments. In section 9.4, we describe our simulation strategy. Next, we derive the expected constraints on $\alpha_{e\mu}$ from DUNE and LBNO in section 9.5.1, and estimate the discovery reach for $\alpha_{e\mu}$ in section 9.5.2. In section 9.5.3, we study how the long-range potential affects the CP-violation search of these future facilities. Section 9.5.4 is devoted to assess the impact of LRF on mass hierarchy measurements. Finally, we summarize our findings in section 9.6.

9.1 Flavor-Dependent Long-Range Forces from Gauged $U(1)$ Symmetries

The SM gauge group $SU(3)_C \times SU(2)_L \times U(1)_Y$ can be extended with minimal matter content by introducing anomaly free $U(1)$ symmetries under which the SM remains invariant and renormalizable [263]. There are three lepton flavor combinations: $L_e - L_\mu$, $L_e - L_\tau$, and $L_\mu - L_\tau$ which can be gauged in an anomaly free way with the particle content of the SM [81, 264, 265]. These $U(1)$ gauge symmetries have to be broken in Nature in order to allow the different neutrino species to mix among each other giving rise to neutrino oscillation as demanded by the recent data [22, 253, 254, 266]. This can be understood from the following example. If we assume that neutrino masses are generated by effective five-dimensional operator following say, seesaw mechanism, then this operator would remain invariant under these $U(1)$ symmetries if they are exact. This will ultimately give us an effective neutrino mass matrix containing a Dirac and a Majorana neutrino which remain unmixed and there will be no neutrino oscillation. For more discussions on these issues, see references [116, 119]. Now, there are two possibilities for the extra gauge boson associated with this abelian symmetry[1]: either it can be very heavy or it is very light but in both the cases, it couples to matter very feebly to escape direct detection. If the electrically neutral gauge boson (Z') corresponding to a flavor-diagonal generator of this new gauge group is relatively heavy[2], then the phenomenological consequences can be quite interesting [81, 263, 264, 265, 273]. On the other hand, if the mass of the gauge boson is very light, then it can introduce LRF with terrestrial range (greater than or equal to the Sun-Earth distance) without call upon extremely low mass scales [116, 117]. Details of the theoretical framework has been given in appendix A. This LRF is composition dependent (depends on the leptonic content and the mass of an object) and violate the universality of free fall which could be tested in the classic lunar ranging [274, 275] and Eötvös type gravity experiments [78, 276]. In fact, this idea was given long back by Lee and Yang [76] and later, using this idea, Okun [77, 277] gave a 2σ bound of $\alpha < 3.4 \times 10^{-49}$ (α denotes the strength of the long-range potential) for a

---

[1] Models with these symmetries necessarily possess a Higgs sector which also discriminates among different lepton families [267], but we will only focus here on the effect of the extra gauge boson.

[2] For an example, the Z' in gauged $L_e - L_{\mu,\tau}$ can be produced in e^+e^- collisions and subsequently decay into e^+e^- or $\mu^+\mu^-$ or $\tau^+\tau^-$ pairs and can be constrained using the data from LEP/LEP2 [268, 269, 270, 271, 272].

range of the Sun-Earth distance or more. Now, the light gauge boson Z' should have a mass $m_{Z'} \sim g\langle v\rangle$ where g is the gauge coupling of the new $U(1)$ symmetry and it should be $\lesssim 0.6\times10^{-24}$ since $g \approx \sqrt{\alpha}$ and $\langle v\rangle$ is the vacuum expectation value of the symmetry breaking scale. If the range of the LRF is comparable to the Sun-Earth distance ($\approx$ 1.5×10^{13} cm) then $m_{Z'} \sim 1/(1.5\times10^{13}\text{ cm}) = 1.3\times10^{-18}$ eV which means $\langle v\rangle \gtrsim 2$ MeV.

9.1.1 Abelian Gauged $L_e - L_{\mu,\tau}$ Symmetries

If the extra $U(1)$ corresponds to $L_e - L_\mu$ or $L_e - L_\tau$ flavor combination[3], the coupling of the solar electron to the $L_e - L_{\mu,\tau}$ gauge boson generates a flavor-dependent long-range potential for neutrinos [278, 279, 280] and can have significant impact on neutrino oscillations [116, 117, 118, 119, 120] inspite of such stringent constraints on α. This is caused due to the fact that the $(L_e - L_{\mu,\tau})$-charge of the electron neutrino is opposite to that of muon or tau flavor, leading to new non-universal FDNC interactions of the neutrinos in matter on top of the SM W-exchange interactions between the matter electrons and the propagating electron neutrinos. These new flavor-dependent FDNC interactions alter the 'running' of the oscillation parameters in matter by considerable amount [281]. Another important point is that the large number of electrons inside the Sun and the long-range nature of interaction balance the smallness of coupling and generate noticeable potential. As an example, the electrons inside the Sun give rise to a potential $V_{e\mu/e\tau}$ at the Earth surface which is given by [116, 119][4]

$$V_{e\mu/e\tau}(R_{SE}) = \alpha_{e\mu/e\tau}\frac{N_e}{R_{SE}} \approx 1.3\times10^{-11}\text{eV}\left(\frac{\alpha_{e\mu/e\tau}}{10^{-50}}\right), \tag{9.1}$$

where $\alpha_{e\mu/e\tau} = \frac{g^2_{e\mu/e\tau}}{4\pi}$, and $g_{e\mu/e\tau}$ is the gauge coupling of the $L_e - L_{\mu,\tau}$ symmetry. In Eq. (9.1), N_e ($\approx 10^{57}$) is the total number of electrons inside the Sun [282] and R_{SE} is the Sun-Earth distance $\approx 1.5\times10^{13}$ cm $= 7.6\times10^{26}$ GeV^{-1}. Here $\alpha_{e\mu/e\tau}$ can be identified as the 'fine-structure constant' of the $U(1)_{L_e-L_{\mu,\tau}}$ symmetry and its value is positive[5]. The corresponding potential due to the electrons inside the Earth with a long-range force

---

[3] Due to the absence of muons or tau leptons inside the Sun or Earth, we do not consider gauged $L_\mu - L_\tau$ symmetry here.

[4] For details see appendix A.

[5] In our work, we consider the case of a light vector boson exchange which makes sure that $\alpha_{e\mu/e\tau}$ is positive. It means that for an example, the force between an isolated electron and ν_e is repulsive.

having the Earth-radius range ($R_E \sim 6400$ km) is roughly one order of magnitude smaller compared to the solar long-range potential and can be safely neglected[6] [116, 119]. The long-range potential $V_{e\mu/e\tau}$ in Eq. (9.1) appears with a negative sign for antineutrinos and can affect the neutrino and antineutrino oscillation probabilities in different fashion. This feature can invoke fake CP-asymmetry like the SM matter effect and can influence the CP-violation search in long-baseline experiments. This is one of the important findings of our work and we will discuss this issue in detail in the later section. Now, it would be quite interesting to compare the strength of the potential given in Eq. (9.1) with the quantity $\Delta m^2/2E$ which governs the neutrino oscillation probability. For long-baseline neutrinos, $\Delta m^2/2E \sim 10^{-12}$ eV (assuming $\Delta m^2 \sim 2 \times 10^{-3}$ eV^2 and $E \sim 1$ GeV) which is comparable to $V_{e\mu/e\tau}$ even for $\alpha_{e\mu/e\tau} \sim 10^{-51}$ and can affect the long-baseline experiments significantly which we are going to explore in this chapter in the context of upcoming facilities DUNE and LBNO.

9.1.2 Existing Phenomenological Constraints on $L_e - L_{\mu,\tau}$ Parameters

There are phenomenological bounds on the effective gauge coupling $\alpha_{e\mu/e\tau}$ of the $L_e - L_{\mu,\tau}$ abelian symmetry[7] using data from various neutrino oscillation experiments. It was shown in [116] that $L_e - L_{\mu,\tau}$ potential at the Earth due to the huge number of electrons inside the Sun suppresses the atmospheric neutrino $\nu_\mu \to \nu_\tau$ oscillations which enabled them to place tight constraints on $\alpha_{e\mu/e\tau}$ using the oscillation of multi-GeV neutrinos observed at the Super-Kamiokande (SK) experiment. They obtained an upper bound of $\alpha_{e\mu} < 5.5 \times 10^{-52}$ and $\alpha_{e\tau} < 6.4 \times 10^{-52}$ at 90% C.L. [116]. In [119], the authors performed a global fit to the solar neutrino and KamLAND data including the flavor-dependent LRF. They quoted an upper bound of $\alpha_{e\mu} < 3.4 \times 10^{-53}$ and $\alpha_{e\tau} < 2.5 \times 10^{-53}$ at 3σ C.L. assuming $\theta_{13} = 0°$ [119]. A similar analysis was performed in [118] to place the constraints on LRF mediated by vector and non-vector (scalar or tensor) neutral bosons where the authors assumed one mass scale dominance. The proposed 50 kt magnetized

---

[6] The possibility of the local screening of the leptonic force (generated due to the solar electrons) by the cosmic antineutrinos is also negligible over the Sun-Earth distance [116].

[7] Flavor-dependent long-range leptonic forces can also be generated via the unavoidable mixing of light Z' boson of the $L_\mu - L_\tau$ symmetry with the Z boson of the SM. This issue was discussed in the context of the MINOS long-baseline experiment in [283, 284].

iron calorimeter (ICAL) detector at the India-based Neutrino Observatory (INO) can also probe the existence of LRF by observing the atmospheric neutrinos and antineutrinos separately over a wide range of energies and baselines [120]. With an exposure of one Mton.yr and using the muon momentum as observable, ICAL would be able to constrain $\alpha_{e\mu/e\tau} \lesssim 1.65 \times 10^{-53}$ at 3σ C.L. [120].

9.2 Three-Flavor Oscillation Picture in Presence of Long-Range Potential

In this section, we focus our attention to study the impact of flavor-dependent long-range leptonic potential (due to the electrons inside the Sun) at the Earth surface when neutrinos travel through the Earth matter. In a three-flavor framework, the long-range potential of Eq. (9.1) due to $L_e - L_\mu$ symmetry modifies the effective Hamiltonian for neutrino propagation in Earth matter in the flavor basis to

$$H_f = \left(U \begin{bmatrix} 0 & 0 & 0 \\ 0 & \frac{\Delta m^2_{21}}{2E} & 0 \\ 0 & 0 & \frac{\Delta m^2_{31}}{2E} \end{bmatrix} U^\dagger + \begin{bmatrix} V_{CC} & 0 & 0 \\ 0 & 0 & 0 \\ 0 & 0 & 0 \end{bmatrix} + \begin{bmatrix} V_{e\mu} & 0 & 0 \\ 0 & -V_{e\mu} & 0 \\ 0 & 0 & 0 \end{bmatrix} \right) , \tag{9.2}$$

where U is the vacuum PMNS matrix [148, 149, 285] which can be parametrized as

$$U = R_{23}(\theta_{23}, 0)\, R_{13}(\theta_{13}, \delta_{\rm CP})\, R_{12}(\theta_{12}, 0) \,. \tag{9.3}$$

In the above equation, E is the neutrino energy and V_{CC} is the Earth matter potential which appears in the form

$$V_{CC} = \sqrt{2} G_F N_e \simeq 7.6 \times Y_e \times \frac{\rho}{10^{14} \mathrm{g/cm^3}} \,\mathrm{eV} \,, \tag{9.4}$$

where G_F is the Fermi coupling constant, N_e is the electron number density inside the Earth, ρ is the matter density, and $Y_e = \frac{N_e}{N_p + N_n}$ is the relative electron number density. N_p, N_n are the proton and neutron densities in Earth matter respectively. In an electrically neutral, isoscalar medium, we have $N_e = N_p = N_n$ and Y_e comes out to be 0.5. In Eq. (9.2), $V_{e\mu}$ is the long-range potential due to $L_e - L_\mu$ symmetry and its strength is given by

Eq. (9.1). In case of $L_e - L_\tau$ symmetry, the contribution due to long-range potential in Eq. (9.2) takes the form $\mathrm{Diag}\,(V_{e\tau}, 0, -V_{e\tau})$. Note that the strength of the long-range potential $V_{e\mu/e\tau}$ does not depend on the Earth matter density[8] and takes the same value for any baseline on the Earth. In case of antineutrino propagation, we have to reverse the sign of V_{CC}, $V_{e\mu}$ (or $V_{e\tau}$), and the CP phase δ_{CP}. To judge the impact of the long-range potential $V_{e\mu}$ in long-baseline experiments with multi-GeV neutrinos, we need to compare its strength with the two other main terms in Eq. (9.2) which are $\frac{\Delta m^2_{31}}{2E}$ and the Earth matter potential V_{CC}. In Table 9.1, we compare the strengths of these three quantities which control the 'running' of the oscillation parameters in matter. The first oscillation maximum for the DUNE (LBNO) experiment occurs at 2.56 GeV (4.54 GeV) assuming $\Delta m^2_{31} = 2.44 \times 10^{-3}$ eV^2 (see Table 9.2). In the fourth column of Table 9.1, the values of V_{CC} have been estimated using Eq. (9.4) where we take the line-averaged constant Earth matter densities[9] for both the baselines: $\rho = 2.87\,\mathrm{g/cm^3}$ for the DUNE baseline and $\rho = 3.54\,\mathrm{g/cm^3}$ for the LBNO baseline. Table 9.1 shows that around first oscillation maximum, the strengths of the terms $\frac{\Delta m^2_{31}}{2E}$, V_{CC}, and $V_{e\mu}$ are comparable for both the set-ups under consideration even if $\alpha_{e\mu}$ is as small as 10^{-52}. It means that these three terms can interfere with each other having significant impact on the oscillation probability which we are going to study in this section with the help of analytical expressions. Before we start deriving our approximate analytical expressions for the effective mass-squared differences and mixing angles in matter in the presence of long-range potential, let us take a look at the current status of the oscillation parameters. The second column of Table 9.2

Set-up	1st osc. max. (GeV)	$\frac{\Delta m^2_{31}}{2E}$ (eV)	V_{CC} (eV)	$V_{e\mu}$ (eV)	
				$\alpha_{e\mu} = 10^{-52}$	$\alpha_{e\mu} = 10^{-53}$
DUNE	2.56	4.8×10^{-13}	1.1×10^{-13}	1.3×10^{-13}	1.3×10^{-14}
LBNO	4.54	2.7×10^{-13}	1.3×10^{-13}	1.3×10^{-13}	1.3×10^{-14}

Table 9.1: The second column shows the first oscillation maxima for Fermilab–Homestake and CERN–Pyhäsalmi baselines considering $\Delta m^2_{31} = 2.44 \times 10^{-3}$ eV^2. The fourth column depicts the strength of the Earth matter potentials for these baselines. The estimate of the long-range potentials $V_{e\mu}$ for two different values of $\alpha_{e\mu}$ is given in the last column.

---

[8] This is in contrast to the usual non-standard interactions (NSI's) whose strengths are proportional to the Earth matter density.

[9] These line-averaged constant Earth matter densities have been estimated using the Preliminary Reference Earth Model (PREM) [260].

Parameter	Best-fit and 1σ error	True value	Marginalization range
$\sin^2\theta_{12}$	$0.304^{+0.013}_{-0.012}$	0.304	Not marginalized
$\sin^2\theta_{13}$	$0.0218^{+0.0010}_{-0.0010}$	0.0218	Not marginalized
$\sin^2\theta_{23}$	$0.452^{+0.052}_{-0.028}$	0.50	[0.38, 0.64]
$\delta_{\mathrm{CP}}/^\circ$	306^{+39}_{-70}	[0, 360]	[0, 360]
$\frac{\Delta m^2_{21}}{10^{-5}\,\mathrm{eV}^2}$	$7.5^{+0.19}_{-0.17}$	7.50	Not marginalized
$\frac{\Delta m^2_{31}}{10^{-3}\,\mathrm{eV}^2}$	$2.457^{+0.047}_{-0.047}$	2.44	Not marginalized
$\frac{\Delta m^2_{\mu\mu}}{10^{-3}\,\mathrm{eV}^2}$	$2.410^{+0.051}_{-0.056}$	2.40	Not marginalized

Table 9.2: The second column shows the current best fit values and 1σ uncertainties on the three-flavor oscillation parameters assuming normal hierarchy in the fit [254]. The third column shows the true values of the oscillation parameters used to simulate the ‘observed’ data set. The fourth column depicts the range over which $\sin^2\theta_{23}$ and δ_{CP} are varied while minimizing the χ^2 to obtain the final results. In our calculations, $\Delta m^2_{\mu\mu}$ serves as an input parameter and then we estimate the value of Δm^2_{31} using the relation given in Eq. (9.5) (see text for details). In the third column, we take $\delta_{\mathrm{CP}} = 0^\circ$ to calculate the value of Δm^2_{31} from $\Delta m^2_{\mu\mu}$.

shows the present best fit values and 1σ errors on the three-flavor oscillation parameters assuming normal hierarchy in the fit [254]. We use the benchmark values of the various oscillation parameters as given in the third column of Table 9.2 to draw the oscillation probability plots in this section and to generate the ‘observed’ data set while estimating the physics reach of the experimental set-ups. The ranges over which $\sin^2\theta_{23}$ and δ_{CP} are marginalized while minimizing the χ^2 are given in the fourth column which we will discuss in detail while describing the simulation method in the later section. In Table 9.2, $\Delta m^2_{\mu\mu}$ is the effective mass-squared difference measured by the accelerator experiments using $\nu_\mu \to \nu_\mu$ disappearance channel [286, 287] and it is a linear combination of Δm^2_{31} and Δm^2_{21}. The value of Δm^2_{31} is estimated from $\Delta m^2_{\mu\mu}$ using the relation [288, 289]

$$\Delta m^2_{31} = \Delta m^2_{\mu\mu} + \Delta m^2_{21}(\cos^2\theta_{12} - \cos\delta_{\mathrm{CP}}\sin\theta_{13}\sin 2\theta_{12}\tan\theta_{23})\,. \tag{9.5}$$

The value of Δm^2_{31} is calculated separately for NH and IH using the above equation assuming $\Delta m^2_{\mu\mu} = \pm\, 2.4 \times 10^{-3}$ eV^2 where positive (negative) sign is for NH (IH). Note that through out this chapter, whenever we vary $\delta_{\rm CP}$ or θ_{23} or both, we calculate a new value for Δm^2_{31} using Eq. (9.5).

9.2.1 Analytical Expressions for the Effective Oscillation Parameters

In a CP-conserving scenario ($\delta_{\rm CP} = 0°$), the effective Hamiltonian in the flavor basis given in Eq. (9.2) takes the form

$$H_f = R_{23}(\theta_{23})R_{13}(\theta_{13})R_{12}(\theta_{12})H_0 R^T_{12}(\theta_{12})R^T_{13}(\theta_{13})R^T_{23}(\theta_{23}) + V\,, \tag{9.6}$$

where H_0 = Diag$(0, \Delta_{21}, \Delta_{31})$ with $\Delta_{21} \equiv \Delta m^2_{21}/2E$ and $\Delta_{31} \equiv \Delta m^2_{31}/2E$. In the above equation, V = Diag$\left(V_{CC} + V_{e\mu}, -V_{e\mu}, 0\right)$ for $L_e - L_\mu$ symmetry. We can rewrite H_f in Eq. (9.6) as

$$H_f = \Delta_{31}\begin{pmatrix} a_{11} & a_{12} & a_{13} \\ a_{12} & a_{22} & a_{23} \\ a_{13} & a_{23} & a_{33} \end{pmatrix}, \tag{9.7}$$

where

$$a_{11} = A + W + \sin^2\theta_{13} + \alpha\cos^2\theta_{13}\sin^2\theta_{12}\,, \tag{9.8}$$

$$a_{12} = \frac{1}{\sqrt{2}}\left[\cos\theta_{13}(\alpha\cos\theta_{12}\sin\theta_{12} + \sin\theta_{13} - \alpha\sin^2\theta_{12}\sin\theta_{13})\right], \tag{9.9}$$

$$a_{13} = \frac{1}{\sqrt{2}}\left[\cos\theta_{13}(-\alpha\cos\theta_{12}\sin\theta_{12} + \sin\theta_{13} - \alpha\sin^2\theta_{12}\sin\theta_{13})\right], \tag{9.10}$$

$$a_{22} = \frac{1}{2}\left[\alpha\cos^2\theta_{12} + \cos^2\theta_{13} - 2\alpha\cos\theta_{12}\sin\theta_{12}\sin\theta_{13} + \alpha\sin^2\theta_{12}\sin^2\theta_{13} - 2W\right], \tag{9.11}$$

$$a_{23} = \frac{1}{2}\left[\cos^2\theta_{13} - \alpha\cos^2\theta_{12} + \alpha\sin^2\theta_{12}\sin^2\theta_{13}\right], \tag{9.12}$$

$$a_{33} = \frac{1}{2}\left[\cos^2\theta_{13} + \alpha\cos^2\theta_{12} + \alpha\sin\theta_{13}(\sin 2\theta_{12} + \sin^2\theta_{12}\sin\theta_{13})\right]. \tag{9.13}$$

In the above equations, we introduce the terms A, W, and α which are defined as

$$A \equiv \frac{V_{CC}}{\Delta_{31}} = \frac{2EV_{CC}}{\Delta m^2_{31}}\,, \; W \equiv \frac{V_{e\mu}}{\Delta_{31}} = \frac{2EV_{e\mu}}{\Delta m^2_{31}}\,, \; \alpha \equiv \frac{\Delta m^2_{21}}{\Delta m^2_{31}}\,, \tag{9.14}$$

and we assume that the vacuum value of θ_{23} is 45°. Note that we have kept the terms of all orders in $\sin\theta_{13}$ and α which are quite important in light of the large value of 1-3 mixing angle as was measured recently by the modern reactor experiments. Now, we need to diagonalize the effective Hamiltonian H_f in Eq. (9.7) to find the effective mass-squared differences and mixing angles in the presence of the Earth matter potential (V_{CC}) and the long-range potential ($V_{e\mu}$). We can almost diagonalize H_f with the help of a unitary matrix

$$\tilde{U} \equiv R_{23}\,(\theta^m_{23})\,R_{13}\,(\theta^m_{13})\,R_{12}\,(\theta^m_{12})\,, \tag{9.15}$$

such that

$$\tilde{U}^T H_f \tilde{U} \simeq \mathrm{Diag}\left(m^2_{1,m}/2E, m^2_{2,m}/2E, m^2_{3,m}/2E\right)\,, \tag{9.16}$$

where off-diagonal terms are quite small and can be safely neglected. The lower right 2×2 block in Eq. (9.7) gives us the angle θ^m_{23} which has the form

$$\tan 2\theta^m_{23} = \frac{\cos^2\theta_{13} - \alpha\cos^2\theta_{12} + \alpha\sin^2\theta_{12}\sin^2\theta_{13}}{W + \alpha\sin 2\theta_{12}\sin\theta_{13}}\,. \tag{9.17}$$

The mixing angles θ^m_{13} and θ^m_{12} can be obtained by subsequent diagonalizations of the (1,3) and (1,2) blocks respectively and we get the following expressions

$$\tan 2\theta^m_{13} = \frac{\sin 2\theta_{13}(1-\alpha\sin^2\theta_{12})\left(\cos\theta^m_{23} + \sin\theta^m_{23}\right) - \alpha\sin 2\theta_{12}\cos\theta_{13}\left(\cos\theta^m_{23} - \sin\theta^m_{23}\right)}{\sqrt{2}\left(\lambda_3 - A - W - \sin^2\theta_{13} - \alpha\sin^2\theta_{12}\cos^2\theta_{13}\right)}\,, \tag{9.18}$$

and

$$\tan 2\theta^m_{12} = \frac{\cos\theta^m_{13}\left[\sin 2\theta_{13}(1-\alpha\sin^2\theta_{12})\left(\cos\theta^m_{23} - \sin\theta^m_{23}\right) + \alpha\sin 2\theta_{12}\cos\theta_{13}(\cos\theta^m_{23} + \sin\theta^m_{23})\right]}{\sqrt{2}\,(\lambda_2 - \lambda_1)}\,, \tag{9.19}$$

where

$$\lambda_3 = \frac{1}{2}\left[\cos^2\theta_{13} + \alpha\cos^2\theta_{12} + \alpha\sin^2\theta_{12}\sin^2\theta_{13} - W + \frac{W + \alpha\sin 2\theta_{12}\sin\theta_{13}}{\cos 2\theta^m_{23}}\right], \quad (9.20)$$

$$\lambda_2 = \frac{1}{2}\left[\cos^2\theta_{13} + \alpha\cos^2\theta_{12} + \alpha\sin^2\theta_{12}\sin^2\theta_{13} - W - \frac{W + \alpha\sin 2\theta_{12}\sin\theta_{13}}{\cos 2\theta^m_{23}}\right], \quad (9.21)$$

and

$$\lambda_1 = \frac{1}{2}\left[\left(\lambda_3 + A + W + \sin^2\theta_{13} + \alpha\cos^2\theta_{13}\sin^2\theta_{12}\right) - \frac{\left(\lambda_3 - A - W - \sin^2\theta_{13} - \alpha\cos^2\theta_{13}\sin^2\theta_{12}\right)}{\cos 2\theta^m_{13}}\right]. \quad (9.22)$$

The eigenvalues $m^2_{i,m}/2E\,(i = 1,2,3)$ are given by the expressions

$$m^2_{3,m}/2E = \frac{\Delta_{31}}{2}\left[\left(\lambda_3 + A + W + \sin^2\theta_{13} + \alpha\cos^2\theta_{13}\sin^2\theta_{12}\right) + \frac{\left(\lambda_3 - A - W - \sin^2\theta_{13} - \alpha\cos^2\theta_{13}\sin^2\theta_{12}\right)}{\cos 2\theta^m_{13}}\right], \quad (9.23)$$

$$m^2_{2,m}/2E = \frac{\Delta_{31}}{2}\left[\lambda_1 + \lambda_2 - \frac{(\lambda_1 - \lambda_2)}{\cos 2\theta^m_{12}}\right], \quad (9.24)$$

and

$$m^2_{1,m}/2E = \frac{\Delta_{31}}{2}\left[\lambda_1 + \lambda_2 + \frac{(\lambda_1 - \lambda_2)}{\cos 2\theta^m_{12}}\right]. \quad (9.25)$$

With the help of Eq. (9.17), Eq. (9.18), and Eq. (9.19), we plot the 'running' of the effective mixing angles θ^m_{23}, θ^m_{13}, and θ^m_{12} respectively in Fig. 9.1 as functions of the neutrino energy E in the presence of V_{CC} and $V_{e\mu}$. Here, we consider L = 1300 km and NH. We give the plots for three different choices of the effective gauge coupling $\alpha_{e\mu}$: 0 (the SM case), 10^{-52}, and 10^{-51}. The vacuum values of the oscillation parameters are taken from the third column of Table 9.2. We do the same for the effective mass-squared differences (see Eqs. (9.23), (9.24), and (9.25)) in Fig. 9.2. The extreme right panel of Fig. 9.1 shows

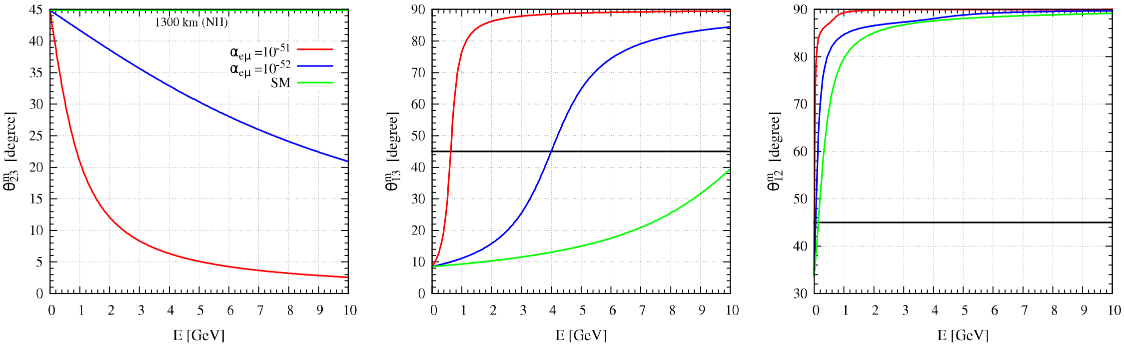

Figure 9.1: The variations in the effective mixing angles with the neutrino energy E in the presence of the Earth matter potential (V_{CC}) and long-range potential ($V_{e\mu}$). The left, middle, and right panels show the 'running' of θ^m_{23}, θ^m_{13}, and θ^m_{12} respectively. Here, we take L = 1300 km which corresponds to the Fermilab–Homestake baseline and assume NH. Plots are given for three different choices of the effective gauge coupling $\alpha_{e\mu}$: 0 (the SM case), 10^{-52}, and 10^{-51}. The vacuum values of the oscillation parameters are taken from the third column of Table 9.2 and we consider $\delta_{\rm CP} = 0°$.

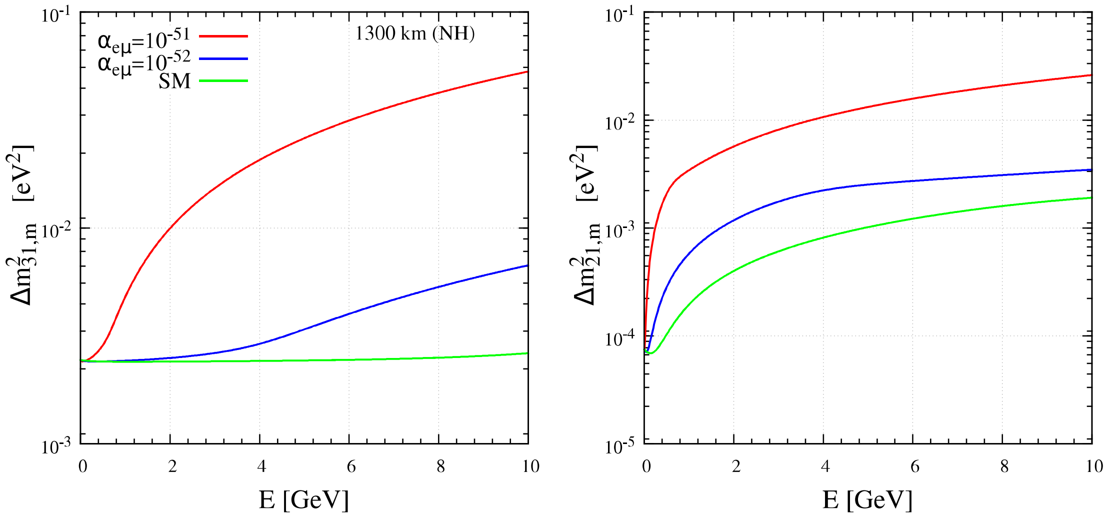

Figure 9.2: The variations in the effective mass-squared differences with the neutrino energy E in the presence of V_{CC} and $V_{e\mu}$. Left panel shows the 'running' of $\Delta m^2_{31,m}(\equiv m^2_{3,m} - m^2_{1,m})$ while right panel is for $\Delta m^2_{21,m}(\equiv m^2_{2,m} - m^2_{1,m})$. Here, we take L = 1300 km and assume NH. We give plots for three different choices of the effective gauge coupling $\alpha_{e\mu}$: 0 (the SM case), 10^{-52}, and 10^{-51}. The vacuum values of the oscillation parameters are taken from the third column of Table 9.2 and we consider $\delta_{\rm CP} = 0°$.

that θ^m_{12} approaches to 90° very rapidly with increasing E in the presence of V_{CC} and this behavior does not change much when we introduce $V_{e\mu}$. This is not the case for θ^m_{23} and θ^m_{13}. The long-range potential $V_{e\mu}$ affects the 'running' of θ^m_{23} (see extreme left panel of Fig. 9.1) significantly. As we go to higher energies, θ^m_{23} deviates from 45° and its value decreases very sharply depending on the strength of $\alpha_{e\mu}$. In case of θ^m_{13}, the effect of $V_{e\mu}$

is quite opposite as compared to θ_{23}^m as can be seen from the middle panel of Fig. 9.1. Assuming NH, as we increase E, θ_{13}^m quickly reaches to 45° (resonance point) in the presence of $V_{e\mu}$ and then finally approaches toward 90° as we further increase E. These two opposite behaviors of θ_{23}^m and θ_{13}^m alter the amplitudes and the locations of oscillation maxima in the transition probability substantially for non-zero $\alpha_{e\mu}$ which we discuss in the later part of this section. For $\alpha_{e\mu} = 10^{-52}$ (10^{-51}), the resonance occurs around 4 GeV (0.6 GeV) for 1300 km baseline. We can obtain an analytical expression for the resonance energy demanding $\theta_{13}^m = 45°$ in Eq. (9.18). In one mass scale dominance approximation where Δm_{21}^2 can be neglected *i.e.* assuming $\alpha = 0$, the condition for the resonance energy (E_{res}) takes the form:

$$\lambda_3 = A + W + \sin^2\theta_{13}\,. \tag{9.26}$$

Now, putting $\alpha = 0$ in Eqs. (9.20) and (9.17), we get a simplified expression for λ_3 which has the following form

$$\lambda_3 = \frac{1}{2}\left[\cos^2\theta_{13} - W + \sqrt{W^2 + (\cos^2\theta_{13})^2}\right] \simeq \frac{1}{2}\left[2\cos^2\theta_{13} - W\right]\,, \tag{9.27}$$

since at resonance energies, the term W^2 is small compared to $\cos^4\theta_{13}$ and can be safely neglected. Now, comparing Eq. (9.26) and Eq. (9.27), we get a simple and compact expression for the resonance energy

$$E_{res} = \frac{\Delta m_{31}^2 \cos 2\theta_{13}}{2V_{cc} + 3V_{e\mu}}\,. \tag{9.28}$$

In the absence of long-range potential $V_{e\mu}$, Eq. (9.28) gives us the standard expression for the resonance energy in the SM framework. Eq. (9.28) suggests that for a given baseline, in the presence of $V_{e\mu}$, the resonance occurs at lower energy as compared to the SM case and this is exactly what we observe in the middle panel of Fig. 9.1. The right panel of Fig. 9.2 demonstrates that the effective solar mass-squared difference $\Delta m_{21,m}^2$ increases with energy and can be comparable to the vacuum value of Δm_{31}^2 at higher energies in the SM case. In the presence of $V_{e\mu}$, $\Delta m_{21,m}^2$ increases with energy even faster and can become quite large at higher energies depending on the strength of $\alpha_{e\mu}$. In the SM framework, the effective atmospheric mass-squared difference $\Delta m_{31,m}^2$ does not run with energy for this choice of baseline (see left panel of Fig. 9.2). But, in the presence of $V_{e\mu}$, the value of $\Delta m_{31,m}^2$ enhances a lot depending on the strength of $\alpha_{e\mu}$ as energy is increased. Next, to check the accuracy of our approximate analytical results, we compare the oscillation probabilities calculated with our approximate effective running mixing angles and mass-squared differences with those calculated numerically for the same baseline and line-averaged constant matter density along it.

9.2.2 Demonstration of the Accuracy of the Approximation

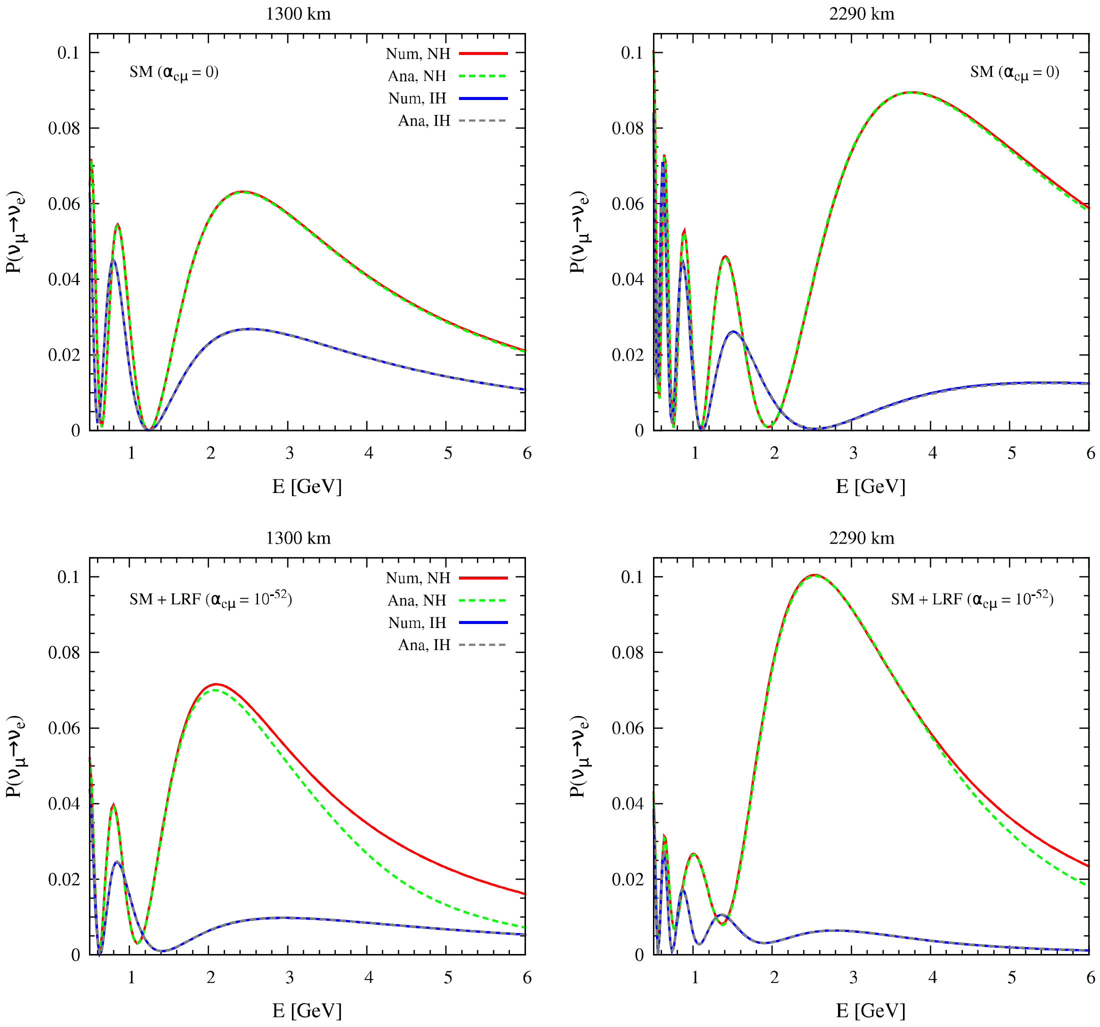

Figure 9.3: $\nu_\mu \to \nu_e$ transition probability as a function of neutrino energy E in GeV for 1300 km (2290 km) baseline in left (right) panels. The upper panels are for the SM case without long-range potential. The lower panels correspond to $\alpha_{e\mu} = 10^{-52}$. In all the panels, we compare our analytical expressions (dashed curves) to the exact numerical results (solid curves) for NH and IH. The vacuum values of the oscillation parameters are taken from the third column of Table 9.2 and we take $\delta_{\text{CP}} = 0^\circ$.

The neutrino oscillation probabilities in the presence of V_{CC} and $V_{e\mu}$ can be obtained by

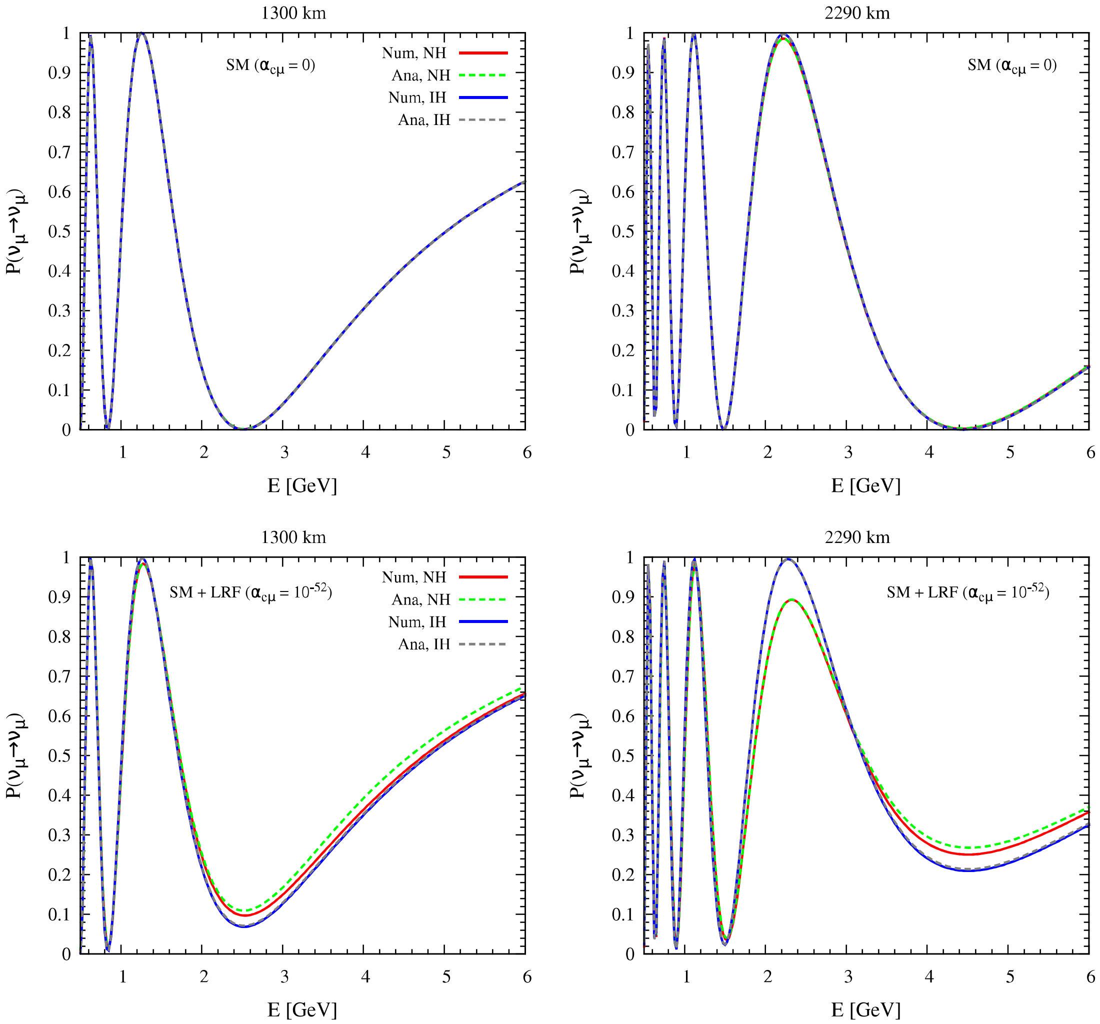

Figure 9.4: $\nu_\mu \to \nu_\mu$ transition probability as a function of neutrino energy E in GeV for 1300 km (2290 km) baseline in left (right) panels. The upper panels are for the SM case without long-range potential. The lower panels correspond to $\alpha_{e\mu} = 10^{-52}$. In all the panels, we compare our analytical expressions (dashed curves) to the exact numerical results (solid curves) for NH and IH. The vacuum values of the oscillation parameters are taken from the third column of Table 9.2 and we take $\delta_{\mathrm{CP}} = 0°$.

replacing the vacuum expressions of the elements of the mixing matrix U and the mass-square differences Δm^2_{ij} with their effective ‘running’ values

$$U_{\alpha i} \to \tilde{U}_{\alpha i}\left(\theta_{12} \to \theta^m_{12}, \theta_{13} \to \theta^m_{13}, \theta_{23} \to \theta^m_{23}\right), \; \Delta m^2_{ij} \to \Delta m^2_{ij,m} = m^2_{i,m} - m^2_{j,m} \,. \quad (9.29)$$

Incorporating the modifications due to V_{CC} and $V_{e\mu}$, the new transition probability in a

CP-conserving scenario can be written as

$$P\left(\nu_\alpha \to \nu_\beta\right) = \delta_{\alpha\beta} - 4\sum_{i>j} \tilde{U}_{\alpha i}\tilde{U}_{\beta i}\tilde{U}_{\alpha j}\tilde{U}_{\beta j} \sin^2\left(\frac{\Delta m^2_{ij,m} L}{4E}\right) . \tag{9.30}$$

Using Eq. (9.30), we obtain the following expressions for the appearance and disappearance channels [257]

$$\begin{aligned} P(\nu_\mu \to \nu_e) &= 4\tilde{U}^2_{\mu 2}\tilde{U}^2_{e2} \sin^2\frac{\Delta m^2_{21,m}L}{4E} + 4\tilde{U}^2_{\mu 3}\tilde{U}^2_{e3} \sin^2\frac{\Delta m^2_{31,m}L}{4E} \\ &\quad +2\,\tilde{U}_{\mu 3}\tilde{U}_{e3}\tilde{U}_{\mu 2}\tilde{U}_{e2}\left(4\sin^2\frac{\Delta m^2_{21,m}L}{4E}\sin^2\frac{\Delta m^2_{31,m}L}{4E}\right) \\ &\quad +2\,\tilde{U}_{\mu 3}\tilde{U}_{e3}\tilde{U}_{\mu 2}\tilde{U}_{e2}\left(\sin\frac{\Delta m^2_{21,m}L}{2E}\sin\frac{\Delta m^2_{31,m}L}{2E}\right) , \end{aligned} \tag{9.31}$$

$$\begin{aligned} P(\nu_\mu \to \nu_\mu) &= 1 - 4\tilde{U}^2_{\mu 2}\left(1-\tilde{U}^2_{\mu 2}\right)\sin^2\frac{\Delta m^2_{21,m}L}{4E} - 4\tilde{U}^2_{\mu 3}\left(1-\tilde{U}^2_{\mu 3}\right)\sin^2\frac{\Delta m^2_{31,m}L}{4E} \\ &\quad +2\tilde{U}^2_{\mu 2}\tilde{U}^2_{\mu 3}\left(4\sin^2\frac{\Delta m^2_{21,m}L}{4E}\sin^2\frac{\Delta m^2_{31,m}L}{4E}\right) \\ &\quad +2\tilde{U}^2_{\mu 2}\tilde{U}^2_{\mu 3}\left(\sin\frac{\Delta m^2_{21,m}L}{2E}\sin\frac{\Delta m^2_{31,m}L}{2E}\right) . \end{aligned} \tag{9.32}$$

In Fig. 9.3, we present our approximate $\nu_\mu \to \nu_e$ oscillation probabilities (dashed curves) as a function of the neutrino energy against the exact numerical results (solid curves) considering $L = 1300$ km (left panels) and 2290 km (right panels). We give the plots for both NH and IH in all the panels considering line-averaged constant Earth matter densities for both the baselines. The upper panels are drawn for the SM case ($\alpha_{e\mu} = 0$) where our approximate results match exactly with the numerically obtained probabilities. In the lower panels, we give the probabilities considering $\alpha_{e\mu} = 10^{-52}$ and find that our approximate expressions work quite well in the presence of long-range potential and can predict almost accurate L/E patterns of the oscillation probability. In Fig. 9.4, we study the same for $\nu_\mu \to \nu_\mu$ oscillation channel and find that our approximate expressions match quite nicely with the numerical results. Here, we present our analytical results for NH. We can obtain the same for IH by changing $\Delta m^2_{31} \to -\Delta m^2_{31}$. Following the same procedure and reversing the sign of V in Eq. (9.6), we can derive the analytical expressions for antineutrino as well. Note that in this work, we limit our investigation to $L_e - L_\mu$ symmetry, though similar procedure can be adopted for $L_e - L_\tau$ symmetry.

9.2.3 Discussion at the Probability Level – Neutrino Case

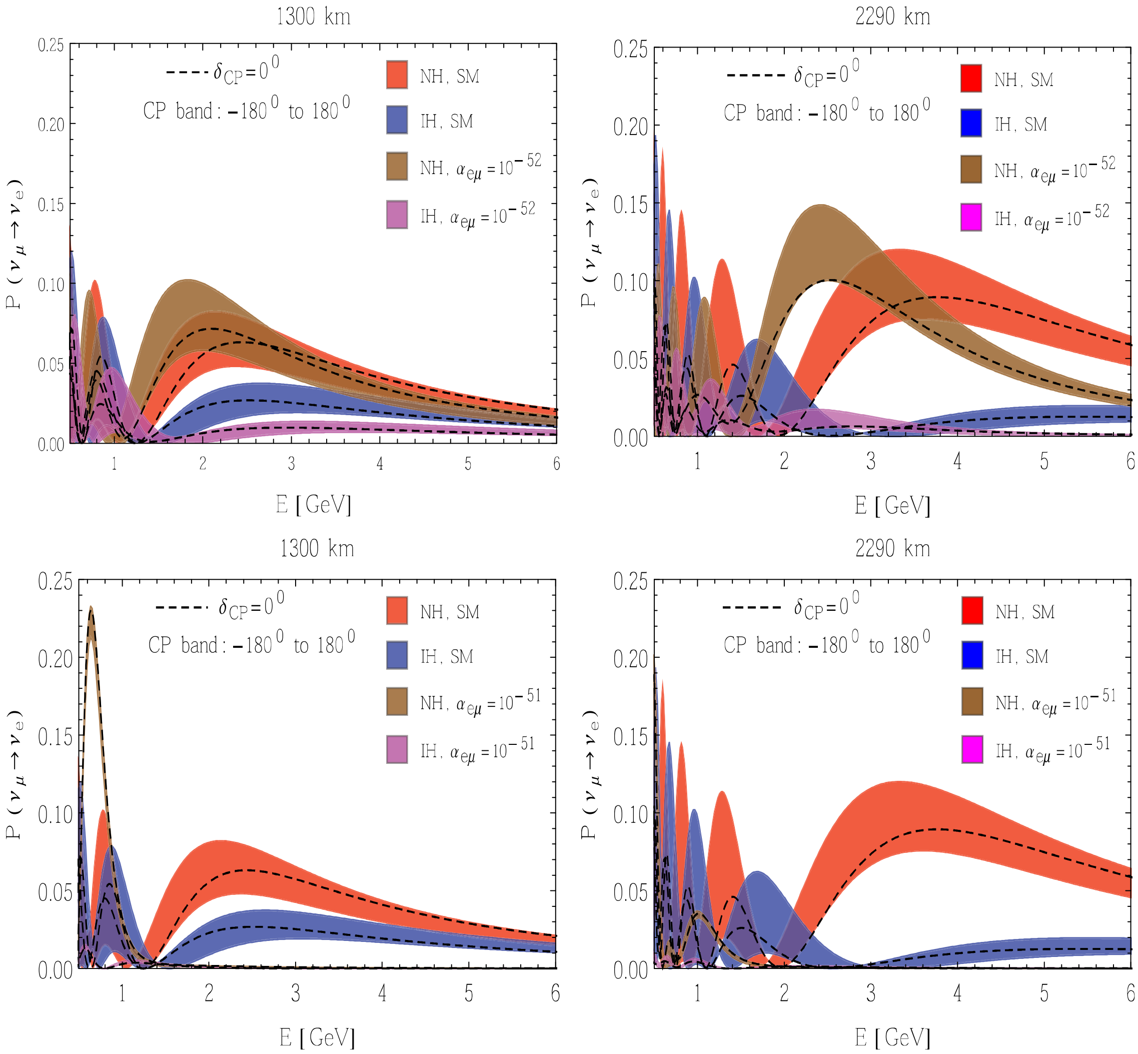

Figure 9.5: The transition probability $P_{\mu e}$ as a function of neutrino energy. The band reflects the effect of unknown $\delta_{\rm CP}$. Inside each band, the probability for $\delta_{\rm CP} = 0°$ case is shown by the black dashed line. The left panels (right panels) are for 1300 km (2290 km) baseline. In each panel, we compare the probabilities for NH and IH with and without long-range potential. In the upper (lower) panels, we take $\alpha_{e\mu} = 10^{-52}$ ($\alpha_{e\mu} = 10^{-51}$) for the cases with long-range potential.

In this section, we discuss in detail how the long-range potential affects the full three-flavor neutrino oscillation probabilities in matter considering non-zero values of $\delta_{\rm CP}$. In Fig. 9.5, we show the exact numerical transition probability $P_{\mu e}$ as a function of the neutrino energy using the line-averaged constant Earth matter densities for 1300 km (left

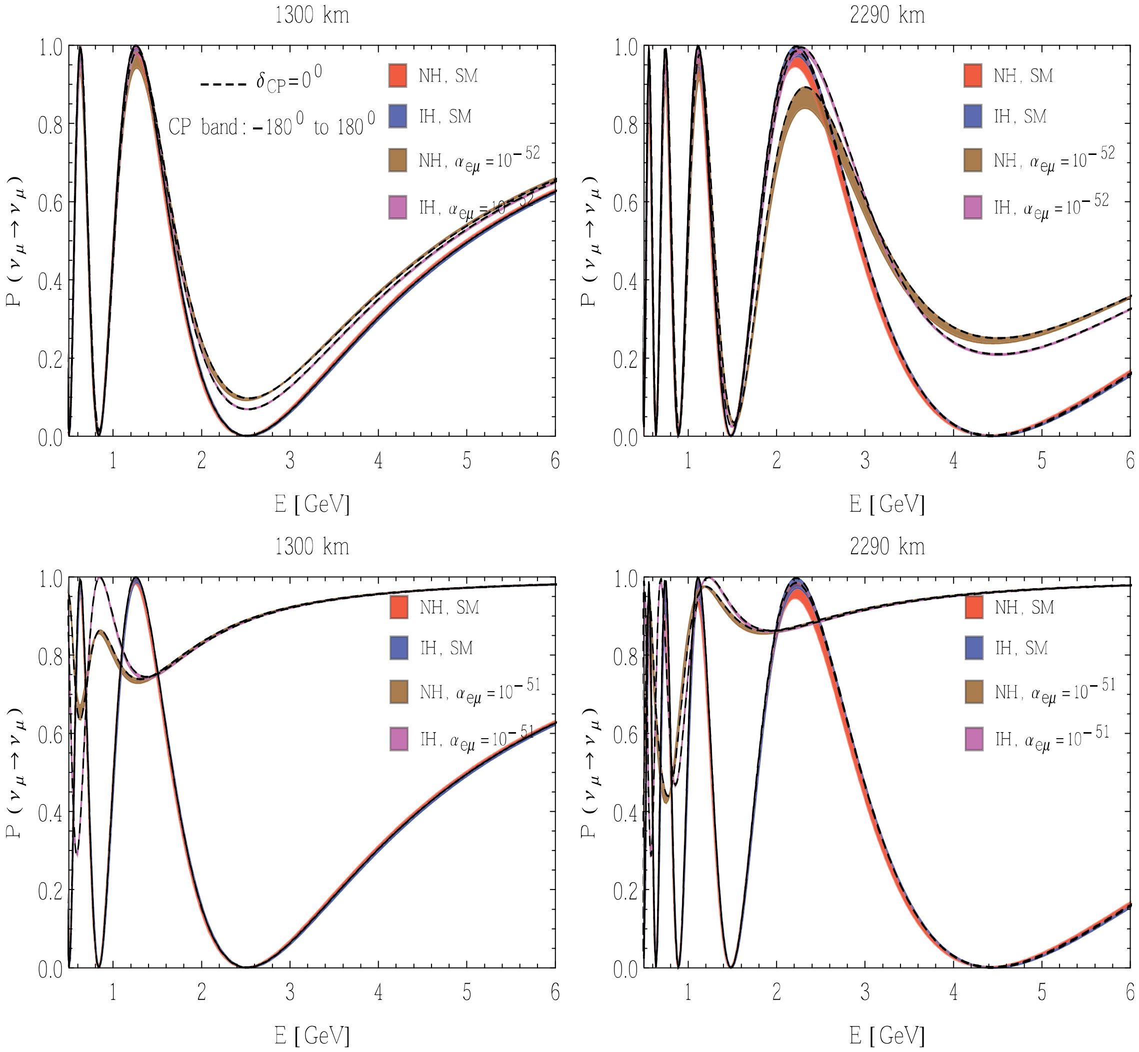

Figure 9.6: The transition probability $P_{\mu\mu}$ as a function of neutrino energy. The band reflects the effect of unknown $\delta_{\rm CP}$. Inside each band, the probability for $\delta_{\rm CP}=0°$ case is shown by the black dashed line. The left panels (right panels) are for 1300 km (2290 km) baseline. In each panel, we compare the probabilities for NH and IH with and without long-range potential. In the upper (lower) panels, we take $\alpha_{e\mu}=10^{-52}$ ($\alpha_{e\mu}=10^{-51}$) for the cases with long-range potential.

panels) and 2290 km (right panels) baselines. We vary $\delta_{\rm CP}$ within the range $-180°$ to $180°$ and the resultant probability is shown as a band, with the thickness of the band reflecting the effect of $\delta_{\rm CP}$ on $P_{\mu e}$. Inside each band, the probability for $\delta_{\rm CP}=0°$ case is shown explicitly by the black dashed line. The left panels (right panels) are for 1300 km (2290 km) baseline. In each panel, we compare the probabilities for NH and IH with and without long-range potential. In the upper (lower) panels, we take $\alpha_{e\mu}=10^{-52}$ ($\alpha_{e\mu}=10^{-51}$) for the cases with long-range potential. We study the same for the disappearance ($\nu_\mu \to \nu_\mu$) channel in Fig. 9.6. We give the similar plots for the antineutrino case in the next section

9.2.4.

To explain the behavior of the oscillation probabilities in Fig. 9.5 and Fig. 9.6 at the qualitative level, we can simplify the analytical expressions given in Eqs. (9.31) and (9.32) in the following fashion. The extreme right panel of Fig. 9.1 suggests that $\sin\theta_{12}^m \to 1$ and $\cos\theta_{12}^m \to 0$ very quickly as we increase E in the SM case or with non-zero $\alpha_{e\mu}$. So, we set $\sin\theta_{12}^m \approx 1$ and $\cos\theta_{12}^m \approx 0$ in Eqs. (9.31) and (9.32) and obtain the following simple expressions:

$$P(\nu_\mu \to \nu_e) = \sin^2\theta_{23}^m \sin^2 2\theta_{13}^m \sin^2 \frac{\Delta m^2_{32,m} L}{4E}\,, \tag{9.33}$$

and

$$\begin{aligned} P(\nu_\mu \to \nu_\mu) \quad = \quad & 1 - \sin^2 2\theta_{23}^m \sin^2\theta_{13}^m \sin^2 \frac{\Delta m^2_{21,m} L}{4E} \\ & - \sin^2 2\theta_{23}^m \cos^2\theta_{13}^m \sin^2 \frac{\Delta m^2_{31,m} L}{4E} \\ & - \sin^4\theta_{23}^m \sin^2 2\theta_{13}^m \sin^2 \frac{\Delta m^2_{32,m} L}{4E}\,. \end{aligned} \tag{9.34}$$

In Fig. 9.5, we can see that for $\alpha_{e\mu} = 10^{-52}$ case (upper panels), the locations of the first oscillation maxima have been shifted toward lower energies for both the baselines and also the amplitudes of the first oscillation maxima have been enhanced when we assume NH. This can be understood from the ‘running’ of θ_{23}^m, θ_{13}^m (extreme left and middle panels of Fig. 9.1), and $\Delta m^2_{32,m}$ (left and right panels of Fig. 9.2). As we go to higher energies, θ_{13}^m increases and θ_{23}^m decreases and there is a trade-off between the terms $\sin^2\theta_{23}^m$ and $\sin^2 2\theta_{13}^m$ in Eq. (9.33). Also, the value of $\Delta m^2_{32,m}$ ($\Delta m^2_{31,m}$ - $\Delta m^2_{21,m}$) decreases with energy as $\Delta m^2_{21,m}$ increases by substantial amount compared to $\Delta m^2_{31,m}$, which shifts the location of the first oscillation maxima toward lower energies. For IH, the value of θ_{13}^m decreases fast with non-zero $\alpha_{e\mu}$ compared to the SM case, causing a depletion in the probabilities over a wide range of energies. In case of $\alpha_{e\mu} = 10^{-51}$ (lower panels), there is a huge suppression in the probabilities at both the baselines over a wide range of energies above 1 GeV assuming NH. The main reason behind this large damping in the probabilities is that θ_{13}^m approaches very quickly to 90° around 1 GeV or so for $\alpha_{e\mu} = 10^{-51}$ (see middle panel of Fig. 9.1) and therefore, $\sin^2 2\theta_{13}^m \to 0$, vanishing the probability amplitude for $\nu_\mu \to \nu_e$ oscillation channel. Below 1 GeV, θ_{13}^m runs toward 45° and therefore, $\sin^2 2\theta_{13}^m \to 1$, causing the enhancement in the probabilities. When we take IH, θ_{13}^m quickly advances to zero, causing a huge damping in the probabilities at all the energies. These 'running' behaviors of θ_{23}^m, θ_{13}^m, and the mass-squared differences in the presence of long-range potential as discussed above also affect $\nu_\mu \to \nu_\mu$ oscillation channel (see Fig. 9.6) which can be explained with the help of Eq. (9.34).

9.2.4 Discussion at the Probability Level – Antineutrino Case

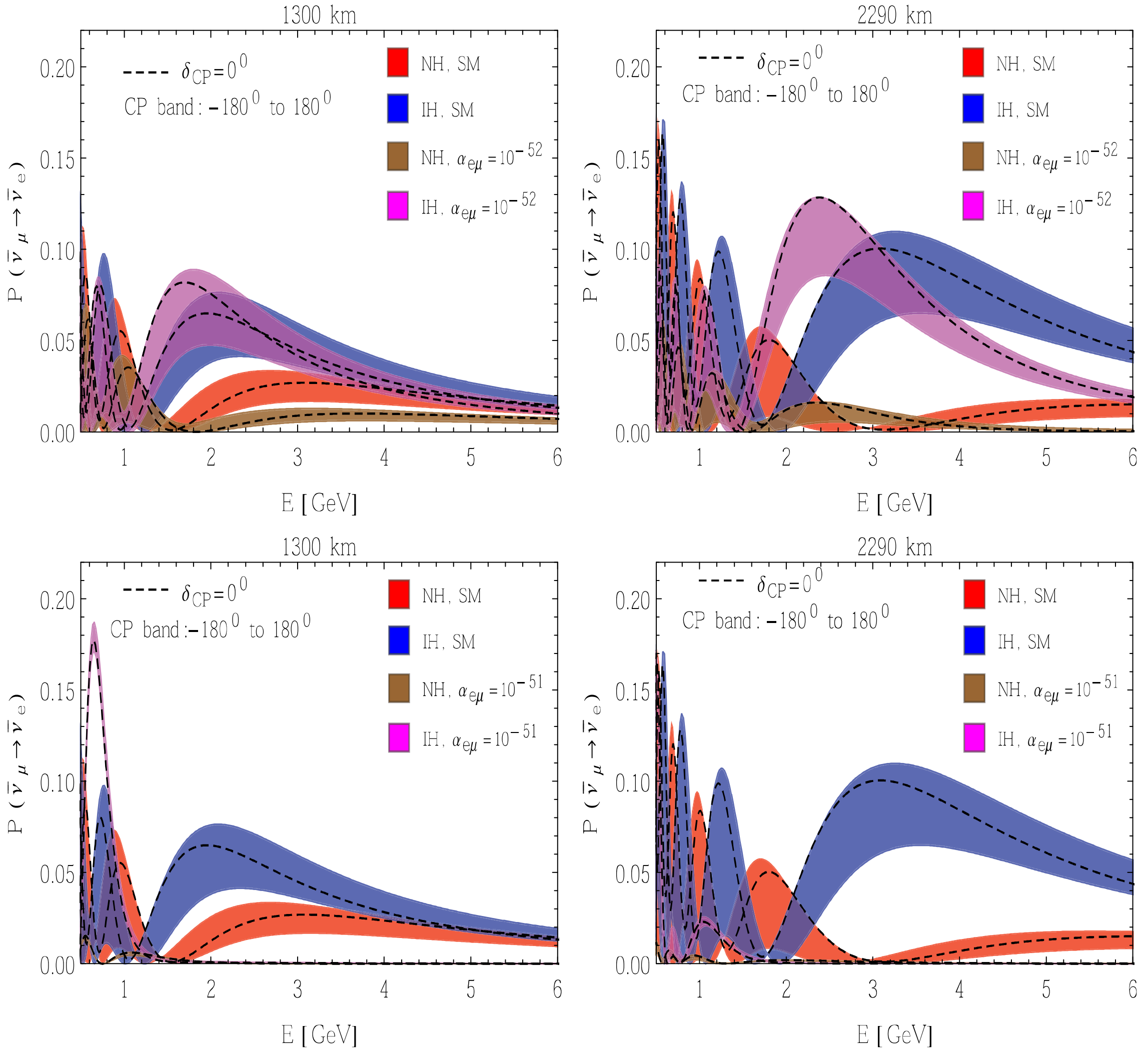

Figure 9.7: The transition probability $P_{\bar{\mu}\bar{e}}$ as a function of antineutrino energy. The band reflects the effect of unknown $\delta_{\rm CP}$. Inside each band, the probability for $\delta_{\rm CP} = 0°$ case is shown by the black dashed line. The left panels (right panels) are for 1300 km (2290 km) baseline. In each panel, we compare the probabilities for NH and IH with and without long-range potential. In the upper (lower) panels, we take $\alpha_{e\mu} = 10^{-52}$ ($\alpha_{e\mu} = 10^{-51}$) for the cases with long-range potential.

For completeness let us now show the probability plots for antineutrino case. In Fig. 9.7, we plot the exact numerical transition probability $\bar{\nu}_\mu \to \bar{\nu}_e$ as a function of antineutrino energy. The band shows the impact of unknown δ_{CP}. Inside each band, the probability for $\delta_{\text{CP}} = 0^\circ$ case is shown by the black dashed line. The left panels (right panels) are drawn for 1300 km (2290 km) baseline. In each panel, we compare the probabilities for NH and IH with and without long-range potential. In the upper (lower) panels, we consider $\alpha_{e\mu} = 10^{-52}$ ($\alpha_{e\mu} = 10^{-51}$) for the cases with long-range potential. Fig. 9.8 shows the

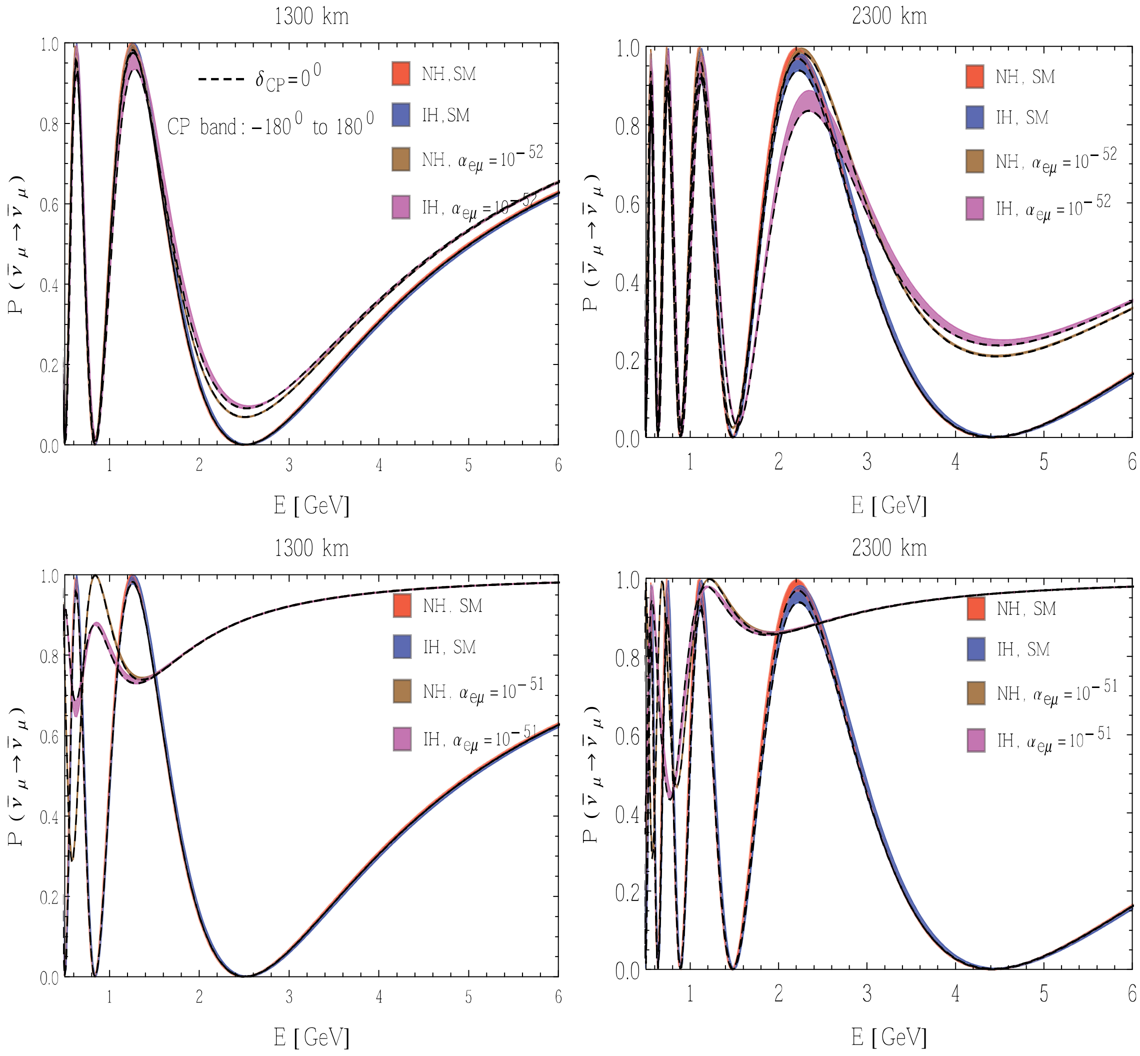

Figure 9.8: The transition probability $P_{\bar{\mu}\bar{\mu}}$ as a function of antineutrino energy. The band reflects the effect of unknown δ_{CP}. Inside each band, the probability for $\delta_{\text{CP}} = 0^\circ$ case is shown by the black dashed line. The left panels (right panels) are for 1300 km (2290 km) baseline. In each panel, we compare the probabilities for NH and IH with and without long-range potential. In the upper (lower) panels, we take $\alpha_{e\mu} = 10^{-52}$ ($\alpha_{e\mu} = 10^{-51}$) for the cases with long-range potential.

exact numerical $\bar{\nu}_\mu \to \bar{\nu}_\mu$ disappearance probability as a function of antineutrino energy. The thin band portrays the mild impact of unknown δ_{CP}. Inside each band, the probability for $\delta_{\rm CP} = 0^\circ$ case is given by the black dashed line. The left panels (right panels) are drawn for 1300 km (2290 km) baseline. In each panel, we compare the probabilities for NH and IH with and without long-range potential. In the upper (lower) panels, we consider $\alpha_{e\mu} = 10^{-52}$ ($\alpha_{e\mu} = 10^{-51}$) for the cases with long-range potential. It should be noted here that the behavior of the oscillation probabilities in antineutrino case can also be explained in a similar manner as done in section 9.2.3.

9.3 Impact of Long-Range Potential at the Event Level

We start this section with a detail discussion on event spectrum and event rates followed by an useful discussion on bi-events plot. It is worth to mention here that all the description of the main experimental features of the DUNE and LBNO set-ups has been presented in the subsection 5.1.1 and 5.1.2 respectively.

9.3.1 Event Spectrum and Rates

In this section, we present the expected event spectra and total event rates for both the set-ups under consideration in the presence of long-range potential. We calculate the number of expected electron events[10] in the i-th energy bin in the detector using the following expression

$$N_i = \frac{T\, n_n\, \varepsilon}{4\pi L^2} \int_0^{E_{\rm max}} dE \int_{E_{A_i}^{\rm min}}^{E_{A_i}^{\rm max}} dE_A\, \phi(E)\, \sigma_{\nu_e}(E)\, R(E,E_A)\, P_{\mu e}(E)\,, \qquad (9.35)$$

where $\phi(E)$ is the neutrino flux, T is the total running time, n_n is the number of target nucleons in the detector, ε is the detector efficiency, and $R(E,E_A)$ is the Gaußian energy resolution function of the detector. σ_{ν_e} is the neutrino interaction cross-section which has been taken from Refs. [232, 233], where the authors estimated the cross-section for water and isoscalar targets. In order to have LAr cross-sections, we have scaled the inclusive charged current cross-sections of water by a factor of 1.06 for neutrino and 0.94 for antineutrino [234, 235]. The quantities E and E_A are the true and reconstructed (anti-)neutrino energies respectively, and L is the path length. In our study, we consider the ν_e

---

[10] The number of positron events can be estimated using Eq. (9.35), by considering appropriate oscillation probability and cross-section. The same is true for $\mu^\pm$ events.

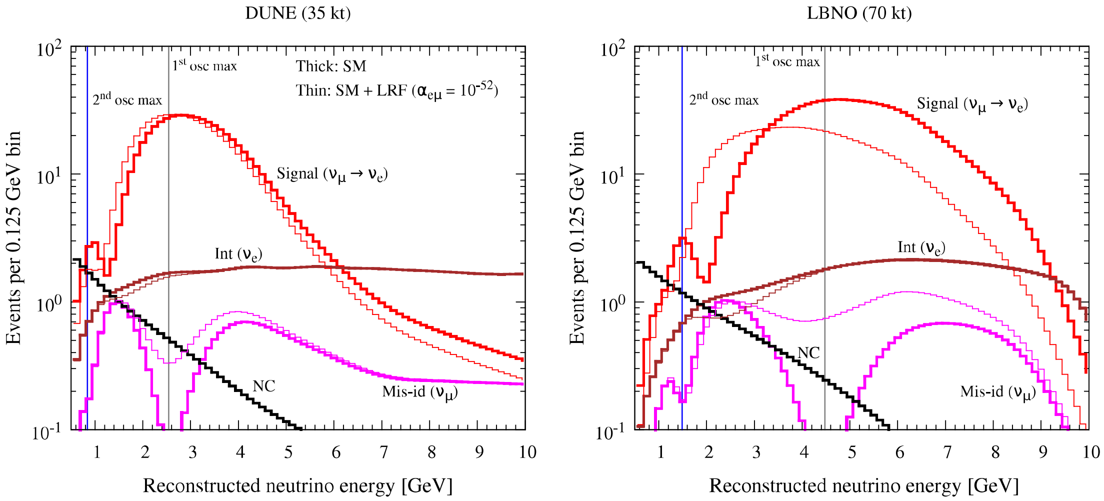

Figure 9.9: Expected signal and background event spectra in the ν_e appearance channel as a function of the reconstructed neutrino energy including the efficiency and background rejection capabilities. The left panel is for the DUNE (35 kt) and the right one is for the LBNO (70 kt). In each panel, the thick lines correspond to the SM case, whereas the thin lines are drawn assuming $\alpha_{e\mu} = 10^{-52}$. In both the panels, the solid grey (blue) vertical lines display the locations of the first (second) oscillation maxima. We assume $\delta_{\rm CP} = 0^\circ$ and NH. For other oscillation parameters, the values are taken from the third column of Table 9.2.

and $\bar{\nu}_e$ appearance channels, where the backgrounds mainly stem from the the intrinsic $\nu_e/\bar{\nu}_e$ contamination of the beam, the number of muon events which will be misidentified as electron events, and the neutral current events. In Fig. 9.9, we show the expected signal and background event spectra as a function of reconstructed neutrino energy including the efficiency and background rejection capabilities. The left panel shows the results for the DUNE set-up with 35 kt far detector mass. The right panel displays the same for the LBNO set-up with 70 kt far detector. In both the panels, the thick lines correspond to the SM case, whereas the thin lines are drawn assuming $\alpha_{e\mu} = 10^{-52}$. In both the set-ups, we can clearly see a systematic downward bias in the reconstructed energy for the neutral current background events due to the final state neutrino included via the migration matrices. The solid grey (blue) vertical lines display the locations of the first (second) oscillation maxima. The red solid histogram shows the signal event spectrum. Note that in the presence of long-range potential, both the signal and background (intrinsic ν_e contamination and misidentified muons) event spectra get modified substantially. For both the baselines, we have considerable number of signal events around the second oscillation maximum. But, these event samples are highly contaminated with the neutral current and other backgrounds at lower energies, limiting their impact. In Table 9.3, we show a comparison between the total signal and background event rates in the $\nu_e/\bar{\nu}_e$ appearance channel for DUNE (35 kt) and LBNO (70 kt) set-ups. For both the set-ups, we assume five years of neutrino run and five years of antineutrino run. For the cases denoted by ‘SM+LRF’, we take $\alpha_{e\mu} = 10^{-52}$. The results are shown for both NH and IH assuming

Channel	**DUNE (35 kt)**		**LBNO (70 kt)**	
	Signal	Background	Signal	Background
	CC	Int+Mis-id+NC=Total	CC	Int+Mis-id+NC=Total
$P_{\mu e}$ (NH, SM)	590	125+29+24=178	1228	115+31+29=175
$P_{\mu e}$ (NH, SM+LRF)	588	123+34+24=181	786	112+53+29=194
$P_{\mu e}$ (IH, SM)	268	129+29+24=182	220	126+31+29=186
$P_{\mu e}$ (IH, SM+LRF)	108	130+33+24=187	49	128+50+29=207
$P_{\bar{\mu}\bar{e}}$ (NH, SM)	116	43+10+7=60	117	33+11+13=57
$P_{\bar{\mu}\bar{e}}$ (NH, SM+LRF)	44	44+12+7=63	22	34+19+13=66
$P_{\bar{\mu}\bar{e}}$ (IH, SM)	210	42+10+7=59	484	30+11+13=54
$P_{\bar{\mu}\bar{e}}$ (IH, SM+LRF)	220	41+12+7=60	343	29+19+13=61

Table 9.3: Comparison of the total signal and background event rates in the $\nu_e/\bar{\nu}_e$ appearance channel for DUNE (35 kt) and LBNO (70 kt) set-ups. Here ‘Int’ means intrinsic beam contamination, ‘Mis-id’ means misidentified muon events, and ‘NC’ stands for neutral current. For the cases denoted by ‘SM+LRF’, we take $\alpha_{e\mu} = 10^{-52}$. The results are shown for both NH and IH assuming $\delta_{\mathrm{CP}} = 0^\circ$. For both the set-ups, we assume five years of neutrino run and five years of antineutrino run.

Channel	**DUNE (35 kt)**		**LBNO (70 kt)**	
	Signal	Background	Signal	Background
	CC	NC	CC	NC
$P_{\mu\mu}$ (NH, SM)	4889	24	5222	29
$P_{\mu\mu}$ (NH, SM+LRF)	5806	24	8949	29
$P_{\mu\mu}$ (IH, SM)	4882	24	5203	29
$P_{\mu\mu}$ (IH, SM+LRF)	5569	24	8519	29
$P_{\bar{\mu}\bar{\mu}}$ (NH, SM)	1751	7	1936	13
$P_{\bar{\mu}\bar{\mu}}$ (NH, SM+LRF)	2012	7	3257	13
$P_{\bar{\mu}\bar{\mu}}$ (IH, SM)	1752	7	1923	13
$P_{\bar{\mu}\bar{\mu}}$ (IH, SM+LRF)	2063	7	3309	13

Table 9.4: Comparison of the total signal and background event rates in the $\nu_\mu/\bar{\nu}_\mu$ disappearance channel for DUNE (35 kt) and LBNO (70 kt) set-ups. For the cases denoted by ‘SM+LRF’, we take $\alpha_{e\mu} = 10^{-52}$. The results are shown for both NH and IH assuming $\delta_{\mathrm{CP}} = 0^\circ$. For both the set-ups, we consider five years of neutrino run and five years of antineutrino run.

$\delta_{\rm CP} = 0^\circ$. The Earth matter effects play an important role for both the baselines which is evident from the fact that in the neutrino channel, the number of expected events is quite large compared to the IH case and in the antineutrino channel, the situation is totally opposite where we have larger event rates for IH than for NH. The relative difference between the number of events for NH and IH is larger for the CERN-Pyhäsalmi baseline than the FNAL-Homestake baseline, since the impact of matter effects is more significant at the 2290 km baseline compared to the 1300 km baseline. In the presence of long-range potential with a benchmark choice of $\alpha_{e\mu} = 10^{-52}$, qualitatively, the trend remains the same as mentioned above. Table 9.3 clearly shows that in all the cases, the most dominant contribution to the background comes from the intrinsic $\nu_e/\bar{\nu}_e$ beam contamination. Note that though the total signal event rate for the DUNE set-up in the neutrino mode with NH, does not change much due to long-range potential with $\alpha_{e\mu} = 10^{-52}$, but, the shape of the signal event spectrum gets affected by considerable amount as can be seen from Fig. 9.9, which enables us to place tight constraints on $\alpha_{e\mu}$ as we discuss in the results section. In our simulation, we also include the information coming from the $\nu_\mu/\bar{\nu}_\mu$ disappearance channels. For these type of channels, neutral current events are the main source of background. Table 9.4 shows the total signal and background event rates in the $\nu_\mu/\bar{\nu}_\mu$ disappearance channels for both the set-ups, considering five years of neutrino run and five years of antineutrino run. For the cases marked by 'SM+LRF', we take $\alpha_{e\mu} = 10^{-52}$ and we present results for both NH and IH assuming $\delta_{\rm CP} = 0^\circ$. Interestingly, the $\nu_\mu/\bar{\nu}_\mu$ disappearance channels are also quite sensitive to the long-range potential and in all the cases, we see a significant change in the total signal event rates with $\alpha_{e\mu} = 10^{-52}$ as compared to the SM case. Also, the rates are different for NH and IH in the presence of long-range potential. The $\nu_\mu/\bar{\nu}_\mu$ disappearance channels also play an important role to constrain the atmospheric oscillation parameters in the fit.

9.3.2 Bi-events Plot

In this section, we make an attempt to unravel the impact of long-range potential with the help of bi-events plot. In Fig. 9.10, we have plotted ν_e vs. $\bar{\nu}_e$ appearance events, for DUNE (left panel) and LBNO (right panel), considering both NH and IH and with and without long-range potential. Since $\delta_{\rm CP}$ is not known, events are generated for the full range $[-180^\circ, 180^\circ]$, leading to the ellipses. For the cases labelled by 'SM+LRF', we

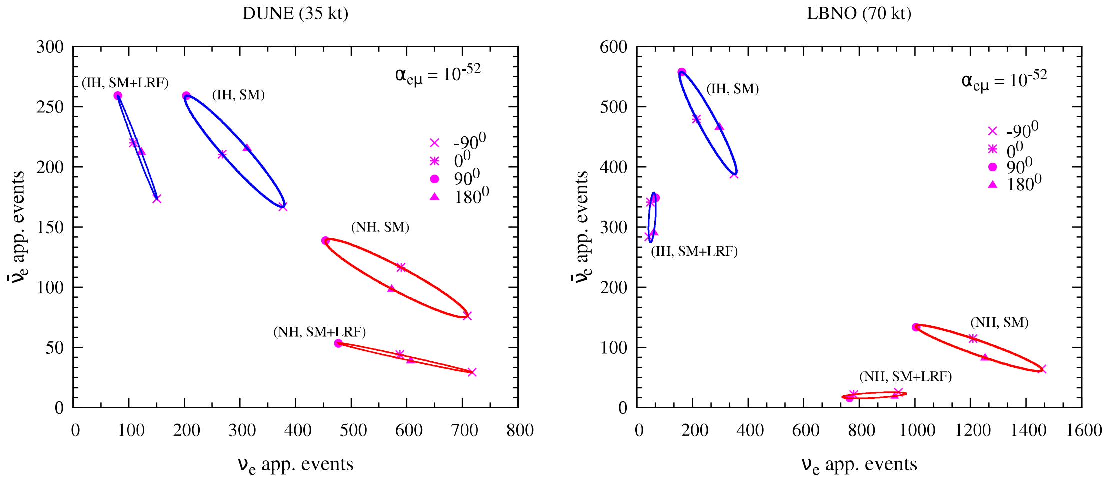

Figure 9.10: Bi-events (ν_e and $\bar{\nu}_e$ appearance) plots for NH and IH with and without long-range potential. The ellipses are due to all possible $\delta_{\rm CP}$ values. For the cases labelled by 'SM+LRF', we take $\alpha_{e\mu} = 10^{-52}$. The left panel is for the DUNE set-up (35 kt) and the right panel is for the LBNO set-up (70 kt).

take $\alpha_{e\mu} = 10^{-52}$. We generate these plots with $\sin^2\theta_{23} = 0.5$ as mentioned in Table 9.2. The ellipses in Fig. 9.10 suggest that both the set-ups can discriminate between NH and IH at high confidence level, irrespective of the choice of $\delta_{\rm CP}$, and the presence of long-range potential with $\alpha_{e\mu} = 10^{-52}$ does not spoil this picture. We can see from the left panel that for the DUNE set-up, the antineutrino (neutrino) event rates get reduced for NH (IH) with LRF as compared to the SM case. But, for CERN-Pyhäsalmi baseline (see right panel) with more matter effect, both the neutrino and antineutrino event rates get diminished for NH and IH in the presence of long-range potential as compared to the SM case. Now, let us make an attempt to understand this behavior. In the presence of long-range potential, the locations of the first oscillation maxima shift towards lower energies (see the upper panels of Fig. 9.5 and Fig. 9.7), where both the fluxes and the interaction cross-sections are small. On the contrary, at higher energies, we see a suppression in the probability where we have most of the neutrino fluxes and the cross-sections are also high at these energies. These opposite bahaviors are responsible for the large depletions in the event rates. Fig. 9.10 also portrays that the asymmetries between the neutrino and antineutrino appearance events are largest for the combinations: (NH, $\delta_{\rm CP} = -90°$) and (IH, $\delta_{\rm CP} = 90°$). One striking feature emerging from both the panels is that all the ellipses get shrunk in the presence of long-range potential, reducing the differences in the number of events due to the CP-conserving and CP-violating phases. It ultimately affects the

CP-coverage for the leptonic CP-violation searches, where we study the choices of the CP phase, $\delta_{\rm CP}$ which can be distinguished from both 0° and 180° at a given confidence level. The right panel shows that this effect is more prominent for the LBNO set-up, severely limiting its discovery reach for CP-violation which we discuss in detail in the results section.

9.4 Simulation Method

In this section, we give a brief description of the numerical technique and analysis procedure which we adopt to estimate the physics reach of the experimental set-ups. We have made suitable changes in the GLoBES software [219, 220] to obtain our results. The entire numerical analysis is performed using the full three-flavor oscillation probabilities. Unless stated otherwise, we generate our simulated data considering the true values of the oscillation parameters given in the third column of Table 9.2. These choices of the oscillation parameters are well within their 1σ allowed ranges which are obtained in recent global fit analysis [254]. In the fit, we marginalize over test $\sin^2\theta_{23}$ and test $\delta_{\rm CP}$ in their allowed ranges which are given in the fourth column of Table 9.2, without assuming any prior on these parameters. We also marginalize over both the hierarchy choices in the fit for all the analyses, except for the mass hierarchy discovery studies where our goal is to exclude the wrong hierarchy in the fit. We keep θ_{13} fixed in the fit as the Daya Bay experiment is expected to achieve a relative 1σ precision of $\sim 3\%$ by the end of 2017 [187], and needless to say that the global oscillation data will severely constrain θ_{13} beyond the Daya Bay limit before these future experiments will come online. For the atmospheric mass-squared splitting, we take the true value of $\Delta m^2_{\mu\mu} = \pm\, 2.4 \times 10^{-3}$ eV^2 where positive (negative) sign is for NH (IH), and we do not marginalize over this parameter in the fit since the projected combined data from the currently running T2K and NOνA experiments will be able to improve the precision in $|\Delta m^2_{\mu\mu}|$ to sub-percent level for maximal θ_{23} [259]. On top of the standard three-flavor oscillation parameters, we have also the LRF parameter $\alpha_{e\mu}$ which enters into the oscillation probability. As far as the true and test values of $\alpha_{e\mu}$ are concerned, we vary our choices in the range 10^{-54} to 10^{-51}, where the lower limit[11] corresponds to the cases where the oscillation probabilities *almost* over-

---

[11] If the range of the long-range force is equal or larger than our distance from the galactic center, then the collective long-range potential due to all the electrons in the galaxy becomes significant. In such cases,

lap with the SM cases for the set-ups that we consider in this work. We take the upper limit of $\alpha_{e\mu}$ as 10^{-51} which covers all the existing bounds on this parameter available from the oscillation experiments as discussed in section 9.1.2. To calculate all the physics sensitivities of these two experiments, we have used the same Poissonian χ^2 function as discussed in section 5.2 with all the details given in the same section. However it should be noted here that in that definition of χ^2, λ^{test} must be replaced as $\alpha_{e\mu}(\text{test})$ and λ^{true} must be replaced by $\alpha_{e\mu}(\text{true})$ in presence of long-range force. For both the set-ups, we consider $\pi^s = 5\%$ for signal normalization error and $\pi^b = 5\%$ for the background normalization error in case of appearance and disappearance channels both. Now to estimate the total χ^2, we add the χ^2 contributions coming from all the relevant channels in a given experiment in the following way

$$\chi^2_{\text{total}} = \chi^2_{\nu_\mu \to \nu_e} + \chi^2_{\nu_\mu \to \nu_\mu} + \chi^2_{\bar{\nu}_\mu \to \bar{\nu}_e} + \chi^2_{\bar{\nu}_\mu \to \bar{\nu}_\mu}\,, \tag{9.36}$$

where we assume that all these channels are completely uncorrelated, all the energy bins in a given channel are fully correlated, and the systematic errors on signal and background are fully uncorrelated. Finally, χ^2_{total} is marginalized in the fit over the oscillation parameters, both the hierarchy choices, the LRF parameter $\alpha_{e\mu}$ (as needed), and the systematic parameters to obtain $\Delta\chi^2_{\text{min}}$.

9.5 Results

In this section, we report our main findings. First, we present the expected constraints on $\alpha_{e\mu}$ from the proposed DUNE and LBNO experiments. Next, we quantify the discovery reach for $\alpha_{e\mu}$ of these future facilities. Then, we address how the flavor-dependent LRF, mediated by the extremely light $L_e - L_\mu$ gauge boson can affect the CP-violation searches and the mass hierarchy measurements at these upcoming facilities.

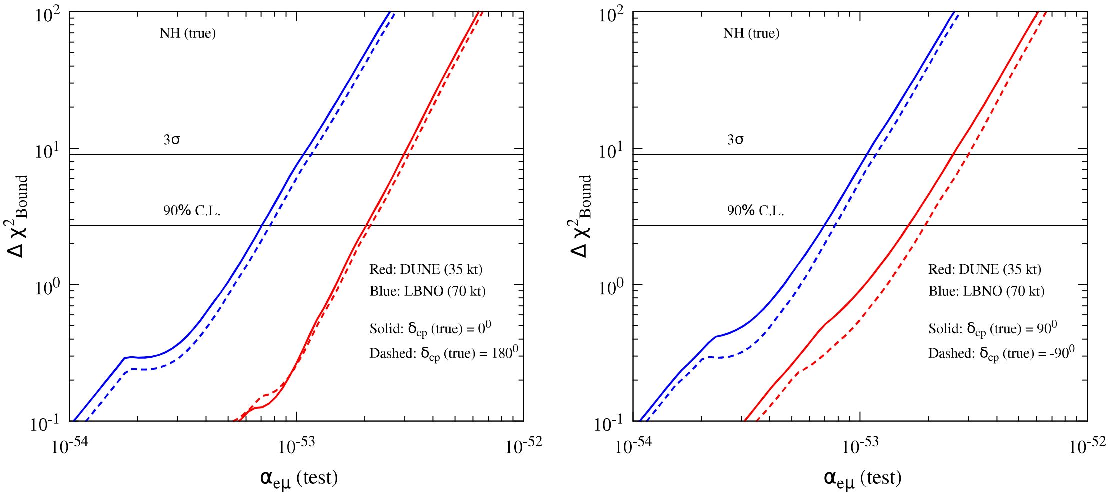

Figure 9.11: Expected bounds on $\alpha_{e\mu}$ from the DUNE (35 kt) and LBNO (70 kt) experiments in the scenarios when the data show no signal of LRF. Results are given for four different choices of true values of $\delta_{\rm CP}$. The left panel is for CP-conserving choices: $\delta_{\rm CP}$(true) = 0° (solid lines), 180° (dashed lines). The right panel is for maximal CP-violating choices: $\delta_{\rm CP}$(true) = 90° (solid lines), −90° (dashed lines). In all the cases, we assume NH as true hierarchy.

Expt.	$\delta_{\rm CP}$(true)	90% C.L.	3σ	Expt.	$\delta_{\rm CP}$(true)	90% C.L.	3σ
DUNE (35 kt)	0^0	2.0×10^{-53}(NH) 2.1×10^{-53}(IH)	3.0×10^{-53}(NH) 3.1×10^{-53}(NH)	**LBNO (70 kt)**	0^0	7.0×10^{-54}(NH) 7.8×10^{-54}(IH)	1.1×10^{-53}(NH) 1.2×10^{-53}(IH)
	180^0	2.1×10^{-53}(NH) 2.0×10^{-53}(IH)	3.1×10^{-53}(NH) 3.0×10^{-53}(IH)		180^0	7.6×10^{-54}(NH) 7.0×10^{-54}(IH)	1.2×10^{-53}(NH) 1.1×10^{-53}(IH)
	90^0	1.7×10^{-53}(NH) 1.8×10^{-53}(IH)	2.7×10^{-53}(NH) 2.8×10^{-53}(IH)		90^0	7.0×10^{-54}(NH) 7.0×10^{-54}(IH)	1.1×10^{-53}(NH) 1.1×10^{-53}(IH)
	-90^0	1.9×10^{-53}(NH) 1.5×10^{-53}(IH)	3.0×10^{-53}(NH) 2.4×10^{-53}(IH)		-90^0	7.8×10^{-54}(NH) 6.0×10^{-54}(IH)	1.2×10^{-53}(NH) 9.6×10^{-54}(IH)

Table 9.5: The expected bounds on $\alpha_{e\mu}$ from the DUNE (35 kt) and LBNO (70 kt) experiments if there is no signal of LRF in the data. The results are presented at 90% and 3σ confidence levels for four different choices of true values of $\delta_{\rm CP}$: 0°, 180°, 90°, and −90°. For each $\delta_{\rm CP}$(true) value, we show the results for both the choices of true hierarchy: NH and IH.

9.5.1 Expected Constraints on the Effective Gauge Coupling $\alpha_{e\mu}$

In this section, we estimate the upper bounds on $\alpha_{e\mu}$ from the proposed DUNE and LBNO experiments if there is no signal of LRF in the data. This performance indicator corresponds to the new upper limit on $\alpha_{e\mu}$ if the experiment does not see a signal of LRF in oscillations. We simulate this situation in our analysis by generating the data at $\alpha_{e\mu}$(true) = 0 and fitting it with some non-zero value of $\alpha_{e\mu}$ by means of the χ^2 technique as

---

these experimental set-ups can be sensitive to even lower values of $\alpha_{e\mu}$ [119].

outlined in section 9.4. The corresponding $\Delta\chi^2_{\rm Bound}$ obtained after marginalizing over oscillation parameters (θ_{23}, $\delta_{\rm CP}$, and mass hierarchy) and systematic parameters in the fit, is plotted in Fig. 9.11 as a function of $\alpha_{e\mu}$ (test), which gives a measure of the sensitivity reach of the DUNE or LBNO set-up to the effective gauge coupling of the LRF. New limits are given for four different choices of true values of $\delta_{\rm CP}$. The left panel is for CP-conserving choices: $\delta_{\rm CP}$(true) = 0° (solid lines), 180° (dashed lines). The right panel is for maximal CP-violating choices: $\delta_{\rm CP}$(true) = 90° (solid lines), −90° (dashed lines). In all the cases, we assume NH as true hierarchy. Fig. 9.11 clearly shows that the LBNO set-up with 70 kt detector mass can place better limits on $\alpha_{e\mu}$ as compared to the DUNE set-up with 35 kt detector and the limits are not very sensitive to the choice of unknown $\delta_{\rm CP}$(true) for both the set-ups. Table 9.5 lists the precise upper limits on $\alpha_{e\mu}$ which are expected from these future facilities if there is no trace of LRF in the data. We present the bounds at 90% (1.64σ) and 3σ confidence levels[12] for four different choices of true values of $\delta_{\rm CP}$: 0°, 180°, 90°, and −90°. For each $\delta_{\rm CP}$(true) value, we give the results for both NH and IH as true hierarchy choice. For an example, if $\delta_{\rm CP}$(true) = −90° and true hierarchy is NH, then the 90% C.L. limit from the DUNE (LBNO) experiment is $\alpha_{e\mu} < 1.9 \times 10^{-53}$ (7.8×10^{-54}), suggesting that the constraint from the LBNO experiment is ~ 2.4 times better than the DUNE set-up[13]. This future limit from the DUNE (LBNO) experiment is ~ 30 (70) times better than the existing limit[14] from the SK experiment [116] which is also mainly sensitive to the atmospheric mass scale like long-baseline experiments. At 3σ, we see the same relative improvement in the LBNO experiment in constraining $\alpha_{e\mu}$ compared to the DUNE set-up. Table 9.5 also suggests that the limits are not highly dependent on the true choices of mass hierarchy. The variation in the upper limits on $\alpha_{e\mu}$ is also not significant as we vary $\delta_{\rm CP}$(true) in the range -180° to 180° as can be seen from Fig. 9.12, where we give the expected bounds at 3σ and 5σ confidence levels from both the set-ups assuming NH as true hierarchy. Next, we discuss the discovery reach for $\alpha_{e\mu}$ if we find a positive signal of LRF in the expected event spectra at DUNE

---

[12] To calculate this, we use the relation $n\sigma = \sqrt{\Delta\chi^2_{\rm min}}$. In [261], it was shown that the above relation is valid in the frequentist method of hypothesis testing.

[13] We have checked that the larger detector mass (two times) in the LBNO set-up compared to the DUNE set-up is partially responsible for this improvement in the sensitivity, but also the larger path length with more matter effect plays an important role in this direction.

[14] This limit is quite old and was derived in a two-flavor scheme assuming $\theta_{13} = 0°$ [116]. One needs to revise this limit using the presently available full data set from the SK experiment in light of the non-zero and large θ_{13}.

and LBNO.

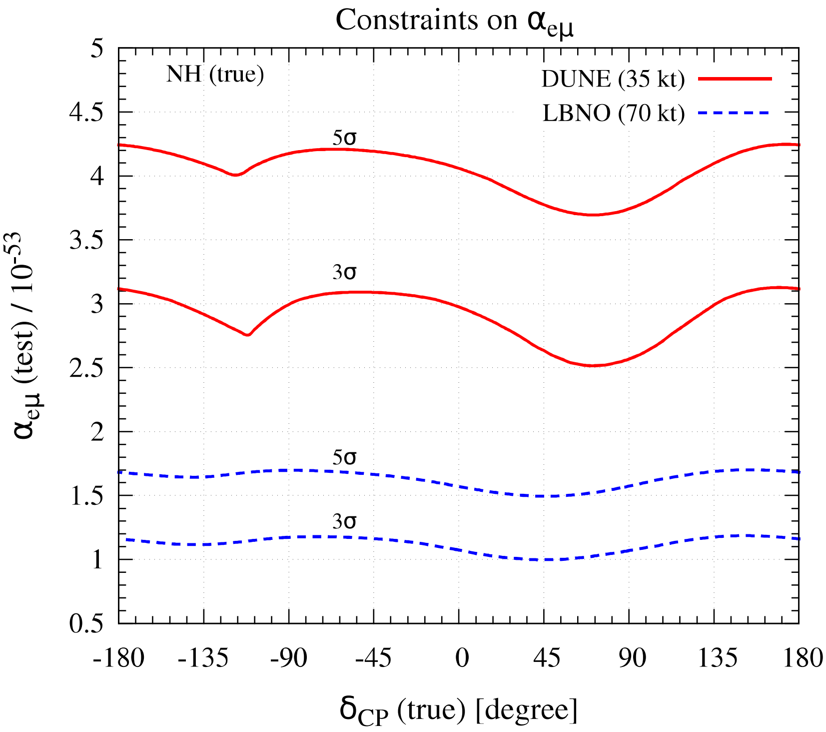

Figure 9.12: Constraints on $\alpha_{e\mu}$ as a function of true value of δ_{CP} assuming NH as true hierarchy. Results are shown for DUNE (35 kt) and LBNO (70 kt) at 3σ and 5σ confidence levels.

9.5.2 Discovery Reach for $\alpha_{e\mu}$

How good are our chances of observing a positive signal for LRF and hence $\alpha_{e\mu}$ in these proposed facilities? We answer this question in terms of the parameter indicator which we call the "discovery reach" of the experiment for $\alpha_{e\mu}$. We define this performance indicator as the expected lower limit on true values of $\alpha_{e\mu}$ above which the projected data at DUNE or LBNO would give us a signal for LRF at a certain confidence level. To find these limiting values, we simulate the data for various true values of $\alpha_{e\mu}$ and fit it with a predicted event spectrum corresponding to $\alpha_{e\mu} = 0$. We marginalize over θ_{23}, δ_{CP}, mass hierarchy, and systematic parameters in the fit to estimate the resultant $\Delta\chi^2_{\mathrm{Discovery}}$ which is plotted in Fig. 9.13 for DUNE (35 kt) and LBNO (70 kt) set-ups, considering four different choices of true values of δ_{CP}. In the left panel, we take the CP-conserving choices: $\delta_{\mathrm{CP}}(\mathrm{true}) = 0°$ (solid lines), 180° (dashed lines). In the right panel, we consider the maximal CP-violating choices: $\delta_{\rm CP}$(true) = 90° (solid lines), $-90°$ (dashed lines). In all the cases, we take NH as true hierarchy. The nature of the curves in Fig. 9.13 are quite similar to the curves which are shown in Fig. 9.11, and LBNO with 70 kt detector has better discovery reach for $\alpha_{e\mu}$ as compared to DUNE with 35 kt, like in the case of constraints on $\alpha_{e\mu}$. In Table 9.6, we give the precise lower limits on true values of $\alpha_{e\mu}$ which can be separated from $\alpha_{e\mu} = 0$ in the fit at 90% and 3σ confidence levels. The results are given for both the set-ups and for four different choices of true values of $\delta_{\rm CP}$: 0°, 180°, 90°, and $-90°$. For each $\delta_{\rm CP}$(true) value, we show the results for both the choices of true hierarchy: NH and IH. If we compare the entries in Table 9.6 and Table 9.5, then we can see that the values of the discovery reach for $\alpha_{e\mu}$ are slightly different than the constraints on $\alpha_{e\mu}$ at a given confidence level and for the same choices of true oscillation parameters. Also, we can see that the values of discovery reach are marginally dependent on the choices of true $\delta_{\rm CP}$ and mass hierarchy as we have seen for the constraints in the previous section.

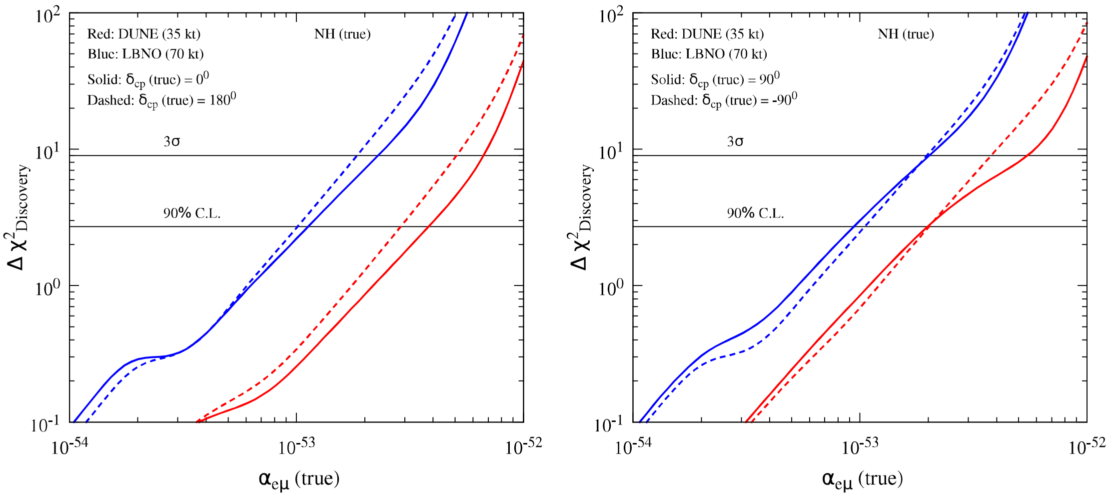

Figure 9.13: $\Delta\chi^2_{\rm Discovery}$ showing the discovery reach for $\alpha_{e\mu}$ expected from the DUNE (35 kt) and LBNO (70 kt) set-ups in the cases when one finds a signal of LRF in the data. Results are given for four different choices of true values of $\delta_{\rm CP}$. The left panel is for CP-conserving choices: $\delta_{\rm CP}$(true) = 0° (solid lines), 180° (dashed lines). The right panel is for maximal CP-violating choices: $\delta_{\rm CP}$(true) = 90° (solid lines), $-90°$ (dashed lines). In all the cases, we assume NH as true hierarchy.

Expt.	δ_{CP}(true)	90% C.L.	3σ	Expt.	δ_{CP}(true)	90% C.L.	3σ
DUNE (35 kt)	0^0	3.8×10^{-53}(NH) 3.7×10^{-53}(IH)	6.5×10^{-53}(NH) 7.2×10^{-53}(IH)	**LBNO (70 kt)**	0^0	1.2×10^{-53}(NH) 1.4×10^{-53}(IH)	2.2×10^{-53}(NH) 2.6×10^{-53}(IH)
	180^0	2.9×10^{-53}(NH) 4.0×10^{-53}(IH)	5.0×10^{-53}(NH) 7.8×10^{-53}(IH)		180^0	9.5×10^{-54}(NH) 1.4×10^{-53}(IH)	1.9×10^{-53}(NH) 2.6×10^{-53}(IH)
	90^0	2.0×10^{-53}(NH) 2.3×10^{-53}(IH)	5.4×10^{-53}(NH) 4.4×10^{-53}(IH)		90^0	9.0×10^{-54}(NH) 1.0×10^{-53}(IH)	2.0×10^{-53}(NH) 2.0×10^{-53}(IH)
	-90^0	2.0×10^{-53}(NH) 1.8×10^{-53}(IH)	3.7×10^{-53}(NH) 4.8×10^{-53}(IH)		-90^0	1.0×10^{-53}(NH) 7.6×10^{-54}(IH)	2.0×10^{-53}(NH) 1.5×10^{-53}(IH)

Table 9.6: The discovery reach for $\alpha_{e\mu}$ as expected from the DUNE (35 kt) and LBNO (70 kt) experiments if the data show a signal of LRF. The results are presented at 90% and 3σ confidence levels for four different choices of true values of δ_{CP}: 0°, 180°, 90°, and $-90°$. For each δ_{CP}(true) value, we show the results for both the choices of true hierarchy: NH and IH.

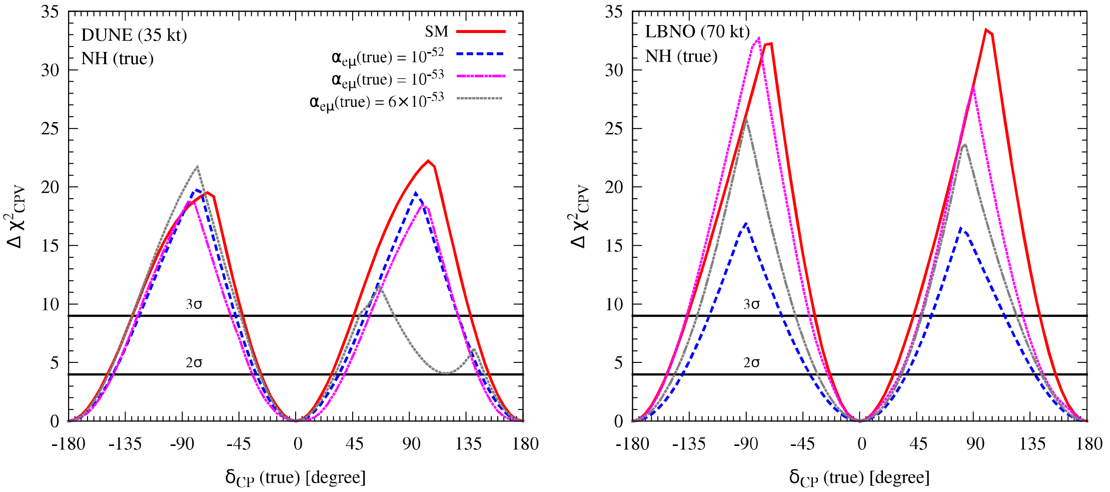

Figure 9.14: CP-violation discovery reach as a function of true value of δ_{CP} assuming NH as true hierarchy. In the left panel, we show the results for DUNE (35 kt) and the right panel is for LBNO (70 kt). For the 'SM' case, $\alpha_{e\mu} = 0$ in the data and also in the fit. For each δ_{CP}(true), we also give the results generating the data with three different true values of $\alpha_{e\mu}$ which are mentioned in the figure legends. In all these three cases, in the fit, we marginalize over test values of $\alpha_{e\mu}$ in its allowed range. The rest of the simulation details are exactly similar to the 'SM' case (see text for details).

9.5.3 How Robust are CP-violation Searches in Presence of LRF?

This section is devoted to study how the long-range potential due to $L_e - L_\mu$ symmetry affects the CP-violation search which is the prime goal of these future facilities. Can we reject both the CP-conserving values of 0°, 180° at a given confidence level? The performance indicator "discovery reach of leptonic CP-violation" addresses this question and obviously, this measurement becomes extremely difficult for the δ_{CP} values which are

True Hierarchy		**DUNE (35 kt)**		**LBNO (70 kt)**	
		SM	$\alpha_{e\mu}$(true) = 10^{-52}	SM	$\alpha_{e\mu}$(true) = 10^{-52}
2σ C.L.	NH (true)	0.67	0.62	0.71	0.56
	IH (true)	0.68	0.59	0.73	0.44
3σ C.L.	NH (true)	0.48	0.41	0.55	0.30
	IH (true)	0.53	0.37	0.60	0.12

Table 9.7: Fraction of $\delta_{\rm CP}$(true) for which a discovery is possible for CP-violation from DUNE (35 kt) and LBNO (70 kt) set-ups at 2σ and 3σ confidence levels. We show the coverage in $\delta_{\rm CP}$(true) for both the choices of true hierarchy: NH and IH. For the 'SM' cases, we consider $\alpha_{e\mu} = 0$ in the data and also in the fit. We also give the results generating the data with $\alpha_{e\mu}(\text{true}) = 10^{-52}$ and in the fit, we marginalize over test values of $\alpha_{e\mu}$ in its allowed range. The rest of the simulation details are exactly similar to the 'SM' case (see text for details).

close to 0° and 180°. In Fig. 9.14, we present the CP-violation discovery reach of DUNE (left panel) and LBNO (right panel) as a function of true value of $\delta_{\rm CP}$ assuming NH as true hierarchy. In this plot, we generate our predicted event spectrum (data) considering the true value of $\delta_{\rm CP}$ as shown in the x-axis, along with the other true values of the oscillation parameters given in the third column of Table 9.2. Then, we estimate the various theoretical event spectra assuming the test $\delta_{\rm CP}$ to be the CP-conserving values 0° and 180°, and by varying simultaneously θ_{23} in its 3σ allowed range and both the choices of mass hierarchy. We calculate the $\Delta\chi^2$ between each set of predicted and theoretical event spectra using the procedure described in section 9.4. The smallest of all such $\Delta\chi^2$ values: $\Delta\chi^2_{\rm CPV}$ is plotted in Fig. 9.14 as a function of $\delta_{\rm CP}$(true) in the range -180° to 180°. In both the panels, the solid red lines depict the 'SM' case where $\alpha_{e\mu} = 0$ in the data and also in the fit. For each $\delta_{\rm CP}$(true), we also give the results generating the data with three different true values of $\alpha_{e\mu}$ which are mentioned in the figure legends. In all these three cases, in the fit, we also marginalize over test values of $\alpha_{e\mu}$ in the range 10^{-54} to 10^{-51} along with the other three-flavor oscillation parameters as discussed before. Fig. 9.14 clearly shows that the CP-violation discovery reach can be altered by substantial amount as compared to the 'SM' case depending on the true choice of $\alpha_{e\mu}$. In case of $\alpha_{e\mu}(\text{true}) = 6 \times 10^{-53}$, we see a large suppression in the CP-violation discovery reach of DUNE (left panel) in the range $45° \leq \delta_{\rm CP}(\text{true}) \leq 135°$. We have checked that this mainly happens due to the marginalization over θ_{23} in the fit where we vary $\sin^2\theta_{23}$ over a wide range (0.38 to 0.64) without imposing any prior on it. In case $\alpha_{e\mu}(\text{true}) = 10^{-52}$, the LBNO set-up (right panel) suffers a large depletion in the CP-violation discovery reach which can be easily explained with the help of bi-events plot (Fig. 9.10) shown in section 9.3.2. In the right panel of Fig. 9.10, we have seen a large reduction in the ν and $\bar{\nu}$ event rates for CERN-Pyhäsalmi baseline with $\alpha_{e\mu} = 10^{-52}$ and this is true for both NH and IH. The differences in the number of events for the CP-conserving and CP-violating phases get reduced as the ellipses in Fig. 9.10 get shrunk in the presence of LRF, severely deteriorating the CP-violation discovery reach of LBNO as can be seen from the right panel of Fig. 9.14. Table 9.7 also validates this result, where we compare the precise fraction of $\delta_{\rm CP}$(true) for which a discovery is possible for CP-violation from LBNO (70 kt) and DUNE (35 kt) at 2σ and 3σ confidence levels. For LBNO set-up with true NH and $\alpha_{e\mu}$(true) = 10^{-52}, the coverage in $\delta_{\rm CP}$(true) at 3σ C.L. reduces to 30% from 55% as we have in the 'SM' case. In case of true IH, the impact of long-range potential is even more dramatic for these future facilities. At 3σ with $\alpha_{e\mu}$(true) = 10^{-52}, their CP-violation reach is quite minimal: only 12% for LBNO and 37% for DUNE while in the 'SM' framework, the coverage is 60% for LBNO and 53% for DUNE. Since, the sign of the long-range potential $V_{e\mu}$ is opposite for neutrino and antineutrino, it affects the neutrino and antineutrino oscillation probabilities in different fashion. This feature introduces fake CP-asymmetry like the SM matter effect and severely limits the CP-violation search in these long-baseline facilities which can be clearly seen from Table 9.7. Finally, to see the complete picture, the fraction of $\delta_{\rm CP}$(true) for which a discovery is possible for CP-violation is shown in Fig. 9.15 as a function of true value of $\alpha_{e\mu}$ assuming NH as true hierarchy. In each panel, we compare the performances of DUNE (35 kt) and LBNO (70 kt) which are shown by red and blue lines respectively. We give the results at 2σ (left panel) and 3σ (right panel) confidence levels. In both the panels, the solid horizontal lines depict the 'SM' case where $\alpha_{e\mu} = 0$ in the data and also in the fit. For the 'SM+LRF' case (dashed lines), the data is generated with the true value of $\alpha_{e\mu}$ as shown in the x-axis and in the fit, we marginalize over test values of $\alpha_{e\mu}$ in its allowed range. The rest of the simulation details are exactly similar to the 'SM' case as discussed before. For the values close to $\alpha_{e\mu}$(true) = 10^{-54}, the event spectra in the data is almost similar to the 'SM' case, but since we allow $\alpha_{e\mu}$ to vary in the fit in the range 10^{-54} to 10^{-51} along with the other three-flavor oscillation parameters as discussed before, we see a small suppression in the fraction of $\delta_{\rm CP}$(true). In both the panels, around $\alpha_{e\mu}$(true) = 6×10^{-53}, the CP-violation discovery reach of DUNE deteriorates substantially, which we also observe in Fig. 9.14, and the marginalization over θ_{23} is mainly responsible for this as we have already discussed. Once

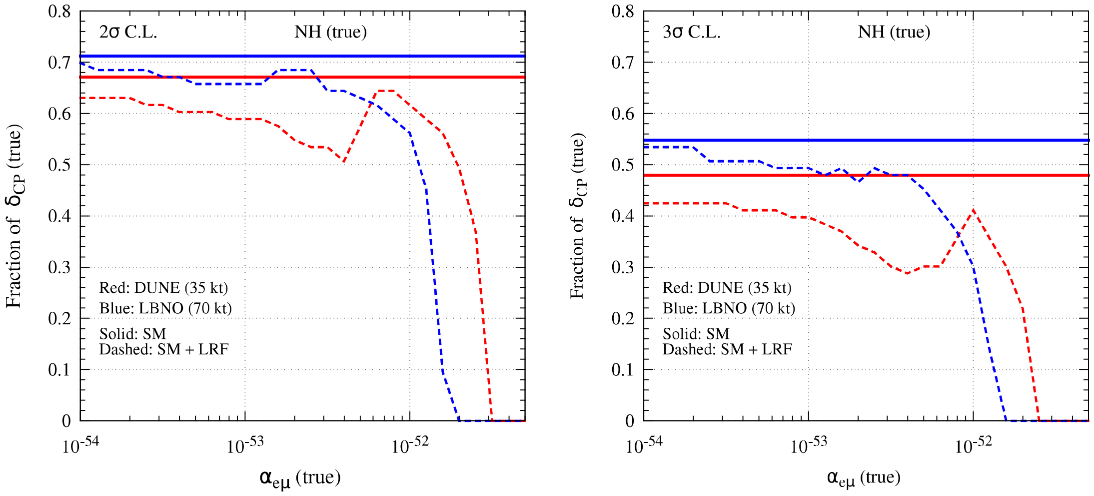

Figure 9.15: Fraction of $\delta_{\rm CP}$(true) for which a discovery is possible for CP-violation is plotted as a function of true value of $\alpha_{e\mu}$ assuming NH as true hierarchy. In each panel, we compare the performances of DUNE (35 kt) and LBNO (70 kt) which are shown by red and blue lines respectively. We give the results at 2σ (left panel) and 3σ (right panel) confidence levels. In both the panels, the solid lines portray the 'SM' scenario where $\alpha_{e\mu}$ = 0 in the data and also in the fit. For the 'SM+LRF' case (dashed lines), the data is generated with the true value of $\alpha_{e\mu}$ as shown in the x-axis and in the fit, we marginalize over test values of $\alpha_{e\mu}$ in its allowed range. The rest of the simulation details are exactly similar to the 'SM' case (see text for details).

$\alpha_{e\mu}$(true) approaches toward 10^{-52}, the coverages in $\delta_{\rm CP}$(true) for which CP-violation can be observed, shrink very rapidly for both the set-ups, and ultimately around $\alpha_{e\mu}$(true) = 2×10^{-52}, the coverages almost become zero. We can understand this feature from our discussions in section 9.2.1, where we have seen that in the presence of $V_{e\mu}$, as we increase E, θ_{13}^{m} quickly approaches toward 45° (see middle panel of Fig. 9.1), and the resonance occurs at much lower energies as compared to the SM case. Finally, θ_{13}^{m} reaches to 90° as we further increase E, and the $\nu_\mu \to \nu_e$ oscillation probabilities vanish for most of the energies where we have significant amount of neutrino flux. It causes a huge suppression in the event rates and as a result, the sensitivity goes to zero. Next, we turn our attention to the mass hierarchy discovery potential of DUNE and LBNO.

9.5.4 Impact of LRF on Mass Hierarchy Measurements

The large Earth matter effects at both the DUNE and LBNO baselines enhance the separation between the oscillation spectra of NH and IH, and hence, we have large differences in the event rates for NH and IH, leading to unprecedented sensitivity toward neutrino mass

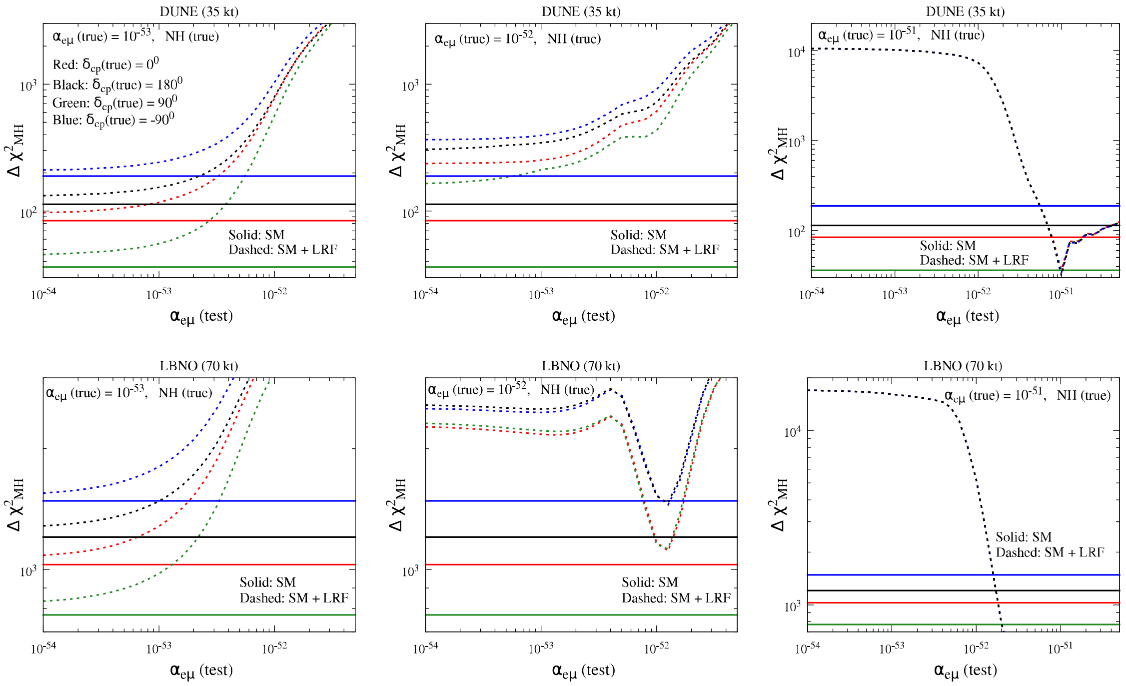

Figure 9.16: Discovery reach for mass hierarchy as a function of test $\alpha_{e\mu}$ assuming NH in the data and IH in the fit. The upper (lower) panels are for DUNE (LBNO). We give the results for four different true values of $\delta_{\rm CP}$ in each panel. The solid horizontal lines in each panel show the 'SM' case where $\alpha_{e\mu} = 0$ in the data and also in the fit. For the 'SM+LRF' case (dashed lines), the data is generated with the true value of $\alpha_{e\mu} = 10^{-53}$ (left panels), 10^{-52} (middle panels), and 10^{-51} (right panels). Then, in the fit, we vary the test values of $\alpha_{e\mu}$ while marginalizing over θ_{23} and $\delta_{\rm CP}$. The rest of the simulation details are exactly similar to the 'SM' case (see text for details). Also, note that the ranges in the x-axis and y-axis are different in some of the panels.

hierarchy. Now, it would be quite interesting to see how robust are these measurements in the presence of LRF? A 'discovery' of the mass hierarchy is a discrete measurement and is defined as the ability to exclude any degenerate solution for the wrong (fit) hierarchy at a given confidence level. For hierarchy sensitivity, we first assume NH to be the true hierarchy and we choose a true value of $\delta_{\rm CP}$ and $\alpha_{e\mu}$. We compute the NH event spectrum for these assumptions and the other true values of the oscillation parameters (see the third column of Table 9.2) and label it to be data. Then, we estimate the various theoretical event spectra assuming IH and a test value of $\alpha_{e\mu}$ as shown in the x-axis of Fig. 9.16, and by varying simultaneously test θ_{23} in its 3σ allowed range and test $\delta_{\rm CP}$ in the full allowed range (-180° to 180°). Next, we compute the $\Delta\chi^2$ between each set of predicted and theoretical event spectra using the numerical technique described in section 9.4. The smallest of all such $\Delta\chi^2$ values: $\Delta\chi^2_{\rm MH}$ is shown in Fig. 9.16 as a function of $\alpha_{e\mu}$(test) for

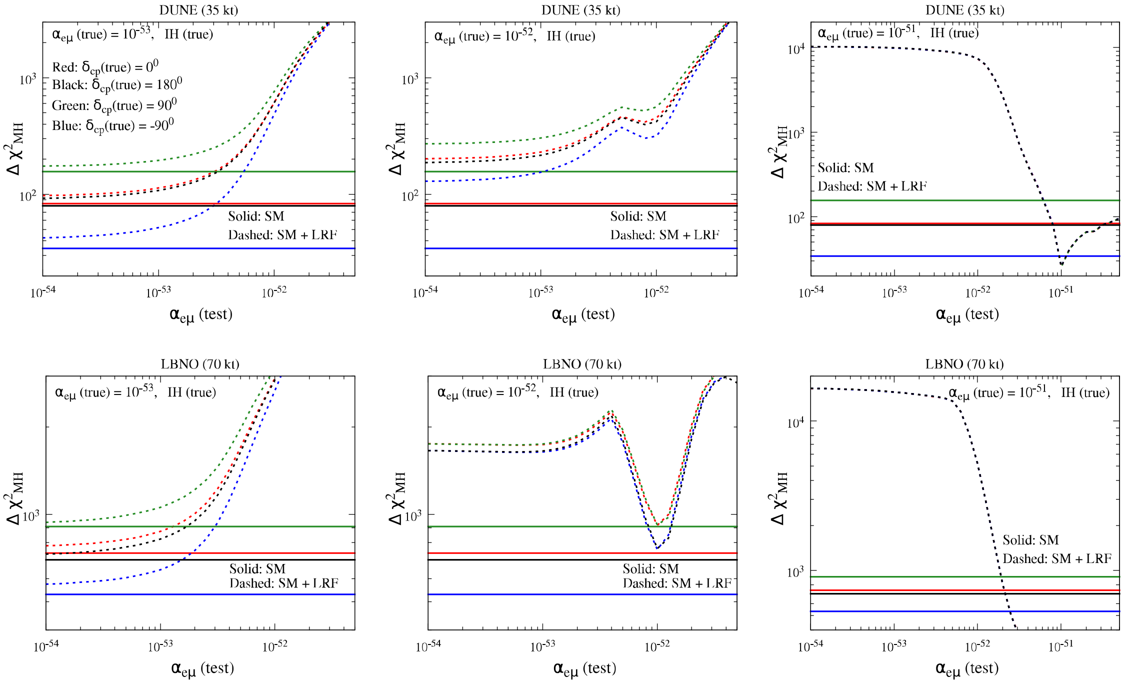

Figure 9.17: Discovery reach for mass hierarchy as a function of test $\alpha_{e\mu}$ assuming IH in the data and NH in the fit. The upper (lower) panels are for DUNE (LBNO). We give the results for four different true values of δ_{CP} in each panel. The solid horizontal lines in each panel show the 'SM' case where $\alpha_{e\mu} = 0$ in the data and also in the fit. For the 'SM+LRF' case (dashed lines), the data is generated with the true value of $\alpha_{e\mu} = 10^{-53}$ (left panels), 10^{-52} (middle panels), and 10^{-51} (right panels). Then, in the fit, we vary the test values of $\alpha_{e\mu}$ while marginalizing over θ_{23} and δ_{CP}. The rest of the simulation details are exactly similar to the 'SM' case (see text for details). Also, note that the ranges in the x-axis and y-axis are different in some of the panels.

given choices of $\alpha_{e\mu}$(true) and δ_{CP}(true). As mentioned above, we always assume NH in the data and IH in the fit while generating the curves in Fig. 9.16. The upper panels portray the performance of DUNE (35 kt), while the lower panels are for LBNO (70 kt). In each panel, the results are given for four different choices of δ_{CP}(true) and the solid horizontal lines depict the 'SM' case where $\alpha_{e\mu}$ is zero in the data and also in the fit. For the 'SM+LRF' case (dashed lines), the data is generated with the true value of $\alpha_{e\mu}$ as mentioned in the top part of each panel, and in the fit, we vary the test values of $\alpha_{e\mu}$ while marginalizing over θ_{23} and δ_{CP}. The rest of the simulation details are exactly similar to the 'SM' case as mentioned above. Though in Fig. 9.16, we have shown the results for three benchmark values of $\alpha_{e\mu}$(true) = 10^{-53} (left panels), 10^{-52} (middle panels), and 10^{-51} (right panels), but, we have checked that for DUNE, the mass hierarchy sensitivity always stays above the standard expectations irrespective of δ_{CP}(true) provided the true value of $\alpha_{e\mu} < 5 \times 10^{-52}$. There is a large suppression in the appearance event rates when we generate the data with a true value of $\alpha_{e\mu}$ around 5×10^{-52}, and if we further increase the value of $\alpha_{e\mu}$(true), the statistical strength of the data reduces very rapidly, and the sensitivity goes below the standard expectation. The upper right panel in Fig. 9.16 clearly shows this behavior. In case of LBNO, the mass hierarchy discovery reach never goes below the 'SM' value irrespective of $\delta_{\rm CP}$(true) if the true choice of $\alpha_{e\mu}$ is smaller than 10^{-52}. Once we consider the true value of $\alpha_{e\mu} \geq 10^{-52}$, the appearance event rates get reduced in data by considerable amount, causing a significant drop in the sensitivity which can be clearly seen from the lower middle and right panels in Fig. 9.16. In Fig. 9.17, we generate the data with IH and fit it with NH. We see almost similar behavior in all the panels of Fig. 9.17 as we have noticed in Fig. 9.16.

9.6 Summary

Let us now make a brief summary of what we have studied in this chapter. First of all we have derived approximate analytical expressions for the effective neutrino oscillation parameters to study how they 'run' as functions of the neutrino energy in the presence of both long-range and Earth matter potentials. We have also obtained a compact and simple expression for the resonance energy, where θ_{13} becomes 45° in the presence of both V_{CC} and $V_{e\mu}$. We have observed that in the presence of $V_{e\mu}$, as we increase the neutrino energy, θ_{13} in matter quickly approaches toward 45°, and the resonance occurs at much lower energies as compared to the SM case. Finally, θ_{13} in matter reaches to 90° as we further increase the energy, causing a large suppression in the appearance probability for most of the energies where we have significant amount of neutrino flux for both the set-ups. As a result, the event rates get reduced which can be clearly seen from the bi-events plot in Fig. 9.10.

As the long-range potential due to gauged $L_e - L_\mu$ symmetry can change the standard oscillation picture of these future facilities significantly, we can expect to place strong constraints on $\alpha_{e\mu}$ if these experiments do not observe a signal of LRF in oscillations. For an example, if $\delta_{\rm CP}$(true) is $-90°$ and true hierarchy is NH, then the expected bound from the DUNE (35 kt) set-up at 90% C.L. is $\alpha_{e\mu} < 1.9 \times 10^{-53}$. The same from the LBNO (70 kt) experiment is $\alpha_{e\mu} < 7.8 \times 10^{-54}$, suggesting that the constraint from LBNO is 2.4

times better than DUNE. This future limit from the DUNE (LBNO) experiment is almost 30 (70) times better than the existing bound from the SK experiment [116]. We have noticed that these future limits on $\alpha_{e\mu}$ from DUNE and LBNO are not very sensitive to the true choice of $\delta_{\rm CP}$ and mass hierarchy. We have also estimated the discovery reach for $\alpha_{e\mu}$ if we find a positive signal of LRF in the expected event spectra at DUNE and LBNO. We have found that the spectral information on the signal and background events is quite crucial to constrain/discover this new long-range force.

We have also studied in detail the CP-violation discovery reach of DUNE (35 kt) and LBNO (70 kt) in the presence of LRF. We have seen that the CP-violation measurements can be deteriorated by considerable amount as compared to the standard expectation depending on the true value of $\alpha_{e\mu}$. At 3σ with $\alpha_{e\mu}(\text{true}) = 10^{-52}$ and true NH, the coverage in $\delta_{\rm CP}(\text{true})$ for which a discovery is possible for CP-violation is 41% (30%) for DUNE (LBNO) while in the standard case, the coverage is 48% for DUNE and 55% for LBNO. In case of true IH, the impact of long-range potential is even more striking for these future facilities. As an example, if $\alpha_{e\mu}(\text{true}) = 10^{-52}$, their chances of establishing CP-violation are quite minimal: only for 37% (12%) values of $\delta_{\rm CP}(\text{true})$, DUNE (LBNO) can reject both the CP-conserving values 0° and 180° in the fit at 3σ, while in the 'SM' framework, DUNE (LBNO) can do so for 53% (60%) values of true $\delta_{\rm CP}$. As the true value of $\alpha_{e\mu}$ approaches toward 10^{-52}, the coverages in $\delta_{\rm CP}(\text{true})$ for which CP-violation can be observed, diminish very quickly for both the set-ups, and ultimately around $\alpha_{e\mu}(\text{true}) = 2 \times 10^{-52}$, the coverages almost become zero.

Finally, we have asked the question, how robust are mass hierarchy measurements in these future facilities in the presence of LRF? In the standard case, due to the large Earth matter effects at the Fermilab-Homestake and CERN-Pyhäsalmi baselines, both DUNE and LBNO can resolve the issue of mass hierarchy at very high confidence level. Now, if LRF exists in Nature, then for DUNE, the mass hierarchy sensitivity remains above the standard expectations provided the true value of $\alpha_{e\mu} < 5 \times 10^{-52}$. In case of LBNO, the mass hierarchy discovery reach does not go below the 'SM' value as long as the true value of $\alpha_{e\mu}$ is smaller than 10^{-52}.

Chapter 10

Conclusion : Present Status and Future Outlook

In this thesis we have mainly focused on two important areas of new physics which can be probed or constrained in long-baseline neutrino oscillation experiments. One is the presence of an eV-scale sterile neutrino and other one is the presence of long-range force in Nature.

Sterile Neutrino : In the first part of the thesis we have discussed the impact of an eV-scale sterile neutrino on the expected full data coming from the LBL experiments like T2K, NOνA, and DUNE. As a common to all these experiments, we have presented a detailed discussion on the behavior of the 4-flavor $\nu_\mu \to \nu_e$ and $\bar{\nu}_\mu \to \bar{\nu}_e$ transition probabilities, and then we have extended our discussions by representing the bi-probability and bi-event plots for the first time in 3+1 scheme, commonly used in the 3-flavor framework. In chapter 6, in case of T2K and NOνA (taken alone and in combination), we have accomplished an extensive sensitivity study in order to evaluate their discovery potential in the presence of a sterile neutrino. We found that the performance of both the experiments in claiming the discovery of the CP-violation induced by the standard CP-phase $\delta_{13} \equiv \delta_{\rm CP}$, and the neutrino mass hierarchy gets substantially deteriorated. The degree of loss of sensitivity depends on the value of the unknown CP-phase δ_{14}. We have also assessed the discovery potential of total CP-violation (i.e., induced simultaneously by the two CP-phases δ_{13} and δ_{14}) and the capability of the two experiments of reconstructing the true values of such CP-phases. In case of total CP-violation, the most important conclusion to make is that if we do not know the exact source of the CP-violation (induced by δ_{13} or δ_{14}) then we may have chance to observe CP-violation at more than 3σ confidence level in case of the combined operation of T2K and NOνA. Now in case of CP reconstruction analysis, we have found that the typical (1σ level) uncertainty on the reconstructed phases is approximately 40^0 for δ_{13} and 50^0 for δ_{14}.

Similar to T2K and NOνA, in chapter 7, we have also performed a detailed study of the physics potential of the highly sophisticated future generation experiment DUNE from the perspective of CPV, mass hierarchy, and octant sensitivity. We have found that the discovery potential of the neutrino mass hierarchy (MH), remains well above the 5σ level if all the three active-sterile mixing angles are relatively small ($\theta_{14} = \theta_{24} = \theta_{34} = 9^0$). In contrast, if the third mixing angle θ_{34} is taken at its upper limit ($\theta_{34} = 30^0$), the MH sensitivity can drop to the 4σ level. From the analysis it is clear that the spectral information of the wide-band beam in DUNE plays a fruitful role in preserving a good MH sensitivity even in the 3+1 scheme. We have also assessed the sensitivity to the CPV induced both by the standard CP-phase $\delta_{13} \equiv \delta_{\mathrm{CP}}$ and by the new CP-phases (δ_{14} and δ_{34} in our parameterization). We have found that the performance of DUNE in claiming the discovery of CPV induced by δ_{13} is appreciably degraded with respect to the 3-flavor case. In particular, the maximal sensitivity (reached around $\delta_{13} = \pm 90^0$) decreases from the 5σ to the 4σ level if all the three new mixing angles are small ($\theta_{14} = \theta_{24} = \theta_{34} = 9^0$) and can drop almost to the 3σ level for $\theta_{34} = 30^0$. The sensitivity to the CP-violation induced by the new CP-phase δ_{14} can reach the 3σ level for an appreciable fraction of its true values but never reaches the 4σ level. The sensitivity to the third CP-phase δ_{34}, which arises exclusively through matter effects, is appreciable only if θ_{34} is large. We have also shown that the typical 1σ level uncertainty on the reconstructed CP-phases is approximately 20^0 (30^0) for δ_{13} (δ_{14}) in the case $\theta_{34} = 0$. The reconstruction of δ_{14} (but not that of δ_{13}) appreciably degrades if θ_{34} is large.

Now concerning to octant issue, in chapter 8, we have addressed for the first time the impact of a light eV-scale sterile neutrino in identifying the octant of the mixing angle θ_{23} at DUNE. We have shown that in the 3+1 scheme, the new recently identified interference term [104] that enters the $\nu_\mu \to \nu_e$ transition probability can perfectly mimic a swap of the θ_{23} octant, even when we use the information from both the neutrino and antineutrino channels. As a consequence, the sensitivity to the octant of θ_{23} can be completely lost in the presence of active-sterile oscillations. It remains to be seen if other kinds of experiments, in particular those using atmospheric neutrinos, can lift or at least alleviate the degeneracy that we have found in the context of LBL experiments. Our educated guess is that this would prove to be very difficult since obtaining a satisfying θ_{23} octant sensitivity with atmospheric neutrinos is a very hard task already in the 3-flavor framework, and in the enlarged 3+1 scheme, the situation should naturally worsen. At the end, we just want to emphasize the fact that the presence of light sterile neutrinos will have far-reaching consequences on the physical effects that we are going to observe in future long-baseline experiments such as DUNE, and we may land up with a different interpretation of the measured event spectra.

So, we have seen that the presence of a sterile neutrino can highly affect the so-called standard 3-flavor phenomena. However there are few important points need to be addressed here. First of all, the discovery of a sterile neutrino at the new short-baseline experiments may be around the corner and, if realized, it may have formidable consequences on our understanding of the microcosmos. Now in the process of discovering the sterile neutrino at the new short-baseline experiments, we will face two challenges. First, we will have to reassess the status of the 3-flavor parameters whose best fit values will change in the 3+1 scheme. The second, perhaps more stimulating challenge, will be that of determining all the new parameters that govern the enlarged 3+1 scheme. According to our study, the LBL experiments may be able to give the first indications on the new CP-phases involved in the 3+1 scheme. Although, for establishing the existence of sterile neutrino and for the determination of the new mixing angles we need more and more dedicated SBL experiments. However we hope that the comprehensive analysis presented in this thesis would give much deeper insight in exploring light sterile neutrinos at the long-baseline facilities.

LRF : Let us now come to the second part of the thesis. In chapter 9, we have studied the impact of long-range force in the long-baseline neutrino oscillation experiments taking DUNE and LBNO as a case study.

Flavor-dependent long-range leptonic forces mediated by the extremely light and neutral bosons associated with gauged $L_e - L_\mu$ or $L_e - L_\tau$ symmetries, constitute a minimal extension of the SM preserving its renormalizability and can lead to interesting phenomenological consequences. For an example, the electrons inside the Sun can generate a flavor-dependent long-range potential $V_{e\mu/e\tau}$ at the Earth surface which can give rise to non-trivial three neutrino mixing effects in terrestrial experiments, and could influence the neutrino propagation through matter. The sign of this potential is opposite for antineutrinos, and affects the neutrino and antineutrino oscillation probabilities in a different fashion. This feature invokes fake CP-asymmetry like the SM matter effect and can severely affect the leptonic CP-violation searches in long-baseline experiments. In this thesis for the first time, we have investigated in detail the possible impacts of these long-range flavor-diagonal neutral current interactions in the oscillations of neutrinos and antineutrinos in the context of future high-precision superbeam facilities, DUNE and LBNO. The key point here is that for long-baseline neutrinos, $\Delta m^2/2E \sim 2.5 \times 10^{-13}$ eV (assuming $\Delta m^2 \sim 2.5 \times 10^{-3}$ eV^2 and $E \sim 5$ GeV) which is comparable to $V_{e\mu}$ even for $\alpha_{e\mu} \sim 10^{-52}$, and can influence the long-baseline experiments significantly. For the Fermilab-Homestake (1300 km) and CERN-Pyhäsalmi (2290 km) baselines, the Earth matter potentials are also around 10^{-13} eV (see Table 9.1), suggesting that V_{CC} can also interfere with $V_{e\mu}$ and $\Delta m^2_{31}/2E$, having substantial impact on the oscillation probability. We have explored these interesting possibilities in detail in this thesis.

We have asked few questions which can be studied in these LBL experiments in presence of LRF. First is related to constraining the new physics. Whenever there is some new physics appears on top of standard model, a simple question comes into our mind that can we discover this new physics or can we give stringent bound on it. Second is related to the CP-violation sensitivity in presence of LRF, and third is related to the possibility of determining MH in presence of LRF. We have addressed all these issues systematically and sufficiently.

To start with first we derived the very simple and compact analytical expressions of $\nu_\mu \to \nu_e$ appearance and $\nu_\mu \to \nu_\mu$ survival oscillation probabilities in presence of long-range and earth matter potentials. There we have also shown the running behavior of all the standard oscillation parameters as a function of neutrino energy, which is quite helpful to have better understanding about the numerical behavior of all the results.

As mentioned above, the long-range potential due to gauged $L_e - L_\mu$ symmetry can change the standard oscillation picture of these future facilities significantly. In that case we have explored the possibility of constraining this new physics. We found that for $\delta_{\rm CP}\,(true) = -90^\circ$ and for NH true, the expected bound from the DUNE (35 kt) setup at 90% C.L. is $\alpha_{e\mu} < 1.9 \times 10^{-53}$. The same from the LBNO (70 kt) experiment is

$\alpha_{e\mu} < 7.8 \times 10^{-54}$, suggesting that the constraint from LBNO is 2.4 times better than DUNE. We have noticed that these limits are robust with respect to the true choice of $\delta_{\rm CP}$ and mass hierarchy. This future limit from the DUNE (LBNO) experiment is almost 30 (70) times better than the existing bound from the SK experiment [116].

We have also studied in detail the CP-violation discovery reach of DUNE (35 kt) and LBNO (70 kt) in the presence of LRF. We have seen that the chance of CP-violation (CPV) discovery gets substantially deteriorated as compared to the standard expectation depending on the true value of $\alpha_{e\mu}$. At 3σ with $\alpha_{e\mu}$(true) = 10^{-52} and true NH, the CPV coverage in $\delta_{\rm CP}$(true) is 41% (30%) for DUNE (LBNO) while in SM case, the coverage is 48% for DUNE and 55% for LBNO. In case of true IH, the impact is even more striking. For example, if $\alpha_{e\mu}$(true) = 10^{-52}, the 3σ C.L. CPV coverage in $\delta_{\rm CP}$(true) is 37% (12%) for DUNE (LBNO), while in the 'SM' framework, DUNE (LBNO) can do so for 53% (60%) values of true $\delta_{\rm CP}$. As the true value of $\alpha_{e\mu}$ approaches toward 10^{-52}, the CPV coverages in $\delta_{\rm CP}$(true) fall sharply for both the set-ups, and ultimately around $\alpha_{e\mu}$(true) = 2×10^{-52}, the coverages almost become zero.

Finally, we have investigated the possibility of mass hierarchy determination in presence of LRF. In the standard case, due to the large Earth matter effects, DUNE and LBNO both can resolve the issue of mass hierarchy at very high confidence level. However, if LRF exists in Nature, then for DUNE, the MH sensitivity remains above the standard expectations provided the true value of $\alpha_{e\mu} < 5 \times 10^{-52}$, and for LBNO, the MH discovery reach does not go below the 'SM' value as long as $\alpha_{e\mu}$ (true) is smaller than 10^{-52}.

The last but not the least, it is worth to mention that here we have presented all the results considering the $L_e - L_\mu$ symmetry. But similar analysis can also be performed for the $L_e - L_\tau$ or other kind of anomaly free leptonic symmetries which we will present elsewhere. The important point to note here is that, even if the mass of the new gauge boson is very light due to the long-range nature of this new force, and the value of the gauge coupling parameter is very low, it can have significant effect on the standard neutrino oscillation physics. As a consequence, we can either constrain or discover this new physics using the neutrino oscillation data. Another noteworthy point to make is that this is one of such new physics examples where the behavior for neutrinos and antineutrinos is different and for that we do not need to invoke the scenarios like CP or CPT violation. This special characteristic emphasizes the importance of analyzing this double behavior separately.

We hope that our rigorous efforts would certainly help to explore this new physics in detail in near future.

Appendix A

Derivation of the Long-Range Potential

Here we give the details of the derivation of the long-range potential arises because of the inclusion of an additional $U(1)$ gauge symmetry in addition to the SM gauge group. The impact of this potential in long-baseline neutrino oscillation experiments has been discussed in chapter 9.

A.1 Introduction:

To include an additional $U(1)_X$ gauge symmetry keeping in mind the standard Model (SM) particle content one gets these following three anomaly free symmetries with minimal matter content, which includes $X \equiv L_e - L_\mu$, $L_e - L_\tau$ or, $L_\mu - L_\tau$.

For the purpose of our work, here we present the details of the calculation of long-range potential arising because of the $U(1)_{L_e - L_\mu}$ symmetry, however the same approach can be followed in case of $U(1)_{L_e - L_\tau}$ or $U(1)_{L_\mu - L_\tau}$ symmetries. The new renormalizable Lagrangian after breaking of $SU(3)_C \times SU(2)_L \times U(1)_Y \times U(1)_{L_e - L_\mu}$ symmetry will look like,

$$\mathscr{L} = \mathscr{L}_{SM} + \mathscr{L}_{Z'} + \mathscr{L}_{mix}, \tag{A.1}$$

where we have followed the notations used in [290].

Now, the Lagrangians $\mathscr{L}_{SM}$, $\mathscr{L}_{Z'}$, and $\mathscr{L}_{mix}$ can be written as

$$
\begin{aligned}
\mathscr{L}_{SM} &= -\frac{1}{4}\hat{B}_{\mu\nu}\hat{B}^{\mu\nu} - \frac{1}{4}\hat{W}^{a}_{\mu\nu}\hat{W}^{\mu\nu a} + \frac{1}{2}\hat{M}_Z^2\hat{Z}_\mu\hat{Z}^\mu - \frac{\hat{e}}{2\hat{c}_W} j^\mu_Y\hat{B}_\mu - \frac{\hat{e}}{\hat{s}_W} j^{\mu a}_W\hat{W}^a_\mu, \\
\mathscr{L}_{Z'} &= -\frac{1}{4}\hat{Z}'_{\mu\nu}\hat{Z}'^{\mu\nu} + \frac{1}{2}\hat{M}_{Z'}^2\hat{Z}'_\mu\hat{Z}'^\mu - \hat{g}_{z'} j^\mu_{Z'}\hat{Z}'_\mu, \\
\mathscr{L}_{mix} &= -\frac{\sin\chi}{2}\hat{Z}'^{\mu\nu}\hat{B}_{\mu\nu} + \delta\hat{M}^2\hat{Z}'_\mu\hat{Z}^\mu.
\end{aligned}
\tag{A.2}
$$

Where, $\hat{c}_W = \cos\theta_W$, $\hat{s}_W = \sin\theta_W$ and θ_W is the Weinberg angle. The currents above are defined as,

$$
\begin{aligned}
j^\mu_Y &= -\sum_{l=e,\mu,\tau}\left[\bar{l}_L\gamma^\mu l_L + 2\bar{l}_R\gamma^\mu l_R\right] + \frac{1}{3}\sum_{quarks}\left[\bar{Q}_L\gamma^\mu Q_L + 4\bar{u}_R\gamma^\mu u_R - 2\bar{d}_R\gamma^\mu d_R\right], \\
j^{\mu a}_W &= \sum_{l=e,\mu,\tau}\bar{l}_L\gamma^\mu\frac{\sigma^a}{2}l_L + \sum_{quarks}\bar{Q}_L\gamma^\mu\frac{\sigma^a}{2}Q_L, \\
j^\mu_{Z'} &= \bar{e}\gamma^\mu e + \bar{\nu}_e\gamma^\mu P_L\nu_e - \bar{\mu}\gamma^\mu\mu - \bar{\nu}_\mu\gamma^\mu P_L\nu_\mu.
\end{aligned}
\tag{A.3}
$$

Where, $P_L = (1-\gamma_5)/2$. Q_L and l_L are the left-handed $SU(2)_L$ doublets for quark and leptons. u_R, d_R, and l_R are the right handed components of up-quark, down-quark and charged leptons. σ^a are the pauli matrices. Here the electromagnetic current can be defined as $j^\mu_{EM} = j^{\mu 3}_W + \frac{1}{2}j^\mu_Y$ and the weak neutral current is $j^\mu_{WNC} = 2j^{\mu 3}_W - 2\hat{s}^2_W j^\mu_{EM}$. From the above Lagrangian we can see that the term $\frac{1}{2}\hat{M}^2_{Z'}\hat{Z}'_\mu\hat{Z}'^\mu$ breaks the $U(1)_{L_e-L_\mu}$ symmetry which in turn is generated from a vev of Higgs sector not shown here explicitly. The mixing of the $\hat{Z}-\hat{Z}'$ is shown in the $\mathscr{L}_{mix}$, where $\sin\chi$ can arise directly or radiatively [291].

A.2 Derivation of Current:

The derivations of the above mentioned currents are given below. The gauge invariant Lagrangian in SM is given by,

$$
\mathscr{L} = \bar{Q}_L i\not{D} Q_L + \bar{l}_L i\not{D} l_L + \bar{u}_R i\not{\partial}' u_R + \bar{d}_R i\not{\partial}' d_R + \bar{l}_R i\not{\partial}' l_R, \tag{A.4}
$$

where,

$$\begin{aligned} D_\mu &\equiv \partial_\mu + ig\frac{\sigma^a}{2}\hat{W}^a_\mu + ig'Y\hat{B}_\mu, \\ \partial'_\mu &\equiv \partial_\mu + ig'Y\hat{B}_\mu. \end{aligned} \tag{A.5}$$

From spontaneous symmetry breaking we know that,

$$\begin{aligned} \frac{g'}{g} &= \tan\theta_W = \frac{g'/\sqrt{g^2+g'^2}}{g/\sqrt{g^2+g'^2}} = \frac{\sin\theta_W}{\cos\theta_W}, \\ \hat{e} &= \frac{gg'}{\sqrt{g^2+g'^2}}. \end{aligned} \tag{A.6}$$

Weak current part:

$$\mathscr{L}^q_w = -g\bar{Q}_L\gamma^\mu\frac{\sigma^a}{2}Q_L\hat{W}^a_\mu = -\frac{\hat{e}}{\hat{s}_W}\bar{Q}_L\gamma^\mu\frac{\sigma^a}{2}Q_L\hat{W}^a_\mu, \tag{A.7}$$

and,

$$\mathscr{L}^l_w = -g\bar{l}_L\gamma^\mu\frac{\sigma^a}{2}l_L\hat{W}^a_\mu = -\frac{\hat{e}}{\hat{s}_W}\bar{l}_L\gamma^\mu\frac{\sigma^a}{2}l_L\hat{W}^a_\mu. \tag{A.8}$$

Combining Eqs. (A.7) and (A.8), we can write,

$$\mathscr{L}^{q+l}_w = -\frac{\hat{e}}{\hat{s}_W}\left(\bar{Q}_L\gamma^\mu\frac{\sigma^a}{2}Q_L + \bar{l}_L\gamma^\mu\frac{\sigma^a}{2}l_L\right)\hat{W}^a_\mu = -\frac{\hat{e}}{\hat{s}_W}j^{\mu a}_W\hat{W}^a_\mu. \tag{A.9}$$

Electromagnetic part:

$$\begin{aligned} \mathscr{L}^{q+l}_{EM} = &-g'(\bar{Q}_L\gamma^\mu Y_{QL}Q_L)\hat{B}_\mu - g'(\bar{l}_L\gamma^\mu Y_{lL}l_L)\hat{B}_\mu - g'(\bar{u}_R\gamma^\mu Y_{uR}u_R)\hat{B}_\mu \\ &-g'(\bar{d}_R\gamma^\mu Y_{dR}d_R)\hat{B}_\mu - g'(\bar{l}_R\gamma^\mu Y_{lR}l_R)\hat{B}_\mu. \end{aligned} \tag{A.10}$$

hypercharge	Q_L	l_L	u_R	d_R	l_R
Y	$+\frac{1}{6}$	$-\frac{1}{2}$	$+\frac{2}{3}$	$-\frac{1}{3}$	-1

Table A.1: Hypercharge quantum numbers of quarks and leptons in the SM.

So,

$$\begin{aligned}\mathscr{L}_{EM}^{q+l} &= -\left(\frac{g'}{6}\bar{Q}_L\gamma^\mu Q_L - \frac{g'}{2}\bar{l}_L\gamma^\mu l_L + \frac{2g'}{3}\bar{u}_R\gamma^\mu u_R - \frac{g'}{3}\bar{d}_R\gamma^\mu d_R - g'\bar{E}_R\gamma^\mu l_R\right)\hat{B}_\mu \\ &= -\frac{g'}{2}\left[-\left(\bar{l}_L\gamma^\mu l_L + 2\bar{l}_R\gamma^\mu l_R\right) + \frac{1}{3}\left(\bar{Q}_L\gamma^\mu Q_L + 4\bar{u}_R\gamma^\mu u_R - 2\bar{d}_R\gamma^\mu d_R\right)\right]\hat{B}_\mu \\ &= -\frac{\hat{e}}{2\hat{c}_W} j_Y^\mu \hat{B}_\mu. \end{aligned} \tag{A.11}$$

Adding Eqs. (A.9) and (A.11), we get,

$$\mathscr{L}_{WNC}^{q+l} + \mathscr{L}_{EM}^{q+l} = -\frac{\hat{e}}{\hat{s}_W} j_W^{\mu 3}\hat{W}_\mu^3 - \frac{\hat{e}}{2\hat{c}_W} j_Y^\mu \hat{B}_\mu. \tag{A.12}$$

Using the transformation,

$$\begin{pmatrix} \hat{B}_\mu \\ \hat{W}_\mu^3 \end{pmatrix} = \begin{pmatrix} \hat{c}_W & -\hat{s}_W \\ \hat{s}_W & \hat{c}_W \end{pmatrix} \begin{pmatrix} \hat{A}_\mu \\ \hat{Z}_\mu \end{pmatrix}, \tag{A.13}$$

we get,

$$\begin{aligned}\mathscr{L}_{WNC}^{q+l} + \mathscr{L}_{EM}^{q+l} &= -\frac{\hat{e}}{\hat{s}_W} j_W^{\mu 3}\hat{W}_\mu^3 - \frac{\hat{e}}{2\hat{c}_W} j_Y^\mu \hat{B}_\mu \\ &= -\frac{\hat{e}}{\hat{s}_W} j_W^{\mu 3}(\hat{c}_W\hat{Z}_\mu + \hat{s}_W\hat{A}_\mu) - \frac{\hat{e}}{2\hat{c}_W} j_Y^\mu(-\hat{s}_W\hat{Z}_\mu + \hat{c}_W\hat{A}_\mu) \\ &= \left(-\frac{\hat{e}}{\hat{s}_W}\hat{c}_W j_W^{\mu 3} + \frac{\hat{e}}{2\hat{c}_W}\hat{s}_W j_Y^\mu\right)\hat{Z}_\mu - \left(\frac{\hat{e}}{\hat{s}_W}\hat{s}_W j_W^{\mu 3} + \frac{\hat{e}}{2\hat{c}_W}\hat{c}_W j_Y^\mu\right)\hat{A}_\mu \end{aligned} \tag{A.14}$$

From above expression, it is very clear that the electromagnetic current is given by

$$j_{EM}^\mu = j_W^{\mu 3} + \frac{j_Y^\mu}{2}. \tag{A.15}$$

Similarly, the weak neutral current is given by,

$$\begin{aligned}
\mathscr{L}_W^{NC} &= -\frac{\hat{e}\hat{c}_W}{\hat{s}_W}\left(j_W^{\mu 3} - \frac{\hat{s}_W^2}{2\hat{c}_W^2}\, j_Y^{\mu}\right)\hat{Z}_\mu \\
&= -\frac{\hat{e}\hat{c}_W}{2\hat{s}_W}\left(2\, j_W^{\mu 3} - 2\frac{\hat{s}_W^2}{\hat{c}_W^2}\, j_{EM}^{\mu} + 2\frac{\hat{s}_W^2}{\hat{c}_W^2}\, j_W^{\mu 3}\right)\hat{Z}_\mu \\
&= -\frac{\hat{e}\hat{c}_W}{2\hat{s}_W}\left(2\frac{\hat{c}_W^2 + \hat{s}_W^2}{\hat{c}_W^2}\, j_W^{\mu 3} - 2\frac{\hat{s}_W^2}{\hat{c}_W^2}\, j_{EM}^{\mu}\right)\hat{Z}_\mu \\
&= -\frac{\hat{e}}{2\hat{s}_W\hat{c}_W}\left(2\, j_W^{\mu 3} - 2\hat{s}_W^2\, j_{EM}^{\mu}\right)\hat{Z}_\mu .
\end{aligned} \tag{A.16}$$

So,

$$j_{WNC}^{\mu} = \left(2\, j_W^{\mu 3} - 2\hat{s}_W^2\, j_{EM}^{\mu}\right). \tag{A.17}$$

From Eq. (A.14), we see that,

$$\mathscr{L}_{WNC}^{q+l} + \mathscr{L}_{EM}^{q+l} = -\frac{\hat{e}}{2\hat{s}_W\hat{c}_W}\, j_{WNC}^{\mu}\hat{Z}_\mu - \hat{e}\, j_{EM}^{\mu}\hat{A}_\mu . \tag{A.18}$$

A.3 Diagonalization of kinetic terms:

From Eq. (A.2), we can write down the kinetic terms as,

$$\begin{aligned}
&-\frac{1}{4}\hat{B}_{\mu\nu}\hat{B}^{\mu\nu} - \frac{1}{4}\hat{Z'}_{\mu\nu}\hat{Z'}^{\mu\nu} - \frac{\sin\chi}{2}\hat{Z'}^{\mu\nu}\hat{B}_{\mu\nu} \\
&= -\frac{1}{4}\left[\hat{B}_{\mu\nu}\hat{B}^{\mu\nu} + \hat{Z'}_{\mu\nu}\hat{Z'}^{\mu\nu} + 2\sin\chi\hat{Z'}^{\mu\nu}\hat{B}_{\mu\nu}\right] \\
&= -\frac{1}{4}\Big[\left(\partial_\mu\hat{B}_\nu - \partial_\nu\hat{B}_\mu\right)\left(\partial^\mu\hat{B}^\nu - \partial^\nu\hat{B}^\mu\right) + \left(\partial_\mu\hat{Z'}_\nu - \partial_\nu\hat{Z'}_\mu\right)\left(\partial^\mu\hat{Z'}^\nu - \partial^\nu\hat{Z'}^\mu\right) \\
&\qquad\qquad + 2\sin\chi\left(\partial^\mu\hat{Z'}^\nu - \partial^\nu\hat{Z'}^\mu\right)\left(\partial_\mu\hat{B}_\nu - \partial_\nu\hat{B}_\mu\right)\Big].
\end{aligned} \tag{A.19}$$

Now after a straight forward calculation we can show that if we replace the fields $\hat{B}_\nu$ and $\hat{Z'}_\nu$ as

$$\hat{B}_\nu \to \hat{B}_\nu + \sin\chi\hat{Z'}_\nu = B_\nu, \tag{A.20}$$

$$\hat{Z'}_\nu \to \cos\chi\hat{Z'}_\nu = Z'_\nu . \tag{A.21}$$

We can write down the fully diagonalized kinetic terms as,

$$
\begin{aligned}
&-\frac{1}{4}\left(\partial_\mu B_\nu-\partial_\nu B_\mu\right)\left(\partial^\mu B^\nu-\partial^\nu B^\mu\right)-\frac{1}{4}\left(\partial_\mu Z'_\nu-\partial_\nu Z'_\mu\right)\left(\partial^\mu Z'^\nu-\partial^\nu Z'^\mu\right)\\
&=\frac{1}{4}B_{\mu\nu}B^{\mu\nu}-\frac{1}{4}Z'_{\mu\nu}Z'^{\mu\nu}.
\end{aligned}
\tag{A.22}
$$

After the diagonalization of kinetic terms, the new gauge fields are,

$$
\begin{aligned}
\hat{A}^\mu &= \hat{c}_W\hat{B}^\mu+\hat{s}_W\hat{W}^{\mu 3},\\
\hat{A}^\mu &\to \hat{c}_W\left(\hat{B}^\mu+\sin\chi\hat{Z'}^\mu\right)+\hat{s}_W\hat{W}^{\mu 3},\\
\hat{A}^\mu &\to \hat{A}^\mu+\hat{c}_W\sin\chi\hat{Z'}^\mu .
\end{aligned}
\tag{A.23}
$$

Again,

$$
\begin{aligned}
\hat{Z}^\mu &= -\hat{s}_W\hat{B}^\mu+\hat{c}_W\hat{W}^{\mu 3},\\
\hat{Z}^\mu &\to -\hat{s}_W\left(\hat{B}^\mu+\sin\chi\hat{Z'}^\mu\right)+\hat{c}_W\hat{W}^{\mu 3},\\
\hat{Z}^\mu &\to \hat{Z}^\mu-\hat{s}_W\sin\chi\hat{Z'}^\mu .
\end{aligned}
\tag{A.24}
$$

A.4 Diagonalization of mass terms:

From Eq. (A.2), we have the mass terms,

$$
\frac{1}{2}\left(\hat{M}_Z^2\hat{Z}_\mu\hat{Z}^\mu+\hat{M}_{Z'}^2\hat{Z'}_\mu\hat{Z'}^\mu+2\delta\hat{M}^2\hat{Z'}_\mu\hat{Z}^\mu\right).
\tag{A.25}
$$

In matrix form, we can write it as,

$$
\begin{pmatrix}\hat{Z}_\mu & \hat{Z'}_\mu\end{pmatrix}\begin{pmatrix}\hat{M}_Z^2 & \delta\hat{M}^2\\ \delta\hat{M}^2 & \hat{M}_{Z'}^2\end{pmatrix}\begin{pmatrix}\hat{Z}^\mu\\ \hat{Z'}^\mu\end{pmatrix}.
\tag{A.26}
$$

To diagonalize it, let us write down the fields in mass basis as,

$$
\begin{pmatrix}Z_1^\mu\\ Z_2^\mu\end{pmatrix}=\begin{pmatrix}\cos\xi & \sin\xi\\ -\sin\xi & \cos\xi\end{pmatrix}\begin{pmatrix}\hat{Z}^\mu\\ \hat{Z'}^\mu\end{pmatrix},
\tag{A.27}
$$

where, Z_1 and Z_2 are the two physical fields. So the new fields in mass basis are,

$$\begin{aligned} Z_1^\mu &= \cos\xi \hat{Z}^\mu + \sin\xi \hat{Z'}^\mu \\ &\to \cos\xi \left(\hat{Z}^\mu - \hat{s}_W \sin\chi \hat{Z'}^\mu\right) + \sin\xi \cos\chi \hat{Z'}^\mu \\ &\to \cos\xi \hat{Z}^\mu + (\sin\xi \cos\chi - \hat{s}_W \cos\xi \sin\chi) \hat{Z'}^\mu . \end{aligned} \tag{A.28}$$

and,

$$\begin{aligned} Z_2^\mu &= -\sin\xi \hat{Z}^\mu + \cos\xi \hat{Z'}^\mu \\ &\to -\sin\xi \left(\hat{Z}^\mu - \hat{s}_W \sin\chi \hat{Z'}^\mu\right) + \cos\xi \cos\chi \hat{Z'}^\mu \\ &\to -\sin\xi \hat{Z}^\mu + (\cos\xi \cos\chi + \hat{s}_W \sin\xi \sin\chi) \hat{Z'}^\mu . \end{aligned} \tag{A.29}$$

In matrix form these fields can be written as,

$$\begin{pmatrix} \hat{Z}^\mu \\ \hat{Z'}^\mu \end{pmatrix} = \frac{1}{\cos\chi} \begin{pmatrix} \cos\xi \cos\chi + \hat{s}_W \sin\xi \sin\chi & \hat{s}_W \cos\xi \sin\chi - \sin\xi \cos\chi \\ \sin\xi & \cos\xi \end{pmatrix} \begin{pmatrix} Z_1^\mu \\ Z_2^\mu \end{pmatrix} . \tag{A.30}$$

Now using Eq. (A.30), we can write the Eq. (A.25) as

$$\begin{aligned} &\frac{1}{2c_\chi^2} \Big\{ \hat{M}_Z^2 (\cos\xi \cos\chi + \hat{s}_W \sin\xi \sin\chi)^2 Z_{1\mu} Z_1^\mu + \hat{M}_Z^2 (\hat{s}_W \cos\xi \sin\chi - \sin\xi \cos\chi)^2 Z_{2\mu} Z_2^\mu \\ &+ 2\hat{M}_Z^2 (\cos\xi \cos\chi + \hat{s}_W \sin\xi \sin\chi)(\hat{s}_W \cos\xi \sin\chi - \sin\xi \cos\chi) Z_{1\mu} Z_2^\mu \\ &+ \hat{M}_{Z'}^2 s_\xi^2 Z_{1\mu} Z_1^\mu + \hat{M}_{Z'}^2 c_\xi^2 Z_{2\mu} Z_2^\mu + 2\hat{M}_{Z'}^2 s_\xi c_\xi Z_{1\mu} Z_2^\mu + 2\delta\hat{M}^2 \left(s_\xi c_\xi c_\chi + s_\xi^2 \hat{s}_W s_\chi\right) Z_{1\mu} Z_1^\mu \\ &+ 2\delta\hat{M}^2 \left(c_\xi^2 \hat{s}_W s_\chi - s_\xi c_\xi c_\chi\right) Z_{2\mu} Z_2^\mu + 2\delta\hat{M}^2 \left(2 s_\xi c_\xi \hat{s}_W s_\chi + c_\chi \cos 2\xi\right) Z_{1\mu} Z_2^\mu \Big\} . \end{aligned} \tag{A.31}$$

The diagonalization of the above equation requires,

$$\begin{aligned} &2\hat{M}_Z^2 (\cos\xi \cos\chi + \hat{s}_W \sin\xi \sin\chi)(\hat{s}_W \cos\xi \sin\chi - \sin\xi \cos\chi) \\ &\qquad + \hat{M}_{Z'}^2 \sin 2\xi + 2\delta\hat{M}^2 \left(\sin 2\xi \hat{s}_W s_\chi + c_\chi \cos 2\xi\right) = 0 . \end{aligned} \tag{A.32}$$

So,

$$\tan 2\xi = \frac{-2\cos\chi\left(\delta\hat{M}^2+\hat{M}_Z^2\hat{s}_W s_\chi\right)}{\hat{M}_{Z'}^2-\hat{M}_Z^2 c_\chi^2+\hat{M}_Z^2\hat{s}_W^2 s_\chi^2+2\delta\hat{M}^2\hat{s}_W\sin\chi}. \tag{A.33}$$

Alternatively, we can follow this procedure also. If we have a matrix like this,

$$\begin{pmatrix} a & b \\ b & c \end{pmatrix}, \tag{A.34}$$

then, the angle for which it becomes diagonal is,

$$\tan 2\theta = \frac{2b}{c-a}. \tag{A.35}$$

Where,

$$\begin{aligned} b &= \hat{s}_W\tan\chi\hat{M}_Z^2+\frac{\delta\hat{M}^2}{\cos\chi}, \quad a=\hat{M}_Z^2, \\ c &= \frac{1}{\cos^2\chi}\left(\hat{M}_Z^2\hat{s}_W\sin^2\chi+2\hat{s}_W\sin\chi\delta\hat{M}^2+\hat{M}_{Z'}^2\right). \end{aligned} \tag{A.36}$$

Now, the masses of the physical fields Z_1 and Z_2 are given as

$$M_{Z_1,Z_2}^2=\frac{a+c}{2}\pm\left[b^2+\left(\frac{a-c}{2}\right)^2\right]^{1/2}. \tag{A.37}$$

For the $\hat{Z}'$ to be very light, we need to consider $\chi \ll 1$ and $\delta\hat{M}^2 \ll \hat{M}_Z^2$, due to which M_{Z_1,Z_2}^2 becomes,

$$M_{Z_1}^2=\hat{M}_Z^2\,,\; M_{Z_2}^2\simeq c-\frac{b^2}{a-c}\,,$$

and the corresponding mixing angle becomes,

$$\xi \simeq \hat{s}_W\chi+\frac{\delta\hat{M}^2}{\hat{M}_Z^2}. \tag{A.38}$$

For $\chi \ll 1$ and $\delta\hat{M}^2 \ll \hat{M}_Z^2$, ξ becomes very small, as can be confirmed from Eq. (A.38).

Now we have the total Lagrangian density associated with the $\hat{W}^{\mu 3}$, $\hat{B}_\mu$, $\hat{Z'}_\mu$ currents can be written as,

$$\begin{aligned}
\mathcal{L}^{total}_{current} &= -\frac{\hat{e}}{\hat{s}_W} j_W^{\mu 3}\hat{W}^3_\mu - \frac{\hat{e}}{2\hat{c}_W} j_Y^\mu \hat{B}_\mu - \hat{g}_{z'} j^\mu_{Z'} \hat{Z'}_\mu \\
&= \left(-\frac{\hat{e}}{\hat{s}_W}\hat{c}_W j_W^{\mu 3} + \frac{\hat{e}}{2\hat{c}_W}\hat{s}_W j_Y^\mu\right)\hat{Z}_\mu - \left(\hat{e} j_W^{\mu 3} + \frac{\hat{e}}{2} j_Y^\mu\right)\hat{A}_\mu - \hat{g}_{z'} j^\mu_{Z'}\hat{Z'}_\mu \\
&\xrightarrow{\hat{A}_\mu \to (\hat{A}_\mu + \hat{c}_W \sin\chi \hat{Z'}_\mu)} \left(-\frac{\hat{e}}{\hat{s}_W}\hat{c}_W j_W^{\mu 3} + \frac{\hat{e}}{2\hat{c}_W}\hat{s}_W j_Y^\mu\right)\hat{Z}_\mu \\
&- \left(\hat{e} j_W^{\mu 3} + \frac{\hat{e}}{2} j_Y^\mu\right)\hat{A}_\mu - \left[\hat{c}_W \sin\chi \left(\hat{e} j_W^{\mu 3} + \frac{\hat{e}}{2} j_Y^\mu\right) + \hat{g}_{z'} j^\mu_{Z'}\right]\hat{Z'}_\mu .
\end{aligned} \tag{A.39}$$

Now from Eq. (A.30), we use the following relations to calculate the Lagrangian for the physical particles A, Z_1, and Z_2,

$$\hat{Z}_\mu = \frac{1}{\cos\chi}\left(\cos\xi \cos\chi + \hat{s}_W \sin\xi \sin\chi\right) Z_1^\mu + \frac{1}{\cos\chi}\left(\hat{s}_W \cos\xi \sin\chi - \sin\xi \cos\chi\right) Z_2^\mu , \tag{A.40}$$

and,

$$\hat{Z'}_\mu = \frac{1}{\cos\chi}\left(\sin\xi Z_1^\mu + \cos\xi Z_2^\mu\right). \tag{A.41}$$

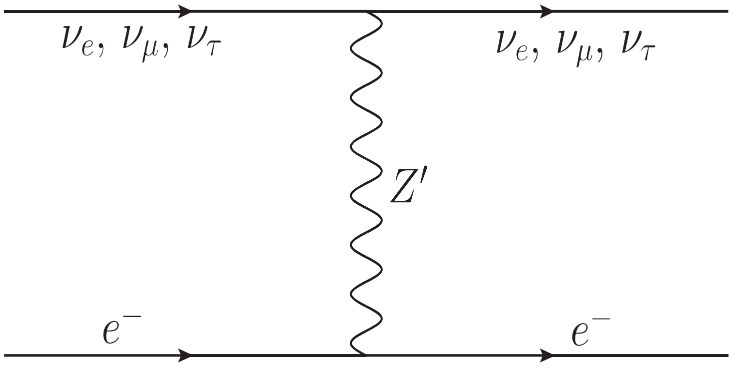

Figure A.1: $(\nu_e, \nu_\mu, \nu_\tau) - e^-$ long-range interaction through Z' light mediator.

A.5 Current Lagrangian for A, Z_1, and Z_2 fields:

Using Eqns. (A.40) and (A.41), we can write down the current Lagrangians for the fields A, Z_1, and Z_2 from Eq. (A.39) as,

For A field:

$$\mathscr{L}_A = -\hat{e}\, j^{\mu}_{EM} \hat{A}_{\mu} \equiv -e\, j^{\mu}_{EM} A_{\mu}. \tag{A.42}$$

For Z_1 field:

$$\begin{aligned}\mathscr{L}_{Z_1} = \Bigg[&-\frac{e}{\hat{s}_W \hat{c}_W c_\chi} \left(j^{\mu 3}_W - \hat{s}^2_W\, j^{\mu}_{EM} \right) \left(c_\xi c_\chi + \hat{s}_W s_\xi s_\chi \right) \\ &- \frac{1}{c_\chi} e \hat{c}_W \sin\chi \sin\xi\, j^{\mu}_{EM} - \frac{1}{c_\chi} \sin\xi\, g_{z'}\, j^{\mu}_{z'} \Bigg] Z_{1\mu}.\end{aligned} \tag{A.43}$$

For Z_2 field:

$$\begin{aligned}\mathscr{L}_{Z_2} = \Bigg[&-\frac{e}{\hat{s}_W \hat{c}_W c_\chi} \left(j^{\mu 3}_W - \hat{s}^2_W\, j^{\mu}_{EM} \right) \left(c_\xi \hat{s}_W s_\chi - s_\xi c_\chi \right) \\ &- \frac{\cos\xi}{\cos\chi} e\, \hat{c}_W\, s_\chi\, j^{\mu}_{EM} - \frac{\cos\xi}{\cos\chi} g_{z'}\, j^{\mu}_{z'} \Bigg] Z_{2\mu}.\end{aligned} \tag{A.44}$$

From Eq. (A.42), we see that the Lagrangian density for A_μ field is canonical one and that is why we write $\hat{e} = e$. Also the other gauge coupling $\hat{g}_{z'}$ is simply $g_{z'}$ in the physical basis.

We know for, $\chi \ll 1$ and $\delta \hat{M}^2 \ll \hat{M}^2_Z$, ξ becomes very small. Also, the physical Weinberg angle can be defined as $s^2_W c^2_W = \frac{\pi\alpha(M_{Z_1})}{\sqrt{2} G_F M^2_{Z_1}}$. This equation is also true with the replacement of $\hat{c}_W \to c_W$, $\hat{s}_W \to s_W$ and $\hat{M}_Z \to M_{Z_1}$ which ultimately leads to the identity $\hat{c}_W\, \hat{s}_W\, \hat{M}_Z \to c_W\, s_W\, M_{Z_1}$ [290].

Using all these approximations, Eq. (A.43) and Eq. (A.44) can be written as,

$$\mathscr{L}_{Z_1} = -\left[\left(j^{\mu 3}_W - s^2_W\, j^{\mu}_{EM} \right) \frac{e}{s_W c_W} + g_{z'}\, \xi\, j^{\mu}_{z'} \right] Z_{1\mu}. \tag{A.45}$$

$$\mathscr{L}_{Z_2} = -\left[g_{z'}\, j^{\mu}_{z'} - (\xi - s_W \chi) \frac{e}{s_W c_W} \left(j^{\mu 3}_W - s^2_W\, j^{\mu}_{EM} \right) + e c_W \chi\, j^{\mu}_{EM} \right] Z_{2\mu}. \tag{A.46}$$

A.6 Derivation of the Potential:

Now to calculate the potential created by this new gauged symmetry, we have to know the dynamiticity of the new particle (Z_2) [283]. The full Lagrangian for the particle (Z_2) is given as

$$\mathscr{L}_{Z_2}^{Full} = -\frac{1}{4} Z_{2\alpha\beta} Z_2^{\alpha\beta} + \frac{1}{2} M_{Z_2}^2 Z_{2\alpha} Z_2^{\alpha} + \mathscr{L}_{Z_2}, \tag{A.47}$$

where,

$$\mathscr{L}_{Z_2} = -\left[g_{z'} j_{z'}^{\alpha} - (\xi - s_W \chi) \frac{e}{s_W c_W} \left(j_W^{\alpha 3} - s_W^2 j_{EM}^{\alpha} \right) + e c_W \chi j_{EM}^{\alpha} \right] Z_{2\alpha}. \tag{A.48}$$

Let us now give the derivation of the static potential generated by the electrons in Sun for the neutrinos (ν_e, ν_μ, and ν_τ) on Earth. The potential due to the gauged symmetries $L_e - L_\mu$ and $L_e - L_\tau$ is exactly same except the corresponding gauge coupling parameters $\alpha_{e\mu}$ and $\alpha_{e\tau}$ respectively. Considering the time-like components in Eq. (A.48), we have $j_{EM}^0 = 0$, $j_{z'}^0 = n_e$ (electron number density) assuming that Sun is not polarized, and we should also note that since the particle Z' couples directly to the electrons in the Sun, we do not consider the contribution of $Z - Z'$ mixing term $(\xi - s_W \chi) \frac{e}{s_W c_W} \left(j_W^{\alpha 3} - s_W^2 j_{EM}^{\alpha} \right)$ in Eq. (A.48).

Now using Euler-Lagrangian equation, we solve the Lagrangian of the new particle Z_2, which is followed as,

$$\begin{aligned} &\partial_\nu \frac{\partial}{\partial \left(\partial_\nu Z_{2\mu} \right)} \left[-\frac{1}{4} Z_2^{\alpha\beta} Z_{2\alpha\beta} \right] \\ &- \frac{\partial}{\partial Z_{2\mu}} \left[\frac{1}{2} M_{Z_2}^2 Z_{2\alpha} Z_2^{\alpha} - \left(g_{z'} j_{z'}{}^{\alpha} - \frac{e(\xi - s_W \chi)}{s_W c_W} \left(j_W^{\alpha 3} - s_W^2 j_{EM}^{\alpha} \right) + e c_W \chi j_{EM}^{\alpha} \right) Z_{2\alpha} \right] = 0. \end{aligned} \tag{A.49}$$

Solution:

$$\begin{aligned}
&\left(-\partial^2+M_{Z_2}^2\right) Z_2^0 = g_{z'}\, j_{z'}^0(\vec{x})\,,\\
&\Rightarrow \left(\partial^2-M_{Z_2}^2\right) Z_2^0 = -g_{z'}\, j_{z'}^0(\vec{x})\,,\\
&\Rightarrow \left(\partial^2-M_{Z_2}^2\right) G(\vec{x}-\vec{y}) = -\delta^3(\vec{x}-\vec{y})\,,\\
&\Rightarrow Z_2^0 = -\int G(\vec{x}-\vec{y})\,\left(-g_{z'}\, j_{z'}^0(\vec{y})\right)\, d^3y. \qquad \text{(A.50)}
\end{aligned}$$

Now we write down the Green's function and delta function as a fourier transform of momentum space.

$$\begin{aligned}
G(\vec{x}-\vec{y}) &= \int \frac{d^3\vec{k}}{(2\pi)^3}\, e^{-i\vec{k}.(\vec{x}-\vec{y})}\, \tilde{G}(\vec{k})\,,\\
\delta^3(\vec{x}-\vec{y}) &= \int \frac{d^3\vec{k}}{(2\pi)^3}\, e^{-i\vec{k}.(\vec{x}-\vec{y})}. \qquad \text{(A.51)}
\end{aligned}$$

Again,

$$\left(\partial^2-M_{Z_2}^2\right) e^{-i\vec{k}.(\vec{x}-\vec{y})} = -\left(k^2+M_{Z_2}^2\right) e^{-i\vec{k}.(\vec{x}-\vec{y})}\,. \qquad \text{(A.52)}$$

So from equation (A.50), we can write,

$$\begin{aligned}
&\left(\partial^2-M_{Z_2}^2\right) G(\vec{x}-\vec{y}) = -\delta^3(\vec{x}-\vec{y})\,,\\
&\Rightarrow -\int \frac{d^3\vec{k}}{(2\pi)^3}\, e^{-i\vec{k}.(\vec{x}-\vec{y})}\,\left(k^2+M_{Z_2}^2\right)\tilde{G}(\vec{k}) = -\int \frac{d^3\vec{k}}{(2\pi)^3}\, e^{-i\vec{k}.(\vec{x}-\vec{y})}\,,\\
&\Rightarrow \tilde{G}(\vec{k}) = \frac{1}{\left(k^2+M_{Z_2}^2\right)}\,. \qquad \text{(A.53)}
\end{aligned}$$

Now putting the value of $\tilde{G}(\vec{k})$ in the expression of $G(\vec{x}-\vec{y})$, we get

$$G(\vec{x}-\vec{y}) = \int \frac{d^3\vec{k}}{(2\pi)^3}\, \frac{e^{-i\vec{k}.(\vec{x}-\vec{y})}}{\left(k^2+M_{Z_2}^2\right)}\,. \qquad \text{(A.54)}$$

Let, $(\vec{x}-\vec{y})=\vec{r}$. So,

$$\begin{aligned}
G(\vec{r}) &= \frac{1}{(2\pi)^3}\int \frac{2\pi k^2 \sin\theta\, e^{-ikr\cos\theta}\, d\theta\, dk}{\left(k^2+M_{Z_2}^2\right)}\,,\\
\Rightarrow G(\vec{r}) &= \frac{1}{(2\pi)^2}\int_0^\infty \frac{2k^2 \sin(kr)\, dk}{kr\left(k^2+M_{Z_2}^2\right)}\,,\\
\Rightarrow G(\vec{r}) &= \frac{1}{8\pi^2 ri}\left[\int_{-\infty}^{\infty}\frac{k\, e^{ikr}}{k^2+M_{Z_2}^2}\,dk-\int_{-\infty}^{\infty}\frac{k\, e^{-ikr}}{k^2+M_{Z_2}^2}\,dk\right],\\
&= I_1 - I_2\,.
\end{aligned} \tag{A.55}$$

Here,

$$I_1=\frac{1}{8\pi^2 ri}\int_{-\infty}^{\infty}\frac{k\, e^{ikr}}{(k+iM_{Z_2})\,(k-iM_{Z_2})}\,dk\,. \tag{A.56}$$

The integrand has two poles, $k=\pm iM_{Z_2}$.

For I_1, e^{ikr} goes to zero when k has a large positive imaginary part i.e; $k=+iM_{Z_2}$. The solution is,

$$\begin{aligned}
I_1 &= 2\pi i \lim_{k\to iM_{Z_2}} \frac{(k-iM_{Z_2})\, k\, e^{ikr}}{8\pi^2 ri\,(k+iM_{Z_2})\,(k-iM_{Z_2})}\,,\\
&= \frac{1}{8\pi r}\, e^{-rM_{Z_2}}\,.
\end{aligned} \tag{A.57}$$

and,

$$\begin{aligned}
I_2 &= -2\pi i \lim_{k\to -iM_{Z_2}} \frac{(k+iM_{Z_2})\, k\, e^{-ikr}}{8\pi^2 ri\,(k+iM_{Z_2})\,(k-iM_{Z_2})} \quad (\text{anti-clockwise contour})\,,\\
&= -\frac{1}{8\pi r}\, e^{-rM_{Z_2}}\,.
\end{aligned} \tag{A.58}$$

So, from Eq. (A.55),

$$G(\vec{r})=\frac{1}{4\pi r}\, e^{-rM_{Z_2}}\,. \tag{A.59}$$

We have $j^0_{z'}=n_e$. In static case outside the Sun, $n_e(\vec{x})=N_e\delta^3(\vec{x})$, where N_e is the total electron number in the Sun. Also for $M_{Z_2} \to 0$,

$$\begin{aligned}
V(r) &= Z_2^0 = \int G(\vec{x}-\vec{y})\, g_{z'}\, j_{z'}^0\,(\vec{y})\, d^3\vec{y}\,, \\
Z_2^0 &= \int \frac{e^{-|\vec{x}-\vec{y}|M_{Z_2}}}{4\pi|\vec{x}-\vec{y}|}\, g_{z'}\, N_e\, \delta^3(\vec{y})\, d^3\vec{y}\,, \\
&= \frac{1}{4\pi|\vec{x}-0|}\, g_{z'}\, N_e\,, \\
&= g_{z'}\, N_e\, \frac{1}{4\pi r}\,.
\end{aligned} \tag{A.60}$$

So the potential for ν_e and ν_μ on Earth is,

$$V_{e,\mu} = \pm g_{z'}^2 N_e \frac{1}{4\pi r} = \pm \alpha_{e\mu} \frac{N_e}{r}\,. \tag{A.61}$$

We can also write the above potential as,

$$\begin{aligned}
V_{ee} &= +\frac{g_{z'}^2}{4\pi}\frac{N_e^\odot}{R_{ES}} \equiv \alpha_{e\mu}\frac{N_e^\odot}{R_{ES}} \equiv V_{e\mu}\,, \\
V_{\mu\mu} &= -\frac{g_{z'}^2}{4\pi}\frac{N_e^\odot}{R_{ES}} \equiv -\alpha_{e\mu}\frac{N_e^\odot}{R_{ES}} \equiv -V_{e\mu}\,, \\
V_{\tau\tau} &= 0.
\end{aligned}$$

Where, $N_e^\odot$ $(\approx 10^{57})$ is the total number of electrons in the Sun, and R_{ES} $(\approx 7.6 \times 10^{26}\,\mathrm{GeV}^{-1})$ is the Sun-Earth distance. We should also note that this potential changes sign for antineutrinos.

Bibliography

[1] A. D. Dolgov, "Neutrinos in cosmology," *Phys. Rept.* **370** (2002) 333–535, arXiv:hep-ph/0202122 [hep-ph].

[2] J. Lesgourgues and S. Pastor, "Massive neutrinos and cosmology," *Phys. Rept.* **429** (2006) 307–379, arXiv:astro-ph/0603494 [astro-ph].

[3] S. Hannestad, "Neutrinos in cosmology," *New Journal of Physics* **6** no. 1, (2004) 108. http://stacks.iop.org/1367-2630/6/i=1/a=108.

[4] C. Patrignani and P. D. Group, "Review of particle physics," *Chinese Physics C* **40** no. 10, (2016) 100001. http://stacks.iop.org/1674-1137/40/i=10/a=100001.

[5] E. K. Akhmedov, "Neutrino physics," in *Proceedings, Summer School in Particle Physics: Trieste, Italy, June 21-July 9, 1999*, pp. 103–164. 1999. arXiv:hep-ph/0001264 [hep-ph].

[6] S. F. King, "Neutrino mass," *Contemp. Phys.* **48** (2007) 195, arXiv:0712.1750 [physics.pop-ph].

[7] T. Kajita, "Nobel lecture: Discovery of atmospheric neutrino oscillations," *Rev. Mod. Phys.* **88** (Jul, 2016) 030501. https://link.aps.org/doi/10.1103/RevModPhys.88.030501.

[8] A. B. McDonald, "Nobel lecture: The sudbury neutrino observatory: Observation of flavor change for solar neutrinos," *Rev. Mod. Phys.* **88** (Jul, 2016) 030502. https://link.aps.org/doi/10.1103/RevModPhys.88.030502.

[9] D. Semikoz, "High-energy astroparticle physics," in *High-energy physics. Proceedings, 5th CERN-Latin-American School, Recinto Quirama, Colombia,*

March 15-28, 2009. 2010. `arXiv:1010.2647 [hep-ph]`.
`https://inspirehep.net/record/872738/files/arXiv:1010.2647.pdf`.

[10] F. Halzen, “High-energy neutrino astrophysics,” *Nature Phys.* **13** no. 3, (2016) 232–238.

[11] E. Giusarma, M. Gerbino, O. Mena, S. Vagnozzi, S. Ho, and K. Freese, “Improvement of cosmological neutrino mass bounds,” *Phys. Rev.* **D94** no. 8, (2016) 083522, `arXiv:1605.04320 [astro-ph.CO]`.

[12] M. Drewes *et al.*, “A White Paper on keV Sterile Neutrino Dark Matter,” *JCAP* **1701** no. 01, (2017) 025, `arXiv:1602.04816 [hep-ph]`.

[13] T. Kajita and A. B. McDonald, “For the discovery of neutrino oscillations, which shows that neutrinos have mass.”. The Nobel Prize in Physics 2015, `http://www.nobelprize.org/nobel_prizes/physics/laureates/2015/`.

[14] **Daya Bay** Collaboration, F. An *et al.*, “A new measurement of antineutrino oscillation with the full detector configuration at Daya Bay,” `arXiv:1505.03456 [hep-ex]`.

[15] **RENO** Collaboration, J. H. Choi *et al.*, “Observation of Energy and Baseline Dependent Reactor Antineutrino Disappearance in the RENO Experiment,” `arXiv:1511.05849 [hep-ex]`.

[16] **Double Chooz** Collaboration, Y. Abe *et al.*, “Improved measurements of the neutrino mixing angle θ_{13} with the Double Chooz detector,” *JHEP* **1410** (2014) 086, `arXiv:1406.7763 [hep-ex]`.

[17] S. Pascoli and T. Schwetz, “Prospects for neutrino oscillation physics,” *Adv.High Energy Phys.* **2013** (2013) 503401.

[18] S. K. Agarwalla, S. Prakash, and S. Uma Sankar, “Exploring the three flavor effects with future superbeams using liquid argon detectors,” *JHEP* **1403** (2014) 087, `arXiv:1304.3251 [hep-ph]`.

[19] S. K. Agarwalla, “Physics Potential of Long-Baseline Experiments,” *Adv.High Energy Phys.* **2014** (2014) 457803, `arXiv:1401.4705 [hep-ph]`.

[20] G. Feldman, J. Hartnell, and T. Kobayashi, "Long-baseline neutrino oscillation experiments," *Adv.High Energy Phys.* **2013** (2013) 475749, `arXiv:1210.1778 [hep-ex]`.

[21] L. Stanco, "Next Generation of Neutrino Studies and Facilities," `arXiv:1511.09409 [hep-ph]`.

[22] D. Forero, M. Tortola, and J. Valle, "Neutrino oscillations refitted," *Phys.Rev.* **D90** no. 9, (2014) 093006, `arXiv:1405.7540 [hep-ph]`.

[23] F. Capozzi, E. Lisi, A. Marrone, D. Montanino, and A. Palazzo, "Neutrino masses and mixings: Status of known and unknown 3ν parameters," *Nucl. Phys.* **B908** (2016) 218–234, `arXiv:1601.07777 [hep-ph]`.

[24] I. Esteban, M. C. Gonzalez-Garcia, M. Maltoni, I. Martinez-Soler, and T. Schwetz, "Updated fit to three neutrino mixing: exploring the accelerator-reactor complementarity," *JHEP* **01** (2017) 087, `arXiv:1611.01514 [hep-ph]`.

[25] P. F. de Salas, D. V. Forero, C. A. Ternes, M. Tortola, and J. W. F. Valle, "Status of neutrino oscillations 2018: first hint for normal mass ordering and improved CP sensitivity," `arXiv:1708.01186 [hep-ph]`.

[26] **NOvA** Collaboration, P. Adamson *et al.*, "Measurement of the neutrino mixing angle θ_{23} in NOvA," *Phys. Rev. Lett.* **118** no. 15, (2017) 151802, `arXiv:1701.05891 [hep-ex]`.

[27] R. Mohapatra and A. Smirnov, "Neutrino Mass and New Physics," *Ann.Rev.Nucl.Part.Sci.* **56** (2006) 569–628, `arXiv:hep-ph/0603118 [hep-ph]`.

[28] C. H. Albright and M.-C. Chen, "Model Predictions for Neutrino Oscillation Parameters," *Phys.Rev.* **D74** (2006) 113006, `arXiv:hep-ph/0608137 [hep-ph]`.

[29] G. Altarelli and F. Feruglio, "Discrete Flavor Symmetries and Models of Neutrino Mixing," *Rev. Mod. Phys.* **82** (2010) 2701–2729, `arXiv:1002.0211 [hep-ph]`.

[30] S. F. King, A. Merle, S. Morisi, Y. Shimizu, and M. Tanimoto, "Neutrino Mass and Mixing: from Theory to Experiment," *New J. Phys.* **16** (2014) 045018, `arXiv:1402.4271 [hep-ph]`.

[31] S. F. King, "Models of Neutrino Mass, Mixing and CP Violation," *J. Phys.* **G42** (2015) 123001, `arXiv:1510.02091 [hep-ph]`.

[32] A. Merle, S. Morisi, and W. Winter, "Common origin of reactor and sterile neutrino mixing," *JHEP* **07** (2014) 039, `arXiv:1402.6332 [hep-ph]`.

[33] D. C. Rivera-Agudelo and A. Pérez-Lorenzana, "Generating θ_{13} from sterile neutrinos in μ-τ symmetric models," *Phys. Rev.* **D92** no. 7, (2015) 073009, `arXiv:1507.07030 [hep-ph]`.

[34] T. Fukuyama and H. Nishiura, "Mass matrix of Majorana neutrinos," `arXiv:hep-ph/9702253 [hep-ph]`.

[35] R. N. Mohapatra and S. Nussinov, "Bimaximal neutrino mixing and neutrino mass matrix," *Phys.Rev.* **D60** (1999) 013002, `arXiv:hep-ph/9809415 [hep-ph]`.

[36] C. Lam, "A 2-3 symmetry in neutrino oscillations," *Phys.Lett.* **B507** (2001) 214–218, `arXiv:hep-ph/0104116 [hep-ph]`.

[37] P. Harrison and W. Scott, "mu - tau reflection symmetry in lepton mixing and neutrino oscillations," *Phys.Lett.* **B547** (2002) 219–228, `arXiv:hep-ph/0210197 [hep-ph]`.

[38] T. Kitabayashi and M. Yasue, "S(2L) permutation symmetry for left-handed mu and tau families and neutrino oscillations in an SU(3)-L x SU(1)-N gauge model," *Phys.Rev.* **D67** (2003) 015006, `arXiv:hep-ph/0209294 [hep-ph]`.

[39] W. Grimus and L. Lavoura, "A Discrete symmetry group for maximal atmospheric neutrino mixing," *Phys.Lett.* **B572** (2003) 189–195, `arXiv:hep-ph/0305046 [hep-ph]`.

[40] Y. Koide, "Universal texture of quark and lepton mass matrices with an extended flavor 2->3 symmetry," *Phys.Rev.* **D69** (2004) 093001, `arXiv:hep-ph/0312207 [hep-ph]`.

[41] R. Mohapatra and W. Rodejohann, "Broken mu-tau symmetry and leptonic CP violation," *Phys.Rev.* **D72** (2005) 053001, `arXiv:hep-ph/0507312 [hep-ph]`.

[42] E. Ma, "Plato's fire and the neutrino mass matrix," *Mod.Phys.Lett.* **A17** (2002) 2361–2370, `arXiv:hep-ph/0211393 [hep-ph]`.

[43] E. Ma and G. Rajasekaran, "Softly broken A(4) symmetry for nearly degenerate neutrino masses," *Phys.Rev.* **D64** (2001) 113012, `arXiv:hep-ph/0106291 [hep-ph]`.

[44] K. Babu, E. Ma, and J. Valle, "Underlying A(4) symmetry for the neutrino mass matrix and the quark mixing matrix," *Phys.Lett.* **B552** (2003) 207–213, `arXiv:hep-ph/0206292 [hep-ph]`.

[45] W. Grimus and L. Lavoura, "S(3) x Z(2) model for neutrino mass matrices," *JHEP* **0508** (2005) 013, `arXiv:hep-ph/0504153 [hep-ph]`.

[46] E. Ma, "Tetrahedral family symmetry and the neutrino mixing matrix," *Mod.Phys.Lett.* **A20** (2005) 2601–2606, `arXiv:hep-ph/0508099 [hep-ph]`.

[47] M. Raidal, "Relation between the neutrino and quark mixing angles and grand unification," *Phys.Rev.Lett.* **93** (2004) 161801, `arXiv:hep-ph/0404046 [hep-ph]`.

[48] H. Minakata and A. Y. Smirnov, "Neutrino mixing and quark-lepton complementarity," *Phys.Rev.* **D70** (2004) 073009, `arXiv:hep-ph/0405088 [hep-ph]`.

[49] J. Ferrandis and S. Pakvasa, "Quark-lepton complenmentarity relation and neutrino mass hierarchy," *Phys.Rev.* **D71** (2005) 033004, `arXiv:hep-ph/0412038 [hep-ph]`.

[50] S. Antusch, S. F. King, and R. N. Mohapatra, "Quark-lepton complementarity in unified theories," *Phys.Lett.* **B618** (2005) 150–161, `arXiv:hep-ph/0504007 [hep-ph]`.

[51] L. J. Hall, H. Murayama, and N. Weiner, "Neutrino mass anarchy," *Phys.Rev.Lett.* **84** (2000) 2572–2575, `arXiv:hep-ph/9911341 [hep-ph]`.

[52] A. de Gouvea and H. Murayama, "Neutrino Mixing Anarchy: Alive and Kicking," `arXiv:1204.1249 [hep-ph]`.

[53] G. L. Fogli and E. Lisi, "Tests of three flavor mixing in long baseline neutrino oscillation experiments," *Phys.Rev.* **D54** (1996) 3667–3670, `arXiv:hep-ph/9604415 [hep-ph]`.

[54] V. Barger, D. Marfatia, and K. Whisnant, "Breaking eight fold degeneracies in neutrino CP violation, mixing, and mass hierarchy," *Phys.Rev.* **D65** (2002) 073023, `arXiv:hep-ph/0112119 [hep-ph]`.

[55] H. Minakata and H. Nunokawa, "Exploring neutrino mixing with low-energy superbeams," *JHEP* **0110** (2001) 001, `arXiv:hep-ph/0108085 [hep-ph]`.

[56] K. Hiraide, H. Minakata, T. Nakaya, H. Nunokawa, H. Sugiyama, *et al.*, "Resolving θ_{23} degeneracy by accelerator and reactor neutrino oscillation experiments," *Phys.Rev.* **D73** (2006) 093008, `arXiv:hep-ph/0601258 [hep-ph]`.

[57] J. Burguet-Castell, M. Gavela, J. Gomez-Cadenas, P. Hernandez, and O. Mena, "Superbeams plus neutrino factory: The Golden path to leptonic CP violation," *Nucl.Phys.* **B646** (2002) 301–320, `arXiv:hep-ph/0207080 [hep-ph]`.

[58] S. K. Agarwalla, S. Prakash, and S. U. Sankar, "Resolving the octant of theta23 with T2K and NOvA," *JHEP* **1307** (2013) 131, `arXiv:1301.2574 [hep-ph]`.

[59] P. Machado, H. Minakata, H. Nunokawa, and R. Zukanovich Funchal, "What can we learn about the lepton CP phase in the next 10 years?," *JHEP* **1405** (2014) 109, `arXiv:1307.3248`.

[60] H. Minakata and S. J. Parke, "Correlated, precision measurements of θ_{23} and δ using only the electron neutrino appearance experiments," *Phys. Rev.* **D87** no. 11, (2013) 113005, `arXiv:1303.6178 [hep-ph]`.

[61] A. Chatterjee, P. Ghoshal, S. Goswami, and S. K. Raut, "Octant sensitivity for large theta(13) in atmospheric and long baseline neutrino experiments," *JHEP* **1306** (2013) 010, `arXiv:1302.1370 [hep-ph]`.

[62] **JUNO** Collaboration, F. An *et al.*, "Neutrino Physics with JUNO," *J. Phys.* **G43** no. 3, (2016) 030401, `arXiv:1507.05613 [physics.ins-det]`.

[63] L. Wolfenstein, “Neutrino Oscillations in Matter,” *Phys.Rev.* **D17** (1978) 2369–2374.

[64] C. Biggio, M. Blennow, and E. Fernandez-Martinez, “General bounds on non-standard neutrino interactions,” *JHEP* **0908** (2009) 090, `arXiv:0907.0097 [hep-ph]`.

[65] T. Ohlsson, “Status of non-standard neutrino interactions,” *Rept. Prog. Phys.* **76** (2013) 044201, `arXiv:1209.2710 [hep-ph]`.

[66] O. Miranda and H. Nunokawa, “Non standard neutrino interactions,” `arXiv:1505.06254 [hep-ph]`.

[67] Y. Farzan, “A model for large non-standard interactions of neutrinos leading to the LMA-Dark solution,” *Phys. Lett.* **B748** (2015) 311–315, `arXiv:1505.06906 [hep-ph]`.

[68] Y. Farzan and I. M. Shoemaker, “Lepton Flavor Violating Non-Standard Interactions via Light Mediators,” `arXiv:1512.09147 [hep-ph]`.

[69] M. Jacobson and T. Ohlsson, “Extrinsic CPT violation in neutrino oscillations in matter,” *Phys. Rev.* **D69** (2004) 013003, `arXiv:hep-ph/0305064 [hep-ph]`.

[70] P. Arias, J. Gamboa, F. Méndez, A. Das, and J. López-Sarrión, “Cpt/lorentz invariance violation and neutrino oscillation,” *Physics Letters B* **650** no. 5, (2007) 401 – 406. `http://www.sciencedirect.com/science/article/pii/S0370269307005746`.

[71] N. Engelhardt, A. E. Nelson, and J. R. Walsh, “Apparent *cpt* violation in neutrino oscillation experiments,” *Phys. Rev. D* **81** (Jun, 2010) 113001. `https://link.aps.org/doi/10.1103/PhysRevD.81.113001`.

[72] P. Huber, “CP, T and CPT violation in future long baseline experiments,” *J. Phys.* **G29** (2003) 1853–1856, `arXiv:hep-ph/0210140 [hep-ph]`.

[73] G. Barenboim, J. F. Beacom, L. Borissov, and B. Kayser, “CPT violation and the nature of neutrinos,” *Phys. Lett.* **B537** (2002) 227–232, `arXiv:hep-ph/0203261 [hep-ph]`.

[74] S. Pakvasa, "CPT and Lorentz violations in neutrino oscillations," in *CPT and Lorentz symmetry. Proceedings: 2nd Meeting, Bloomington, USA, Aug 15-18, 2001*, pp. 208–215. 2002. `arXiv:hep-ph/0110175 [hep-ph]`.

[75] G. Barenboim, L. Borissov, J. Lykken, and A. Y. Smirnov, "Neutrinos as the messengers of cpt violation," *Journal of High Energy Physics* **2002** no. 10, (2002) 001. `http://stacks.iop.org/1126-6708/2002/i=10/a=001`.

[76] T. Lee and C.-N. Yang, "Conservation of Heavy Particles and Generalized Gauge Transformations," *Phys.Rev.* **98** (1955) 1501.

[77] L. B. Okun, "On muonic charge and muonic photons," *Yad. Fiz.* **10** (1969) 358–362.

[78] E. G. Adelberger, B. R. Heckel, and A. E. Nelson, "Tests of the gravitational inverse square law," *Ann. Rev. Nucl. Part. Sci.* **53** (2003) 77–121, `arXiv:hep-ph/0307284 [hep-ph]`.

[79] R. Foot, "New Physics from Electric Charge Quantization?," *Modern Physics Letters A* **6** (1991) 527–529. `http://adsabs.harvard.edu/abs/1991MPLA....6..527F`.

[80] X.-G. He, G. C. Joshi, H. Lew, and R. R. Volkas, "Simplest Z' model," *Phys. Rev. D* **44** (Oct, 1991) 2118–2132. `https://link.aps.org/doi/10.1103/PhysRevD.44.2118`.

[81] R. Foot, X. G. He, H. Lew, and R. R. Volkas, "Model for a light Z-prime boson," *Phys. Rev.* **D50** (1994) 4571–4580, `arXiv:hep-ph/9401250 [hep-ph]`.

[82] K. Abazajian, M. Acero, S. Agarwalla, A. Aguilar-Arevalo, C. Albright, *et al.*, "Light Sterile Neutrinos: A White Paper," `arXiv:1204.5379 [hep-ph]`.

[83] A. Palazzo, "Phenomenology of light sterile neutrinos: a brief review," *Mod. Phys. Lett.* **A28** (2013) 1330004, `arXiv:1302.1102 [hep-ph]`.

[84] S. Gariazzo, C. Giunti, M. Laveder, Y. F. Li, and E. M. Zavanin, "Light sterile neutrinos," *J. Phys.* **G43** (2016) 033001, `arXiv:1507.08204 [hep-ph]`.

[85] E. Fernandez-Martinez, M. B. Gavela, J. Lopez-Pavon, and O. Yasuda, "CP-violation from non-unitary leptonic mixing," *Phys. Lett.* **B649** (2007) 427–435, `arXiv:hep-ph/0703098 [hep-ph]`.

[86] S. Goswami and T. Ota, "Testing non-unitarity of neutrino mixing matrices at neutrino factories," *Phys. Rev.* **D78** (2008) 033012, `arXiv:0802.1434 [hep-ph]`.

[87] S. Luo, "Non-unitary deviation from the tri-bimaximal lepton mixing and its implications on neutrino oscillations," *Phys. Rev.* **D78** (2008) 016006, `arXiv:0804.4897 [hep-ph]`.

[88] S. Antusch, M. Blennow, E. Fernandez-Martinez, and J. Lopez-Pavon, "Probing non-unitary mixing and CP-violation at a Neutrino Factory," *Phys. Rev.* **D80** (2009) 033002, `arXiv:0903.3986 [hep-ph]`.

[89] W. Rodejohann, "On Non-Unitary Lepton Mixing and Neutrino Mass Observables," *Phys. Lett.* **B684** (2010) 40–47, `arXiv:0912.3388 [hep-ph]`.

[90] M. Malinsky, T. Ohlsson, and H. Zhang, "Non-unitarity effects in a realistic low-scale seesaw model," *Phys. Rev.* **D79** (2009) 073009, `arXiv:0903.1961 [hep-ph]`.

[91] F. J. Escrihuela, D. V. Forero, O. G. Miranda, M. Tortola, and J. W. F. Valle, "On the description of nonunitary neutrino mixing," *Phys. Rev.* **D92** no. 5, (2015) 053009, `arXiv:1503.08879 [hep-ph]`. [Erratum: Phys. Rev.D93,no.11,119905(2016)].

[92] T. Lasserre, "Light Sterile Neutrinos in Particle Physics: Experimental Status," *Phys. Dark Univ.* **4** (2014) 81–85, `arXiv:1404.7352 [hep-ex]`.

[93] A. Palazzo, "Testing the very-short-baseline neutrino anomalies at the solar sector," *Phys. Rev.* **D83** (2011) 113013, `arXiv:1105.1705 [hep-ph]`.

[94] A. Palazzo, "An estimate of θ_{14} independent of the reactor antineutrino flux determinations," *Phys. Rev.* **D85** (2012) 077301, `arXiv:1201.4280 [hep-ph]`.

[95] C. Giunti and Y. F. Li, "Matter Effects in Active-Sterile Solar Neutrino Oscillations," *Phys. Rev.* **D80** (2009) 113007, `arXiv:0910.5856 [hep-ph]`.

[96] H. Nunokawa, O. L. G. Peres, and R. Zukanovich Funchal, “Probing the LSND mass scale and four neutrino scenarios with a neutrino telescope,” *Phys. Lett.* **B562** (2003) 279–290, `arXiv:hep-ph/0302039 [hep-ph]`.

[97] **IceCube** Collaboration, J. Salvadó Serra, “Sterile Neutrino Search in IceCube Neutrino Observatory,” 2015. Talk given at the VII CPAN Days Conference, December 1-3, 2015, Segovia, Spain, `https://indico.ific.uv.es/indico/sessionDisplay.py?sessionId=3&confId=2541#20151201`.

[98] **Super-Kamiokande** Collaboration, K. Abe *et al.*, “Limits on sterile neutrino mixing using atmospheric neutrinos in Super-Kamiokande,” *Phys. Rev.* **D91** (2015) 052019, `arXiv:1410.2008 [hep-ex]`.

[99] A. Timmons, “Searching for Sterile Neutrinos at MINOS,” in *Topical Research Meeting on Prospects in Neutrino Physics (NuPhys2014) London, UK, United Kingdom, December 15-17, 2014*. 2015. `arXiv:1504.04046 [hep-ex]`. `http://inspirehep.net/record/1360279/files/arXiv:1504.04046.pdf`.

[100] **MINOS** Collaboration, P. Adamson *et al.*, “Active to sterile neutrino mixing limits from neutral-current interactions in MINOS,” *Phys. Rev. Lett.* **107** (2011) 011802, `arXiv:1104.3922 [hep-ex]`.

[101] **NOvA** Collaboration, P. Adamson *et al.*, “Search for active-sterile neutrino mixing using neutral-current interactions in NOvA,” `arXiv:1706.04592 [hep-ex]`.

[102] **OPERA** Collaboration, N. Agafonova *et al.*, “Limits on muon-neutrino to tau-neutrino oscillations induced by a sterile neutrino state obtained by OPERA at the CNGS beam,” *JHEP* **06** (2015) 069, `arXiv:1503.01876 [hep-ex]`.

[103] **OPERA** Collaboration, M. Tenti, “Search for sterile neutrino mixing in the $\nu_\mu \to \nu_\tau$ appearance channel with the OPERA detector,” in *Proceedings, 17th Lomonosov Conference on Elementary Particle Physics: Moscow, Russia, August 20-26, 2015*, pp. 151–154. 2017.

[104] N. Klop and A. Palazzo, “Imprints of CP violation induced by sterile neutrinos in T2K data,” *Phys. Rev.* **D91** no. 7, (2015) 073017, `arXiv:1412.7524 [hep-ph]`.

[105] C. Giunti, M. Laveder, Y. F. Li, and H. W. Long, "Pragmatic View of Short-Baseline Neutrino Oscillations," *Phys. Rev.* **D88** (2013) 073008, `arXiv:1308.5288 [hep-ph]`.

[106] J. Kopp, P. A. N. Machado, M. Maltoni, and T. Schwetz, "Sterile Neutrino Oscillations: The Global Picture," *JHEP* **05** (2013) 050, `arXiv:1303.3011 [hep-ph]`.

[107] A. Palazzo, "3-flavor and 4-flavor implications of the latest T2K and NOνA electron (anti-)neutrino appearance results," *Phys. Lett.* **B757** (2016) 142–147, `arXiv:1509.03148 [hep-ph]`.

[108] A. Palazzo, "Consistent analysis of the $\nu_\mu \to \nu_e$ sterile neutrinos searches of ICARUS and OPERA," *Phys. Rev.* **D91** no. 9, (2015) 091301, `arXiv:1503.03966 [hep-ph]`.

[109] M. Antonello *et al.*, "Experimental search for the "LSND anomaly" with the ICARUS detector in the CNGS neutrino beam," *Eur. Phys. J.* **C73** no. 3, (2013) 2345, `arXiv:1209.0122 [hep-ex]`.

[110] M. Antonello *et al.*, "Some conclusive considerations on the comparison of the ICARUS ν_μ to ν_e oscillation search with the MiniBooNE low-energy event excess," `arXiv:1502.04833 [hep-ph]`.

[111] **OPERA** Collaboration, N. Agafonova *et al.*, "Search for $\nu_\mu \to \nu_e$ oscillations with the OPERA experiment in the CNGS beam," *JHEP* **07** (2013) 004, `arXiv:1303.3953 [hep-ex]`. [Addendum: JHEP07,085(2013)].

[112] **LBNE** Collaboration, M. Bass *et al.*, "Baseline optimization for the measurement of CP violation and mass hierarchy in a long-baseline neutrino oscillation experiment," `arXiv:1311.0212 [hep-ex]`.

[113] K. Bora, D. Dutta, and P. Ghoshal, "Determining the Octant of θ_{23} at LBNE in conjunction with Reactor Experiments," `arXiv:1405.7482 [hep-ph]`.

[114] C. R. Das, J. Maalampi, J. Pulido, and S. Vihonen, "Determination of the θ_{23} octant in LBNO," *JHEP* **02** (2015) 048, `arXiv:1411.2829 [hep-ph]`.

[115] N. Nath, M. Ghosh, and S. Goswami, "The Physics of antineutrinos in DUNE and resolution of octant degeneracy," `arXiv:1511.07496 [hep-ph]`.

[116] A. S. Joshipura and S. Mohanty, "Constraints on flavor dependent long range forces from atmospheric neutrino observations at super-Kamiokande," *Phys.Lett.* **B584** (2004) 103–108, `arXiv:hep-ph/0310210 [hep-ph]`.

[117] J. Grifols and E. Masso, "Neutrino oscillations in the sun probe long range leptonic forces," *Phys.Lett.* **B579** (2004) 123–126, `arXiv:hep-ph/0311141 [hep-ph]`.

[118] M. Gonzalez-Garcia, P. de Holanda, E. Masso, and R. Zukanovich Funchal, "Probing long-range leptonic forces with solar and reactor neutrinos," *JCAP* **0701** (2007) 005, `arXiv:hep-ph/0609094 [hep-ph]`.

[119] A. Bandyopadhyay, A. Dighe, and A. S. Joshipura, "Constraints on flavor-dependent long range forces from solar neutrinos and kamland," *Phys. Rev. D* **75** (May, 2007) 093005. `http://link.aps.org/doi/10.1103/PhysRevD.75.093005`.

[120] A. Samanta, "Long-range Forces : Atmospheric Neutrino Oscillation at a magnetized Detector," *JCAP* **1109** (2011) 010, `arXiv:1001.5344 [hep-ph]`.

[121] **T2K** Collaboration, K. Abe *et al.*, "The T2K Experiment," *Nucl.Instrum.Meth.* **A659** (2011) 106–135, `arXiv:1106.1238 [physics.ins-det]`.

[122] **T2K** Collaboration, Y. Itow *et al.*, "The JHF-Kamioka neutrino project," `arXiv:hep-ex/0106019 [hep-ex]`.

[123] **NOvA** Collaboration, P. Adamson *et al.*, "First measurement of electron neutrino appearance in NOvA," `arXiv:1601.05022 [hep-ex]`.

[124] **NOvA** Collaboration, D. Ayres *et al.*, "The NOvA Technical Design Report,".

[125] **DUNE** Collaboration, R. Acciarri *et al.*, "Long-Baseline Neutrino Facility (LBNF) and Deep Underground Neutrino Experiment (DUNE) Conceptual Design Report Volume 2: The Physics Program for DUNE at LBNF," `arXiv:1512.06148 [physics.ins-det]`.

[126] **LBNE** Collaboration, T. Akiri *et al.*, "The 2010 Interim Report of the Long-Baseline Neutrino Experiment Collaboration Physics Working Groups," `arXiv:1110.6249 [hep-ex]`.

[127] **LAGUNA-LBNO** Collaboration, S. Agarwalla *et al.*, "The mass-hierarchy and CP-violation discovery reach of the LBNO long-baseline neutrino experiment," *JHEP* **1405** (2014) 094, `arXiv:1312.6520 [hep-ph]`.

[128] **LAGUNA-LBNO** Collaboration, S. Agarwalla *et al.*, "Optimised sensitivity to leptonic CP violation from spectral information: the LBNO case at 2300 km baseline," `arXiv:1412.0593 [hep-ph]`.

[129] A. Donini and D. Meloni, "The 2+2 and 3+1 four family neutrino mixing at the neutrino factory," *Eur. Phys. J.* **C22** (2001) 179–186, `arXiv:hep-ph/0105089 [hep-ph]`.

[130] A. Donini, M. Lusignoli, and D. Meloni, "Telling three neutrinos from four neutrinos at the neutrino factory," *Nucl. Phys.* **B624** (2002) 405–422, `arXiv:hep-ph/0107231 [hep-ph]`.

[131] A. Donini, M. Maltoni, D. Meloni, P. Migliozzi, and F. Terranova, "3+1 sterile neutrinos at the CNGS," *JHEP* **12** (2007) 013, `arXiv:0704.0388 [hep-ph]`.

[132] A. Dighe and S. Ray, "Signatures of heavy sterile neutrinos at long baseline experiments," *Phys. Rev.* **D76** (2007) 113001, `arXiv:0709.0383 [hep-ph]`.

[133] A. Donini, K.-i. Fuki, J. Lopez-Pavon, D. Meloni, and O. Yasuda, "The Discovery channel at the Neutrino Factory: numu to nutau pointing to sterile neutrinos," *JHEP* **08** (2009) 041, `arXiv:0812.3703 [hep-ph]`.

[134] O. Yasuda, "Sensitivity to sterile neutrino mixings and the discovery channel at a neutrino factory," in *Physics beyond the standard models of particles, cosmology and astrophysics. Proceedings, 5th International Conference, Beyond 2010, Cape Town, South Africa, February 1-6, 2010*, pp. 300–313. 2011. `arXiv:1004.2388 [hep-ph]`. `http://inspirehep.net/record/851933/files/arXiv:1004.2388.pdf`.

[135] D. Meloni, J. Tang, and W. Winter, "Sterile neutrinos beyond LSND at the Neutrino Factory," *Phys. Rev.* **D82** (2010) 093008, `arXiv:1007.2419 [hep-ph]`.

[136] B. Bhattacharya, A. M. Thalapillil, and C. E. M. Wagner, "Implications of sterile neutrinos for medium/long-baseline neutrino experiments and the determination of θ_{13}," *Phys. Rev.* **D85** (2012) 073004, `arXiv:1111.4225 [hep-ph]`.

[137] A. Donini, P. Hernandez, J. Lopez-Pavon, M. Maltoni, and T. Schwetz, "The minimal 3+2 neutrino model versus oscillation anomalies," *JHEP* **07** (2012) 161, `arXiv:1205.5230 [hep-ph]`.

[138] D. Hollander and I. Mocioiu, "Sterile neutrinos at LBNE," `arXiv:1408.1749 [hep-ph]`.

[139] J. M. Berryman, A. de Gouvêa, K. J. Kelly, and A. Kobach, "Sterile neutrino at the Deep Underground Neutrino Experiment," *Phys. Rev.* **D92** no. 7, (2015) 073012, `arXiv:1507.03986 [hep-ph]`.

[140] R. Gandhi, B. Kayser, M. Masud, and S. Prakash, "The impact of sterile neutrinos on CP measurements at long baselines," *JHEP* **11** (2015) 039, `arXiv:1508.06275 [hep-ph]`.

[141] S. K. Agarwalla, T. Li, and A. Rubbia, "An Incremental approach to unravel the neutrino mass hierarchy and CP violation with a long-baseline Superbeam for large θ_{13}," *JHEP* **1205** (2012) 154, `arXiv:1109.6526 [hep-ph]`.

[142] **LAGUNA-LBNO** Collaboration, S. Agarwalla *et al.*, "The mass-hierarchy and CP-violation discovery reach of the LBNO long-baseline neutrino experiment," `arXiv:1312.6520 [hep-ph]`.

[143] **Hyper-Kamiokande Working Group** Collaboration, K. Abe *et al.*, "A Long Baseline Neutrino Oscillation Experiment Using J-PARC Neutrino Beam and Hyper-Kamiokande," `arXiv:1412.4673 [physics.ins-det]`. `http://inspirehep.net/record/1334360/files/arXiv:1412.4673.pdf`.

[144] **Hyper-Kamiokande Proto-Collaboration** Collaboration, K. Abe *et al.*, "Physics potential of a long-baseline neutrino oscillation experiment using a J-PARC

neutrino beam and Hyper-Kamiokande," *PTEP* **2015** (2015) 053C02, `arXiv:1502.05199 [hep-ex]`.

[145] K. C. Wang, "A suggestion on the detection of the neutrino," *Phys. Rev.* **61** (Jan, 1942) 97–97. `http://link.aps.org/doi/10.1103/PhysRev.61.97`.

[146] C. L. Cowan, F. Reines, F. B. Harrison, H. W. Kruse, and A. D. McGuire, "Detection of the free neutrino: A Confirmation," *Science* **124** (1956) 103–104.

[147] B. Pontecorvo, "Mesonium and anti-mesonium," *Sov.Phys.JETP* **6** (1957) 429.

[148] Z. Maki, M. Nakagawa, and S. Sakata, "Remarks on the unified model of elementary particles," *Prog.Theor.Phys.* **28** (1962) 870–880.

[149] B. Pontecorvo, "Neutrino Experiments and the Problem of Conservation of Leptonic Charge," *Sov.Phys.JETP* **26** (1968) 984–988.

[150] **Super-Kamiokande** Collaboration, Y. Fukuda *et al.*, "Evidence for oscillation of atmospheric neutrinos," *Phys.Rev.Lett.* **81** (1998) 1562–1567, `arXiv:hep-ex/9807003 [hep-ex]`.

[151] **SNO** Collaboration, Q. R. Ahmad *et al.*, "Measurement of the rate of $\nu_e + d \to p + p + e^-$ interactions produced by ^8B solar neutrinos at the Sudbury Neutrino Observatory," *Phys. Rev. Lett.* **87** (2001) 071301, `arXiv:nucl-ex/0106015 [nucl-ex]`.

[152] J. Barry, W. Rodejohann, and H. Zhang, "Light Sterile Neutrinos: Models and Phenomenology," *JHEP* **07** (2011) 091, `arXiv:1105.3911 [hep-ph]`.

[153] **Particle Data Group** Collaboration, C. Caso *et al.*, "Review of particle physics. Particle Data Group," *Eur. Phys. J.* **C3** (1998) 1–794.

[154] **Particle Data Group** Collaboration, K. Hagiwara *et al.*, "Review of particle physics. Particle Data Group," *Phys. Rev.* **D66** (2002) 010001.

[155] B. Pontecorvo, "Inverse beta processes and nonconservation of lepton charge," *Sov.Phys.JETP* **7** (1958) 172–173.

[156] E. K. Akhmedov, R. Johansson, M. Lindner, T. Ohlsson, and T. Schwetz, "Series expansions for three flavor neutrino oscillation probabilities in matter," *JHEP* **0404** (2004) 078, `arXiv:hep-ph/0402175 [hep-ph]`.

[157] S. Mikheev and A. Y. Smirnov, "Resonant amplification of neutrino oscillations in matter and solar neutrino spectroscopy," *Nuovo Cim.* **C9** (1986) 17–26.

[158] **LSND** Collaboration, C. Athanassopoulos *et al.*, "Candidate events in a search for anti-muon-neutrino —> anti-electron-neutrino oscillations," *Phys. Rev. Lett.* **75** (1995) 2650–2653, `arXiv:nucl-ex/9504002 [nucl-ex]`.

[159] **LSND** Collaboration, A. Aguilar-Arevalo *et al.*, "Evidence for neutrino oscillations from the observation of anti-neutrino(electron) appearance in a anti-neutrino(muon) beam," *Phys. Rev.* **D64** (2001) 112007, `arXiv:hep-ex/0104049 [hep-ex]`.

[160] **MiniBooNE** Collaboration, A. A. Aguilar-Arevalo *et al.*, "A Combined $\nu_\mu \to \nu_e$ and $\bar{\nu}_\mu \to \bar{\nu}_e$ Oscillation Analysis of the MiniBooNE Excesses," 2012. `arXiv:1207.4809 [hep-ex]`. `http://lss.fnal.gov/archive/2012/pub/fermilab-pub-12-394-ad-ppd.pdf`.

[161] **MiniBooNE** Collaboration, A. A. Aguilar-Arevalo *et al.*, "Event Excess in the MiniBooNE Search for $\bar{\nu}_\mu \to \bar{\nu}_e$ Oscillations," *Phys. Rev. Lett.* **105** (2010) 181801, `arXiv:1007.1150 [hep-ex]`.

[162] **MiniBooNE** Collaboration, A. A. Aguilar-Arevalo *et al.*, "Improved Search for $\bar{\nu}_\mu \to \bar{\nu}_e$ Oscillations in the MiniBooNE Experiment," *Phys. Rev. Lett.* **110** (2013) 161801, `arXiv:1303.2588 [hep-ex]`.

[163] **NOMAD** Collaboration, P. Astier *et al.*, "Final NOMAD results on muon-neutrino —> tau-neutrino and electron-neutrino —> tau-neutrino oscillations including a new search for tau-neutrino appearance using hadronic tau decays," *Nucl. Phys.* **B611** (2001) 3–39, `arXiv:hep-ex/0106102 [hep-ex]`.

[164] **Daya Bay** Collaboration, F. P. An *et al.*, "Improved Search for a Light Sterile Neutrino with the Full Configuration of the Daya Bay Experiment," *Phys. Rev. Lett.* **117** no. 15, (2016) 151802, `arXiv:1607.01174 [hep-ex]`.

[165] **MINOS, Daya Bay** Collaboration, P. Adamson *et al.*, "Limits on Active to Sterile Neutrino Oscillations from Disappearance Searches in the MINOS, Daya Bay, and Bugey-3 Experiments," *Phys. Rev. Lett.* **117** no. 15, (2016) 151801, `arXiv:1607.01177 [hep-ex]`. [Addendum: Phys. Rev. Lett.117,no.20,209901(2016)].

[166] **IceCube** Collaboration, M. G. Aartsen *et al.*, "Searches for Sterile Neutrinos with the IceCube Detector," *Phys. Rev. Lett.* **117** no. 7, (2016) 071801, `arXiv:1605.01990 [hep-ex]`.

[167] **MINOS** Collaboration, P. Adamson *et al.*, "Search for Sterile Neutrinos Mixing with Muon Neutrinos in MINOS," *Phys. Rev. Lett.* **117** no. 15, (2016) 151803, `arXiv:1607.01176 [hep-ex]`.

[168] **T2K** Collaboration, K. Abe *et al.*, "Search for short baseline ν_e disappearance with the T2K near detector," *Phys. Rev.* **D91** no. 5, (2015) 051102, `arXiv:1410.8811 [hep-ex]`.

[169] J. N. Abdurashitov *et al.*, "Measurement of the response of a Ga solar neutrino experiment to neutrinos from an Ar-37 source," *Phys. Rev.* **C73** (2006) 045805, `arXiv:nucl-ex/0512041 [nucl-ex]`.

[170] C. Giunti and M. Laveder, "Short-Baseline Active-Sterile Neutrino Oscillations?," *Mod. Phys. Lett.* **A22** (2007) 2499–2509, `arXiv:hep-ph/0610352 [hep-ph]`.

[171] C. Giunti and M. Laveder, "Statistical Significance of the Gallium Anomaly," *Phys. Rev.* **C83** (2011) 065504, `arXiv:1006.3244 [hep-ph]`.

[172] C. Giunti, M. Laveder, Y. F. Li, Q. Y. Liu, and H. W. Long, "Update of Short-Baseline Electron Neutrino and Antineutrino Disappearance," *Phys. Rev.* **D86** (2012) 113014, `arXiv:1210.5715 [hep-ph]`.

[173] P. Anselmann *et al.*, "First results from the 51cr neutrino source experiment with the gallex detector," *Physics Letters B* **342** no. 1, (1995) 440 – 450. `http://www.sciencedirect.com/science/article/pii/0370269394015862`.

[174] W. Hampel *et al.*, "Final results of the 51cr neutrino source experiments in {GALLEX}," *Physics Letters B* **420** no. 1–2, (1998) 114 – 126. `http://www.sciencedirect.com/science/article/pii/S0370269397015621`.

[175] F. Kaether, W. Hampel, G. Heusser, J. Kiko, and T. Kirsten, "Reanalysis of the GALLEX solar neutrino flux and source experiments," *Phys. Lett.* **B685** (2010) 47–54, `arXiv:1001.2731 [hep-ex]`.

[176] J. N. Abdurashitov *et al.*, "The russian-american gallium experiment (sage) cr neutrino source measurement," *Phys. Rev. Lett.* **77** (Dec, 1996) 4708–4711. `https://link.aps.org/doi/10.1103/PhysRevLett.77.4708`.

[177] **SAGE** Collaboration, J. N. Abdurashitov *et al.*, "Measurement of the response of the Russian-American gallium experiment to neutrinos from a Cr-51 source," *Phys. Rev.* **C59** (1999) 2246–2263, `arXiv:hep-ph/9803418 [hep-ph]`.

[178] **SAGE** Collaboration, J. N. Abdurashitov *et al.*, "Measurement of the solar neutrino capture rate with gallium metal. III: Results for the 2002–2007 data-taking period," *Phys. Rev.* **C80** (2009) 015807, `arXiv:0901.2200 [nucl-ex]`.

[179] **KARMEN** Collaboration, B. Armbruster *et al.*, "Upper limits for neutrino oscillations muon-anti-neutrino —> electron-anti-neutrino from muon decay at rest," *Phys. Rev.* **D65** (2002) 112001, `arXiv:hep-ex/0203021 [hep-ex]`.

[180] B. Armbruster *et al.*, "Search for v¯μ→v¯e oscillations with karmen2," *Nuclear Physics A* **663** (2000) 803c – 806c. `http://www.sciencedirect.com/science/article/pii/S0375947499007575`.

[181] P. Huber, "On the determination of anti-neutrino spectra from nuclear reactors," *Phys. Rev.* **C84** (2011) 024617, `arXiv:1106.0687 [hep-ph]`. [Erratum: Phys. Rev.C85,029901(2012)].

[182] G. Mention, M. Fechner, T. Lasserre, T. Mueller, D. Lhuillier, *et al.*, "The Reactor Antineutrino Anomaly," *Phys.Rev.* **D83** (2011) 073006, `arXiv:1101.2755 [hep-ex]`.

[183] S. Gariazzo, C. Giunti, M. Laveder, and Y. F. Li, "Updated Global 3+1 Analysis of Short-BaseLine Neutrino Oscillations," *JHEP* **06** (2017) 135, `arXiv:1703.00860 [hep-ph]`.

[184] M. Dentler, A. Hernandez-Cabezudo, J. Kopp, M. Maltoni, and T. Schwetz, "Sterile neutrinos or flux uncertainties? — Status of the reactor anti-neutrino anomaly," *JHEP* **11** (2017) 099, `arXiv:1709.04294 [hep-ph]`.

[185] **Daya Bay** Collaboration, C. Zhang, "Recent Results from the Daya Bay Experiment," *AIP Conf. Proc.* **1666** (2015) 080003, `arXiv:1501.04991 [hep-ex]`.

[186] **Daya Bay** Collaboration, F. P. An *et al.*, "Measurement of the Reactor Antineutrino Flux and Spectrum at Daya Bay," *Phys. Rev. Lett.* **116** no. 6, (2016) 061801, `arXiv:1508.04233 [hep-ex]`. [Erratum: Phys. Rev. Lett.118,no.9,099902(2017)].

[187] **Daya Bay** Collaboration, L. Zhan, "Recent Results from Daya Bay," `arXiv:1506.01149 [hep-ex]`.

[188] **RENO** Collaboration, S.-H. Seo, "New Results from RENO and The 5 MeV Excess," *AIP Conf. Proc.* **1666** (2015) 080002, `arXiv:1410.7987 [hep-ex]`.

[189] **Double Chooz** Collaboration, J. I. Crespo-Anadón, "Double Chooz: Latest results," *Nucl. Part. Phys. Proc.* **265-266** (2015) 99–104, `arXiv:1412.3698 [hep-ex]`.

[190] A. M. Gago, M. M. Guzzo, P. C. de Holanda, H. Nunokawa, O. L. G. Peres, V. Pleitez, and R. Zukanovich Funchal, "Global analysis of the postSNO solar neutrino data for standard and nonstandard oscillation mechanisms," *Phys. Rev.* **D65** (2002) 073012, `arXiv:hep-ph/0112060 [hep-ph]`.

[191] **KamLAND** Collaboration, T. Araki *et al.*, "Measurement of neutrino oscillation with KamLAND: Evidence of spectral distortion," *Phys.Rev.Lett.* **94** (2005) 081801, `arXiv:hep-ex/0406035 [hep-ex]`.

[192] **KamLAND** Collaboration, A. Gando *et al.*, "Constraints on θ_{13} from A Three-Flavor Oscillation Analysis of Reactor Antineutrinos at KamLAND," *Phys. Rev.* **D83** (2011) 052002, `arXiv:1009.4771 [hep-ex]`.

[193] Y. Farzan and M. Tortola, "Neutrino oscillations and Non-Standard Interactions," `arXiv:1710.09360 [hep-ph]`.

[194] **Super-Kamiokande** Collaboration, Y. Ashie *et al.*, "A Measurement of atmospheric neutrino oscillation parameters by Super-Kamiokande I," *Phys.Rev.* **D71** (2005) 112005, `arXiv:hep-ex/0501064 [hep-ex]`.

[195] **MINOS** Collaboration, P. Adamson *et al.*, "Combined analysis of ν_μ disappearance and $\nu_\mu \to \nu_e$ appearance in MINOS using accelerator and atmospheric neutrinos," *Phys.Rev.Lett.* (2014) , `arXiv:1403.0867 [hep-ex]`.

[196] **Daya Bay** Collaboration, F. An *et al.*, "Observation of electron-antineutrino disappearance at Daya Bay," *Phys.Rev.Lett.* **108** (2012) 171803, `arXiv:1203.1669 [hep-ex]`.

[197] **RENO** Collaboration, J. Ahn *et al.*, "Observation of Reactor Electron Antineutrino Disappearance in the RENO Experiment," *Phys.Rev.Lett.* **108** (2012) 191802, `arXiv:1204.0626 [hep-ex]`.

[198] **Daya Bay** Collaboration, F. P. An *et al.*, "Measurement of electron antineutrino oscillation based on 1230 days of operation of the Daya Bay experiment," *Phys. Rev.* **D95** no. 7, (2017) 072006, `arXiv:1610.04802 [hep-ex]`.

[199] **T2K** Collaboration, K. Abe *et al.*, "Measurements of neutrino oscillation in appearance and disappearance channels by the T2K experiment with 6.6×10^{20} protons on target," *Phys.Rev.* **D91** (2015) 072010, `arXiv:1502.01550 [hep-ex]`.

[200] H. Minakata, H. Nunokawa, S. J. Parke, and R. Zukanovich Funchal, "Determining neutrino mass hierarchy by precision measurements in electron and muon neutrino disappearance experiments," *Phys. Rev.* **D74** (2006) 053008, `arXiv:hep-ph/0607284 [hep-ph]`.

[201] **Intensity Frontier Neutrino Working Group** Collaboration, A. de Gouvea *et al.*, “Working Group Report: Neutrinos,” in *Proceedings, 2013 Community Summer Study on the Future of U.S. Particle Physics: Snowmass on the Mississippi (CSS2013): Minneapolis, MN, USA, July 29-August 6, 2013*. 2013. `arXiv:1310.4340 [hep-ex]`. `https://inspirehep.net/record/1260555/files/arXiv:1310.4340.pdf`.

[202] http://t2k-experiment.org/2017/08/t2k-2017-cpv/.

[203] G. H. Collin, C. A. Argüelles, J. M. Conrad, and M. H. Shaevitz, “First Constraints on the Complete Neutrino Mixing Matrix with a Sterile Neutrino,” *Phys. Rev. Lett.* **117** no. 22, (2016) 221801, `arXiv:1607.00011 [hep-ph]`.

[204] S. Choubey, “Signature of sterile species in atmospheric neutrino data at neutrino telescopes,” *JHEP* **12** (2007) 014, `arXiv:0709.1937 [hep-ph]`.

[205] S. Razzaque and A. Yu. Smirnov, “Searching for sterile neutrinos in ice,” *JHEP* **07** (2011) 084, `arXiv:1104.1390 [hep-ph]`.

[206] S. Razzaque and A. Yu. Smirnov, “Searches for sterile neutrinos with IceCube DeepCore,” *Phys. Rev.* **D85** (2012) 093010, `arXiv:1203.5406 [hep-ph]`.

[207] A. Esmaili, F. Halzen, and O. L. G. Peres, “Constraining Sterile Neutrinos with AMANDA and IceCube Atmospheric Neutrino Data,” *JCAP* **1211** (2012) 041, `arXiv:1206.6903 [hep-ph]`.

[208] A. Esmaili and A. Y. Smirnov, “Restricting the LSND and MiniBooNE sterile neutrinos with the IceCube atmospheric neutrino data,” *JHEP* **1312** (2013) 014, `arXiv:1307.6824 [hep-ph]`.

[209] A. Esmaili, F. Halzen, and O. L. G. Peres, “Exploring $\nu_\tau - \nu_s$ mixing with cascade events in DeepCore,” *JCAP* **1307** (2013) 048, `arXiv:1303.3294 [hep-ph]`.

[210] M. Lindner, W. Rodejohann, and X.-J. Xu, “Sterile neutrinos in the light of IceCube,” `arXiv:1510.00666 [hep-ph]`.

[211] **IceCube** Collaboration, M. G. Aartsen *et al.*, “Search for sterile neutrino mixing using three years of IceCube DeepCore data,” *Phys. Rev.* **D95** no. 11, (2017) 112002, `arXiv:1702.05160 [hep-ex]`.

[212] C. Giunti, M. Laveder, Y. F. Li, and H. W. Long, "Short-baseline electron neutrino oscillation length after troitsk," *Phys. Rev.* **D87** no. 1, (2013) 013004, `arXiv:1212.3805 [hep-ph]`.

[213] G. H. Collin, C. A. Argüelles, J. M. Conrad, and M. H. Shaevitz, "Sterile Neutrino Fits to Short Baseline Data," *Nucl. Phys.* **B908** (2016) 354–365, `arXiv:1602.00671 [hep-ph]`.

[214] F. Capozzi, C. Giunti, M. Laveder, and A. Palazzo, "Joint short- and long-baseline constraints on light sterile neutrinos," *Phys. Rev.* **D95** no. 3, (2017) 033006, `arXiv:1612.07764 [hep-ph]`.

[215] S. K. Agarwalla, S. S. Chatterjee, A. Dasgupta, and A. Palazzo, "Discovery Potential of T2K and NOvA in the Presence of a Light Sterile Neutrino," *JHEP* **02** (2016) 111, `arXiv:1601.05995 [hep-ph]`.

[216] S. K. Agarwalla, S. S. Chatterjee, and A. Palazzo, "Physics Reach of DUNE with a Light Sterile Neutrino," *JHEP* **09** (2016) 016, `arXiv:1603.03759 [hep-ph]`.

[217] S. K. Agarwalla, S. S. Chatterjee, and A. Palazzo, "Octant of θ_{23} in danger with a light sterile neutrino," *Phys. Rev. Lett.* **118** no. 3, (2017) 031804, `arXiv:1605.04299 [hep-ph]`.

[218] S. S. Chatterjee, A. Dasgupta, and S. K. Agarwalla, "Exploring Flavor-Dependent Long-Range Forces in Long-Baseline Neutrino Oscillation Experiments," *JHEP* **12** (2015) 167, `arXiv:1509.03517 [hep-ph]`.

[219] P. Huber, M. Lindner, and W. Winter, "Simulation of long-baseline neutrino oscillation experiments with GLoBES (General Long Baseline Experiment Simulator)," *Comput.Phys.Commun.* **167** (2005) 195, `arXiv:hep-ph/0407333 [hep-ph]`.

[220] P. Huber, J. Kopp, M. Lindner, M. Rolinec, and W. Winter, "New features in the simulation of neutrino oscillation experiments with GLoBES 3.0: General Long Baseline Experiment Simulator," *Comput.Phys.Commun.* **177** (2007) 432–438, `arXiv:hep-ph/0701187 [hep-ph]`.

[221] J. Kopp, "Sterile neutrinos and non-standard neutrino interactions in GLoBES,".

[222] **DUNE** Collaboration, R. Acciarri *et al.*, “Long-Baseline Neutrino Facility (LBNF) and Deep Underground Neutrino Experiment (DUNE) Conceptual Design Report Volume 1: The LBNF and DUNE Projects,” `arXiv:1601.05471 [physics.ins-det]`.

[223] **DUNE** Collaboration, J. Strait *et al.*, “Long-Baseline Neutrino Facility (LBNF) and Deep Underground Neutrino Experiment (DUNE) Conceptual Design Report Volume 3: Long-Baseline Neutrino Facility for DUNE June 24, 2015,” `arXiv:1601.05823 [physics.ins-det]`.

[224] **DUNE** Collaboration, R. Acciarri *et al.*, “Long-Baseline Neutrino Facility (LBNF) and Deep Underground Neutrino Experiment (DUNE) Conceptual Design Report, Volume 4 The DUNE Detectors at LBNF,” `arXiv:1601.02984 [physics.ins-det]`.

[225] **LBNE** Collaboration, C. Adams *et al.*, “The Long-Baseline Neutrino Experiment: Exploring Fundamental Symmetries of the Universe,” `arXiv:1307.7335 [hep-ex]`.

[226] M. Diwan, D. Beavis, M.-C. Chen, J. Gallardo, S. Kahn, *et al.*, “Very long baseline neutrino oscillation experiments for precise measurements of mixing parameters and CP violating effects,” *Phys.Rev.* **D68** (2003) 012002, `arXiv:hep-ph/0303081 [hep-ph]`.

[227] V. Barger, M. Bishai, D. Bogert, C. Bromberg, A. Curioni, *et al.*, “Report of the US long baseline neutrino experiment study,” `arXiv:0705.4396 [hep-ph]`.

[228] P. Huber and J. Kopp, “Two experiments for the price of one? – The role of the second oscillation maximum in long baseline neutrino experiments,” *JHEP* **1103** (2011) 013, `arXiv:1010.3706 [hep-ph]`.

[229] `http://www.dunescience.org`. Deep Underground Neutrino Experiment (DUNE), http://www.dunescience.org.

[230] **ICARUS** Collaboration, S. Amerio *et al.*, “Design, construction and tests of the ICARUS T600 detector,” *Nucl. Instrum. Meth.* **A527** (2004) 329–410.

[231] Mary Bishai. private communication, 2012.

[232] M. D. Messier, *Evidence for neutrino mass from observations of atmospheric neutrinos with Super-Kamiokande*. PhD thesis, Boston U., 1999. `http://wwwlib.umi.com/dissertations/fullcit?p9923965`.

[233] E. A. Paschos and J. Y. Yu, "Neutrino interactions in oscillation experiments," *Phys. Rev.* **D65** (2002) 033002, `arXiv:hep-ph/0107261 [hep-ph]`.

[234] Geralyn Zeller. private communication, 2012.

[235] R. Petti and G. Zeller, "Nuclear Effects in Water vs. Argon.". Tech. Rep. LBNE docdb No. 740.

[236] A. Stahl, C. Wiebusch, A. Guler, M. Kamiscioglu, R. Sever, *et al.*, "Expression of Interest for a very long baseline neutrino oscillation experiment (LBNO),".

[237] Silvestro di Luise, "Optimization of Neutrino Fluxes for Future Long Baseline Neutrino Experiment," 2012. Poster presented at the ICHEP2012 Conference, July 4-11, 2012, Melbourne, Australia, `www.ichep2012.com.au/`.

[238] A. Para and M. Szleper, "Neutrino oscillations experiments using off-axis NuMI beam," `arXiv:hep-ex/0110032 [hep-ex]`.

[239] **T2K** Collaboration, K. Abe *et al.*, "Observation of Electron Neutrino Appearance in a Muon Neutrino Beam," *Phys.Rev.Lett.* **112** (2014) 061802, `arXiv:1311.4750 [hep-ex]`.

[240] **T2K** Collaboration, M. Ravonel, "Antineutrino oscillations with T2K," 2015. Talk given at the EPS-HEP 2015 Conference, July 22-29, 2015, Vienna, Austria, `https://indico.cern.ch/event/356420/session/10/contribution/322`.

[241] **T2K** Collaboration, M. R. Salzgeber, "Anti-neutrino oscillations with T2K," `arXiv:1508.06153 [hep-ex]`.

[242] **T2K** Collaboration, K. Abe *et al.*, "Neutrino oscillation physics potential of the T2K experiment," *PTEP* **2015** no. 4, (2015) 043C01, `arXiv:1409.7469 [hep-ex]`.

[243] **NOvA** Collaboration, D. Ayres *et al.*, "NOvA: Proposal to build a 30 kiloton off-axis detector to study nu(mu) —> nu(e) oscillations in the NuMI beamline," `arXiv:hep-ex/0503053 [hep-ex]`.

[244] **NOvA** Collaboration, R. Patterson, "The NOvA Experiment: Status and Outlook," *Nucl.Phys.Proc.Suppl.* **235-236** (2013) 151–157, `arXiv:1209.0716 [hep-ex]`.

[245] **NuMI, NOvA and LBNE** Collaboration, S. Childress and J. Strait, "Long baseline neutrino beams at Fermilab," `arXiv:1304.4899 [physics.acc-ph]`.

[246] **NOvA** Collaboration, R. Patterson, "First oscillation results from NOvA," 2015. Talk given at the Joint Experimental-Theoretical Physics Seminar, Fermilab, 6th August, 2015, `http://nova-docdb.fnal.gov/cgi-bin/RetrieveFile?docid=13883&filename=20150806_nova_docdb.pdf&version=2`.

[247] **NOvA** Collaboration, J. Bian, "First Results of ν_e Appearance Analysis and Electron Neutrino Identification at NOvA," in *Meeting of the APS Division of Particles and Fields (DPF 2015) Ann Arbor, Michigan, USA, August 4-8, 2015*. 2015. `arXiv:1510.05708 [hep-ex]`. `http://inspirehep.net/record/1399048/files/arXiv:1510.05708.pdf`.

[248] **NOvA** Collaboration, P. Adamson *et al.*, "First measurement of muon-neutrino disappearance in NOvA," `arXiv:1601.05037 [hep-ex]`.

[249] S. K. Agarwalla, S. Prakash, S. K. Raut, and S. U. Sankar, "Potential of optimized NOvA for large $\theta_(13)$ and combined performance with a LArTPC and T2K," *JHEP* **1212** (2012) 075, `arXiv:1208.3644 [hep-ph]`.

[250] P. Huber, M. Lindner, and W. Winter, "Superbeams versus neutrino factories," *Nucl.Phys.* **B645** (2002) 3–48, `arXiv:hep-ph/0204352 [hep-ph]`.

[251] G. Fogli, E. Lisi, A. Marrone, D. Montanino, and A. Palazzo, "Getting the most from the statistical analysis of solar neutrino oscillations," *Phys.Rev.* **D66** (2002) 053010, `arXiv:hep-ph/0206162 [hep-ph]`.

[252] D. Ayres, G. Drake, M. Goodman, V. Guarino, T. Joffe-Minor, *et al.*, "Letter of Intent to build an Off-axis Detector to study numu to nue oscillations with the NuMI Neutrino Beam," `arXiv:hep-ex/0210005 [hep-ex]`.

[253] F. Capozzi, G. Fogli, E. Lisi, A. Marrone, D. Montanino, *et al.*, "Status of three-neutrino oscillation parameters, circa 2013," *Phys.Rev.* **D89** (2014) 093018, `arXiv:1312.2878 [hep-ph]`.

[254] M. Gonzalez-Garcia, M. Maltoni, and T. Schwetz, “Updated fit to three neutrino mixing: status of leptonic CP violation,” *JHEP* **1411** (2014) 052, `arXiv:1409.5439 [hep-ph]`.

[255] A. Cervera *et al.*, “Golden measurements at a neutrino factory,” *Nucl. Phys.* **B579** (2000) 17–55, `arXiv:hep-ph/0002108`. [Erratum-ibid.B593:731-732,2001].

[256] K. Asano and H. Minakata, “Large-Theta(13) Perturbation Theory of Neutrino Oscillation for Long-Baseline Experiments,” *JHEP* **06** (2011) 022, `arXiv:1103.4387 [hep-ph]`.

[257] S. K. Agarwalla, Y. Kao, and T. Takeuchi, “Analytical approximation of the neutrino oscillation matter effects at large θ_{13},” *JHEP* **1404** (2014) 047, `arXiv:1302.6773 [hep-ph]`.

[258] A. Friedland and I. M. Shoemaker, “Searching for Novel Neutrino Interactions at NOvA and Beyond in Light of Large θ_{13},” `arXiv:1207.6642 [hep-ph]`.

[259] S. K. Agarwalla, S. Prakash, and W. Wang, “High-precision measurement of atmospheric mass-squared splitting with T2K and NOvA,” `arXiv:1312.1477 [hep-ph]`.

[260] A. M. Dziewonski and D. L. Anderson, “Preliminary reference earth model,” *Physics of the Earth and Planetary Interiors* **25** (1981) 297–356.

[261] M. Blennow, P. Coloma, P. Huber, and T. Schwetz, “Quantifying the sensitivity of oscillation experiments to the neutrino mass ordering,” *JHEP* **1403** (2014) 028, `arXiv:1311.1822 [hep-ph]`.

[262] M. C. Gonzalez-Garcia, M. Maltoni, and T. Schwetz, “Global Analyses of Neutrino Oscillation Experiments,” `arXiv:1512.06856 [hep-ph]`.

[263] P. Langacker, “The Physics of Heavy Z' Gauge Bosons,” *Rev. Mod. Phys.* **81** (2009) 1199–1228, `arXiv:0801.1345 [hep-ph]`.

[264] R. Foot, “New Physics From Electric Charge Quantization?,” *Mod.Phys.Lett.* **A6** (1991) 527–530.

[265] X.-G. He, G. C. Joshi, H. Lew, and R. Volkas, "Simplest Z-prime model," *Phys.Rev.* **D44** (1991) 2118–2132.

[266] **Particle Data Group** Collaboration, K. Olive *et al.*, "Review of Particle Physics," *Chin.Phys.* **C38** (2014) 090001.

[267] R. Foot, "Avoiding the gauge hierarchy problem with see-sawed neutrino masses," *Mod. Phys. Lett.* **A20** (2005) 3035–3044, `arXiv:hep-ph/0505154 [hep-ph]`.

[268] **L3** Collaboration, M. Acciarri *et al.*, "Search for manifestations of new physics in fermion pair production at LEP," *Phys. Lett.* **B489** (2000) 81–92, `arXiv:hep-ex/0005028 [hep-ex]`.

[269] **OPAL** Collaboration, G. Abbiendi *et al.*, "Tests of the standard model and constraints on new physics from measurements of fermion pair production at 189-GeV to 209-GeV at LEP," *Eur. Phys. J.* **C33** (2004) 173–212, `arXiv:hep-ex/0309053 [hep-ex]`.

[270] **DELPHI** Collaboration, J. Abdallah *et al.*, "Measurement and interpretation of fermion-pair production at LEP energies above the Z resonance," *Eur. Phys. J.* **C45** (2006) 589–632, `arXiv:hep-ex/0512012 [hep-ex]`.

[271] **ALEPH** Collaboration, S. Schael *et al.*, "Fermion pair production in e^+e^- collisions at 189-209-GeV and constraints on physics beyond the standard model," *Eur. Phys. J.* **C49** (2007) 411–437, `arXiv:hep-ex/0609051 [hep-ex]`.

[272] M. Honda, Y. Kao, N. Okamura, A. Pronin, and T. Takeuchi, "Constraints on New Physics from Long Baseline Neutrino Oscillation Experiments," `arXiv:0707.4545 [hep-ph]`.

[273] G. Dutta, A. S. Joshipura, and K. B. Vijaykumar, "Leptonic flavor violations in the presence of an extra Z," *Phys. Rev.* **D50** (1994) 2109–2115, `arXiv:hep-ph/9405292 [hep-ph]`.

[274] J. G. Williams, S. G. Turyshev, and D. H. Boggs, "Progress in lunar laser ranging tests of relativistic gravity," *Phys. Rev. Lett.* **93** (2004) 261101, `arXiv:gr-qc/0411113 [gr-qc]`.

[275] J. Williams, X. Newhall, and J. Dickey, “Relativity parameters determined from lunar laser ranging,” *Phys.Rev.* **D53** (1996) 6730–6739.

[276] A. Dolgov, “Long range forces in the universe,” *Phys.Rept.* **320** (1999) 1–15.

[277] L. Okun, “Leptons and photons,” *Phys. Lett.* **B382** (1996) 389–392, `arXiv:hep-ph/9512436 [hep-ph]`.

[278] J. Grifols, E. Masso, and S. Peris, “Supernova neutrinos as probes of long range nongravitational interactions of dark matter,” *Astropart.Phys.* **2** (1994) 161–165.

[279] J. Grifols, E. Masso, and R. Toldra, “Majorana neutrinos and long range forces,” *Phys.Lett.* **B389** (1996) 563–565, `arXiv:hep-ph/9606377 [hep-ph]`.

[280] R. Horvat, “Supernova MSW effect in the presence of leptonic long range forces,” *Phys.Lett.* **B366** (1996) 241–247.

[281] S. K. Agarwalla, Y. Kao, D. Saha, and T. Takeuchi, “Running of Neutrino Oscillation Parameters in Matter with Flavor-Diagonal Non-Standard Interactions of the Neutrino,” `arXiv:1506.08464 [hep-ph]`.

[282] J. N. Bahcall, *Neutrino Astrophysics*. Cambridge University Press, Cambridge, England, 1989.

[283] J. Heeck and W. Rodejohann, “Gauged Lmu - Ltau and different Muon Neutrino and Anti-Neutrino Oscillations: MINOS and beyond,” *J.Phys.* **G38** (2011) 085005, `arXiv:1007.2655 [hep-ph]`.

[284] H. Davoudiasl, H.-S. Lee, and W. J. Marciano, “Long-Range Lepton Flavor Interactions and Neutrino Oscillations,” *Phys.Rev.* **D84** (2011) 013009, `arXiv:1102.5352 [hep-ph]`.

[285] B. Pontecorvo, “Inverse beta-processes and non-conservation of lepton charge,”.

[286] **MINOS** Collaboration, R. Nichol, “New results from MINOS,” *Nucl.Phys.Proc.Suppl.* **235-236** (2013) 105–111.

[287] **MINOS** Collaboration, P. Adamson *et al.*, “Measurement of Neutrino and Antineutrino Oscillations Using Beam and Atmospheric Data in MINOS,” *Phys.Rev.Lett.* **110** no. 25, (2013) 251801, `arXiv:1304.6335 [hep-ex]`.

[288] H. Nunokawa, S. J. Parke, and R. Zukanovich Funchal, "Another possible way to determine the neutrino mass hierarchy," *Phys.Rev.* **D72** (2005) 013009, `arXiv:hep-ph/0503283 [hep-ph]`.

[289] A. de Gouvea, J. Jenkins, and B. Kayser, "Neutrino mass hierarchy, vacuum oscillations, and vanishing |U(e3)|," *Phys. Rev.* **D71** (2005) 113009, `arXiv:hep-ph/0503079 [hep-ph]`.

[290] K. S. Babu, C. Kolda, and J. March-Russell, "Implications of generalized $Z - Z'$ mixing," *Phys. Rev. D* **57** (Jun, 1998) 6788–6792. `http://link.aps.org/doi/10.1103/PhysRevD.57.6788`.

[291] B. Holdom, "Two U(1)'s and Epsilon Charge Shifts," *Phys.Lett.* **B166** (1986) 196.